University of Liverpool

Doctoral Thesis

Meteotsunami generation, amplification and occurrence in north-west Europe

Thesis submitted in accordance with the requirements of the University of Liverpool for the degree of Doctor in Philosophy

by

David Alan Williams

November 2019

Declaration of Authorship

I declare that this thesis titled “Meteotsunami generation, amplification and occurrence in north-west Europe” and the work presented in it are my own work. The material contained in the thesis has not been presented, nor is currently being presented, either wholly or in part, for any other degree or qualification.

Signed

_____

Date

_____

David A Williams

Meteotsunami generation, amplification and occurrence in north-west Europe

David A Williams

Abstract

Meteotsunamis are atmospherically generated tsunamis with characteristics similar to all other tsunamis, and periods between 2–120 minutes. They are associated with strong currents and may unexpectedly cause large floods. Of highest concern, meteotsunamis have injured and killed people in several locations around the world. To date, a few meteotsunamis have been identified in north-west Europe. This thesis aims to increase the preparedness for meteotsunami occurrences in north-west Europe, by understanding how, when and where meteotsunamis are generated.

A summer-time meteotsunami in the English Channel is studied, and its generation is examined through hydrodynamic numerical simulations. Simple representations of the atmospheric system are used, and termed synthetic modelling. The identified meteotsunami was partly generated by an atmospheric system moving at the shallow-water wave speed, a mechanism called Proudman resonance. Wave heights in the English Channel are also sensitive to the tide, because tidal currents change the shallow-water wave speed.

To explain meteotsunami growth in a wider range of conditions, a generalised understanding of Proudman resonance is developed through idealised simulations and analytical models. Most surprisingly, wave amplification near predictions of Proudman resonance can occur even if the instantaneous forcing speed deviates from the mean forcing speed by 18%. This amplification can happen if the atmospheric forcing remains over the meteotsunami.

Broader context is given to meteotsunami case studies in north-west Europe through an 8-yr climatology. In total, 349 meteotsunamis are identified and 256 associated mesoscale atmospheric systems are classified. Of meteotsunamis between 2010–2017, 79% were smaller than 0.5 m and about half occurred in winter. Of the classified atmospheric systems, 46% were quasi-linear systems and 33% were open-cellular convection. For 45 meteotsunamis in France, the mesoscale atmospheric systems occurred within well-documented synoptic atmospheric conditions, and there is evidence of repeated favourable conditions for Proudman resonance.

Finally, a new explanation of how open-cellular convection generates meteotsunamis is developed through synthetic models. Open-cellular convection is modelled as a repeating field of individual cells moving at the shallow-water wave speed. Each individual cell generates an individual wave. When these individual waves form a linear superposition, constructive interference of repeating waves can lead to a larger meteotsunami than would be expected from single individual cells.

Contents

List of Figures

List of Tables

Acknowledgements

Who let this happen?!

First, I thank the organisation that let me study such an interesting topic. The Natural Environmental Research Council (NERC) funded the project and training, spanning the University of Liverpool and the University of Manchester. I also thank National Oceanography Centre, which provided me the space to work, walk and think. The people within these buildings, my fellow researchers and colleagues, gave invaluable conversations and insight.

I specifically thank my supervisors. First, I thank Kevin Horsburgh, who remained a consistent source of calm encouragement. I think he could tell when I was avoiding a problem—the pragmatic advice to bite the bullet almost always worked. Second, I thank Dave Schultz, for his incredibly patient review of my written work. I will endeavour to remember the grammar of conjunctions, however I might still make mistakes every so often. Third, I thank Chris Hughes, who on more than one occasion managed to understand what I meant as I muddled through an explanation of some half thought-out idea that usually turned out to be wrong. When it was needed, he provided clarity.

Now, it's time to thank my friends. Maybe for some of you (if you ever read this, I'm looking at you Kieran, Shaun, Dave, Kat and Lewis) these words will resonate: burritos, crosswords, Ribena, hope, and anchor. I think that one of my biggest surprises over the past four years is that some of you even managed to get me into a gym, albeit through the initial sly guise of playing squash.

To my friends outside of academia, thank you for your friendship and support, especially those of you came to support me at talks and shows, or let me ramble on at length about my work or problems. A special thank you to Felicity, who probably hasn't even realised how much she has kept my chin up whilst I've put my head down to work. Those walks really did the trick.

Finally, I cannot thank my family enough. For all that I have done over the past 4 years (and 22 years before that), not one part, ounce or drop of it would have been possible without your continued support. I can only apologise for the stress I've caused.

Chapter 1

Introduction

1.1 Motivation, Problem and Solution

On a sunny day in July 1929, an unexpectedly large wave, accompanied by a line of storms, hit the south coast of the United Kingdom. This wave rose up to between 3.5–6.0-m high, killing two people (Douglas 1929). Even though it was "remarkable" and presented "such interesting problems" (Douglas 1929), there was no English word for such a wave. However, unknown to anyone at the time, waves of this description had previously occurred around the world. They were called *abiki* in Japan (Hibiya and Kajiura 1982), *rissaga* in Spain (Monserrat et al. 1991), and *sčiga* in Croatia (Orlić 1980). Tsunami-like waves that are generated by the atmosphere are now called *meteotsunamis*. For those of us lucky enough to study meteotsunamis, they remain as remarkable and interesting today as they were for C.K.M. Douglas ninety years ago.

Meteotsunamis are not often large (meaning more than about 2-m high). In fact, they are often small (less than about 0.5-m high) (e.g. Bechle et al. 2016; Olabarrieta et al. 2017; Vilibić and Šepić 2017; Dusek et al. 2019). However, when large meteotsunamis do happen they are *noticed* (e.g. Orlić 1980; Hibiya and Kajiura 1982; Monserrat et al. 2006). For example, a video from the Netherlands of a tsunami-like wave on 29 May 2017 has accumulated nearly 1.5 million views on social media (Figure 1.1). Over a few minutes, at about 0620 local time, this wave approached from the south-west and flooded Zandvoort beach. At the time, many people were unsure what this wave was (with some interested members of the public claiming on the video that there was no possible way that a tsunami could occur in the Netherlands). However, no one could deny that it was both large and unexpected. Since then, this wave has been confirmed as a meteotsunami through numerical simulations, revealing it was generated by a passing line of storms (Vatvani et al. 2018). Interestingly, this line of storms in 2019 follows a similar description to the "line squall" that accompanied the fatal wave in 1929 (Douglas 1929).

Thus, there is a problem. There are dangerous waves that can cause injuries (e.g. Sibley et al. 2016) and fatalities (e.g. Douglas 1929; Ewing et al. 1954; Monserrat et al. 2006; Linares et al. 2019), but they are often unexpected, and so it is difficult to

keep people safe. Preparing for these unexpectedly large, yet rare, ocean waves is essentially the overarching aim of modern meteotsunami research (Vilibić et al. 2016).

Preparing for a meteotsunami, it first helps to understand how, where and when meteotsunamis occur. This requires a multidisciplinary research approach, combining the fields of physical oceanography, atmospheric dynamics and atmosphere–ocean interactions. Four distinct chapters, which each include aspects from all three disciplines, are developed in this dissertation. Linking these four chapters is a focus on meteotsunamis in north-west Europe.

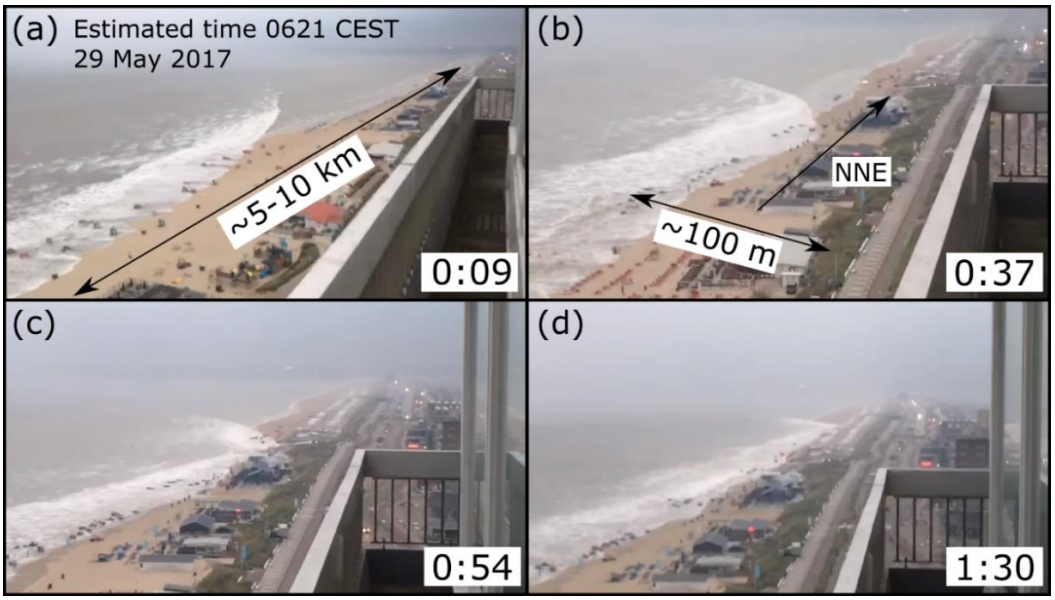

Figure 1.1 The Dutch meteotsunami (Jan Konig 2017) that approached Zandvoort on 29 May 2017, at about 0620 CEST (local time). Each panel refers to a screenshot from the video, with the video time in the bottom-right corner (a) 9 seconds (b) 37 seconds, (c) 54 seconds, (d) 1 minute 30 seconds. The view of the beach spans about 5–10 km, and the beach is about 100 m from the trees to high tide, and the bearing of the beach is about 023º (NNE) (estimated with Google Earth).

North-west Europe has had a handful of documented historical meteotsunami events (Haslett et al. 2009; Tappin et al. 2013; Frère et al. 2014; Sibley et al. 2016) and a few long-term statistical analyses of atmospherically-generated waves that are similar to meteotsunamis (e.g. de Jong et al. 2003; de Jong and Battjes 2004; Oszoy et al. 2016). However, understanding how, where and when meteotsunamis occur across the region is unknown. As north-west Europe is potentially under-prepared for another large

meteotsunami (e.g. Douglas 1929), this dissertation focusses on the ocean dynamics and atmosphere–ocean interactions that are relevant to north-west Europe.

1.2 Thesis approach and structure

This dissertation includes an introduction to meteotsunamis (Chapter 1), the relevant meteotsunami dynamics to understand (Chapter 2), and a general review of the methods (Chapter 3). Then, four article-format chapters (Chapters 4–7) answer a different question surrounding meteotsunamis in north-west Europe. These article-format chapters are linked by expanding upon questions that arose from the results of previous chapters. Each of the four article-format chapters has a multidisciplinary approach, with contributions from physical oceanography, atmospheric dynamics and atmosphere–ocean interactions.

In the first article-format chapter, Chapter 4, simulations are produced that are based on observational analyses of a case study in the English Channel. Evidence from this case study supports previously proposed meteotsunami generation mechanisms, and also reveals interactions between tidal currents and meteotsunami growth that had been previously overlooked. However, a generalised understanding of meteotsunami formation in north-west Europe could not be developed from a case study alone.

Therefore, in Chapter 5, a more generalised understanding of meteotsunami formation is developed. Using both highly idealised simulations and analytical models, how tides, bathymetry, and atmospheric variability affects meteotsunami growth is explained. By understanding meteotsunami generation processes, this helps guide which physical processes are important to include, or omit, when simulating or forecasting meteotsunamis (e.g. Whitmore and Knight 2014; Linares et al. 2016; Denamiel et al. 2019; Romero et al. 2019).

Then, in Chapter 6, context is given to the case study and other meteotsunamis around north-west Europe through a climatology. This climatology quantifies the size-occurrence rates of meteotsunamis across north-west Europe, shows when meteotsunamis happen over seasonal and diurnal cycles, classifies atmospheric weather systems that were coincident with meteotsunamis, and analyses the coincident large-scale atmospheric conditions. The information collected in this climatology provides the first quantification of meteotsunami hazard and reveals which

atmospheric systems are most commonly associated with meteotsunamis in north-west Europe.

Using insight from this climatology, in Chapter 7, a new explanation for meteotsunami generation is developed for a specific weather system (open-cellular convection) that is associated with meteotsunamis in north-west Europe. This explanation complements previous meteotsunami generation hypotheses (e.g. de Jong and Battjes 2004), but newly recognises the importance of physical properties of open-cellular convection to generate meteotsunamis.

After the article-format chapters, Chapter 8 concludes. This chapter summarises the dissertation narrative, describes the limitations of the work and highlights sensible future directions. Finally, the context of meteotsunamis in a changing climate is addressed, highlighting the importance of understanding meteotsunamis as a source of extreme sea levels in the coming decades.

1.3 A general background of meteotsunamis

1.3.1 Addressing common misconceptions

"But…what exactly is a meteotsunami?" This is probably the most commonly asked question of a meteotsunami researcher, whether it comes from a fellow oceanographer, a meteorologist, or an interested member of the public. To help answer this question, the longer version of the name helps. Meteotsunami is short for meteorological tsunami. A meteotsunami is an ocean wave with the properties of a tsunami that is made by the atmosphere. Non-seismic waves can be tsunamis, because the term "tsunami" only refers to a wave that has tsunami-like properties (e.g. Levin and Nosov 2016). For example, the dynamics that govern the speed of a tsunami wave is consistent between tsunamis. A tsunami can be generated from an earthquake (termed seismogenic tsunamis, e.g. Poisson et al. 2011; Yoshida et al. 2011; Ulutas 2013), a landslide (e.g. Masson et al. 2006; Løvholt et al. 2008; Hill et al. 2014), a volcano (e.g. Latter 1981; Giachetti et al. 2012; Mutaqin et al. 2019; Grilli et al. 2019), a meteorite (e.g. Wünnemann et al. 2010), or even the atmosphere (e.g. Monserrat et al. 2006). Without more background information, it is difficult to tell what has generated a tsunami (e.g. Monserrat et al. 2006; Levin and Nosov 2016).

Therefore, to understand the answer to *"What is a meteotsunami?"*, it is most helpful to start with *"What is a tsunami?*" and how a tsunami has been defined, at least in meteotsunami literature (e.g. Monserrat et al. 2006). Three common but incorrect thoughts tend to persist: (1) a tsunami is a wave generated by an earthquake, (2) a tsunami is either a large or destructive wave, and (3) a tsunami is synonymous with a tidal wave. A tsunami is not necessarily generated by an earthquake, it is not necessarily a large wave, and it is not related to the tide. Quite simply, a tsunami is a "long" wave (e.g. Levin and Nosov 2016). Descriptions of tsunami waves hitting beaches reveal this characteristic. Typically, eye-witnesses report that an unexpected wave arrived, or that the water retreated, and then over a few minutes, or even up to an hour or so, the wave returned and inundated land, sometimes repeating many times (e.g. Papadopoulos et al. 2006; Monserrat et al. 2006; Vučetić et al. 2009). This length of the wave is the basis of how a tsunami is defined; specifically, a tsunami is defined as a wave with a dominant period between 2 minutes and 2 hours (Monserrat et al. 2006).

Although tsunamis are not defined by wave amplitude, they can still be large. Research into tsunami-generation mechanisms substantially increased after the Indonesian tsunami of 26 Dec 2004 that caused over 220,000 fatalities (e.g. Papadopoulos et al. 2006; Geist et al. 2007; Rhie et al. 2007; Seno and Hirata 2007; Poisson et al. 2011; Levin and Nosov 2016). Yet, seven years later, following this uptake in research, the Japanese tsunami on 11 Mar 2011 proved that the behaviour, occurrence and size of tsunamis could still surprise even one of the most prepared nations. The Japanese tsunami caused over 18,000 fatalities (e.g. Hayashi et al. 2011; Yoshida et al. 2011; Grilli et al. 2013; Ulutas 2013; Levin and Nosov 2016) and the tsunami triggered the arguably preventable Fukushima nuclear disaster (Funabashi and Kitazawa 2012). Furthermore, the possibility of very large, landslide-generated "megatsunamis" has warranted study of their possible effects around north-west Europe (e.g. Løvholt et al. 2008; Hill et al. 2014). Even during the work of this dissertation, tsunamis from non-seismic origin have been unexpected and dangerous around the world. The collapse of the south-western portion of the Anak Krakatoa volcano in Indonesia on 22 December 2018 caused a tsunami that killed at least 437 people and injured thousands (Grilli et al. 2019). Unfortunately, a flank collapse of Anak Krakatau and subsequent tsunami had been hypothesised at least six years before the event (Giachetti et al. 2012).

However, there were still hundreds of fatalities due to insufficient warning systems. Furthermore, the short lead-time of such events poses further technological challenges, requiring consistent analysis of many data sources and rapid broadcasting of information.

Finally, to bring us back to misconceptions about meteotsunamis in the context of other tsunami hazards: dangerous tsunamis are not always large tsunamis. Although large tsunamis may lead to very many fatalities and cause floods that extend for tens of kilometres inland, the number of fatalities from meteotsunamis does not seem to be always related to high amplitude waves. This is exemplified by one of the largest meteotsunamis ever recorded, which occurred at Vela Luka Bay in 1978. Inside the bay, the meteotsunami was 6-m high and caused over $7 million in economic damages but had no recorded fatalities (Vučetić et al. 2009). In contrast, on 4 July 2003 in Lake Michigan, a 0.3-m high meteotsunami produced strong seaward currents that led to seven fatalities (Linares et al. 2019). Clearly, tsunamis from any source, with any wave height, can be dangerous when people are unaware of the hazard. This potential danger has prompted development of the tools necessary to prepare for meteotsunamis, and this development is continued in this dissertation.

1.3.2 Where do meteotsunamis happen?

(A lack of) geological and historical records

As of 2016, only 92 out of 2523 tsunamis in the global tsunami database were recognised as meteotsunamis (3.6%), whereas 1838 were generated by earthquakes (73%), and 258 were of "unknown" origin (10.2%) (Levin and Nosov 2016). A relatively low proportion of tsunamis are officially recognised as meteotsunamis, because the global tsunami database is a collection of the results from geological studies (e.g. sedimentary record), historical accounts (e.g. newspapers reports) and modern observational methods (e.g. tide gauges).

Unfortunately for the representation of meteotsunamis in the global tsunami database, meteotsunamis are missing from the geological record. Although the sedimentary deposits from tsunamis of any origin are difficult to identify and correctly interpret (because of repeated deposition and erosion from trains of tsunami waves), these deposits are more easily recognised when they cover a large region (Shiki et al. 2008). Therefore, the geological record favours the identification of sedimentary deposits

from global, seismogenic tsunamis rather than more local meteotsunamis. Other large sedimentary deposits from landslides, known as turbidites, can also be geochemically analysed to interpret tsunami events (e.g. Haflidason et al. 2004; Hunt et al. 2013). However, meteotsunamis may not even be considered in geological tsunami studies (e.g. Papadopoulos et al. 2014), as only sufficiently high-energy events (e.g. tsunamis from earthquakes > 7 M_W, large landslides, volcanic eruptions or meteorite impacts) leave a noticeable geological record (Bourgeois 2009). Thus, meteotsunamis are missing from the geological record, whilst tsunamis of other origins are preserved.

Although there is research literature relating to historical meteotsunami-like events (e.g. Haslett and Bryant 2009; O'Brien et al. 2013), there is reason to be sceptical of meteotsunami identifications from historical documents. Because of the highly local nature of meteotsunamis, only a few pieces of scientific literature, popular literature or newspaper reports are available for each event (e.g. Haslett and Bryant 2009; O'Brien et al. 2013). From these records, it is difficult to distinguish between standing waves that only formed within a basin (known as seiching), distant tsunamis of other origins, and meteotsunamis. For comparison, seismogenic tsunamis are often accompanied by intense ground shaking, meaning that these historical sources are easier to interpret and quantify (e.g. Baptista et al. 1998). There may also be more numerous historical written accounts of tsunamis from more energetic origins. For example, the landslide tsunami from the caldera collapse of Krakatoa in 1883 (Latter 1981) is more easily interpreted than a meteotsunami because of multiple reports of the volcanic eruption. Therefore, the combined lack of geological records and ambiguity in historical databases means that there is an incomplete database of meteotsunami occurrences, at least in comparison to seismogenic tsunamis, landslide-generated tsunamis, and volcano-generated tsunamis.

Oceanographic and atmospheric conditions with documented meteotsunamis

Nonetheless, using modern observational methods (and a few historical reports), meteotsunamis have been identified on every continent apart from Antarctica (Figure 1.2). They have been identified on continental shelves, enclosed seas and lakes across:

- North America (e.g. Ewing et al. 1954; Munk et al. 1956; Churchill et al. 1995; Mecking et al. 2009; Thomson et al. 2009; Wertman et al. 2014; Whitmore and Knight 2014; Vilibić et al. 2014; Šepić and Rabinovich 2014; Bechle et al. 2015; Bechle et al. 2016; Olabarrieta et al. 2017; Dusek et al. 2019; Linares et al. 2019; Shi et al. 2019),
- South America (e.g. Candella 2009; Dragani et al. 2014; Carvajal et al. 2017; Vilibić and Šepić 2017),
- Europe (e.g. Orlić 1980; Monserrat et al. 1991; Papadopoulos 1993; Candela et al. 1999; de Jong et al. 2003; de Jong and Battjes 2004; Belušić et al. 2007; Drago 2009; Haslett et al. 2009; Šepić et al. 2009; Vilibić et al. 2010; Šepić et al. 2012; O'Brien et al. 2013; Tappin et al. 2013; Frère et al. 2014; Pellikka et al. 2014; Vilibić et al. 2014; Sibley et al. 2016; Ličer et al. 2017; Pugh et al. 2019 in prep.),
- Africa (Okal et al. 2014),
- Asia (e.g. Hibiya and Kajiura 1982; Rabinovich and Monserrat 1998; Tanaka 2010; Mehra et al. 2012; Cho et al. 2013; Choi et al. 2014; Kim et al. 2016; Lin and Liang 2017; Heidarzadeh et al. 2019), and
- Australasia (e.g. Goring 2005; Vennell 2007; Pattiaratchi and Wijeratne 2014).

Overall, meteotsunamis tend to be recorded on coastlines that border basins that are relatively large (10^4–10^6 km^2), shallow (< 150 m) and gently sloping (0.1–1 m km^{-1}).

Meteotsunamis also seem to occur regardless of tidal range. They have been identified and reported in basins with microtidal ranges of less than 1 m (e.g. Churchill et al. 1995; Drago 2009; Šepić et al. 2015a; Bechle et al. 2016; Olabarrieta et al. 2017; Romero et al. 2019), mesotidal ranges between 1–4 m (e.g. Hibiya and Kajiura 1982; Dusek et al. 2019), and macrotidal ranges between 4–8 m (e.g. Thomson et al. 2009; Tappin et al. 2013; Choi et al. 2014; Sibley et al. 2016). However, regions with smaller tides (i.e. Florida, the Great Lakes or the Mediterranean) seem to be more affected by meteotsunamis than regions with larger tides (e.g. the North Sea, the Yellow Sea by

the Korean Peninsula, or Vancouver/Washington State) because the proportional contribution to sea-level extremes, or the sea-level variance, from meteotsunamis is much larger in regions with small tides than large tides (Vilibić and Šepić 2017). With modern observational methods, it is not necessarily easier to detect meteotsunamis in small tides than large tides, but it remains easier for eye-witnesses to report a meteotsunami. (Speculatively, this fact may be why regions with smaller tides, such as the Mediterranean, tend to have their own local names for meteotsunamis, but those with large tides do not.)

Meteotsunamis also occur with a variety of weather. The weather phenomena that tend to generate meteotsunamis are a few tens to hundreds of kilometres across and last a few hours (~10^4–10^5 m length scales and ~10^3–10^4 s time scales). This scale of atmospheric phenomena is known as the mesoscale. These atmospheric mesoscale phenomena are at least an order of magnitude smaller than atmospheric synoptic-scale systems (e.g. extra-tropical cyclones, ~10^5–10^7 m, ~10^5–10^6 s), within which mesoscale systems form. However, mesoscale systems are orders of magnitude larger than individual cloud processes (< 10^3 m, < 10^3 s) (e.g. Markowski and Richardson 2011; Houze 2014). Thus, understanding the mesoscale phenomena requires an appreciation of cloud-scale processes (i.e. the generation of precipitation) up to synoptic-scale processes (i.e. how the jet stream behaves). For these reasons, observing mesoscale atmospheric systems have generally involved using dense networks (10–100 km^2 spacing), that cover relatively large regions (> 10^3 km^2), with relatively rapid sampling intervals (10^1–10^2 s). For example, mesoscale atmospheric systems are often analysed using measurements from *in situ* pressure or 10-m wind speed measurements with sampling intervals on the order of minutes (e.g. Wertman et al. 2014; Carvajal et al. 2017; Lin and Liang 2017), or dense radar networks (e.g. Antonescu et al. 2013; Bechle et al. 2016; Fairman et al. 2016; Fairman et al. 2017). Likewise, simulating mesoscale atmospheric systems requires calculations to run in parallel across hundreds of computer processing units (e.g. Mecking et al. 2009; Markowski and Richardson 2011; Horvath and Vilibić 2014; Anderson et al. 2015; Horvath et al. 2018). Nonetheless, the mesoscale systems that generate meteotsunamis have been classified into a few different types around the world.

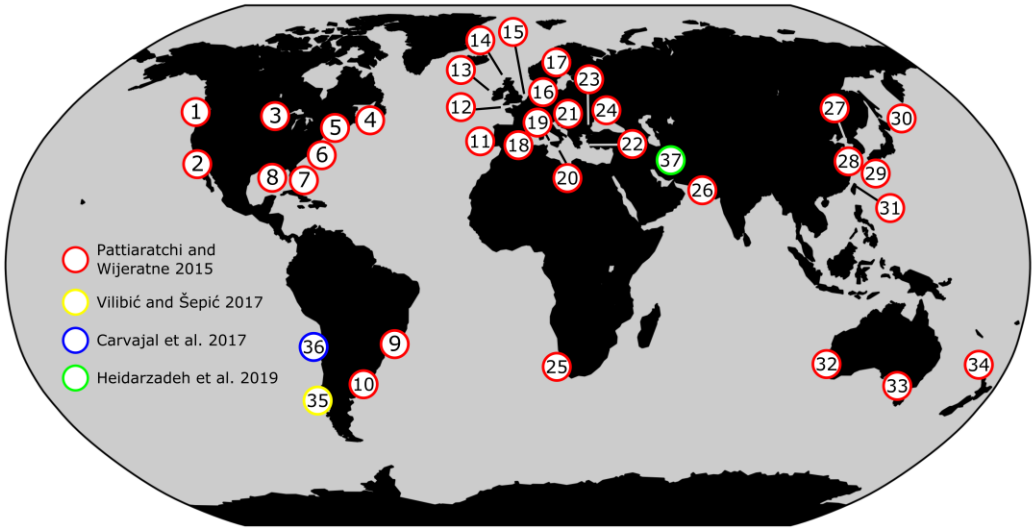

1. Vancouver and British Columbia (Thomson et al. 2009).
2. California (Munk et al. 1956).
3. Great Lakes (Bechle et al. 2016; Linares et al. 2019).
4. Newfoundland (Mecking et al. 2009).
5. Maine (Whitmore and Knight 2014; Vilibić et al. 2014).
6. East US Coast (Wertman et al. 2014; Dusek et al. 2019).
7. Florida (Churchill et al. 1995).
8. Gulf of Mexico (Olabarrieta et al. 2017; Shi et al. 2019).
9. Arraial do Cabo, Brazil (Candella 2009).
10. Buenos Aires, Argentina (Dragani et al. 2014).
11. Portugal/France (Frère et al. 2014).
12. England (Tappin et al. 2013; Sibley et al. 2016).
13. Ireland (O'Brien et al. 2013).
14. Scotland (Sibley et al. 2016; Pugh et al. 2019 in prep).
15. Rotterdam, the Netherlands (de Jong et al. 2003).
16. Baltic Sea (Monserrat et al. 1991).
17. Finland (Pellikka et al. 2014).
18. Balearics (Ličer et al. 2017; Romero et al. 2019).
19. Sicily (Candela et al. 1999; Šepić et al. 2018).
20. Malta (Drago 2009; Šepić et al. 2015b).
21. Croatia (Šepić et al. 2012; Bubalo et al. 2019)
22. Greece (Papadopoulos 1993).
23. Black Sea (Vilibić et al. 2010; Šepić et al. 2015c).
24. Odessa, Ukraine (Vilibić et al. 2014).
25. Dwarskersbos, South Africa (Okal et al. 2014).
26. West Coast of India (Mehra et al. 2012).
27. East China Sea (Tanaka 2010).
28. Yellow Sea (Choi et al. 2014; Kim et al. 2016).
29. Japan (Hibiya and Kajiura 1982; Asano et al. 2012).
30. Kuril Islands (Rabinovich and Monserrat 1998).
31. Taiwan (Lin and Liang 2017).
32. W. Australia (Pattiaratchi and Wijeratne 2014).
33. Tasmania (Pattiaratchi and Wijeratne 2014).
34. New Zealand (Goring 2005; Vennell 2007).
35. Chile (Vilibić and Šepić 2017).
36. Chile/Peru (Carvajal et al. 2017).
37. Persian Gulf (Heidarzadeh et al. 2019).

Figure 1.2 Reported meteotsunamis around the globe, based primarily on Pattiaratchi and Wijeratne (2015). Other original sources are shown with different coloured markers (Vilibić and Šepić 2017; Carvajal et al. 2017; Heidarzadeh et al. 2019). Each number refers to a different basin or coastline, with locations shown below the map. Some references have been updated from Pattiaratchi and Wijeratne (2015). (Sri Lanka, which was in Pattiaratchi and Wijeratne (2015)'s global dataset, originally from Wijeratne et al. (2010), has been omitted from this global dataset. It seems that seiches here occur due to local, tidal atmospheric forces, rather than tsunami waves generated from moving atmospheric systems).

Across most of the Mediterranean (e.g. the Adriatic, the Balearic Islands, Malta, Sicily), meteotsunamis are generated by trains of atmospheric gravity waves (e.g. Orlić 1980; Belušić et al. 2007; Belušić and Mahović 2009; Šepić et al. 2009; Orlić et al. 2010; Šepić et al. 2015a; Šepić et al. 2015c; Ličer et al. 2017; Šepić et al. 2018; Romero et al. 2019). Sometimes, atmospheric gravity waves are ducted within a stable lower tropospheric layer and reflect between a lower boundary (i.e. the ocean) and an upper boundary (i.e. an unstable atmospheric layer). Ducted atmospheric gravity

waves move relative to the surface at a speed guided by the wind speed in the unstable atmospheric layer. Large meteotsunamis generated by atmospheric gravity waves can also be associated with very low 10-m wind speeds (e.g. Orlić 1980; Šepić et al. 2015a).

Other atmospheric phenomena that generate meteotsunamis include mesoscale systems associated with extra-tropical cyclones, such as cold fronts (e.g. Hibiya and Kajiura 1982; de Jong et al. 2003; Tanaka 2010; Pellikka et al. 2014; Kim et al. 2016), open-cellular convection (repeating ~10-km diameter shallow-convective cells that cover ~100 km^2 surface areas), which occurs in the cold air behind cold fronts (e.g. de Jong et al. 2003; de Jong and Battjes 2004), or convective cells associated with the warm sector of extra-tropical cyclones (e.g. Tappin et al. 2013; Frère et al. 2014; Sibley et al. 2016). Depending on the latitude of the basin, meteotsunamis can also be formed by the mesoscale rain-bands of tropical cyclones (Olabarrieta et al. 2017) or rapidly moving low-pressure centres associated with tropical storms (e.g. Mercer et al. 2002). However, there is not always large synoptic-scale low pressure systems close to the mesoscale atmospheric systems. For example, there are numerous instances of meteotsunamis around the world that are generated by convective storms that are linearly organised, which are generally known as squall lines (e.g. Churchill et al. 1995; Pattiaratchi and Wijeratne 2014; Pellikka et al. 2014; Bechle et al. 2016; Olabarrieta et al. 2017). A subset of squall lines, known as *derechos*, which are linearly organised over hundreds of kilometres and are distinguished by straight-line winds, also generate meteotsunamis in North America (e.g. Wertman et al. 2014; Dusek et al. 2019).

These mesoscale atmospheric systems that generate meteotsunamis are not always easily connected to the wave or straightforwardly classified. For example, meteotsunamis may hit the coastline when their generating atmospheric phenomena is far from the waves (e.g. Wertman et al. 2014; Linares et al. 2019), sometimes mesoscale convective systems and atmospheric gravity waves are interconnected (e.g. Belušić et al. 2007), and mesoscale atmospheric systems may change morphologies whilst generating meteotsunamis (e.g. Bechle et al. 2016; personal communication with David Kristovich). Despite these ambiguities, clearly many different mesoscale weather phenomena produce meteotsunamis, and a mix of different weather phenomena can also produce meteotsunamis within the same basin.

1.3.3 The north-west European continental shelf

Both the oceanographic setting (e.g. water shallower than 150 m) and suitable mesoscale atmospheric phenomena (e.g. fronts) are present over the north-west European continental shelf. The north-west European continental shelf is a large (~ 6×10^5 km^2) region of relatively shallow water (< 200 m) located in the mid-latitudes (47 ºN–62ºN, 14ºW–8ºE). It is bordered by the European continental land mass to the east and a continental shelf break to the west, which leads out to deeper water (> 2000 m) in the Bay of Biscay and the open Atlantic Ocean (Figure 1.3a).

There are no large faults that are tectonically active in the region. There are small faults in the North Sea, where a 5–6 M_W earthquake occurs once every few years (according to the Harvard Centroid Moment Tensor Catalog (Dziewoński et al. 1981; Ekström et al. 2012)). However, these earthquakes are too small to generate noticeable seismogenic tsunamis. For context, seismogenic tsunamis are typically generated by earthquakes that are at least 6 M_W, which relates to co-seismic vertical motion of a few centimetres (Levin and Nosov 2016). The only way that a seismogenic tsunami above a few centimetres could hit the coastlines of the north-west European continental shelf would be from a very large earthquake (8–9 M_W) that is hundreds of kilometres from the shelf break (Horsburgh et al. 2008), or the occurrence of an 'inactive' fault rupturing on the shelf (e.g. Roger and Gunnell 2012).

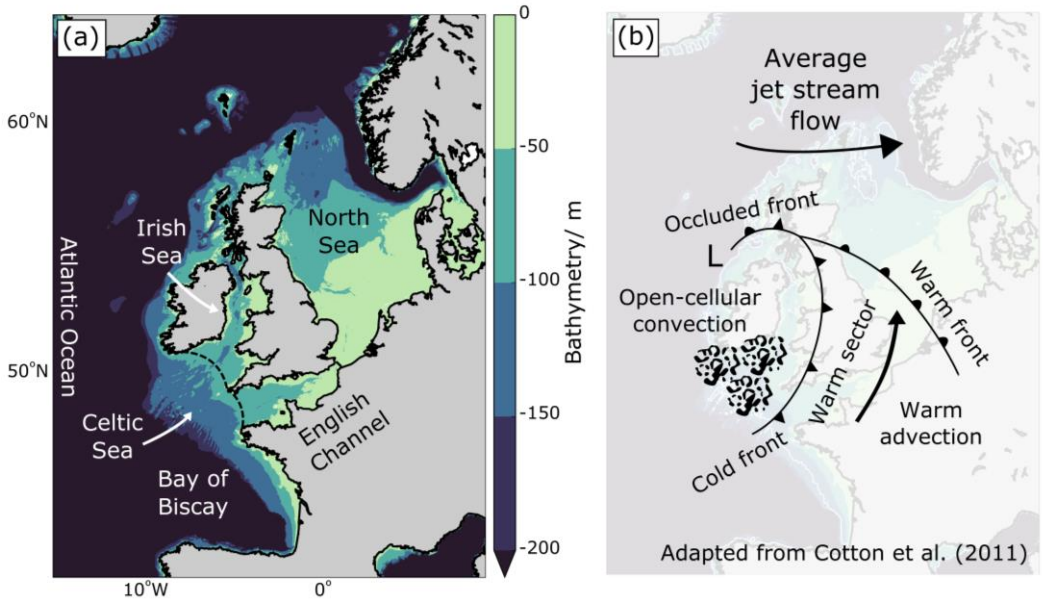

Figure 1.3 a) The bathymetry of the north-west European continental shelf, the study region of focus in this dissertation. The location of sub-basins on the continental shelf (Celtic Sea, Irish Sea, English Channel and North Sea) and off the shelf (Atlantic Ocean, Bay of Biscay) are indicated. b) A generalised structure of an extra-tropical cyclone with mesoscale atmospheric systems that have been associated with meteotsunamis annotated. These mesoscale atmospheric systems include fronts and open-cellular convection. The northward movement of warm air is also depicted that contributes to convective storms during a Spanish Plume. For clarity, the extra-tropical cyclone is at about the same scale as the study region.

In this dissertation, the north-west European continental shelf is split into four sub-basins: the Celtic Sea, the Irish Sea, the English Channel and the North Sea (Figure 1.3a). The Celtic Sea is to the west of France, north of the Bay of Biscay, and has the deepest water out of the four sub-basins (100–150 m). The Irish Sea is north of the Celtic Sea, between Great Britain and the island of Ireland. The Irish Sea is north-south oriented, with deep channels (> 100 m) and a shallow, relatively flat region to the north of Wales (< 50 m). The Irish Sea is also relatively narrow from west to east (100–200 km). The English Channel is similarly narrow (100–200 km) but is east-west oriented and is about 600 km long. The English Channel is also deeper to the west (50–100 m) than the east (0–50 m). Finally, the North Sea is the largest sub-basin (5×10^5 km^2), with a large contiguous area (1.5×10^5 km^2) that is less than 50-m deep. The tidal patterns in the North Sea are fairly complex, with 3 amphidromic points associated with the semi-diurnal lunar component (M_2 tidal constituent), but in general

the North Sea has tidal ranges at coastlines of between 2–4 m (Pugh and Woodworth 2014). In the English Channel, there are some of the largest measured tides in the world: on the French coastline bordering the English Channel, there are up to 8-m tidal ranges and up to 3 m s^{-1} tidal currents (e.g. Pingree and Maddock 1977; Davies 1986; Pugh and Woodworth 2014).

Most weather in north-west Europe is associated with the upper-level mid-latitude jet stream. The jet stream is about 11-km above ground level and means that the predominant environmental flow is from west to east (Figure 1.3b). The jet stream divides polar air to the north, which is cold and dry, from mid-latitude air to the south, which is warmer and moister than polar air. In turn, north-west European weather is dominated by the release of energy and moisture when these two air masses interact. When these large-scale thermodynamic processes occur at mid-latitudes, this results in extra-tropical cyclones (e.g. Haigh et al. 2010; Cotton et al. 2011; Houze 2014; Haigh et al. 2016).

The mesoscale atmospheric systems that could be relevant to meteotsunamis in north-west Europe are fronts, open-cellular convection (open cells), and mesoscale convective systems. Fronts form when at least two air masses with different thermodynamic properties are close and are diagnosed by analysing horizontal temperature gradients with a corresponding cyclonic wind shift. Open cells typically form in the winter, as the cold air behind cold fronts moves over relatively warm surface water, leading to lower tropospheric instability and shallow convection (e.g. Agee and Dowell 1974; Bakan and Schwarz 1992; de Jong et al. 2003; de Jong and Battjes 2004; Vincent et al. 2012). Mesoscale convective systems, such as isolated cells, non-linear clusters and linearly organised convective systems, form when there is sufficient lift, instability and moisture in the atmosphere. In north-west Europe, these three ingredients can co-occur in the summer, when extra-tropical cyclones bring warm air northwards (Figure 1.3b) from the warm and dry Sahara and Iberian Peninsula (e.g. Carlson and Ludlam 1968; Morris 1986). This specific synoptic flow pattern is called a Spanish Plume, although mesoscale convective systems can occur with other synoptic flow patterns (e.g. Lewis and Gray 2010). Thus, there are many types of mesoscale atmospheric systems in north-west Europe, each with well-documented synoptic flow patterns that could generate meteotsunamis.

1.3.4 How are meteotsunamis different to other waves?

But how is a meteotsunami different than other waves generated by the weather that frequently occur in north-west Europe, such as wind waves, swell waves or storm surges? The answer is in the period of the waves, which also relates to how each type of wave is generated. (One similarity between all these waves is that they propagate at the sea-surface, with gravity as a restoring force and are referred to collectively as surface gravity waves).

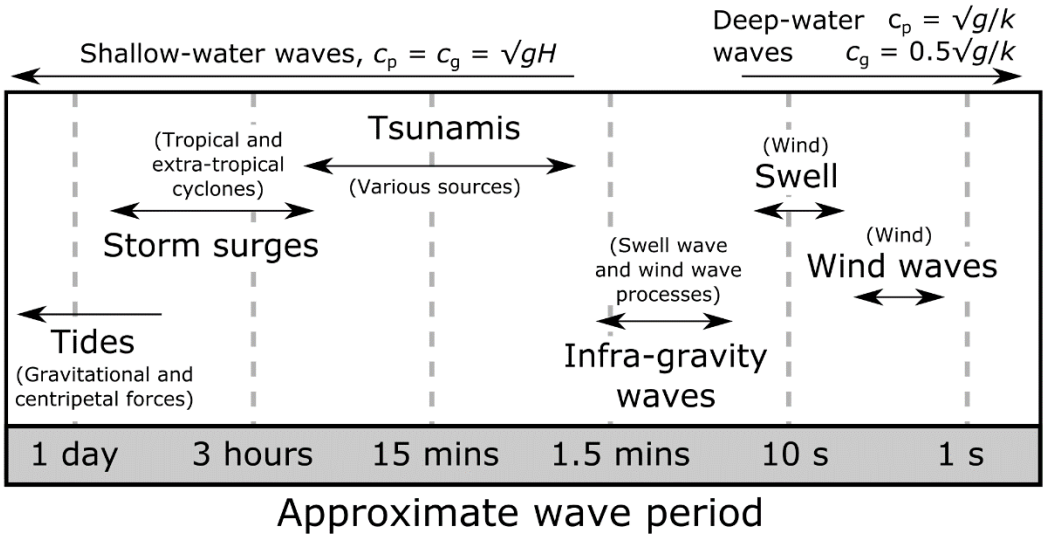

Figure 1.4 Surface gravity waves that give context to tsunamis, grouped by wave periods. From right to left (i.e. shortest to longest period), wind waves are about 1–6 seconds, swell waves are about 6–30 seconds, infra-gravity waves are about 30 seconds – 3 minutes, tsunamis are about 2–120 minutes, storm surges are about 2–12 hours and the main tidal constituents are between about 12–24 hours (semi-diurnal and diurnal).

It seems sensible to start by discussing wind waves and swell waves, which have a fundamentally different expression of surface gravity wave dynamics to tsunamis. Wind waves and swell waves are the typical waves that are seen when standing at the beach, looking out to sea. These waves might be quite large, up to a few metres high, and are generated by wind stress on the ocean surface. As wind transfers energy to the ocean, a spectrum of ocean waves is generated. These waves have predominantly short wave periods, ranging from about 1–30 seconds (e.g. Sorensen 2006; Figure 1.4).

Wind waves and swell waves are known as deep-water waves, that is to say, the water is deep compared to the depth of influence of the wave. For a wave to be classified as a "deep-water wave", half of the wavelength of the wave λ, must be less than the water

depth H (i.e. $\lambda/2 < H$) (e.g. Sorensen 2006). Their wave speeds are not dependent on water depth. Instead, wave speed is controlled almost entirely by the wave period. Consequently, different periods of wind waves and swell waves separate over time (e.g. Sorensen 2006). This separation of waves is known as frequency dispersion, which is described by the dispersion relation. The dispersion relation describes how the angular frequency of a wave ω (which is related to the wave period T as $\omega = 2\pi/T$) depends on gravity g, wavenumber k (where $k = 2\pi/\lambda$) and water depth (e.g. Sorensen 2006), such that

$$\omega^2 = gk \tanh(kH). \tag{1.1}$$

Then, the phase speed c_p of surface gravity waves (the speed at which a specific peak or trough moves) is described by

$$c_p = \frac{\omega}{k} = \sqrt{\frac{g \tanh(kH)}{k}}, \tag{1.2}$$

and the group speed c_g of surface gravity waves (the speed at which the energy of the wave propagates, or the speed of the wave envelope of a collection of waves) is

$$c_g = \frac{\partial\omega}{\partial k} = \frac{\omega}{2k}\left[1 + \frac{2kH}{\sinh(2kH)}\right], \tag{1.3}$$

meaning that for deep-water waves, which have a relatively large wavenumber (large k) and travel in relatively deep water (large H), the term '$\tanh(kH)$' in Equation 1.2 is approximately equal to 1, and the term '$2kH/\sinh(2kH)$' in Equation 1.3 is approximately equal to 0. Therefore, the phase speed of a deep-water wave is $c_p = \sqrt{g/k}$, and the group speed of a deep-water wave is half of the phase speed, $c_g = 0.5\sqrt{g/k}$. In other words, the individual peaks and troughs of deep-water waves move at twice the speed of the envelope of the deep-water waves. As will be made clear, both the phase speed and group speed of deep-water waves are fundamentally different to those of tsunamis and, by extension, meteotsunamis.

As wind waves and swell waves travel towards the shore along sloping beaches, momentum transfer to the water column from breaking waves also leads to wind waves and swell waves travelling within larger wave packets. The oscillations associated with these wave packets are known as infra-gravity waves (Kinsman 1965; Figure 1.4) and have periods of about 30–180 seconds. Infra-gravity waves at the coast are

sometimes referred to more specifically as surf beat (Munk 1949; Pugh and Woodworth 2014). Because infra-gravity waves are longer than wind waves and swell waves, the assumption of deep water (i.e. $\lambda/2 < H$) is not valid.

Moving to even longer waves than infra-gravity waves, there are shallow-water waves, which includes tides, storm surges and tsunamis (e.g. Sorensen 2006; Pugh and Woodworth 2014; Levin and Nosov 2016, Figure 1.4). Some of these waves do not necessarily appear to be "wave-like" when standing on the beach. For example, the tide does not necessarily appear to be a wave. Nonetheless, it rises and falls with a period of approximately 12.4 hours (for semi-diurnal tides), and its motion is described by shallow-water wave dynamics. Shallow-water waves behave fundamentally differently to deep-water waves because the depth of the water is shallow compared to the depth of influence of the wave ($\lambda/20 > H$) (e.g. Sorensen 2006). (Note: eventually a "deep-water wave", such as a wind wave, may behave more as a shallow-water wave when it moves towards coastlines and enters water that is shallow enough that the wave interacts with the ocean bottom, but the "shallow-water waves" described here always behave as shallow-water waves, even over the deepest parts of oceans on Earth). In the case of shallow-water waves, the wavenumber is relatively small (small k) and the depth of the water is relatively shallow (small H), meaning that the term '$\tanh(kH)$' in Equation 1.2 is approximately equal to kH, and the term '$2kH/\sinh(2kH)$' in Equation 1.3 is approximately equal to 1. Thus, the phase speed of a shallow-water wave is equal to the group speed, and $c_p = c_g = \sqrt{gH}$ (Figure 1.4).

In other words, the peaks and troughs of a shallow-water wave move at the same speed as the overall wave envelope, and the speed of a shallow-water wave changes because of changes in water depth. For context, in the open Atlantic ocean, which is about 4-km deep, shallow-water waves propagate at about 200 m s^{-1} (i.e. 720 kph or 450 mph), and over continental shelves, lakes and seas, which are typically shallower than 200 m, shallow-water waves propagate up to about 45 m s^{-1} (i.e. 160 kph or 100 mph).

Furthermore, because the shallow-water wave speed is almost entirely dependent on the depth of the water, seismogenic tsunamis and meteotsunamis are generally non-dispersive (e.g. Monserrat et al. 2006; Levin and Nosov 2016). Sometimes, landslide-generated or impact-generated tsunamis are weakly dispersive, in which case the "Boussinesq equations" are better suited to describe wave propagation (e.g. Løvholt

et al. 2008; Wünnemann et al. 2010). However, for meteotsunamis, the shallow-water approximation suitably describes the wave propagation. Furthermore, meteotsunamis only tend to travel across basins that are a few hundred kilometres across (e.g. the Great Lakes, the Adriatic, the Baltic Sea, or the Yellow Sea), meaning that there is not enough space for dispersive effects to become important.

Meteotsunamis could be confused with other atmospherically generated shallow-water waves, such as storm surges. Again, storm surges do not necessarily appear to be waves when standing at the beach. With periods commonly over 6 hours, the water appears to rise slowly over time (owing to their long period) until, sometimes extreme, flooding occurs. Extreme storm surges are much more dangerous than extreme meteotsunamis: storm surges can be easily over 3-m high for the United Kingdom and 10-m high in tropical regions (compared to meteotsunamis that are rarely over 1-m high), inundate land for tens of kilometres (compared to minimal flooding), cause tens of billions of dollars in damage (compared to tens of millions of dollars), and cause thousands of fatalities during each event (compared to usually less than 20 per event).

Storm surges are typically generated by tropical cyclones in equatorial regions (e.g. Knutson et al. 2010) or extra-tropical cyclones in mid-latitudes (e.g. Haigh et al. 2010; Haigh et al. 2016) that can exert sustained atmospheric forces over the ocean for up to a few days. Storm surges are predominantly generated by high, sustained 10-m wind speeds (e.g. 30 m s^{-1}) over shallow, coastal water (Pugh and Woodworth 2014). These storm surges are generated regardless of how the atmospheric forcing is moving relative to the ocean, but the associated storm surges may be larger and more dangerous when the cyclone moves slowly because the same region of the ocean is forced for a longer time (e.g. Sorensen 2006).

In contrast, meteotsunamis are almost always generated by mesoscale atmospheric systems (Monserrat et al. 2006). Mesoscale atmospheric systems typically have sea-level pressure perturbations on the order of 1 hPa (e.g. Hibiya and Kajiura 1982; Johnson 2001; Wertman et al. 2014; Carvajal et al. 2017; Linares et al. 2019), which is only enough to move the sea surface on the order of 0.01-m from mean sea-level at equilibrium. Likewise, the 10-m average wind speeds of mesoscale atmospheric systems that generate meteotsunamis are often less than 15 m s^{-1} (e.g. Hibiya and Kajiura 1982; Churchill et al. 1995; Belušić et al. 2007; Belušić and Mahović 2009;

Anderson et al. 2015; Šepić et al. 2015a). These low wind speeds are also related to small, centimetre-scale responses in the sea-level elevation at equilibrium (e.g. Sorensen 2006; Pugh and Woodworth 2014; Shi et al. 2019).

So, if the magnitude of the atmospheric forcing suggests that the wave should only be a few centimetres high at equilibrium, how do meteotsunamis grow a factor of 10–100-times, or ever become up to a few metres high? The answer is that meteotsunamis grow through several different amplification mechanisms before reaching the coast.

Chapter 2

Relevant meteotsunami dynamics

2.1 The Navier-Stokes equations and shallow-water equations

To understand how a meteotsunami can grow so large, it helps to understand the equations that describe fluid dynamics, how these equations are simplified when discussing tsunamis, and how this leads to the processes that form meteotsunamis. All fluid dynamics at these scales is related to the Navier-Stokes equations and the following two-dimensional shallow-water approximations, which were first developed in the 18th century. The derivation of the hydrodynamic equations is attributed to Euler (1761), and the derivation of the shallow-water equations to Laplace (1776). Then, came solutions for long plane waves in so-called "shallow" water (Lagrange 1781; Lagrange 1786), waves in channels of variable depth (Green 1838), the linear theory of plane waves and particle path motions (Airy 1841), and further development of how surface gravity waves propagate, incorporating higher-order dynamics (Stokes 1847).

The Navier-Stokes equations describe how the acceleration of a fluid parcel (i.e. an individual "chunk" of fluid) is related to the forces that act upon that parcel, which is of a certain density, and how the convergence or divergence of all the fluid parcels deforms the overall fluid. In other words, the Navier-Stokes equations are the expansion of Newton's Second Law for a fluid (with usually only the largest forcing terms included), combined with a description of how the overall fluid deforms due to those forces (also referred to as continuity or mass conservation) (e.g. Wünnemann et al. 2010; Levin and Nosov 2016)

For shallow-water waves, such as tsunamis, with wavelengths that are at least 20-times larger than both the depth of the water that they propagate within and their wave height, the vertical dimension of the Navier-Stokes equations can be averaged to give the simpler two-dimensional shallow-water equations (e.g. Laplace 1776; Wünnemann et al. 2010; Levin and Nosov 2016). These equations describe the fluid motion in two-dimensions (**i** and **j** unit vector directions), with an average horizontal velocity through the water column, and assume that the vertical motion of the fluid is

not large enough to influence the overall fluid motion. This property of the fluid motion comes from the hydrostatic assumption, meaning that any forces due to vertical fluid motion are negligible compared to the forces due to horizontal gradients in the weight of the water. The vertical motion of the fluid (i.e. sea-surface movement) is instead the result of mass conservation. If the fluid is incompressible (also known as the Boussinesq approximation), and the bottom is rigid (in the case of a non-movable, non-porous ocean floor) but the sea surface is free to move, the sea surface must have a vertical velocity upwards over any point that is directly proportional to the amount of convergence. Likewise, when the fluid diverges, the sea surface must have a proportional vertical velocity downwards.

The shallow-water equations (shown in vector form in Equations 2.1 and 2.2) describe how the speed of individual fluid parcels change over time due to the forces acting on those parcels. In Equation 2.1, the most relevant forcing terms for meteotsunamis to calculate the acceleration of a fluid at a point ($\boldsymbol{u}_t$) are included: the horizontal advection of fluid ($\boldsymbol{u} \cdot \nabla \boldsymbol{u}$), the Coriolis effect ($\boldsymbol{f} \times \boldsymbol{u}$), the gradient in sea-surface elevation ($-g\nabla\eta$), the gradient in atmospheric sea-level pressure ($-\rho^{-1}\nabla P$), the surface wind stresses ($[\rho H]^{-1}\boldsymbol{\tau}$) and the diffusive eddy effects ($A_H\nabla^2\boldsymbol{u}$, $A_H \sim 10^2$ m^2 s^{-1}), which are parameterised as a constant viscosity term (rather than molecular viscosity, which is ~10^{-6} m^2 s^{-1}):

$$\boldsymbol{u}_t + \boldsymbol{u} \cdot \nabla \boldsymbol{u} + (\boldsymbol{f} \times \boldsymbol{u}) = -g\nabla\eta - \rho^{-1}\nabla P + (\rho H)^{-1}\boldsymbol{\tau} + A_H\nabla^2\boldsymbol{u}, \qquad (2.1)$$

$$\eta_t = -\nabla \cdot (H\boldsymbol{u}). \qquad (2.2)$$

Here, $\boldsymbol{u}$ is the velocity vector $u\mathbf{i} + v\mathbf{j}$, t is time, where the subscript indicates a partial derivative $\partial/\partial t$ in time, ∇ is the horizontal gradient vector $\partial/\partial x\,\mathbf{i} + \partial/\partial y\,\mathbf{j}$, $\boldsymbol{f}$ is the vector associated with the rotation of the Earth, pointed vertically upwards, with a magnitude of about 1.1×10^{-4} s^{-1} at 50ºN (assumed constant over a small range of latitudes), g is gravitational acceleration (about 9.81 m s^{-2}), η is the sea-surface elevation measured from the still water depth H, ρ is the water density (about 1000–1029 kg m^{-3} depending on salinity and temperature), P is the atmospheric sea-level pressure, $\boldsymbol{\tau}$ is the surface wind stress vector, which is proportional to the 10-m wind speed squared ($|\boldsymbol{U}_{10}|^2$), and A_H is the horizontal eddy viscosity (about 100–200 m^2 s^{-1}).

2.2 The ocean at equilibrium

Equation 2.1, which describes the conservation of momentum, is often simplified to show how a fluid will behave at equilibrium, or after a period of time long enough for external forces and internal forces to balance. Another way of stating this is the following: at equilibrium the speed of a fluid is no longer changing ($u_t = 0$) but if there is an atmospheric forcing, the fluid must behave in a way to balance this force. For a sustained atmospheric sea-level pressure perturbation on the ocean, for example in the case of a cyclone lasting for a long time (e.g. 18 hours) over the ocean, the sea-surface response can be approximated by balancing the force due to changes in the sea-level elevation and the atmospheric sea-level pressure. The following approximation requires advection, Coriolis and diffusive effects due to turbulence to be negligible and excludes surface wind stress on the ocean. This results in the "inverted barometer effect" (e.g. Sorensen 2006; Pugh and Woodworth 2014),

$$\nabla\eta(x, y) = -\frac{1}{\rho g}\nabla P(x, y)\,, \tag{2.3}$$

showing that the gradient in sea-level elevation is directly proportional to the negative of the gradient in air pressure (e.g. Figure 2.1a), scaled by the weight (per unit volume) of the fluid (ρg). In other words, reductions in atmospheric sea-level pressure perturbations result in a rise in sea-surface elevation and increases in atmospheric sea-level pressure perturbations result in a reduction in sea-surface elevation. A 1-hPa pressure change results in a 1-cm sea-level elevation change. Similarly, for a sustained wind-stress at the ocean surface, excluding sea-level pressure disturbances, but with the all other assumptions as previously applied, the sea-level elevation is given as the cumulative (i.e. integrated) effect of surface wind stress ($\boldsymbol{\tau}$) applied over an area of given water depth (H), scaled by the weight of the water column (ρg):

$$\eta(x, y) = \frac{1}{\rho g}\iint \frac{\boldsymbol{\tau}(x, y)}{H(x, y)}\,\mathrm{d}x\,\mathrm{d}y. \tag{2.4}$$

To simplify Equation 2.4, using a one-dimensional basin (considering the x-direction only), with a flat bottom (constant H) and constant wind-stress (constant τ), Equation 2.5 shows a simple form of an effect called "wind setup" (e.g. Sorensen 2006; Pugh and Woodworth 2014):

$$\eta(x) = \frac{1}{\rho g}\frac{\tau}{H}\,x + \eta_0, \tag{2.5}$$

or, in other words, the sea-surface elevation increases with stronger winds (larger τ) over shallower water (smaller H) and increases linearly along the direction of constant wind stress (Figure 2.1b).

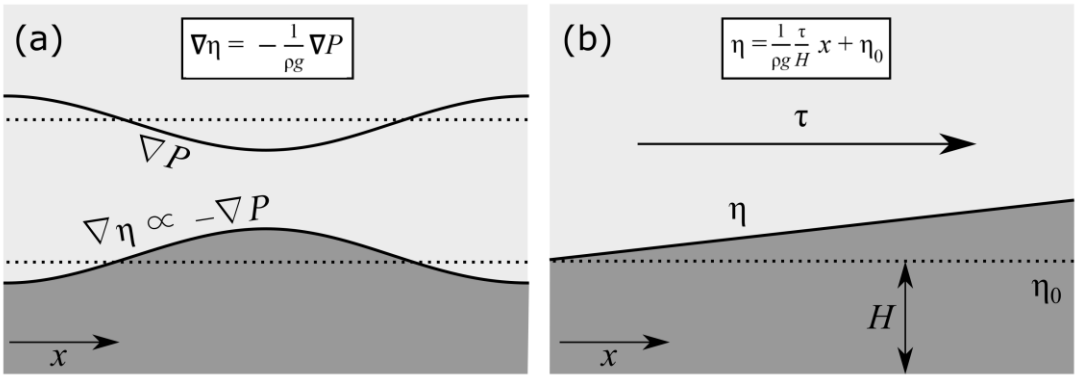

Figure 2.1 The sea-level elevation response that varies around η_0 from a one-dimensional ocean of constant depth H at equilibrium with a) a sea-level pressure forcing giving the inverted barometer effect and b) a constant rightward wind stress, τ, giving wind set-up.

Equation 2.3 and Equation 2.4, which were derived from the shallow-water equations, describe how the ocean will respond under atmospheric pressure forcing and wind forcing at equilibrium. However, the shallow-water equations can also be manipulated to show that waves form on the ocean surface due to pressure and wind forcings.

2.3 Forced shallow-water waves

To understand how meteotsunamis behave over time, understanding them as waves, with the wave equation, is more useful than analysing the ocean response at equilibrium (e.g. Proudman 1929). Under the assumptions of negligible advection, Coriolis and diffusion (validated with a scaling analysis), with an ocean of constant depth (constant H), the momentum (Equation 2.1) and continuity (Equation 2.2) equations can be manipulated to find a forced wave equation for the sea-surface elevation (i.e. taking the spatial gradient of Equation 2.1, and the partial derivative of Equation 2.2 with respect to t and rearranging), to give

$$\eta_{tt} - gH\nabla^2\eta = \boldsymbol{F}(\boldsymbol{k}_F \cdot \boldsymbol{x} - \omega_F t) \tag{2.6}$$

where $\boldsymbol{F}$ is the combined forcing of atmospheric pressure and wind stress on the ocean surface, $\boldsymbol{k}_F$ is the forcing wavenumber vector $k\mathbf{i} + m\mathbf{j}$, and ω_F is the forcing angular frequency, such that $U = \omega_F/|\boldsymbol{k}_F|$. Importantly, the wave equation for a shallow-water

wave shows that the speed of the wave is $\sqrt{gH}$ (the square root of coefficients in the second term on the left-hand side of Equation 2.6). Again, the speed of a shallow-water wave, such as a meteotsunami, changes because of the water depth.

Given that an atmospheric forcing can move over the ocean, it may move at different speeds relative to the wave. In the case that the forcing is not moving, the sea-level elevation (which through continuity is analogous to currents) will eventually reach equilibrium with the forcing (e.g. Equation 2.3, Equation 2.4, or Figure 2.1). In the case of a moving forcing, the wave equation shows that the resultant forced-wave height is different than considered under the case of static equilibrium. By assuming a one-dimensional basin, and rearranging Equation 2.6, the size of a forced wave is related to the ratio of the forcing speed U and the free-wave speed, $c = \sqrt{gH}$, given as the non-dimensional Froude number, $\mathrm{Fr} = U/c$:

$$\eta_F = \frac{1}{1-\mathrm{Fr}^2}\eta_0, \tag{2.7}$$

where η_0 is the size that the wave would be expected at static equilibrium (e.g. Proudman 1929; Vilibić 2008; Levin and Nosov 2016). Simply, the speed of an atmospheric forcing, relative to the speed of a wave, changes how much energy is transferred to the ocean and how large a forced shallow-water wave may become. The resultant behaviour of the forced wave is not always necessarily physically intuitive, and so some time is now spent on developing the physical intuition for this mathematical result.

The transfer of energy from the atmosphere to a surface wave is much like that of other forced oscillators (e.g. a mass on a spring). If an oscillator is forced at a frequency of 0, this is analogous to simply displacing the oscillator to a fixed position, or an atmospheric forcing that is not moving (Figure 2.2a). If an oscillator is forced at a frequency below its natural frequency, which is analogous to an atmospheric forcing moving slower than the shallow-water wave speed, the motion of the oscillator will align with the expected motion from the forcing (Figure 2.2b). However, if an oscillator is forced at a frequency that is higher than its natural frequency, which is analogous to a forcing moving faster than the shallow-water wave speed, then counterintuitively, the motion of the forcing is opposite to the expected motion from the forcing. This means that a high pressure forcing will produce a forced wave with

positive sea-level elevation, which is the opposite to what is expected from static equilibrium (cf. Figure 2.1 and Figure 2.2d). Finally, if an oscillator is forced at natural frequency, there is a resonant response, where the oscillation becomes large (Figure 2.2c). This is analogous to an atmospheric forcing moving at the shallow-water wave speed. In the case of a shallow-water wave (and meeting all assumptions in the derivation of the forced shallow-water wave equation), the denominator of Equation 2.7 becomes 0 when Fr = 1, meaning that the forced-wave height is "undefined". This condition, that an atmospheric forcing moves at the shallow-water wave speed, and the resonant response of the wave to this forcing, is termed Proudman resonance.

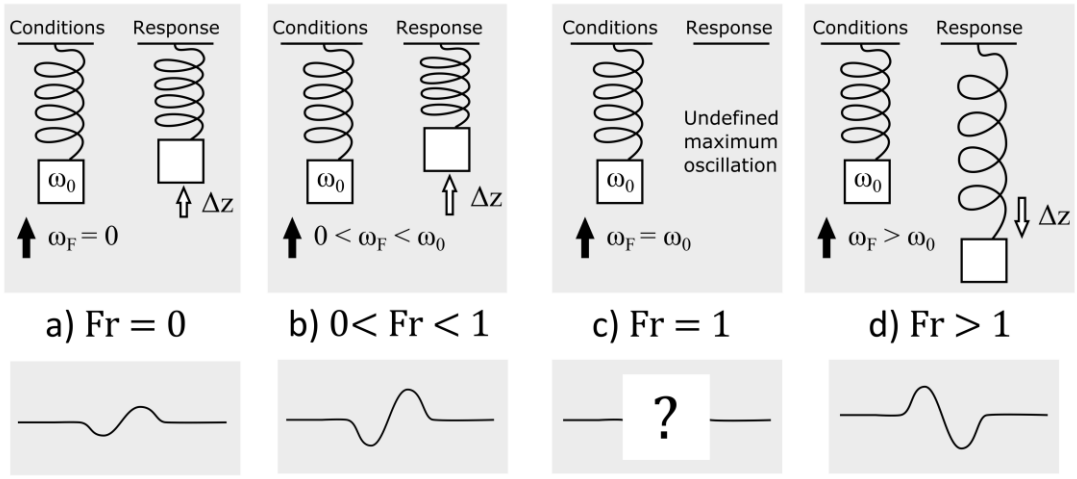

Figure 2.2 The analogy of a mass on a spring, with natural frequency ω_0, to help understand the sign of the forced wave relative to the sign of the forcing. Black arrows indicate the sign of the force applied to the mass on the spring at a forcing frequency ω_F, and the white arrow indicates the sign of the vertical displacement of the mass on the spring, Δz. a) Fr = 0, the atmospheric forcing is not moving, or the force applied to the mass on the spring is not oscillating ($\omega_F = 0$). b) 0 < Fr < 1, the atmospheric forcing is moving slower than the shallow-water wave speed, or the forcing frequency applied is at a lower frequency than the natural frequency of the mass on the spring. c) Fr = 1, the atmospheric forcing is moving at the shallow-water wave speed, or the forcing frequency is the natural frequency of the mass on the spring. The shape of the wave is undefined. d) Fr > 1, the atmospheric forcing is moving faster than the shallow-water wave speed, or the forcing frequency is higher than the natural frequency of the mass on the spring.

2.4 Meteotsunami generation mechanisms

Proudman resonance is the first of seven meteotsunami amplification mechanisms that are covered in this section, which includes Greenspan resonance, reflection and transmission, shoaling, refraction, the effect of currents and seiching. For a meteotsunami, a combination of these individual processes is responsible for the resultant wave height at the coastline.

2.4.1 Proudman resonance

Proudman resonance, which is a kind of external resonance between the atmospheric forcing and the generated wave, states that a resonant response will occur when the atmospheric forcing speed U matches the shallow-water wave speed $\sqrt{gH}$ (e.g. Proudman 1929; Churchill et al. 1995; Mercer et al. 2002; Vilibić 2008; Bubalo et al. 2018; Chen and Niu 2018).

However, clearly, the previously derived "undefined" forced-wave height has no physical meaning. Furthermore, when a forcing moves within 0.1% of the shallow-water wave speed, waves are not expected to be immediately about 50-times larger than the forcing would suggest at static equilibrium. Instead, the wave grows over time from a sustained forcing that moves with the wave (Figure 2.3). This wave growth occurs because when a forcing disturbs the ocean surface, it creates not only one forced wave, but other free waves that are in superposition (in the one-dimensional case, this is one forced wave and two free waves) (Proudman 1929; Levin and Nosov 2016; Ličer et al. 2017). This result is unavoidable because whenever a fluid surface is disturbed, other waves are generated that move away from the disturbance at a certain speed. In the case of a disturbance that produces a wave with appropriate dimensions for a shallow-water wave, this speed is $\sqrt{gH}$. To understand how shallow-water waves grow under Proudman resonance, the one-dimensional solution for the sea-surface elevation (Proudman 1929) is useful to analyse, given as

$$\eta(x, t) = \frac{\eta_0(x - Ut)}{1 - \mathrm{Fr}^2} - \frac{\eta_0(x - ct)}{2\,(1 - \mathrm{Fr})} - \frac{\eta_0(x + ct)}{2\,(1 + \mathrm{Fr})}, \tag{2.8}$$

showing that the solution to the sea-level elevation is composed of a superposition of three waves. The first term on the right-hand side is the forced wave, moving at speed U, as previously described. The second term describes a free wave, moving at speed

c, of opposite sign to the forced wave, but moving in the same direction (Figure 2.3). The third term also describes a free wave, of opposite sign to the forced wave but moving in the opposite direction. Each wave height is related slightly differently to the ratio of the forcing speed and the free-wave speed (denominators in right-hand side of Equation 2.8). The difference between the forcing speed and shallow-water wave speed determines the shape of the rightward moving wave superposition. As the difference between the forcing speed and shallow-water wave speed decreases, the free wave approaches the same magnitude (but opposite sign) to the forced wave. This result is made clearer by the relation

$$\frac{\eta_0(x-ct)}{2\,(1-\mathrm{Fr})} = \frac{\eta_0(x-ct)}{1-\mathrm{Fr}^2}\cdot\frac{1+\mathrm{Fr}}{2}, \tag{2.9}$$

showing more clearly that, in the case that $\mathrm{Fr} \approx 1$ (i.e. $U \approx c$), that

$$\frac{\eta_0(x-ct)}{1-\mathrm{Fr}^2}\cdot\frac{1+\mathrm{Fr}}{2} \approx \frac{\eta_0(x-Ut)}{1-\mathrm{Fr}^2}. \tag{2.10}$$

In the limit that the forcing speed and free-wave speed are equal, Equation 2.8 simplifies, showing what would be observed at the sea surface if there were an atmospheric forcing moving at Proudman resonant speed in a one-dimensional basin, as the distance travelled increases,

$$\eta(x, t) \approx \frac{x}{2}\eta_{0_x}. \tag{2.11}$$

By inspecting the first term on the right-hand side of Equation 2.11, a Proudman resonant wave grows linearly with distance (x) and is the shape of the gradient of the original wave at equilibrium in the x-direction (Figure 2.3).

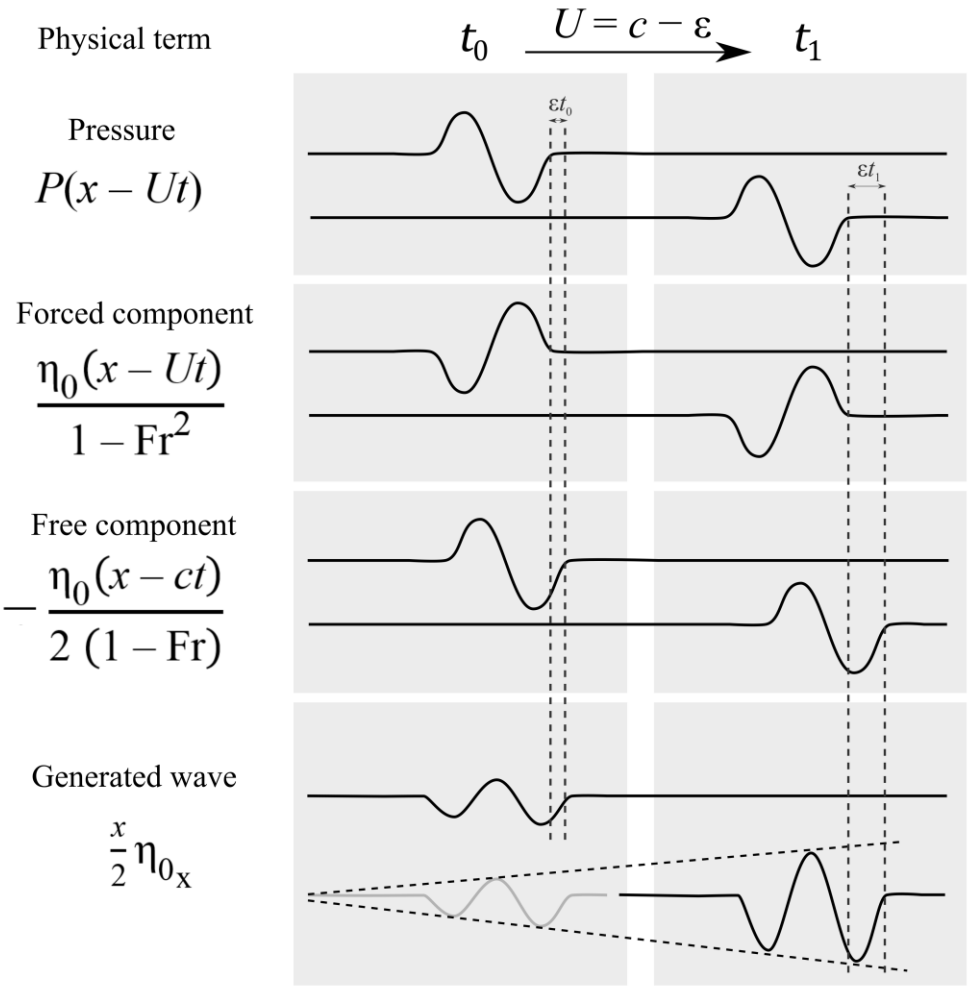

Figure 2.3 The rightward moving terms in for a moving pressure disturbance generating a wave through Proudman resonance. The atmospheric pressure forcing is moving slightly slower than the shallow-water wave speed ($U = c - \varepsilon$). The top panel shows the shape of the pressure forcing at t_0 and t_1, with an offset only applied for clarity. The second panel shows the forced component, the third panel shows the free component and the final panel shows the generated wave, which is the sum of the forced wave and the free wave. The dashed black lines indicate the linear growth of the wave under Proudman resonance.

This wave, which linearly grows, could be physically measured if there were a dense network of measurements of the sea-level elevation. That is, if all the assumptions that are made when constructing Proudman resonance were met. In reality, even with a water of constant depth and an atmospheric forcing moving at the shallow-water wave speed, the wave would eventually grow such that the perturbations in sea-level elevation would influence the wave itself. The wave speed would change between the wave's trough and peak, and the currents would grow large enough to influence the wave through advection, such that the approximation of negligible wave height leads

to an unacceptable description of the fluid motion (e.g. Churchill et al. 1995; Vilibić 2008; Levin and Nosov 2016).

Similarly, the result that the forced wave is "undefined" when the forcing speed is equal to the shallow-water wave speed could not happen, friction always reduces the forced-wave height (e.g. Vilibić 2008). Still, wave growth that is very close to Proudman resonant wave growth has been repeatedly demonstrated by numerical models, and is often a key process to explain meteotsunami wave height observations (e.g. Orlić 1980; Hibiya and Kajiura 1982; Churchill et al. 1995; Rabinovich and Monserrat 1998; Mercer et al. 2002; de Jong et al. 2003; Monserrat et al. 2006; Vilibić 2008; Belušić and Mahović 2009; Orlić et al. 2010; Tanaka 2010; Asano et al. 2012; Tappin et al. 2013; Choi et al. 2014; Šepić and Rabinovich 2014; Wertman et al. 2014; Šepić et al. 2015a; Sibley et al. 2016; Kim et al. 2016; Ličer et al. 2017; Vatvani et al. 2018; Chen and Niu 2018; Bubalo et al. 2019; Shi et al. 2019). However, Proudman resonance is not the only external resonance mechanism between meteotsunamis and atmospheric forcings.

2.4.2 Greenspan resonance

Greenspan resonance, which is the equivalent of Proudman resonance for meteotsunamis that behave as edge waves, has been inferred for a few meteotsunamis in the Great Lakes (e.g. Greenspan 1956; Bechle and Wu 2014) and the continental shelf near California (Munk et al. 1956). Greenspan resonance occurs when the component of the forcing velocity along the coast is near the speed of an edge wave mode (which travel parallel to the coastline). Therefore, Greenspan resonance occurs when

$$U\cos\theta_{\text{coast}} = \frac{gT_{\text{wave}}}{2\pi}\tan[\beta(2n+1)]. \qquad (2.12)$$

The left-hand side of Equation 2.12 describes the atmospheric forcing speed relative to the coastline, where θ_{coast} is the angle between the atmospheric forcing velocity vector and the coastline. Likewise, the right-hand side of Equation 2.12 describes the edge-wave speed, where T_{wave} is the wave period (the same as the forcing period), β is the slope of the bathymetry perpendicular to the coast (up to about 120 km from the coastline) and n is edge wave mode (where the mode is the number of times the edge wave crosses the mean sea-level elevation in the cross-propagation direction) (Ursell

1952; Munk et al. 1956; Greenspan 1956). Despite meteotsunamis sometimes existing as edge waves, edge waves behave differently to the waves that are discussed in more detail throughout the rest of this dissertation. Still, the same principle applies between Greenspan resonance and Proudman resonance—when forcing speeds and wave speeds match, there is a resonant response from the wave.

2.4.3 Reflection and transmission

Generally, these external resonances occur over water depths that do not change considerably in the direction that the wave is moving. However, in the case that the water depth does abruptly change, for example at a continental shelf break, the wave reflects from the boundary and there is a corresponding transmission of the wave through the boundary. Whilst the overall energy of the system is conserved, these reflected and transmitted waves move at different speeds, with different wavelengths and different wave heights according to the ratio of differences between the speeds on either side of the boundary ($\sqrt{gH_0}$ and $\sqrt{gH_1}$, Figure 2.4a). In the case of a step change (Figure 2.4a), the reflection coefficient R describes the change in amplitude for the reflected wave (Lamb 1932; Levin and Nosov 2016):

$$R = \frac{\sqrt{H_0/H_1} - 1}{\sqrt{H_0/H_1} + 1}, \tag{2.13}$$

and the transmission coefficient T describes the change in amplitude for the transmitted wave:

$$T = \frac{2\sqrt{H_0/H_1}}{\sqrt{H_0/H_1} + 1}, \tag{2.14}$$

meaning that at a step from deep water to shallow water (Figure 2.4a), the transmitted wave amplitude increases up to a maximum of 2 times the original amplitude and the reflected wave is of the same sign as the incident wave and transmitted wave. For a wave moving into deeper water, the transmitted wave amplitude decreases, and the reflected wave is of the opposite sign to the incident wave. These reflections from shallow to deep water can occur as meteotsunamis move from the continental shelf to deep water, for example meteotsunamis that are generated by eastward moving systems and cross the continental shelf break off the US East Coast (e.g. Pasquet and Vilibić 2013; Wertman et al. 2014). Interestingly, though not found for any meteotsunamis in this dissertation, external resonance-type mechanisms are also

possible at oceanographic boundaries such as continental shelf breaks (e.g. Vennell 2007; Vennell 2010; Thiebaut and Vennell 2011).

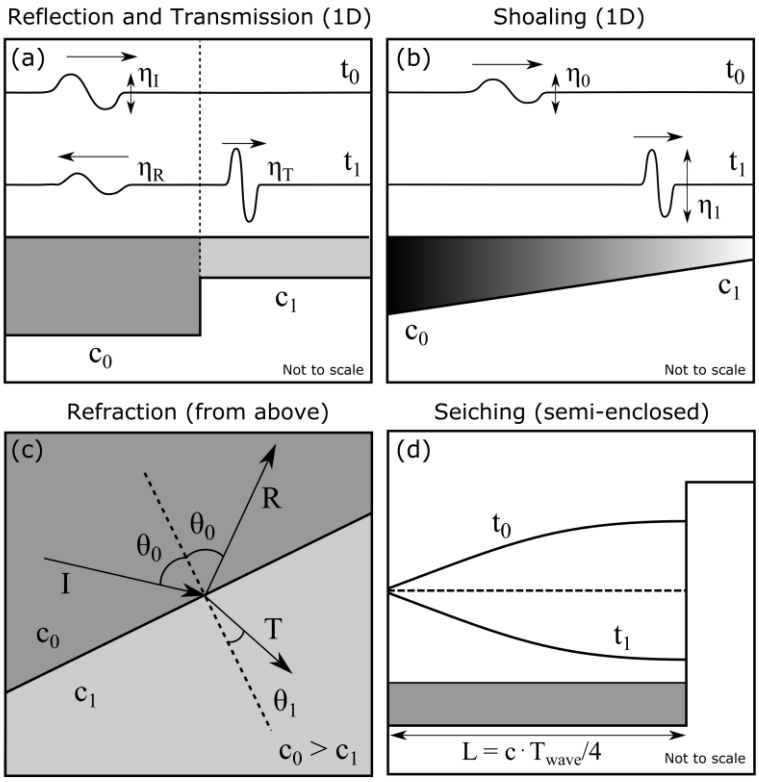

Figure 2.4 Wave processes that are relevant to meteotsunamis. a) reflection and transmission of waves across a boundary from c_0 to c_1 ($c_0 > c_1$), between a time before reaching the boundary, t_0, to a time after hitting the boundary, t_1 (with an offset between times applied for clarity) b) shoaling of a wave as it moves from deep water to shallow water from time t_0 to t_1, (with an offset between times applied for clarity) c) refraction of waves, as a ray crosses a boundary in wave speeds c_0 to c_1 and changes from angle θ_0 to θ_1, the wave heights also change according to transmission and reflection rules from the incident wave (I), transmitted wave (T) and reflected wave (R) and d) seiching within a semi-enclosed basin, with the sea-level elevation shown oscillating between its maximum at t_0 and minimum at t_1.

2.4.4 Shoaling

Water depths could also change more gradually compared to the wavelength, in which case, waves grow through shoaling (Figure 2.4b). Again, the total energy flux (total energy flux = kinetic energy flux + potential energy flux) is conserved with shoaling. Using physical intuition, as a wave propagates, energy cannot be transferred to the wave, or from the wave, unless some source (e.g. a forcing moving with the wave) or sink (e.g. friction) causes this transfer of energy. This means, that in the absence (or

ignorance) of such sources or sinks, as the energy is propagated with the wave (c_g = c_p), it must transfer the same total amount of energy per unit time, per unit of wave crest (i.e. the energy flux must remain constant). However, in the case that the ocean depth is decreasing, it has already been shown that a shallow-water wave must slow down, proportionally to $\sqrt{H_1/H_0}$ (Equation 1.2, Equation 1.3 and Equation 2.6). Instead, as water-depth decreases, the wave-height increases (potential energy-flux is constant) and the currents increase (kinetic energy-flux is constant), conserving total-energy flux (Figure 2.4b). In the case of a one-dimensional plane wave, shoaling is described by Green's Law (e.g. Green 1838):

$$\frac{\eta_1}{\eta_0} \propto \left(\frac{H_0}{H_1}\right)^{1/4}. \tag{2.15}$$

stating that the ratio of the wave height at an initial position (η_0) compared to the wave height at a later position (η_1) is proportional to the water depths at each position (H_0 and H_1).

2.4.5 Refraction

Meteotsunamis move within two-dimensional basins, where the water depth may vary in either the along-propagation direction (along the direction that the wave is moving) or the cross-propagation direction (perpendicular to the direction that the wave is moving). When the water depth varies in the cross-propagation direction, waves will move at different speeds along the wave crest. In this case, it is easier to understand the motion of waves using ray theory (e.g. Satake 1988), where rays are perpendicular to wave crests (Figure 2.4c). Although the assumptions that are needed to use ray theory are not fully valid for tsunamis, ray theory (and its extensions with dispersive effects) tends to work for rapid prediction of when tsunamis will arrive and what the relative wave heights will be for locations outside of the initial source region (e.g. Satake 1988; Titov et al. 2005; Sandanbata et al. 2018). With variable speeds across a boundary, meteotsunami waves will refract according to Snell's Law, which describes how rays change direction at boundaries:

$$c_1/c_0 = \sin\theta_0 / \sin\theta_1, \tag{2.16}$$

where θ is the angle between the ray and the normal that is perpendicular to the boundary of two water depths (subscript 1 and 0) of different speeds c (Figure 2.4c).

Refraction affects meteotsunami wave height through the relative spacing of the rays B as it travels through variable water depths (Green 1838), with the proportionality

$$\frac{\eta_1}{\eta_0} \propto \left(\frac{B_0}{B_1}\right)^{1/2}, \tag{2.17}$$

meaning that if the ray-spacing decreases, wave heights proportionally increase.

2.4.6 Currents

Although wave-flux conservation processes have been discussed in terms of changes in wave speed due changes in water depth, currents can also change wave speed (e.g. Li and Herbich 1982) and is discussed in more detail in Chapter 5. These wave-speed changes due to currents also mean that, to conserve total-energy flux, there are also changes to wave heights and wavelengths when a wave propagates from still water (no current) into an along-propagation current (in the same direction of the wave propagation) or a counter-current (in the opposite direction of the wave propagation). For example, for a wave travelling from no current to an along-propagation current, its wavelength will increase, and its wave height will decrease.

2.4.7 Seiching

The final growth mechanism that will be discussed is seiching, also known as harbour resonance, internal resonance or standing wave formation (e.g. Monserrat et al. 2006; Rabinovich 2009; Ličer et al. 2017). Seiching is the mechanism that means meteotsunamis can be 2–6-m high in one harbour, and less than 1-m high elsewhere. Seiching is a key mechanism in Nagasaki Bay (e.g. Hibiya and Kajiura 1982) and Urauchi Bay (e.g. Asano et al. 2012) in Japan, Vela Luka Bay in Croatia (e.g. Bubalo et al. 2019) and Ciutadella Bay in Menorca (e.g. Ličer et al. 2017).

Generally, seiches can occur within a basin of any size or shape, and whether the basin is fully enclosed by coastlines or open to water at one end (i.e. the basin is semi-enclosed). Meteotsunamis cause seiching in semi-enclosed basins by forming a standing wave (Figure 2.4d). First, the meteotsunami travels down the basin and hits the closed end, then, the meteotsunami reflects and travels back in the opposite direction. If another peak from the meteotsunami is incoming at the same time that the other reflected wave is travelling back, then a constructive superposition can form. If this repeatedly occurs, the meteotsunami can form a standing wave that is many times

larger than the meteotsunami at the bay entrance. In a one-dimensional basin, the formula for a simple standing wave can be found by summing an incident wave, $A\cos(kx - \omega t)$, with a purely reflected wave moving in the opposite direction, $A\cos(kx + \omega t)$:

$$A\cos(kx - \omega t) + A\cos(kx + \omega t) = 2A\cos(kx)\cos(\omega t), \qquad (2.18)$$

in which case, the standing wave is twice the height of the incident wave. The lengths at which a semi-enclosed basin is resonant for a wave of a certain period T_{wave} can also be found by rearranging "Merian's formula" (e.g. Pugh and Woodworth 2014):

$$L_{\text{N}} = \frac{(2N+1)T_{\text{wave}}\sqrt{gH}}{4}, \qquad (2.19)$$

where N is the number of nodes ($N = 0$ in Figure 2.4d), and L_{N} is the basin lengths that are resonant for each standing wave. Thus, for a meteotsunami with a typical 30-minute period that enters a harbour that is about 5-m deep, the harbour will seiche if its length is close to a resonant length given in Equation 2.19 (for example $L_0 \approx 3$ km, $L_1 \approx 9$ km or $L_2 \approx 15$ km).

Because real basins are two-dimensional with variable depths, many more complicated patterns (eigenvectors) at different periods (eigenvalues) of the basin can cause seiching (e.g. Rabinovich 2009). For example, the T-shaped structure of Urauchi Bay allows three modes of oscillation, with periods of 24 mins, 12 mins and 10.5 mins (Asano et al. 2012). These periods are often found by analysing which specific periods have high energy content in tide gauge measurements (requiring a Fourier transform) but can be further clarified by modelling seiches within basins (e.g. Asano et al. 2010). In reality, seiches are most effectively formed in basins that are long and thin with narrow entrances (e.g. Vilibić et al. 2008; Rabinovich 2009; Denamiel et al. 2018).

Chapter 3

Methods Overview

3.1 Observational methods

The relevant background knowledge has now been established to discuss how meteotsunamis are identified from oceanographic and atmospheric measurements.

3.1.1 Identifying meteotsunamis from sea-level records

Tide gauges

Tide gauges are the most frequently used tools to identify meteotsunamis. Tide gauges are versatile tools that measure the sea-level elevation over a range of time-scales, with sampling intervals of a few minutes, and tend to be in use for up to a few decades (10^1–10^8 s). Tide gauges are *in situ* tools, measuring the sea-level relative to a known datum. There are at least 100 tide gauges spanning the north-west European coastline (combined from the Republic of Ireland, United Kingdom, France, Belgium, the Netherlands and Germany) that are near economically important harbours (e.g. Lerwick, Rotterdam), popular tourist beaches (e.g. Newhaven) and interesting locations for oceanographic study (e.g. Severn, Saint Malo).

There are predominantly two methods that tide gauges measure the sea-level elevation (e.g. Woodworth and Smith 2003). The first method is to measure the pressure beneath the sea surface (e.g. bubbler tide gauges or pressure transducers). Bubbler tide gauges and pressure transducers are submerged in water, and work by balancing the pressure of a fluid (typically air or oil) within a tank with the pressure generated by the weight of water above the tide gauge. The average weight of the water is proportional to the average depth of the water above the tide gauge ($P_W = \rho g H$). The second method is to install a transceiver at a known height above ground level, and to measure the time it takes for a transmitted pulse to reflect from the sea-surface and be received. With rapid enough sampling intervals, either method is suitable to study the change in sea-level elevation due to meteotsunamis.

Isolating tsunami-period waves

Although tide gauges can be used to calculate the sea-surface elevation over a wide range of time scales (10^1–10^8 s), tsunamis only occupy a narrow range time scales with a train of a few waves that each have periods between 2–120 minutes (10^2–10^4 s). Therefore, to identify and quantify the properties of meteotsunamis, they must be separated from surges (about 3–12-hour periods lasting a few days) and tides (about 12–24-hour periods). For clarity, the surge in Figure 3.1 only occupies a narrow range of frequencies that are distinct from the tide and meteotsunami, but surge frequencies can overlap with tidal frequencies. Fortunately, tide gauges tend to eliminate higher frequency noise by using averaging intervals of between 1–15 minutes, with 5–6-minute averaging intervals recommended for studying tsunamis by the Intergovernmental Oceanographic Commission (IOC) since at least 2006 (IOC 2006), as part of the Global Sea-Level Observing System (GLOSS).

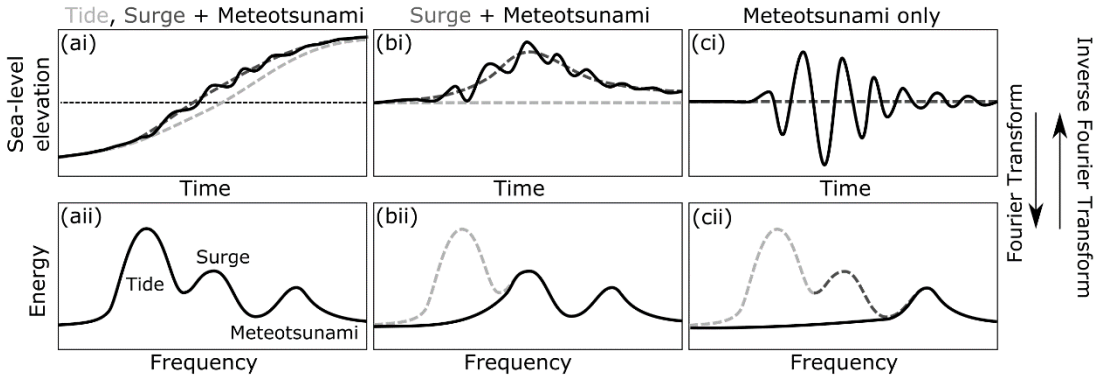

Figure 3.1 Removing tides and surges from sea-level observations to leave only observations in the tsunami-frequency band. Top – sea-level elevation with time, Bottom – energy at each frequency (requiring a Fourier transform of the sea-level elevation in time). a) sea-level elevation with tide, surge and meteotsunami, b) surge and meteotsunami only (tide removed), c) meteotsunami only (tide and surge removed). The black dashed line in (ai) represents the 0 m sea-level elevation, the light grey dashed line represents the tidal signal, the dark grey dashed line represents the surge signal, and the black solid line represents the meteotsunami signal. The direction of Fourier transformations between the time and frequency domain is shown. ii) the energy content at each frequency for a) the full signal with tide, surge and meteotsunami; b) for the signal with tide removed, with the removed tidal signal as the light-grey dashed line; and c) with the tide and surge removed, with the removed surge signal as the dark-grey dashed line.

Tides can be removed from the signal through harmonic analysis (e.g. Pattiaratchi and Wijeratne 2014; Šepić et al. 2015c; Oszoy et al. 2016; Lin and Liang 2017; Carvajal et al. 2017; Dusek et al. 2019). Harmonic analysis relies on the principle that the astronomical tide can be expressed as a sum of individual tidal constituents, where tidal constituents are sinusoids with a set amplitude, phase and period derived from the gravitational and centripetal accelerations due to, primarily, the Moon and the Sun (e.g. Pugh and Woodworth 2014). The amplitude and phase of tidal constituents with known periods are empirically derived using a least-squares approach from many months of sea-level elevation measurements. When these constituents are removed from the sea-level elevation measurements, the tidal signal should also be removed (cf. Figure 3.1a to Figure 3.1b).

Frequency filtering is another method to remove tides, but it can also remove surges (e.g. de Jong and Battjes 2004; Šepić et al. 2012; Asano et al. 2012; Bechle et al. 2015; Linares et al. 2016; Kim et al. 2016; Vilibić and Šepić 2017; Olabarrieta et al. 2017; Carvajal et al. 2017; Dusek et al. 2019). Frequency filtering relies on the principle that the signal of interest (i.e. the meteotsunami) has a different period to the signals to be removed (i.e. the tide or surge) (e.g. Figure 3.1a(ii)). By applying a Fourier Transform to the sea-level measurements, the energy at each frequency (rather than the sea-level elevation at each time) is calculated. Certain frequencies (or periods) can then be preferentially removed from the sea-level elevation measurements by damping the energy of the signal over that range of periods. After damping the undesired period range, an Inverse Fourier Transform is performed, and the filtered sea-level elevation at each time is obtained (cf. Figure 3.1a, Figure 3.1b and Figure 3.1c).

Wave-height thresholds

Unfortunately for studying meteotsunamis, the sea-level elevation at tsunami periods is almost constantly changing. Thus, to identify a meteotsunami, a wave-height threshold is often required. This threshold is typically between 0.2–0.3-m high (peak to trough) (e.g. de Jong and Battjes 2004; Šepić et al. 2009; Šepić et al. 2012; Bechle et al. 2016; Dusek et al. 2019), or a threshold related to the variance of typical measurements at specific tide gauges (once surge and tide have been removed) (e.g. Bechle et al. 2015; Oszoy et al. 2016; Kim et al. 2016; Olabarrieta et al. 2017; Carvajal et al. 2017; Dusek et al. 2019). These amplitude thresholds are designed to ensure that

usual variations around the mean sea-level elevation are not (mis)classified as meteotsunamis. There is further discussion of suitable wave-height threshold choices for meteotsunami identification in Chapter 6. Once a wave that is large enough has been identified and is in the tsunami-frequency band, this wave is typically referred to as a "non-seismic sea-level oscillation with tsunami timescales", or NSLOTTs, as termed in Vilibić and Šepić (2017).

Identifying atmospheric systems that produce meteotsunamis

To finally classify an NSLOTT as a meteotsunami, an atmospheric system must also be demonstrated to have co-occurred with the wave (Monserrat et al. 2006). Again, there are a few ways to identify that an atmospheric system could have generated a meteotsunami. Most commonly, measurements include the atmospheric surface pressure, the 10-m wind speed, the 10-m wind direction, and radar reflectivity.

3.1.2 Atmospheric measurements

Atmospheric surface pressure

Atmospheric surface pressure at the mesoscale and synoptic scale is primarily hydrostatic; it is produced by the weight of the air above the pressure sensor, which itself is dependent on the amount of air and the density of the air above the sensor (e.g. Markowski and Richardson 2011). Near the surface, atmospheric pressure decreases by about 1 hPa with a 10-m increase in elevation. The measured surface air pressure also decreases with increased temperature, because the density of warm air is less than the density of cold air. Therefore, the variation in measured atmospheric surface pressure between stations is because of both variations in station altitude and because of atmospheric processes. Because of estimated dependencies of pressure with height (a logarithmic vertical pressure profile) and air temperature (ideal gas equation of state), calculations can be made to adjust atmospheric surface pressure measurements at stations to an equivalent atmospheric sea-level pressure.

To link a mesoscale atmospheric system to a specific NSLOTT, *in situ* atmospheric surface pressure measurement stations are generally required to be within a few tens of kilometres from tide gauges (e.g. Šepić et al. 2012; Pattiaratchi and Wijeratne 2014; Pellikka et al. 2014; Wertman et al. 2014; Bechle et al. 2016; Oszoy et al. 2016; Lin and Liang 2017). To sufficiently sample the ~ 1 hPa surface pressure perturbations

with the mesoscale atmospheric system (e.g. Johnson 2001), atmospheric measurements should have an accuracy and a precision within about 0.1 hPa and average atmospheric measurements over a few minutes. In Chapter 4 of this dissertation, atmospheric surface pressure measurements are used from France, which were provided at 1-minute averaging intervals and was supplied to the nearest 0.1 hPa (provided by Lotfi Aouf from MétéoFrance).

10-m wind

Alongside atmospheric surface pressure measurements, at the same stations, the 10-m wind speed and 10-m wind direction may be measured and can help characterise the surface wind stress on the ocean. Equation 3.1 shows that the magnitude of the wind stress is assumed to be proportional to the square of the 10-m wind speed (e.g. Sorensen 2006; Pugh and Woodworth 2014),

$$\boldsymbol{\tau} = \rho_a C_a \, |\boldsymbol{U}_{10}| \, \boldsymbol{U}_{10}, \tag{3.1}$$

where ρ_a is the atmospheric surface density (~ 1 kg m^{-3}) and C_a is the coefficient of friction between the atmosphere and sea-surface. There are multiple choices for appropriate values of C_a over the sea-surface. In Chapter 4, a very simple approach is implemented, based on Large and Pond (1981),

$$C_a = \begin{cases} 0.0012 \,, & 4 \leq |\boldsymbol{U}|_{10} \leq 11 \text{ m s}^{-1}, \\ 0.00049 + 0.000065|\boldsymbol{U}|_{10}, & 11 < |\boldsymbol{U}|_{10} \leq 25 \text{ m s}^{-1}. \end{cases} \tag{3.2}$$

In other words, the coefficient of friction is constant, until the 10-m wind speed is above 11 m s^{-1}, at which point the coefficient of friction increases linearly with 10-m wind speed. This parameterisation represents that with higher 10-m wind speeds, the height and steepness of wind waves and swell waves also increase, which means that the sea-surface roughness increases.

Therefore, accurately measuring the 10-m wind speed is important because both the wind stress is directly proportional to the 10-m wind speed, but also because the coefficient of friction increases with higher 10-m wind speeds. In Chapter 4 of this dissertation, the 10-m wind speeds were measured using *in situ* Doppler anemometers, primarily located on mainland France. Measurements were available at a precision of 0.1 m s^{-1}, averaged over 1-minute intervals (provided by Lotfi Aouf from MétéoFrance).

Both 10-m wind speeds and atmospheric surface measurements can be used for more than just quantifying the atmospheric surface forcing amplitude. By identifying the arrival of mesoscale atmospheric systems in these measurements, the surface forcing velocity can be calculated by taking advantage of station triangulation (e.g. Orlić 1980; Thomson et al. 2009). However, if the mesoscale atmospheric system is precipitating, radar and radar-derived products may be more useful to characterise both the velocity and extent of the mesoscale atmospheric system. Ideally, both a network of *in situ* measurements and radar would be used to identify the surface properties of mesoscale atmospheric systems, as is possible in the US (e.g. Wertman et al. 2014).

Radar and radar-derived products

Radar (**RA**dio **D**etection **A**nd **R**anging) is a powerful tool to remotely sense precipitation-sized particles in the atmosphere, with many examples of using radar to understand the dynamics of precipitating mesoscale convective systems in Markowski and Richardson (2011). Radars work by transmitting a pulse of radio waves of known amplitude, phase and polarity, and measure the time lag, amplitude, phase and polarity of waves that have been reflected back to the transmitter. From this data, a reflectivity field of precipitation-sized particles in the atmosphere can be calculated, and radar measurements from individual stations over hundreds of square-kilometres can be combined, to form a "mosaic" of radar-reflectivity fields (e.g. Met Office 2003; Antonescu et al. 2013). From the Met Office, reflectivity data is output as a calculated precipitation rate, by employing the Marshall-Palmer relation (e.g. Met Office 2003; Antonescu et al. 2013). With operational and archived radar mosaics that are available once every 5–15 minutes on 1–5 km horizontal grids, radar reflectivity fields and derived precipitation-rate fields are suitable to identify and characterise precipitating mesoscale atmospheric systems (e.g. Gallus et al. 2008; Liu and Zipser 2013; Antonescu et al. 2013; Fairman et al. 2016; Fairman et al. 2017) and calculate velocities of atmospheric mesoscale systems (e.g. Wertman et al. 2014). In this dissertation, fields of composite radar-derived precipitation-rate are used to supplement *in situ* atmospheric surface measurements, calculate mesoscale atmospheric system velocities, identify mesoscale atmospheric systems that generated meteotsunamis, and classify those mesoscale atmospheric systems.

Reanalysis model output as a tool for classifying synoptic environments

Finally, although not strictly observations of atmospheric systems, reanalysis model output is often treated similarly to synoptic atmospheric observations in meteotsunami research. This output is often used to categorise the mean synoptic atmospheric thermodynamic environments within which meteotsunami-generating mesoscale atmospheric systems form (e.g. Šepić et al. 2015b; Vilibić and Šepić 2017). Reanalysis model output is the result of numerical modelling that assimilates atmospheric measurements from the surface and atmospheric vertical profiling, and then outputs consistent thermodynamic fields once every few hours (1–6 hours) on regular grids (ranging between about 25–250-km horizontal grid spacing). Two reanalysis models are used in this dissertation, the lower-resolution NCEP/NCAR reanalysis model (Kalnay et al. 1996) in Chapter 4 to check the reasonableness of other calculations (e.g. mesoscale system velocity), and the higher-resolution ERA5 reanalysis model (Copernicus Climate Change Service 2017) in Chapter 6 to characterise mean synoptic environments.

3.2 Simulating meteotsunamis

Although the generation and propagation processes of meteotsunamis are understood through analytical tools, and it is possible to identify meteotsunamis from tide gauge records and classify the atmospheric systems that generate meteotsunamis, the specific processes that are important for individual meteotsunamis are often studied with numerical models. Here, numerical models are used for (1) idealised modelling in Chapter 5 and Chapter 7, because controlled experiments are nearly impossible with real data, and (2) the meteotsunami case study in Chapter 4, because individual wave processes are often impossible to differentiate or analytically calculate. The numerical models used here fall broadly into two classes: finite-difference models and finite-element models.

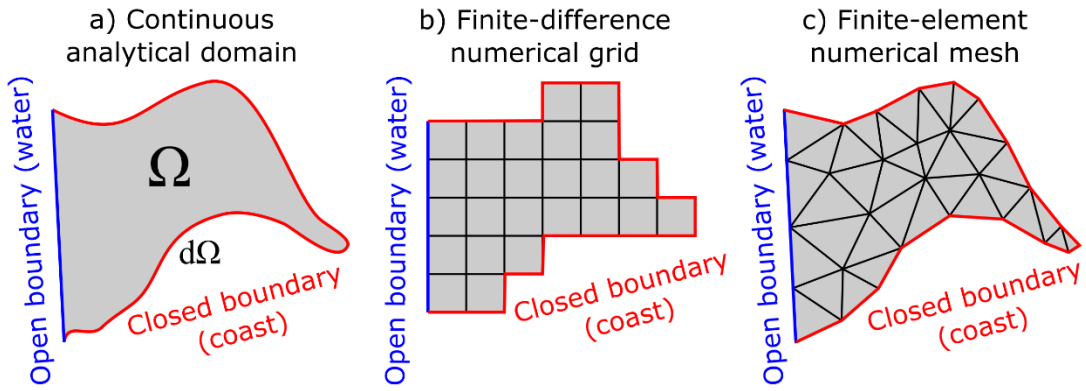

Figure 3.2 The domain Ω on which the governing equations are solved and the boundary dΩ on which boundary conditions are implemented in a) the analytical domain, b) the finite-difference grid representation and c) the finite-element mesh representation. The red and blue boundaries are closed boundaries and open boundaries respectively.

3.2.1 Finite-difference models

The finite-difference approach discretises the continuous partial-differential equations, the continuous space (e.g. Figure 3.2a) and continuous time on which the shallow-water equations are derived, into regular intervals (in one dimension) or into regular grids (in two dimensions) (e.g. Figure 3.2b). In modern meteotsunami research, simple finite-difference methods are now primarily used to study idealised wave processes (e.g. Vilibić 2008; Bubalo et al. 2018), rather than more complex case studies (e.g. Hibiya and Kajiura 1982). For this dissertation, a one-dimensional and two-dimensional finite-difference scheme has been developed in Python 2.7.5 to solve the linear, frictionless, flat-bottomed, one-dimensional and two-dimensional sea-level elevation wave equations for a moving atmospheric sea-level pressure forcing. The developed finite-difference scheme is further discussed in Appendix C. This finite-difference numerical model was developed for rapid simulations and to provide numerical results for highly idealised models that use rectangular domains.

3.2.2 Finite-element models

For more complicated simulations, including the meteotsunami case study in Chapter 4, and initial conditions and time-varying boundary conditions in Chapter 5, the finite-element model Telemac was used to solve the shallow-water equations (also known as Telemac2D). This model was first developed for Electricité de France (EDF) (Hervouet 2000) but has since been used in academia for many hydrodynamic

problems. Telemac has been used for atmospherically generated shallow-water waves (e.g. Maskell 2011), tsunami waves (e.g. Horsburgh et al. 2008) and tides (Hervouet 2000) in north-west Europe.

Finite-element models, such as Telemac, also discretise space and time, over which polynomial approximations of the governing equations are then solved. When each approximation is summed over all the small elements, the overall fluid motion is closely approximated. The most important benefit of finite-element modelling is that two-dimensional elements can be triangular and vary in size, meaning that important regions, such as coastlines, can be more accurately approximated than with regular finite-difference grids (cf. the shape of boundaries of Figure 3.2b and Figure 3.2c with Figure 3.2a). The collection of these triangular elements is commonly called the mesh.

Finite element models often require a mesh created by a separate mesh generator programme. Here, Blue Kenue (Canadian Hydraulics Centre 2016) has been used, which uses Delaunay triangulation to create meshes with triangular elements. Within Blue Kenue, the types of boundary can also be specified, for example, whether a boundary is open (i.e. connected to water which is outside of the model domain) or closed (i.e. a coastline or rigid structure).

3.2.3 Applying boundary conditions and initial conditions

For the numerical models to give suitable approximations to the fluid motion, accurate information of boundary conditions and initial conditions are required. This type of information is required to calculate solutions to the shallow-water equations, or in fact any differential equation that describes the behaviour of a physical quantity over time and space. Specifically, the shallow-water equations require information of the behaviour of fluid against boundaries such as coastlines, rigid structures or connections to other water bodies (boundary conditions) and the initial state of the ocean at all locations, such as the sea-level elevation or initial currents (initial conditions).

Bathymetry and coastlines

There is also the boundary condition that flow cannot pass through the bottom of the ocean. Although this boundary need not be defined (it is already implied in the form of the shallow-water equations), accurate water depths are important to accurately

define the locations of horizontal boundaries, as well as accurately simulating external resonance, wave reflection and transmission, shoaling, refraction and seiching. Here, water depths that are accurate within a few centimetres are taken from the General Bathymetric Chart of the Oceans (GEBCO), the version of which used in this dissertation has been supplied by the British Oceanographic Data Centre (BODC) since 2014, which is referred to as GEBCO 2014 (IOC et al. 2003).

GEBCO 2014 is a two-dimensional gridded dataset, with water-depth grid spacings at 30 arc-seconds (~ 800 m). The GEBCO 2014 dataset was created through a mix of acoustic methods, with water depth calculated from the time it takes sound to travel from the sea-surface and reflect back from the sea floor, and gravitational methods, with water depth calculated from variations in mean sea-surface elevation due to variable gravitational attraction from topographic features (IOC et al. 2003). Since 2019, an updated version of the GEBCO grid spacing with 15 arc-seconds (~ 400 m) has been available, though for typical wavelengths of meteotsunamis (10–50 km), simulations should be insensitive to the changes in grid spacing between 2014 and 2019.

Accurately defining the location and orientation of coastlines is also important for Greenspan resonance, shoaling, refraction, and reflection from the coast, but is probably most important to accurately simulate seiching. Seiching is a resonant process that is highly dependent on the modelled harbour geometry (e.g. Denamiel et al. 2018; Bubalo et al. 2019). In this dissertation, for the case study simulation of a meteotsunami in Chapter 4, the 0-m contour was extracted and used as the coastline. As commonly practised when simulating shallow-water wave generation and propagation, the coastline was then applied in models as a vertical wall, with no flow through the boundary. This assumption is appropriate for simulations of meteotsunami generation and propagation, but would not be appropriate for flood inundation studies, which require wetting and drying schemes (Bubalo et al. 2019).

Including tides

As previously mentioned, north-west Europe has some of the largest tidal ranges (> 8 m) and currents (> 3 m s^{-1}) in the world. Including the total water depth (bathymetry + tidal sea-level elevation) and currents (tidal flow) are also important to accurately simulate shoaling, refraction, reflections and transmissions, but is probably most

important to accurately represent shallow-water wave speeds to simulate external resonance (e.g. Choi et al. 2014) and seiching (e.g. Denamiel et al. 2018).

Realistic and idealised tides can be modelled in Telemac by applying both time-varying boundary conditions, initial velocity fields, and initial sea-level elevation fields. Realistic tidal conditions were taken from the Oregon State University TOPEX/Poseidon Global Inverse Solution tidal model (TPXO, Egbert and Erofeeva 2002) because Telemac is capable of interpolating and applying the output from TPXO as boundary conditions and initial conditions. The boundary conditions were taken specifically from the OTIS regional tidal solution of the European Shelf, which was first released in 2008. This regional model is available at 1/30º grid spacing (~ 30 m), and outputs the amplitude and phase of 11 tidal constituents. When combined, these tidal constituents closely approximate the tidal cycle (with a root mean squared error of a few centimetres) across the north-west European continental shelf (Egbert et al. 2010).

The TPXO model boundary conditions were carefully implemented in the case study model in Chapter 4. Specifically, in the tidal simulation of the English Channel in Chapter 4, the initial velocity was set to 0 m s^{-1} and the initial sea-level elevation was set to 0 m. Then, the boundary conditions were extracted from the TPXO model, bilinearly interpolated to the open boundaries, and the amplitude of tidal constituents were linearly ramped from 0 m to full amplitude over 2 days to avoid introducing non-physical shocks to the model. The tidal simulation was allowed to run for a further 4 days to reach dynamic equilibrium. This more careful approach was needed for model stability, because the bathymetry and coastlines were slightly different between TPXO, which used 60-arc second gridded bathymetry (GEBCO 2008) compared to the simulations in this dissertation, which used 30-arc second gridded bathymetry (GEBCO 2014) (Egbert et al. 2010). The final tidal simulations were checked for agreement between tide gauges, with more detail on the observations and simulations provided in Chapter 4.

In Chapter 5, with simulations of idealised tidal processes, a mix of approaches to implement tidal sea-level elevation and currents were used. Most simply, constant changes to sea-level elevation from tides, or constant tidal currents were included. When time-varying conditions were used, a single sinusoid with set amplitude, phase

and period was introduced at one boundary, and simulations were run for enough time to approach dynamic equilibrium. Again, more detail of these idealised tidal simulations is provided in Chapter 5.

3.2.4 Applying an atmospheric forcing

Probably the most important process to include in meteotsunami generation and amplification is a suitable and accurate atmospheric forcing. There are two main ways to supply an atmospheric forcing to ocean models. The first, which is used most in this dissertation, is by using the measurements from atmospheric observations (e.g. *in situ* surface pressure, 10-m wind fields, radar-derived precipitation rates) to prescribe an atmospheric forcing with a set of analytic forcing functions. This method is known as synthetic modelling (Ličer et al. 2017), or as a heuristic approach when using a synthetic model to forecast a meteotsunami (e.g. Linares et al. 2016). This method is a popular way to input the atmospheric forcing because it is controllable, with forcing velocity, amplitude and period fully prescribed by an analytic forcing function. Synthetic forcing functions are typically fairly simple (e.g. a sinusoid or linear forcing function) and parameters, such as forcing speed, can be easily changed by a known amount. This control means that key wave processes can be more easily isolated and identified through simulations repeated with small variations on the prescribed forcing parameters (i.e. an ensemble) (e.g. Candela et al. 1999; Šepić et al. 2015a; Ličer et al. 2017; Bubalo et al. 2019).

However, synthetic models only represent atmospheric forcing fields as well as can be inferred from sparse atmospheric measurements. These measurements are also often over land, meaning that sea-level pressure and 10-m wind fields are not known over water. Synthetic models are also not able to capture the complexity of mesoscale weather phenomena. Therefore, atmospheric processes that could influence meteotsunami generation, such as the generation of new gust fronts in linear convective systems (e.g. Markowski and Richardson 2011), are typically not included in models that use synthetic forcings (e.g. Anderson et al. 2015).

The problem of an overly simple representation of the atmosphere can be overcome by using numerical weather prediction (NWP) models, which are capable of dynamically modelling mesoscale atmospheric phenomena by solving the three-dimensional thermodynamic and continuity equations (e.g. Horvath and Vilibić 2014;

Anderson et al. 2015; Horvath et al. 2018). Because these simulations are calculated with grid spacing on the order of 0.1–1 km and time steps of a few seconds, they provide sophisticated representations of the three-dimensional structure of mesoscale atmospheric systems, and the two-dimensional ocean-surface forcing fields of sea-level pressure field and 10-m wind velocity. The idea that motivates using NWP model output and more realistic surface forcing fields, is that more realistic meteotsunami simulations could be produced than from synthetic forcings, with smaller discrepancy between the arrival time and wave heights of meteotsunamis. If NWP models are also properly incorporated in ocean modelling, then they can also be used to hindcast meteotsunami wave heights and arrival times as accurately as more commonly used synthetic models (Anderson et al. 2015). Ultimately, NWP models could be used to improve operational forecasts from a simple heuristic approach to an integrated coupled-model approach.

However, in practice, it may be quite difficult to simulate the highly dynamic mesoscale atmospheric systems with current operational systems (e.g. Anderson et al. 2015; Denamiel et al. 2019; Romero et al. 2019). Furthermore, the effect of variable atmospheric system velocity and variable surface-forcing amplitude on external resonance mechanisms are, as yet, unquantified. Therefore, in this dissertation, in Chapter 5, the effects of variable forcing speed and variable surface forcing amplitude are quantified, which in turn may help justify the choices made when using NWP models, and explain the results of meteotsunami simulations with NWP forcing.

A popular NWP model to simulate mesoscale weather phenomena is the Weather Research and Forecasting model (WRF). During this dissertation, there was considerable effort made to simulate idealised linear convective systems in the third version of WRF (Skamarock et al. 2008), and extracting surface atmospheric forcings to supply to Telemac. Whilst the results of these simulations have not been developed enough for publication, they are included in the Appendix D and provide evidence that supports the main conclusions of Chapter 5.

Chapter 4

Examination of Generation Mechanisms for an English Channel Meteotsunami: Combining Observations and Modeling

4.0 Preamble

Study motivation

Prior to this dissertation, there had not yet been a study of meteotsunamis across the north-west European continental shelf that had first identified a meteotsunami and then supplemented these observations with numerical modelling. Thus, any meteotsunami case study lacked quantitative generation mechanism explanations. The primary focus of the work in this chapter was to produce the first simulation of meteotsunami generation in north-west Europe, and to quantify how such a meteotsunami was generated.

The meteotsunami discussed in this study was found by applying previous knowledge of summer-time case studies (e.g. Tappin et al. 2013; Frère et al. 2014; Sibley et al. 2016). Having noticed that there were storms with heavy precipitation across Europe on overnight between 22–23 June 2016, tide gauge measurements were examined. The following work came from identifying a tsunami-like wave in these records, and the accumulation of evidence supporting that this tsunami-like wave was a meteotsunami.

Publication and Author Contribution

The work in this chapter has been published in the *Journal of Physical Oceanography* with four authors: David A Williams, Kevin J Horsburgh, David M Schultz and Chris W Hughes. It was first available as an early online release in November 2018 and first published online in January 2019. The paper went through two rounds of peer review with comments requiring minor corrections. The chapter is in US English, according to the standards of the *Journal of Physical Oceanography*.

David A Williams wrote the publication, noticed the initial phenomenon, analysed the measurements, developed the modelling tools, complete the numerical simulations, and completed the submission and revision process for publication. Kevin J Horsburgh was the primary supervisor for the project and secondary author, secured funding,

provided editorial critique, helped with analysis of oceanographic components, and helped with discussion of ideas. David M Schultz is listed as the third author of the publication, and provided editorial critique, ensured rigorous interpretation in the atmospheric analysis, and was involved in discussion of ideas. Chris W Hughes is listed as fourth author of the publication and provided editorial critique and gave invaluable insight into fundamental wave amplification mechanisms.

Related Appendices

A meteotsunami is not often the first explanation for a tsunami-like wave in tide gauge records. After checking the Harvard Centroid Moment Tensor Catalog (a global earthquake database), a seismic generation mechanism was discounted. Yet a landslide source mechanism still needed discounting. To discount this mechanism, it was shown that the travel times of the tsunami-like wave could not be explained by a shallow-water wave originating from various point-sources across English and French coastlines. In Appendix A, how these travel times were calculated is explained.

Citation and Reference

This chapter is cited as Williams et al. (2019), and can be found in the bibliography:

Williams, D.A., K.J. Horsburgh, D.M. Schultz, and C.W. Hughes, 2019: Examination of generation mechanisms for an English Channel meteotsunami: combining observations and modeling. *J. Phys. Oceanogr.*, **49**, 103–120, doi:10.1175/JPO-D-18-0161.1.

4.1 Paper Abstract

On the morning of 23 June 2016, a 0.70-m meteotsunami was observed in the English Channel between the United Kingdom and France. This wave was measured by several tide gauges and coincided with a heavily precipitating convective system producing 10 m s^{-1} wind speeds at the 10-m level and 1–2.5-hPa surface pressure anomalies. A combination of precipitation rate cross correlations and NCEP–NCAR Reanalysis 1 data showed that the convective system moved northeastward at 19 ± 2 m s^{-1}. To model the meteotsunami, the finite element model Telemac was forced with an ensemble of prescribed pressure forcings, covering observational uncertainty. Ensembles simulated the observed wave period and arrival times within minutes and wave heights within tens of centimeters. A directly forced wave and a secondary coastal wave were simulated, and these amplified as they propagated. Proudman resonance was responsible for the wave amplification, and the coastal wave resulted from strong refraction of the primary wave. The main generating mechanism was the atmospheric pressure anomaly with wind stress playing a secondary role, increasing the first wave peak by 16% on average. Certain tidal conditions reduced modeled wave heights by up to 56%, by shifting the location where Proudman resonance occurred. This shift was mainly from tidal currents rather than tidal elevation directly affecting shallow-water wave speed. An improved understanding of meteotsunami return periods and generation mechanisms would be aided by tide gauge measurements sampled at less than 15-min intervals.

4.2 Introduction

On the morning of 23 June 2016, a 0.70-m-high, 35-min-period wave coinciding with convective storms was observed in the English Channel (Figure 4.1). This study shows this wave to be a meteorologically generated tsunami, also known as a meteotsunami.

Meteotsunamis are atmospherically generated shallow-water waves in the tsunami frequency band, with periods between 2 min and 2 h (Monserrat et al. 2006). Meteotsunami wave heights are on the order of 0.1–1 m (Monserrat et al. 2006). Meteotsunamis have sporadically occurred in water bodies on every continent (except Antarctica, where there is absence of evidence). In specific locations, such as Nagasaki Bay in Japan (Hibiya and Kajiura 1982), Ciutadella Harbor in Menorca (Rabinovich and Monserrat 1998), or Split in Croatia (Šepić et al. 2012), meteotsunamis repeatedly occur and can reach up to 6 m. They are also recurrent in the Laurentian Great Lakes (Bechle et al. 2016), where strong rip currents are particularly dangerous (Anderson et al. 2015; Linares and Bechle 2018). They have caused substantial economic losses;

for example, a 6-m meteotsunami produced $7 million of damages in Vela Luka Bay in 1978 (Vučetić et al. 2009). Furthermore, they may cause injury (Sibley et al. 2016) and sometimes fatalities (Monserrat et al. 2006; Linares and Bechle 2018).

In the United Kingdom, there have been recorded meteotsunamis along the south coast in 2011 (Tappin et al. 2013) and along the east coast in 2008 and 2015 (Sibley et al. 2016). Although they are seldom reported, damage to boats has been associated with possible meteotsunamis (Haslett et al. 2009). Also, in 2015, a confirmed meteotsunami in Scotland was related to at least one serious injury (Sibley et al. 2016), and, in 1929, a suspected meteotsunami was related to two deaths along the U.K. southern coastline (Haslett et al. 2009). In 2017, a large tsunami-like wave was noticed at high tide in the Netherlands and was reported by televised weather reports as a meteotsunami generated by a passing convective system.

However, understanding meteotsunami generation around the United Kingdom, and in wider European seas, remains poor because these reports lack quantitative generation mechanism explanations. To date, there is no study in this region that relates the observed waves to their meteorological initiation and amplification. That is the motivation for this work. We use combined observations and numerical modeling to quantitatively understand the generation mechanisms, the relative role of atmospheric pressure and wind stress, and the wave amplification.

Meteotsunamis are initiated by pressure and wind stress from moving atmospheric weather systems (Monserrat et al. 2006). Typically, meteotsunami-generating atmospheric systems are hundreds of kilometers in scale and last a few hours—they are mesoscale systems. Since the atmospheric pressure perturbations (~ ± 1hPa) and 10-m wind speeds (~ 10 m s^{-1}) in mesoscale systems typically produce centimeter-scale sea surface perturbations, amplification mechanisms are required for large meteotsunamis (Monserrat et al. 2006). This requirement for wave amplification makes meteotsunamis different from storm surges, which are generated over larger time and space scales by cyclones with deep pressure lows (> 50 hPa lower than background pressure) and strong 10-m wind speeds (> 20 m s^{-1}).

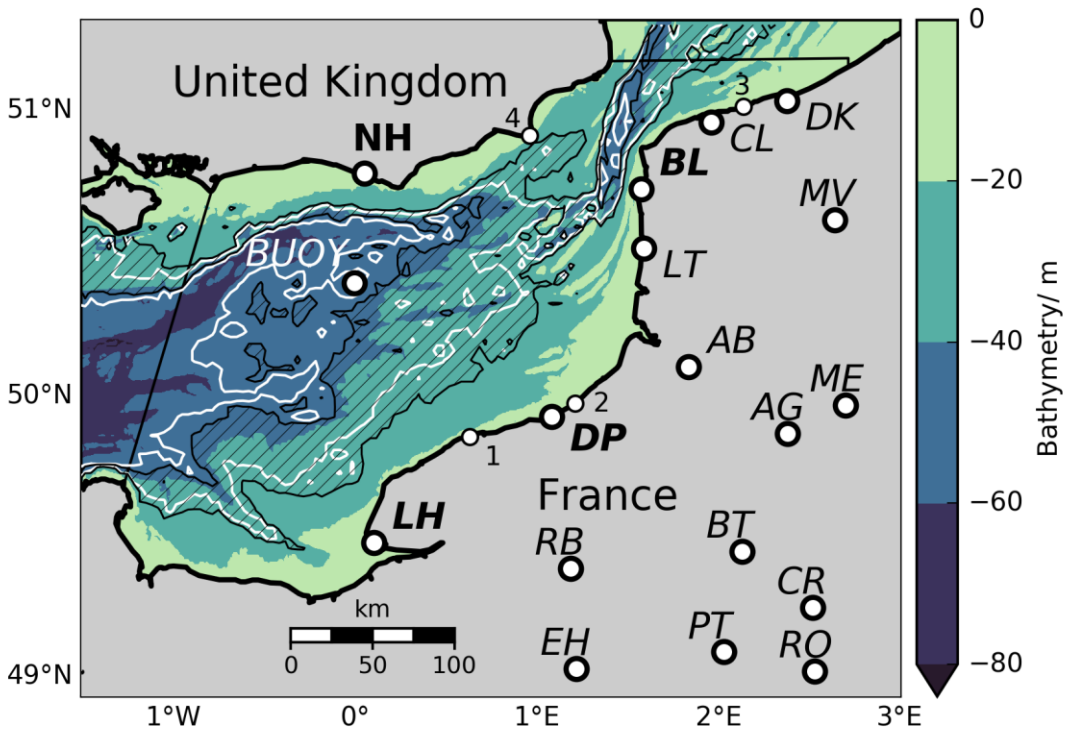

Figure 4.1 English Channel bathymetry (IOC et al. 2003) in filled contours from shallow (light blue) to deep (dark blue). The color saturates when bathymetry is deeper than 80 m. The black, hatched area is the still-water level region where $0.9 \leq Fr \leq 1.1$. The area bounded by white lines is the equivalent region with –0.5-m tidal elevation and –1 m s^{-1} current approximations. Tide gauges locations have bold typeface, atmospheric stations have italic typeface, and locations with both tide gauges and atmospheric stations have italic bold typeface. The locations are Newhaven (NH), Le Havre (LH), Dieppe (DP), Le Touquet (LT), Boulogne (BL), Dunkirk (DK), Rouen Boos (RB), Evreux Huest (EH), Beauvais Tille (BT), Roissy (RO), Creil (CR), Pointoise (PT), Amiens Glisy (AG), Abbeville (AB), Meaulte (ME), Merville (MV), Calais (CL), Paluel (1), Penly (2), Gravelines (3), Dungeness B (4), and Greenwich Lightship buoy (BUOY). A 100-km scale is given. The model open boundaries are shown as thin black lines. Land is shaded gray. Thick black lines are coastlines from the Basemap Python package.

Amplification up to an order of magnitude can be provided by resonance between the meteotsunami and atmospheric forcing (external resonance) (Monserrat et al. 2006). Greenspan resonance and Proudman resonance are two candidate external resonances. Greenspan resonance occurs when the atmospheric forcing speed along the coastline is the same as a coastally trapped edge wave (Greenspan 1956), whereas Proudman resonance occurs when the atmospheric forcing speed is the same as the shallow-water wave speed (Proudman 1929). Numerical models have provided evidence supporting Greenspan resonance in the Great Lakes (Ewing et al. 1954; Anderson et al. 2015) and Proudman resonance in Adriatic (Šepić et al. 2015a), Balearics (Ličer et al. 2017), and East China Sea (Hibiya and Kajiura 1982). Frère et al. (2014) and Tappin et al. (2013) have suggested that Proudman resonance was responsible for observed meteotsunamis around the United Kingdom, but this has never been demonstrated through numerical modeling, as we do here.

Acquiring evidence for meteotsunami mechanisms away from coastal tide gauges is difficult but can be achieved with a dense oceanographic observational network (Sheremet et al. 2016); unfortunately, no such network is in the English Channel. Therefore, we use numerical models for evidence of external resonance. Our approach is to prescribe an analytic atmospheric forcing, guided by observations, to force a hydrodynamic ocean model. We refer to this as a synthetic model, following Ličer et al. (2017). There are two advantages to synthetic models over models forced by numerical weather prediction output (NWP models), despite NWP models' capability for more detailed forcing. First, synthetic models are simpler than NWP models and simulate comparable wave heights and arrival times (Anderson et al. 2015). Second, synthetic models allow full control in sensitivity studies when investigating the relative importance of generation mechanisms such as wind stress and pressure disturbances (Bechle and Wu 2014; Anderson et al. 2015; Šepić et al. 2015a). For instance, in Lake Erie, wind stress accounts for 30–60% of wave height (Anderson et al. 2015), whereas in the Adriatic, pressure accounts for 90% of wave height (Šepić et al. 2015a).

Meteotsunamis may undergo further amplification when approaching coastlines. Basin bathymetry and the coastline shape (referred to in combination as ‘‘geomorphology’’) amplify meteotsunamis through refraction and shoaling (Levin and Nosov 2016 pp. 311–345). Simple calculations (Green's law) suggest that

geomorphology in the English Channel amplifies waves by less than an order of magnitude. In this study, we examine amplification due to both external resonance and geomorphology. Because the English Channel is macrotidal (>4-m tidal range), we also consider the sensitivity of meteotsunami growth to tides. In South Korea, another macrotidal basin, modeled wave heights change by up to 11% from tidal elevation affecting Proudman resonance and change by 9% from tidal currents causing refraction (Choi et al. 2014). Therefore, tides may affect wave growth as much as atmospheric forcing.

This paper presents the observations of the 23 June 2016 meteotsunami in the English Channel and shows, with the help of a prescribed analytic atmospheric forcing, the relative importance of the pressure field versus the wind field, external resonance in the meteotsunami generation, the sensitivity in simulations of external resonance to observational uncertainties, and the sensitivity of wave heights to tides. Progress toward operational hazard warning systems for meteotsunamis, as is being worked on in the Adriatic (Vilibić et al. 2016), requires improved regional understanding of meteotsunami generation. We present and analyze oceanographic and atmospheric observations in section 4.3 and then present numerical modeling in section 4.4. Section 4.5 concludes and gives recommendations for future work.

4.3 Observations

4.3.1 Sea surface observations

The tide gauge locations are shown in Figure 4.1, and 23 June 2016 water-level time series are shown in Figure 4.2. The tidal records show that the English Channel is macrotidal, with tidal ranges of 7–8 m near France and 5 m near the United Kingdom. The sea level signal was high-pass filtered to isolate the high-frequency disturbances. After removing periods greater than 2 h, the largest residual wave height (from peak to trough; red boxes in Figure 4.2) measured at Boulogne, France, was 0.78 m and at Dieppe, France, was 0.42 m (BL and DP in Figure 4.1). No significant residual was measured at Le Havre, France (LH; Figure 4.1). Data were missing from 0527–0534 UTC each day at French tide gauge stations (Figure 4.2) and 0048–0149 UTC at Le Havre, but this did not impede analysis of wave characteristics.

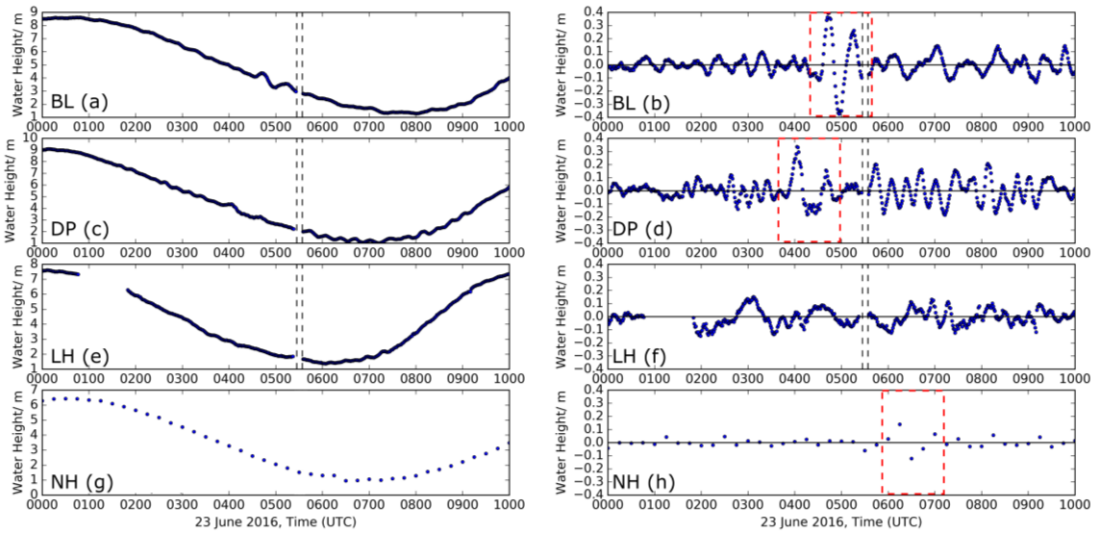

Figure 4.2 (left) Tide gauge raw data. (right) High-pass filtered tide gauge observations (< 2 h periods) at (a), (b) BL, (c), (d) DP, (e), (f) LH, and (g), (h) NH. The red box indicates meteotsunami arrival. Black dashed lines highlight missing data between 0527 and 0534 UTC inclusive.

The 1-min sampled French radar tide gauges also showed that the dominant period of this perturbation was 30–35 min (Figure 4.2), within accepted tsunami-period limits (Monserrat et al. 2006). This dominant tsunami signal, isolated with a 10–60-min-period bandpass filter, had similar wave heights to the nontidal sea level residual—0.70 m at Boulogne and 0.43 m at Dieppe. We took these values as representative wave heights and were deemed large enough to be a meteotsunami (Monserrat et al. 2006). We defined the arrival time as the time at which the residual water level was half of the first peak (which may not be the maximum residual water level) and directly preceded the first peak. The arrival times were 0447 UTC at Boulogne and 0358 UTC at Dieppe, near midtide in France (Figure 4.2). The Newhaven, United Kingdom, tide gauge (NH; Figure 4.1) suggested that a 0.26-m high wave arrived later, at 0608 ± 0007 UTC. However, owing to the 15-min data at Newhaven, there was high uncertainty in wave height and arrival time at this location.

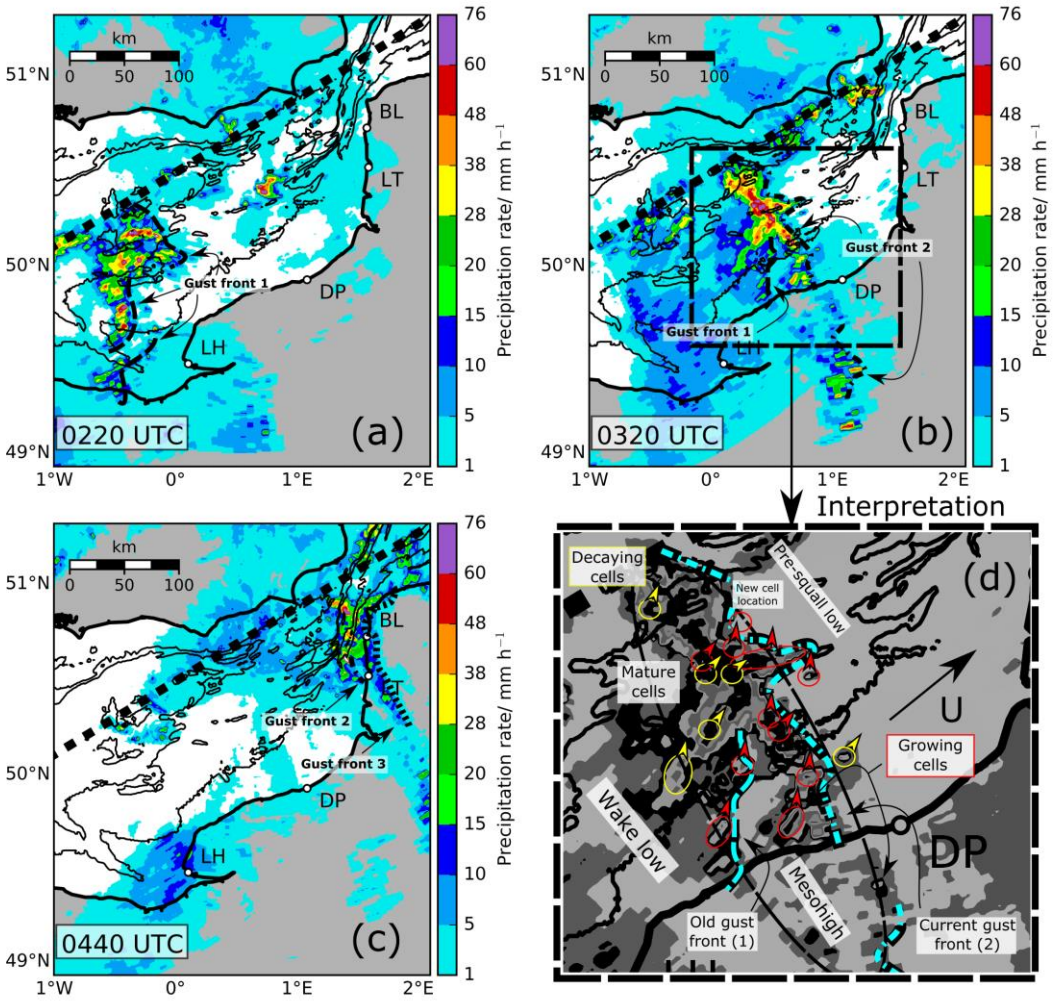

Figure 4.3 Composite radar derived precipitation rates (mm h^{-1}) are shown for (a) 0220, (b) 0320, and (c) 0440 UTC 23 Jun 2016 in the English Channel (Met Office 2003). Thin black lines indicate where the Froude number is 0.9 and 1.1 with GEBCO 2014 bathymetry and a 19 m s^{-1} atmospheric system speed. The thick, dotted line is the calculated maximum horizontal extent of the convective system. Three gust fronts are indicated. Gust front 1 is long-dashed, gust front 2 is dot–dashed, and gust front 3 is dotted. (d) The interpretation is shown. Yellow circles indicate a decaying cell, and red circles indicate a strengthening cell. The arrowheads indicate the direction these cells moved between 0315 and 0325 UTC. The gust fronts are shown in cyan. Locations of atmospheric stations at LH, DP, LT, and BL are shown. A 100-km scale is given. Land is shaded gray. Thick black lines are coastlines from the Basemap Python package.

4.3.2 Atmospheric observations

Convective storms and heavy precipitation were reported across western Europe between 22 and 23 June 2016. Figure 4.3a, Figure 4.3b and Figure 4.3c show 1-km gridded composite radar-derived precipitation rates over the English Channel at 0220, 0320, and 0440 UTC, respectively. A small stratiform-trailing convective storm was embedded in light precipitation (< 5 mm h^{-1}), moving northeastward over the English Channel.

In the following section, the atmospheric properties of this convective system are quantified, and its potential for meteotsunami generation is analyzed. The important atmospheric properties for wave initiation are wind stress and pressure perturbation amplitude.

Pressure perturbations and wind stress

To analyze the convective system pressure perturbations, the total measured pressure was high-pass filtered. Figure 4.4a shows that the maximum pressure perturbations were generally within ±1.5 hPa. As the convective system progressed northeastward (cf. Figure 4.4 and Figure 4.3), the high pressure anomaly (mesohigh) strengthened, with low pressure anomalies (mesolows) forming ahead of (presquall low) and behind (wake low) the mesohigh. The pressure anomalies farther inland, between Evreux-Huest, Pointoise-Aero, Creil, Roissy, Beauvais-Tille, Amiens Glisy, Meaulte, and Merville-Calonne (see locations at Figure 4.1) France, also show a presquall low and mesohigh progressing northeastward. Figure 4.3d shows the interpretation of the convective system at 0320 UTC, guided by the low–high–low pressure pattern described in Markowski and Richardson (2011).

Figure 4.4b shows that at Le Touquet, Boulogne, and Calais, France, moderate winds were measured between the presquall low and the mesohigh, interpreted as the gust front. At Le Touquet and Dunkirk, France, there were also peak winds between the wake low and mesohigh. At Le Touquet, the maximum 10-m wind speed measured prior to the mesohigh was 8 m s^{-1} and reached a maximum of 10 m s^{-1} after the mesohigh. The Greenwich Lightship buoy (BUOY in Figure 4.1) also showed a +1.3-hPa high pressure anomaly and 11 m s^{-1} 14-m wind speeds between 0300 and 0400 UTC (sampled once per hour), broadly agreeing with *in situ* land station observations.

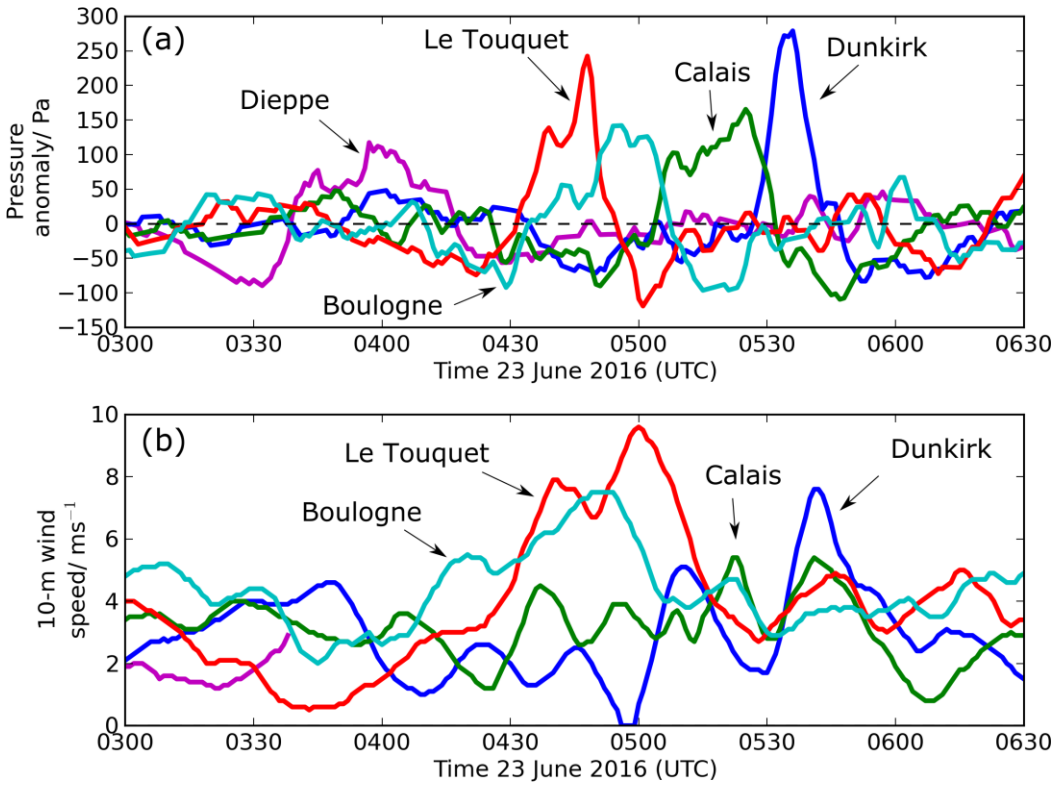

Figure 4.4 High-pass-filtered atmospheric observations at Dieppe (purple), Le Touquet (red), Boulogne (cyan), Calais (green), and Dunkirk (blue). (a) The 2-h cut-off high-pass-filtered air pressure time series. (b) Average 10-m wind speed over 10-min windows. Pressure and wind speed sampled once per minute.

Convective system velocity

By assuming equilibrium between hydrostatic and atmospheric forces (e.g., inverted barometer effect), calculations suggest that this atmospheric forcing would have only produced a 0.04-m high wave. Therefore, if the observed wave (0.70 m) were produced by this convective system, it would have needed amplification mechanisms. This may have happened if the speed of the atmospheric system moved at resonant speed. To determine whether external resonance could have occurred, first we calculated the speed of the convective system using two-dimensional cross correlation of radar-derived precipitation.

Two-dimensional cross correlation has been previously used to estimate meteotsunami forcing velocity with satellite images of cloud tops (Belušić and Mahović 2009) and radar reflectivity (Wertman et al. 2014). Here, cross correlation was used on the radar-derived precipitation fields, which should have provided more representative

velocities compared to cloud tops. We took the displacement required for the maximum cross correlation to calculate the velocity of the convective system between time steps. Following Wertman et al. (2014), multiple time steps were used (5, 10, 15, 20, and 30 min) between 0200 and 0400 UTC. However, precautions were taken to remove effects of individual cells. Here, a binary signal was created, equalling 1 when the precipitation rate was greater than a rain-rate threshold and 0 when the rate was less than the threshold. A range of time steps and thresholds on the two-dimensional cross correlation allowed analysis of convective system velocity to chosen parameters and the best range of parameters to be chosen.

When calculating convective system velocity, we assumed straight line motion. With 10-min time steps and a 15 mm h^{-1} threshold, the convective system velocity was estimated as 19 ± 2 m s^{-1} (all errors here given to 1σ) at a bearing of 35º ± 3º. The speed decreased with larger time steps, from 20 ± 2 m s^{-1} at 5 min time steps to 18 ± 1 m s^{-1} at 20-min time steps. The system's direction of movement was more poorly defined, changing from 21º ± 4º (more northward) to 47º ± 8º (more eastward) between 5- and 20-min time steps. Nevertheless, the speed remained consistently between 17 and 22 m s^{-1}.

The cross-correlation results were related to the movement of the whole convective system and individual storm cells. Figure 4.3 shows that three individual gust fronts were identified as the convective system propagated. We identified the gust front as the leading edge of precipitation, which coincided with higher 10-m wind observations. New gust fronts were identified when a new line of cells was generated ahead of, and disconnected from, previous gust fronts. A gust front that generated new convective cells was a form of discrete propagation and produced unreasonably large velocities at certain time steps, which were subsequently removed. More northward velocities were produced at shorter time steps and higher thresholds and explained by storm cell motion that was more northward than the convective system motion (Figure 4.3d). This was because individual cells were shorter-lived and produced more intense precipitation than the convective system. Multiple analyses of convective system components were necessary to correctly interpret cross-correlation velocities.

To check that the two-dimensional cross-correlation velocity estimates were reasonable, the average 500-hPa wind velocity from NCEP–NCAR Reanalysis 1

(Kalnay et al. 1996) was calculated within 2.5ºW–2.5ºE, 47.5º–52.5ºN at 0600 UTC. The 500-hPa wind speed is correlated to meteotsunami generation (Vilibić and Šepić 2017), and the speed of convective systems are often near the mid-tropospheric wind speed (Markowski and Richardson 2011). The reanalysis data showed 22 ± 2 m s^{-1} and northeastward (40º ± 1º) wind velocities. Considering both the longer, 20-min time-step cross-correlation analysis at 15 mm h^{-1} cut-offs and the NCEP reanalysis wind speed, the system velocity was about 19 m s^{-1} at a bearing of 45º.

4.3.3 Analysis of observations

Given a forcing speed, possible external resonance mechanisms were examined. When the Froude number (Fr; atmospheric forcing speed divided by wave speed) was between 0.9 and 1.1, we considered that external resonance was possible (Vilibić 2008). We used the edge wave speed c_{edge} to determine the Greenspan resonance possibility (Greenspan 1956). The edge wave speed of a tsunami-period wave on a constant slope is

$$c_{edge} = \frac{gT_{wave}}{2\pi} \tan[\beta(2n+1)], \quad (4.1)$$

where g is gravitational acceleration (9.81 m s^{-2}), T_{wave} is wave period, β is bathymetric slope, and n is edge wave mode (corresponding to the number of times the trapped edge wave crosses the still water level in the cross-propagation direction).

Taking transects from near Dieppe across the channel, the bathymetry was approximated by two slopes. The first slope was steeper, decreasing by 21 m between 0 and 6 km from the coastline (β ≈ 0.0035). The second slope was shallower, decreasing by 20 m between 6 and 60 km from the coastline (β ≈ 0.0004). This change in gradient is evident when comparing the 20- and 40-m contours near Dieppe (Figure 4.1). From Equation 4.1 and the observed wave period, the edge wave speed was 1.3 m s^{-1} on the shallow slope and 11.6 m s^{-1} on the steep slope. These edge wave speeds were more than 10% slower than the alongshore forcing speed, meaning that Greenspan resonance was not possible.

Next, we investigated Proudman resonance. Proudman resonance occurs when the atmospheric system speed U is near the shallow-water wave speed c (Proudman 1929). The shallow-water wave speed is proportional to water depth H and is given by

$$c = \sqrt{gH}. \tag{4.2}$$

Using a forcing speed of U = 19 m s^{-1} and depths at mean sea level (Figure 4.1), a Froude number between 0.9 and 1.1 was calculated in the location of the precipitation at 0320 UTC (Figure 4.3). Therefore, Proudman resonance was possible. This result was also retained when accounting for tides. Assuming that the shallow-water wave speed changes with tidal elevation H_T and ocean currents in the wave propagation direction V_T (Choi et al. 2014), the shallow-water wave speed is approximately

$$c \approx \sqrt{g(H + \mathrm{H_T})} + V_T. \tag{4.3}$$

Including tidal elevation and current estimates (H_T = –0.5 m; V_T = –1 m s^{-1}) showed that Proudman resonance was possible, but the Proudman resonant region would have moved away from the coastline (cf. regions in Figure 4.1).

We then analyzed expected wave growth under Proudman resonance. Churchill et al. (1995) derive the following relationship for a linear shallow-water wave η, trapped underneath a constant amplitude, moving forcing assuming one-dimensional, frictionless propagation without planetary rotation:

$$\eta = \frac{x}{2\rho g}\left(-\frac{\partial \mathrm{p}}{\partial x} + \frac{\tau_s}{H_{Pr}}\right), \tag{4.4}$$

where x is distance in the propagation direction, ρ is water density, p is atmospheric pressure, τ_s is surface wind stress, and H_{Pr} is the depth at which Fr is 1. If a sea surface perturbation were amplified by Proudman resonance, it would have grown linearly with distance and been a linear combination of the pressure and wind stress forcing. Simply, the sea surface perturbation would have been the combined pressure induced perturbation η_p and wind stress–induced perturbation η_τ:

$$\eta = \eta_p + \eta_\tau. \tag{4.5}$$

For a pressure field approximated by an advecting sinusoid, with maximum pressure change Δp and wavelength λ, the maximum pressure induced perturbation is

$$\eta_p = \pi \frac{\Delta p}{\rho g} \frac{x}{\lambda}, \tag{4.6}$$

and using approximations from observations, a 40-km wavelength, and 200-Pa pressure perturbation would have produced a wave height of 0.31 m after moving 200 km across the English Channel toward Boulogne.

To calculate the wave induced by wind stress, wind stress was parameterized as $\rho_a C_a U_{10}^2$ [ρ_a is air density (1 kg m^{-3}), C_a is the drag coefficient of air on the water surface, and U_{10} is the 10-m wind speed]. The perturbation η_τ was then approximated by

$$\eta_\tau \approx \frac{1}{2}\frac{\rho_a C_a U_{10}^2}{\rho g}\frac{x}{H_{Pr}}. \quad (4.7)$$

Inputting a 10 m s^{-1} 10-m wind speed, a drag coefficient of 0.0012 (Large and Pond 1981), and 37-m resonant water depth, then η_τ was about 0.03 m. If the wind stress and pressure components of the wave constructively interfered, then the maximum wave height after Proudman resonance would have been 0.34 m.

The maximum wave height at Boulogne was 0.70 m, meaning that 2.1 times more amplification would have been required. From the conservation of wave energy flux, waves grow when moving into shallower water as described by Green's law (Pugh and Woodworth 2014):

$$\frac{\eta_1}{\eta_0} \propto \left(\frac{H_0}{H_1}\right)^{1/4}. \quad (4.8)$$

A wave with original wave height η_0 = 0.34 m, which was generated in depth $H_0 = H_{Pr}$ = 37 m, and shoaled to depth H_1 = 5 m (approximate water depth at Boulogne in Figure 4.2), would have a resultant wave height η_1 = 0.56 m. The wave height may have then further amplified through refraction, but this is difficult to quantify without numerical modeling.

This analysis has provided some evidence toward the generation mechanisms of the observed wave. It has suggested that atmospheric pressure was the primary forcing (91%) and wind stress was secondary (9%), external resonance occurred through Proudman resonance, and shoaling produced further amplification. However, idealized analysis has only partly explained wave heights at Boulogne, rather than provide a deeper understanding of the link between generation mechanisms and the observed meteotsunami. Numerical models could provide this understanding,

alongside stronger evidence for wave growth through Proudman resonance, and quantify wave height sensitivity to atmospheric forcing and tides.

4.4 Modeling

4.4.1 Telemac

We used the finite-element ocean model Telemac (Hervouet 2000) to model the wave, which solved the two-dimensional nonlinear shallow-water momentum and continuity equations. Here they are given in two-dimensional vector form:

$$\frac{\partial \boldsymbol{u}}{\partial t} + \boldsymbol{u} \cdot \nabla \boldsymbol{u} + \boldsymbol{f} \times \boldsymbol{u} = -g\nabla\eta - \frac{1}{\rho}\nabla p - \frac{g}{C^2}\frac{|\boldsymbol{u}|\boldsymbol{u}}{H+\eta} + C_a \frac{\rho_a}{\rho}\frac{|\boldsymbol{U}_{10}|\boldsymbol{U}_{10}}{H+\eta} + A_h \nabla^2 \boldsymbol{u}, \quad (4.9)$$

and

$$\frac{\partial \eta}{\partial t} + \nabla \cdot [\boldsymbol{u}\,(H+\eta)] = 0, \quad (4.10)$$

where $\boldsymbol{u}$ is the depth-averaged horizontal velocity vector, ∇ is the horizontal gradient vector, t is time, C is the Chézy coefficient (60 $m^{1/2}$ s^{-1}), A_h is the eddy viscosity (150 m^2 s^{-1}), and $\boldsymbol{f}$ is the Coriolis parameter, directed vertically upward. With wind in the model, $\boldsymbol{U}_{10}$ is the 10-m wind vector.

Equation 4.9 and Equation 4.10 were solved on a multiscale triangular mesh, generated with Blue Kenue (Canadian Hydraulics Centre 2016), using 30-arc-s bathymetry from General Bathymetric Chart of the Oceans (GEBCO) 2014 (IOC et al. 2003). The mesh node spacing was 500 m in the eastern English Channel. For all nontidal models, we used 2-s, fully implicit time stepping, and simulations ran for at least 22 000 s (6.1 h).

4.4.2 Atmospheric forcing

The atmospheric pressure p was prescribed by an analytical forcing function:

$$p = \begin{cases} p_t \frac{\tanh\psi + 1}{2}\cos\phi + p_b, & \text{if } -\frac{3\pi}{2} \le \phi \le \frac{3\pi}{2}; \\ p_b, & \text{otherwise.} \end{cases} \quad (4.11)$$

The bounds of the argument $\phi = \boldsymbol{k} \cdot \boldsymbol{x} - \omega t$ describe a low–high–low pressure pattern, where $\boldsymbol{k}$ is the wavenumber vector, and $\boldsymbol{x}$ is the position vector. The ω is angular frequency, where $\omega = 2\pi/T$ and T is the forcing period. The maximum pressure perturbation p_t was prescribed on a 1013-hPa background pressure p_b.

The geographical extent of the forcing was also parameterized, because the convective system did not extend to the United Kingdom and could not be completely determined from the observations. The end of the convective system was determined as the last 20 mm h^{-1} precipitation rate along the cross-propagation axis at multiple time steps. A linear regression through the end points was used as the extent of the modeled pressure anomaly (thick dashed line in Figure 4.3). In Equation 4.11, this was given by $\psi = \alpha(\Phi - 0.386\Lambda - 50.49°\text{N})$, where Φ = latitude, Λ = longitude, and α = 1/4000 m^{-1}.

The pressure perturbations were modeled using the best estimates provided by the observations, and ensembles were used to account for observational uncertainties. To create the ensemble, we varied four characteristics: forcing speed U (17–22 m s^{-1}, 1 m s^{-1} increments), forcing direction as a clockwise bearing from north θ (35º–55º, 5º increments), pressure perturbation amplitude (0.9–1.5 hPa, 0.1-hPa increments), and forcing period (30–38 min, 1-min increments). The model that we decided was the best estimate of atmospheric observations (not necessarily producing the most accurate wave height simulations) had 19 m s^{-1} forcing speed, 45º forcing direction, 1-hPa pressure perturbation amplitude, and 36-min forcing period. The behavior in time for this case is shown in Figure 4.5, and contours of p can be seen in Figure 4.6.

4.4.3 Best-estimate model

A time series of the atmospheric pressure forcing with the best-estimate parameters is shown in Figure 4.5. The observed pressure anomaly was 10–60-min bandpass filtered, removing the long-term synoptic signal and high-frequency noise. The model and observation timings were aligned such that the time of modeled high pressure perturbation coincided with the time of maximum pressure perturbation observed at Boulogne. At Le Touquet and Boulogne, the modeled and observed timings and pressure amplitudes were well represented. At Dunkirk, to the northeast, the modeled pressure was much lower amplitude and out of phase with observations. Also, at Le Havre the pressure anomaly was poorly approximated because the convective system approached from a different angle than was modeled. However, in the Proudman-resonant region there was good agreement between the model and the observed pressures, as well as the calculated velocities of radar-derived precipitation fields.

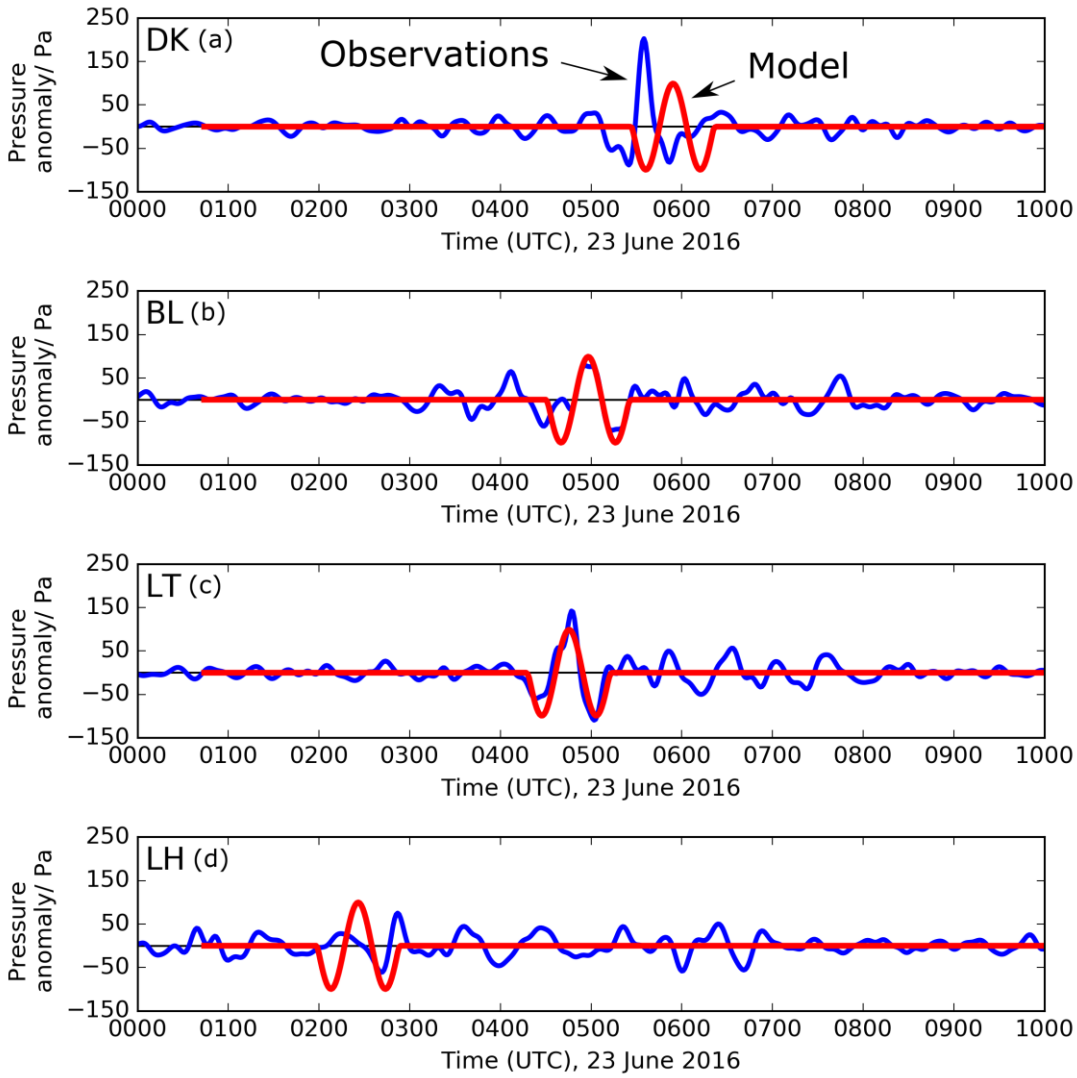

Figure 4.5 Red: modeled pressure anomaly for the model U = 19 m s^{-1}, θ = 45°, T = 36 min, and p_t = 1 hPa. Blue: 10–60-min bandpass-filtered pressure. (a) Dunkirk, (b) Boulogne, (c) Le Touquet, and (d) Le Havre.

From the best-estimate model forcing, the sea surface height fields (Figure 4.6) show that two waves were initially created by the pressure system. The primary forced wave grew in the center of the English Channel (Figure 4.6a, Figure 4.6b and Figure 4.6c). There was also a coastal wave (dashed box in Figure 4.6b and Figure 4.6c), which also grew as it propagated eastward along the French coastline to similar amplitudes as the directly forced wave. At Dieppe it was this coastal wave that was recorded by the tide gauge (Figure 4.7), which was followed by reflections from the French coastline. At Boulogne the directly forced wave arrived first, which was followed by the coastal wave up the French coastline and reflections from the U.K. coastline. At Le Havre the first wave to arrive was a directly forced wave underneath the pressure disturbance,

and then reflections arrived later. At Newhaven the first wave to arrive was freely propagating away from the pressure disturbance. Reflections were also modeled from the French coastline back toward the United Kingdom (Figure 4.6d). In further analysis of the meteotsunami, different components of the wave are referred to as free, directly forced, coastal, and reflected.

Examining the relationship between pressure disturbance and water level, the directly forced wave was proportional to the negative of the pressure gradient (cf. pressure and sea level disturbance in Figure 4.6). This behavior is predicted by Equation 4.4, implying Proudman resonance. The directly forced wave also grew as it propagated along the Channel, in depths appropriate for Proudman resonance ($0.9 \leq Fr \leq 1.1$). Using Equation 4.6, under perfect Proudman resonance, this wave should have grown by 0.10 m between 95 and 155 min. The model simulated 0.08-m wave growth over this time (0.12–0.20 m). The directly forced wave grew within 20% of theoretical calculations of wave amplitude, consistent with the predictions of Proudman resonance. This is the strongest available evidence that this was the amplification mechanism for the directly forced wave.

This wave was not damaging and compared to concurrent wind waves it had a similar wave energy flux density. When the wave uncoupled from the atmospheric forcing, the energy flux density of the directly forced wave was about 3.4 kW m^{-1}, which is similar to the energy flux density of 0.4-m-high, 9-s period wind waves measured at the Greenwich Lightship Buoy (1.4 kW m^{-1}). However, meteotsunamis may be more damaging than this wave flux density suggests. Long, coherent wave crests mean that a relatively large total energy flux is available for focusing. Here, 340 MW was available for focusing from the 100-km crest. Nonetheless, this meteotsunami was not damaging, and the simulations did not suggest considerable wave energy focusing through refraction in the English Channel.

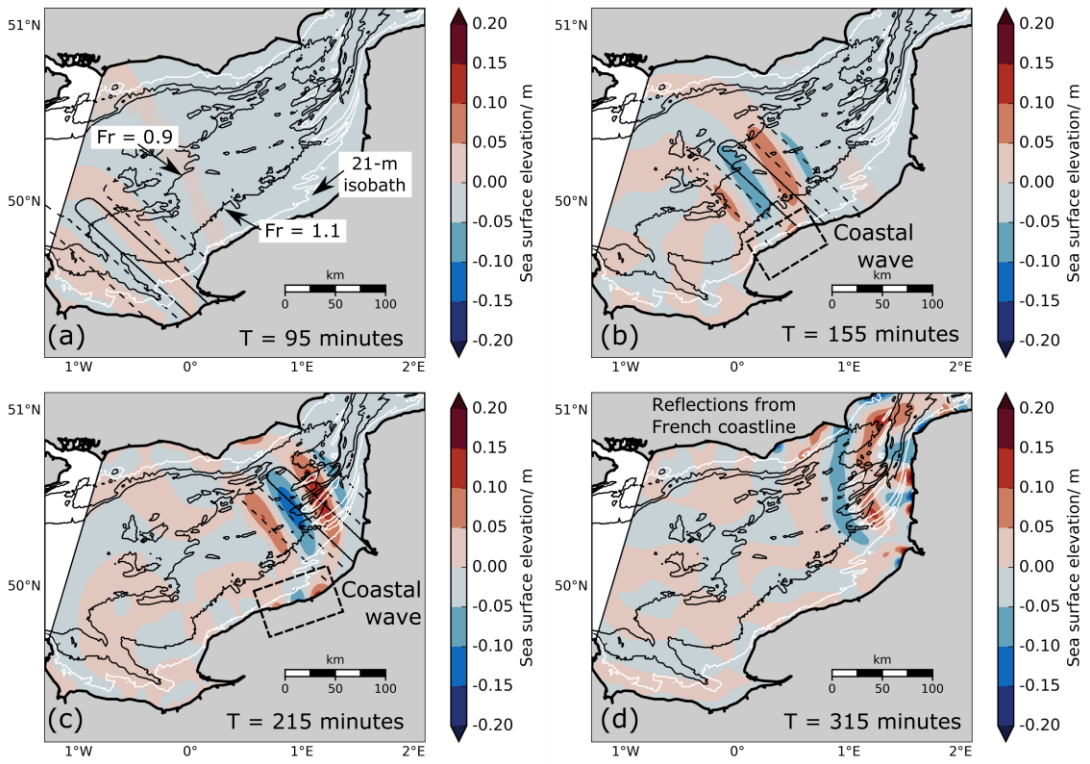

Figure 4.6 Modeled sea level elevation (colors) at (a) 95, (b) 155, (c) 215 and (d) 315 min into the best-estimate simulation. Froude number contours at 0.9 and 1.1 from unaltered GEBCO bathymetry are shown as thin black lines. The western open boundary is shown in black. The sea level pressure is shown in black solid (+0.5 hPa) and dashed (–0.5 hPa) lines. All panels give interpretation of the modeled sea level elevation, with the coastal wave in a dashed black box in (b) and (c). The 21-m isobath is shown as a thin white line. Note the color saturates at –0.2 and +0.2 m.

The coastal wave growth was further investigated through idealized numerical models, because its growth mechanism was unclear and Greenspan resonance was previously discounted through Froude number arguments. In these models the bathymetry was assigned the previously approximated shallow and steep slopes near the French coastline, and a moving sinusoidal pressure forcing was prescribed (Figure 4.8). This idealized model reproduced the coastal wave under baseline slope approximations (Figure 4.8a). First, we changed the gradient of the steep slope between 0.002 and 0.01, and a coastal wave with a similar amplitude to the forced wave was modeled (Figure 4.8e and Figure 4.8f). The coastal wave was also reproduced when the pressure forcing was cut off at y = 6 km, showing that it was not produced by direct forcing

(Figure 4.8b). We then altered the shallow slope section such that Proudman resonance could not produce a large forced wave (Figure 4.8g). If the coastal wave were directly forced by the pressure disturbance over the steep slope, this should not affect the coastal wave amplitude. However, the coastal wave magnitude also decreased to the amplitude of the Proudman resonance forced wave. Therefore, the coastal wave was directly related to the forced wave generated in the English Channel by Proudman resonance and appeared to be separate because it was heavily refracted by the steep slope.

The arrival times and periods for both the coastal wave and directly forced wave were modeled well at Dieppe and Boulogne. The modeled arrival time at Boulogne, 0449 UTC, was only 2 min behind the observed arrival time, 0447 UTC (Figure 4.7). The arrival time at Dieppe was more poorly recreated, which was measured as 0358 UTC and modeled as 0405 UTC, a lag in the model of 7 min. The difference in arrival times between the waves at Boulogne and Dieppe gave a 5-min relative difference of modeled arrival times (44 min) compared to observations (49 min). The dominant period of the modeled wave is approximately 34–39 min at Boulogne and Dieppe, which is approximately 5 min longer than observed. The wave traveled faster in the model between Dieppe and Boulogne by a few minutes, and the period of the wave was longer than expected.

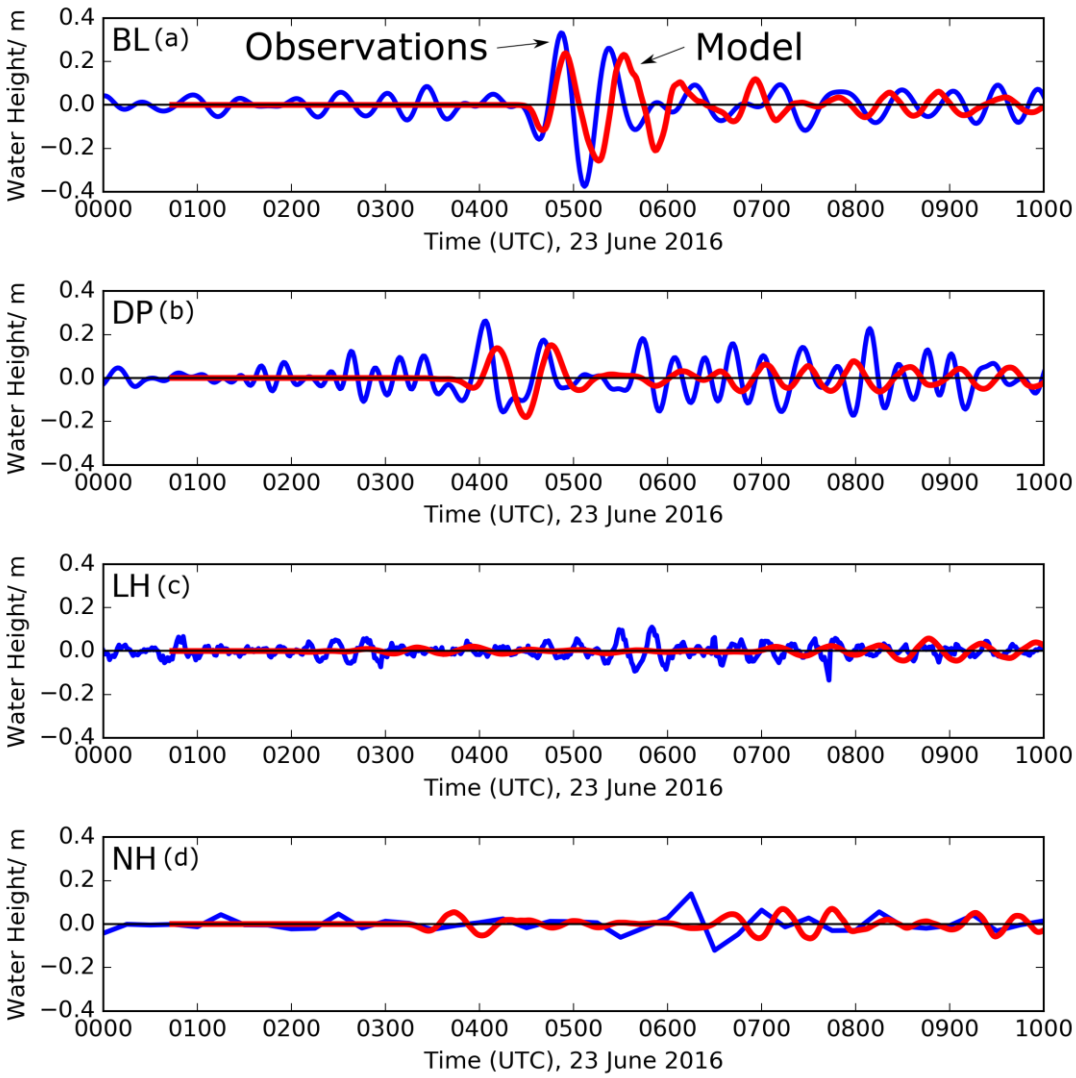

Figure 4.7 Red: modeled sea surface elevation at tide gauges for the model U = 19 m s^{-1}, θ = 45°, T = 36 min, and p_t = 1 hPa. Blue: 10–60-min bandpass-filtered observations. (a) Boulogne, (b) Dieppe, (c) Le Havre, and (d) Newhaven.

The maximum wave heights, given by the maximum difference between consecutive peaks and troughs, were simulated to within tens of centimeters. At Boulogne, a 0.70-m wave was observed, compared to the best-estimate model 0.50-m wave height (29% underestimate). At Dieppe, a 0.43-m wave was observed, compared to the best-estimate model 0.33-m wave height (23% underestimate). The model did not produce a large wave at Le Havre, but there were no discernible observations here either.

The model was poorer at representing sea surface elevation at Newhaven than at other locations. The best-estimate model produced a perturbation at Newhaven due to the initial movement of the convective system over the English Channel, which was not discernible in the observations. Also, the first peak of the reflected wave at Newhaven

was about 30 min after the maximum observed peak, and the largest modeled peak was about 60 min after the maximum observed peak. However, the amplitudes of later perturbations were similar to observations (Figure 4.7). We accept the model limitations at Newhaven as the result of forcing simplifications, which did not include other storms that occurred prior to, and after, the synthetically modeled convective system (cf. Figure 4.3 and Figure 4.6). These other storms could have produced forced waves (0.06-m high) that shoaled up to 0.10–0.14-m high at the Newhaven coastline [Fr ≈ 0.85, H_0 ≈ 50 m, H_1 ≈ 1 m, ΔP ≈ ±0.75 hPa, and $\eta_0 = -\Delta P/\rho g(1- \mathrm{Fr}^2)$]. Furthermore, the simplicity of the larger convective system would have affected both the initial free wave and the initial angles of freely reflected waves at the French coastline (Vennell 2010). Nonetheless, it is difficult to compare the model output with sea surface observations sampled at 15-min intervals.

4.4.4 Atmospheric forcing ensembles

To understand the sensitivities of the predictions of meteotsunami height and arrival times, we created ensembles by varying forcing velocity, amplitude of the pressure perturbations, and forcing period.

Forcing velocity

Model results from forcing speeds at 17, 19, and 21 m s^{-1} across angles 35°–55° are shown in Figure 4.9. The arrival time difference between the wave arriving in Boulogne and Dieppe was mostly dependent on the propagation time of the atmospheric forcing. The average of the relative differences in arrival times was 53, 42, and 34 min at 17, 19, and 21 m s^{-1}, respectively. The faster the forcing speed, the smaller the modeled arrival time difference at each location. The relative arrival time of the wave was controlled by the forcing speed because the directly forced wave was trapped underneath the forcing. The modeled arrival time difference between Dieppe and Boulogne was 5 min too short, suggesting that the atmospheric system speed may have been slower than our best estimate but falls within error estimates (19 ± 2 m s^{-1}).

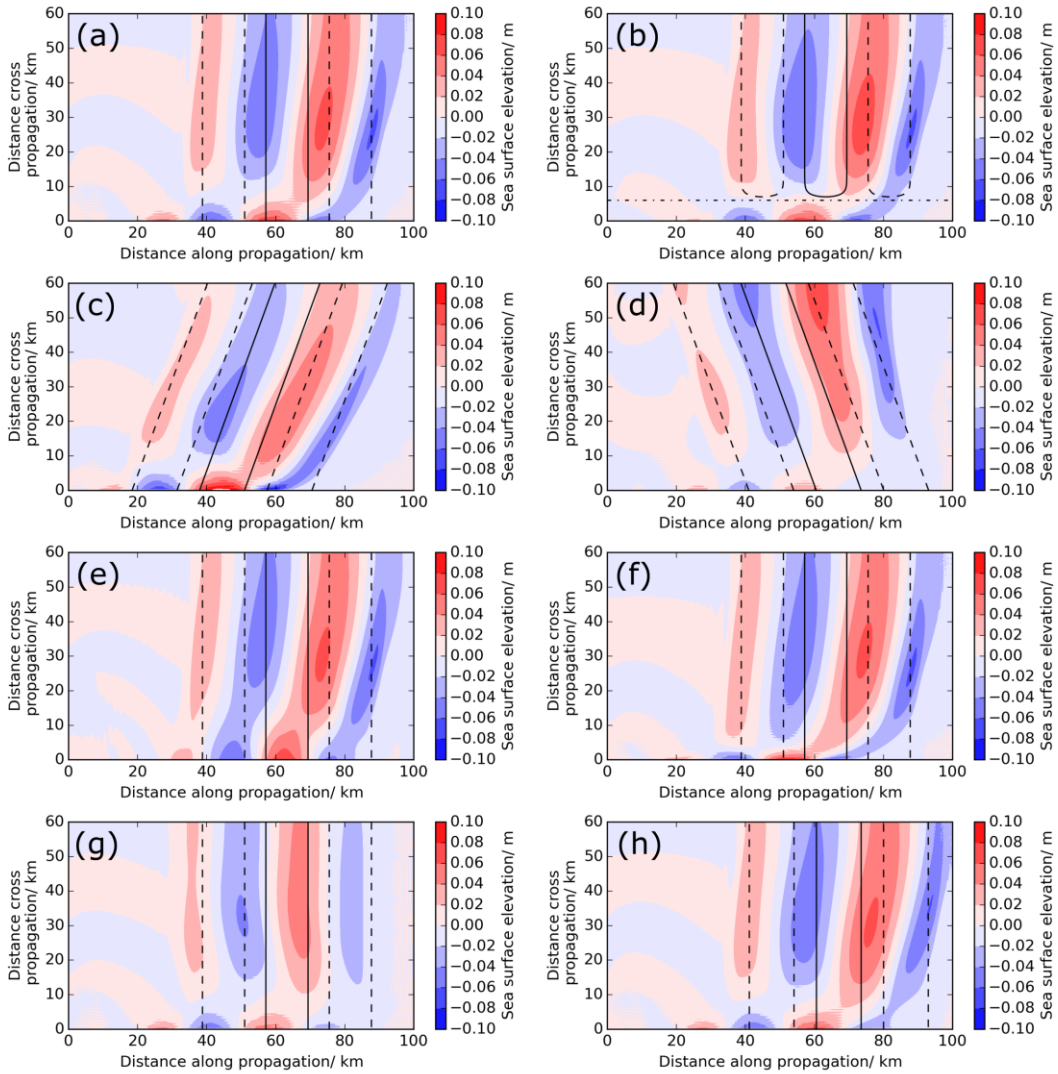

Figure 4.8 Idealized simulations investigating coastal wave generation mechanism. Colors range from –0.1 to +0.1 m. Black contours are –0.5- and +0.5-hPa pressure anomalies. (a) Base line model. Infinite cross-propagation length, U = 17 m s^{-1}, normal bathymetry β_0 = 0.0035, β_1 = 0.00037. (b) Pressure cut off in the cross propagation direction at 6 km (dot–dashed black line). (c) Moving toward the coastline, (d) moving away from coastline, (e) steep slope made steeper (β_0 = 0.01), (f) steep slope made shallower (β_0 = 0.002), (g) shallow slope between 6 and 60 km made flat (β_1 = 0), and (h) forcing speed is 18 m s^{-1}.

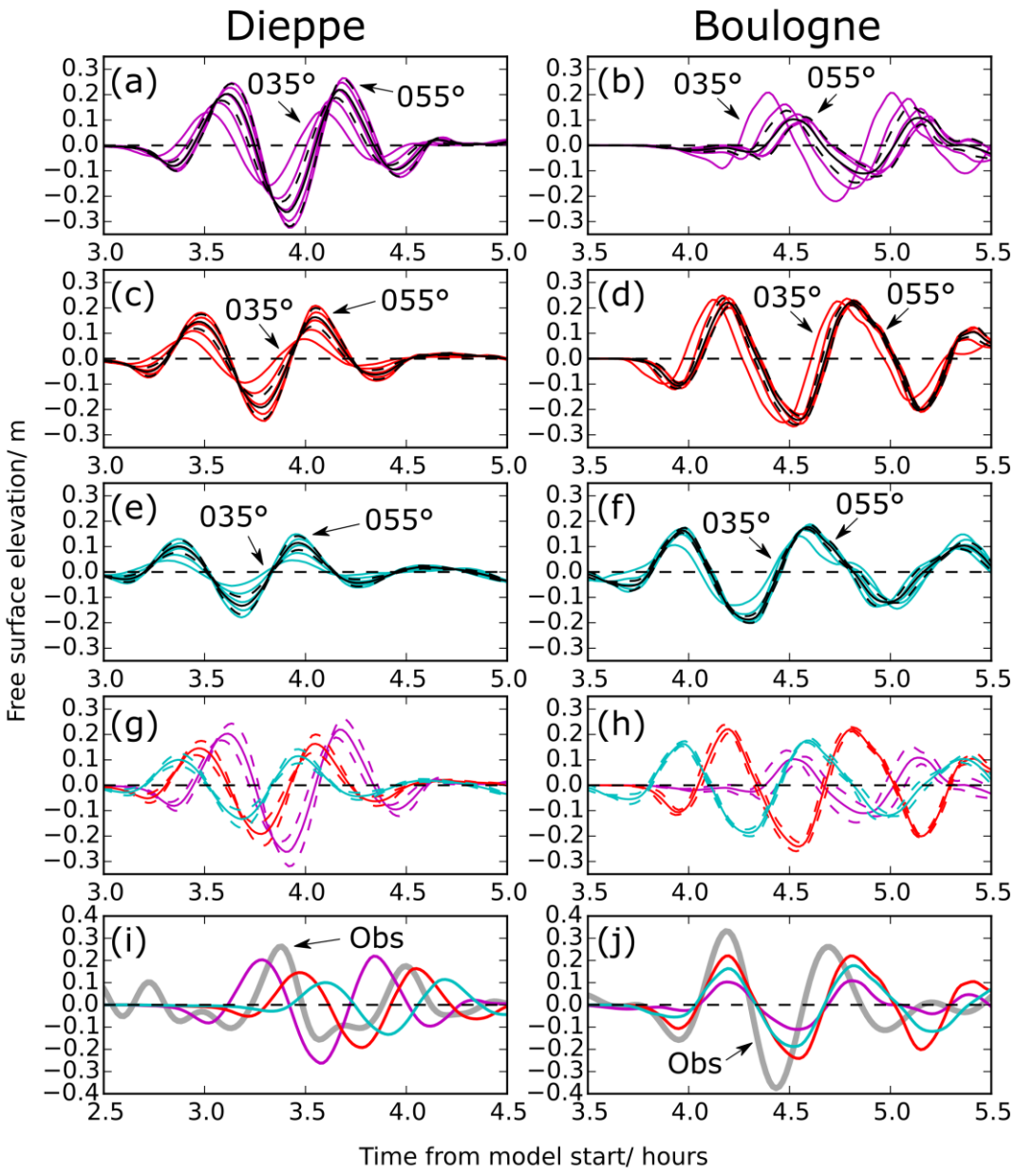

Figure 4.9 Sea surface elevation sensitivity to forcing angles and speeds. Model runs at each angle (35º–55º) are shown (a), (b) at 17 m s^{-1} in purple, (c), (d) at 19 m s^{-1} in red, and (e), (f) at 21 m s^{-1} in cyan. The model results (left) from Dieppe and (right) from Boulogne. Each individual colored line in (a)–(f) represents an individual simulation at a specific forcing speed and angle. The solid black line is the mean across individual models, and the dashed black lines are one standard deviation from the mean. (g), (h) Comparison of the averages and standard deviations from 17, 19, and 21 m s^{-1} at Dieppe and Boulogne in respective colors. (i), (j) Comparison of the averages from each speed with the bandpass-filtered observations in gray. In (i) and (j), simulation timings and observation timings are aligned with respect to the average of U = 19 m s^{-1} simulations. Note the change in scale and time shift in (i) and (j).

Figure 4.9 shows that the modeled maximum wave heights varied with both forcing speeds and angles but were mainly dependent on forcing speeds. Across 30 simulations, maximum wave heights at Boulogne were consistently obtained at 19 m s^{-1}, with greater than 0.4-m maximum wave heights averages obtained between 19 and 20 m s^{-1}. At Boulogne, wave height was relatively insensitive to forcing angle when the forcing speed was 19 m s^{-1}, ranging from 0.43 to 0.52 m (0.48 m ± 9.5%); the largest wave heights were achieved at forcing angles between 40º and 50º and decreased away from these angles. Wave height was more sensitive to angle when the speed was 17 m s^{-1}, with maximum wave heights between 0.20 and 0.43 m (0.32 m ± 36%) at Boulogne. Dieppe was more sensitive to forcing angle than Boulogne, with maximum wave heights between 0.19 and 0.48 m (0.34 ± 44%) at 19 m s^{-1} and 0.29 and 0.59 m (0.44 m ± 34%) at 17 m s^{-1}. At Dieppe wave heights were largest at 55º and decreased with more northward forcing angles.

The wave height at Dieppe decreased as the forcing moved faster and more northward (Figure 4.9). Again, idealized models showed wave height sensitivity to forcing velocity; forcings moving toward the coastline produced larger waves (Figure 4.8c) and forcings moving away from the coastline produced smaller waves (Figure 4.8d). Also, because the Proudman resonant region was further from the coastline for faster forcings, smaller wave heights should be expected (Figure 4.8h).

Our sensitivity analysis in the English Channel also revealed that a forcing speed between 18 and 19 m s^{-1} would have improved arrival times, without degrading wave heights, at Boulogne and Dieppe (Figure 4.9i and Figure 4.9j). The cause of arrival time error was probably because the atmospheric forcing velocity was treated as a constant velocity, whereas observations showed more complicated system movement (Figure 4.3). Nevertheless, the accuracy of modeled arrival times, period, and wave height give confidence that the convective system moved at Proudman resonant velocity and produced the observed meteotsunami.

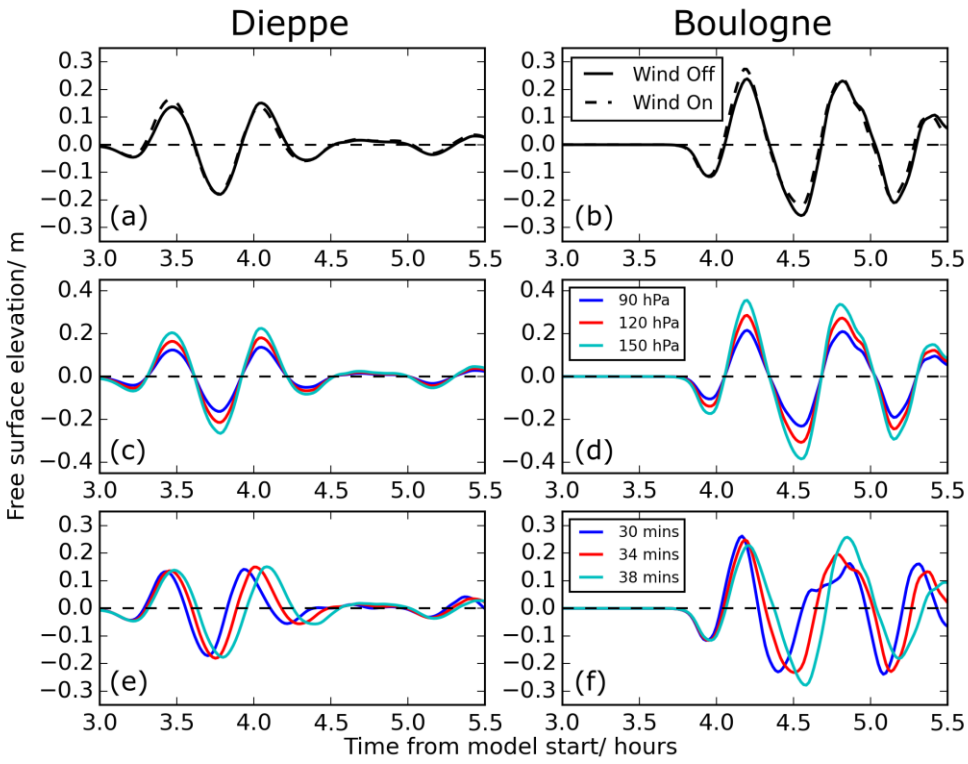

Figure 4.10 Sea surface elevation sensitivity to wind, amplitude, and period. (left) Dieppe and (right) Boulogne. (a),(b) The 10 m s^{-1} wind component on (solid line) and off (dashed) where U = 19 m s^{-1}, θ = 45º, *T* = 36 min, and p_t = 1 hPa. (c), (d) Varying p_t between 0.9 (blue), 1.2 (red), and 1.5 hPa (cyan), where *U* = 19 m s^{-1}, θ = 45º, *T* = 36 min. (e),(f) Varying *T* between 30 (blue), 34 (red), and 38 min (cyan), where *U* = 19 m s^{-1}, θ = 45º, and p_t = 1 hPa. Note the change in y-axis scale for (c) and (d).

Pressure perturbation amplitude

Increasing the pressure perturbation amplitude increased the maximum wave height. A 0.9-hPa forcing produced a 0.45-m wave at Boulogne and using a 1.5-hPa forcing produced a 0.74-m wave (Figure 4.10c and Figure 4.10d). At Dieppe, a 0.9-hPa forcing produced a 0.30-m wave, and a 1.5-hPa forcing produced a 0.49-m wave. Linear regression of the maximum wave heights at Boulogne and Dieppe from 0.9–1.5-hPa forcings, revealed a strongly linear relationship between pressure amplitude and maximum wave height. This linear relationship is a well-known result.

Forcing period

Changing the forcing period created more complicated resultant behavior in the modeled meteotsunami than altering the amplitude of the forcing (Figure 4.10e and

Figure 4.10f). There was some expected behavior in the absence of seiching. A longer period forcing generated a proportionally longer period meteotsunami, and all models with 30–38-min period forcings agreed with the shape of the meteotsunami waveform at Dieppe. However, at Boulogne, the modeled meteotsunami maximum wave heights behaved unpredictably after the first trough. Furthermore, the largest modeled wave was from the shortest period forcing at Boulogne, whereas at Dieppe the largest modeled wave was from the longest period forcing.

This sensitivity was from wave superposition of the direct forced wave at Boulogne and the coastal wave traveling up the coastline from Dieppe. From these results, hazard assessments should use various forcing periods.

4.4.5 Wind

When including wind, the 10-m wind velocity was modelled as two 10 m s^{-1} amplitude half-sinusoids with the same period as the pressure disturbance. The two wind maxima were aligned with where the pressure disturbance was 0 hPa, between the simulated mesohigh and mesolows, representing observations at Le Touquet (Figure 4.4). The wind vector field, which moved at the same velocity as *p*, was prescribed:

$$\boldsymbol{U_{10}} = U_{10} \cos\chi \, \hat{\mathbf{i}} + U_{10} \sin\chi \, \hat{\mathbf{j}} \,, \tag{4.12}$$

where $\chi = 45^{\circ}$ (northeastward 10-m winds), $\hat{\mathbf{i}}$ and $\hat{\mathbf{j}}$ were unit vectors in the eastward and northward directions, respectively, and

$$U_{10} = \begin{cases} \left| A \frac{\tanh\psi + 1}{2} \sin\phi \right|, & \text{if } -\pi \le \phi \le \pi; \\ 0.01, & \text{otherwise,} \end{cases} \tag{4.13}$$

where *A* was 10 m s^{-1}, and all other variables were the same as for the pressure forcing.

The model locations corresponding to tide gauges at Boulogne and Dieppe showed that wind changed the resultant maximum sea surface height by a few centimeters (Figure 4.10a and Figure 4.10b). The first peak of the wave increased at Boulogne from 0.24 to 0.27 m (+13%). At Dieppe a similar increase is seen in the first peak, increasing from 0.14 to 0.17 m (+21%). This was a 16% average increase in first peaks. The second wave peak was reduced by the wind by similar magnitudes; at Dieppe, the secondary peak decreased from 0.15 to 0.14 m (–6.7%). Overall, the wind forcing was secondary to the pressure forcing for this meteotsunami.

The contribution from wind here was small compared to meteotsunamis generated by similar convective systems in the Great Lakes. Wind stress contribution can be large because of shallow water depths (Anderson et al. 2015), strong winds (Bechle and Wu 2014), or a combination of both factors (Šepić and Rabinovich 2014). Even with similar atmospheric forcings, wind stress and pressure disturbances may contribute different amounts to wave height between different basins owing to basin bathymetry and geometry (Šepić and Rabinovich 2014). In Lake Erie, wind stress has accounted for up to 59% of wave heights because of shallow average water depths (20 m), despite moderate observed wind speeds (10–15 m s^{-1}) (Anderson et al. 2015). In Lake Michigan, wind stress has contributed up to 40% of the wave height because of high 10-m wind speeds (25 m s^{-1}), despite deeper water (75–90 m) (Bechle and Wu 2014). Further analysis for the 23 June 2016 meteotsunami has suggested that if the 10-m wind speeds were larger (25 m s^{-1}) or the Proudman-resonant water depths were shallower (20 m), wind stress would have contributed 30%–50% of the wave height. The contribution of wind here was low (16%) because of low 10-m wind speeds and deep water.

4.4.6 Tides

Previous calculations (section 4.3.3) have shown that tides may have changed the location of Proudman resonance through local depth change and currents, which may have affected propagation speed and wave growth. Therefore, tides were included using boundary conditions from the TPXO European shelf model. Tide was spun up from a cold start from 0000 UTC 17 June 2016. A larger mesh with maximum 5-km node spacing extended the previous mesh across the western English Channel and above the southern North Sea amphidrome. Maximum modeled currents were ~ 3 m s^{-1} near Cherbourg, and tidal ranges were about 10% smaller than observations, which were reasonable compared to other English Channel tidal models (Pingree and Maddock 1977; Davies 1986). It was not our intention to develop a precise tidal model, rather to adequately simulate tides to assess their influence.

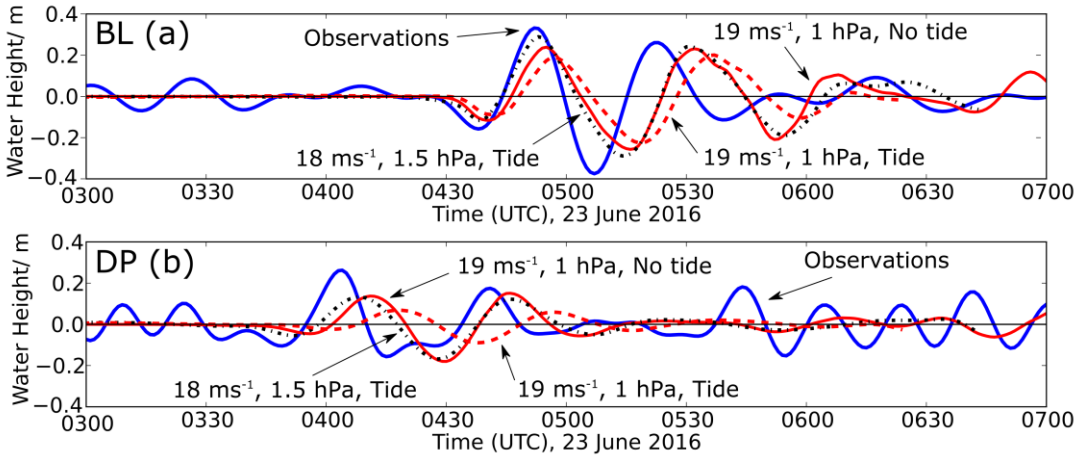

Figure 4.11 Sensitivity of the meteotsunami to tides in the model. (a) Boulogne, (b) Dieppe. Blue: 10–60-min bandpass-filtered observations. Red solid line: forcing model U = 19 m s^{-1}, θ = 45°, T = 36 min, and p_t = 1 hPa without tides. Red dashed line: atmospheric forcing as in the red solid line but with tides. Black dash–dotted line: for the model U = 18 m s^{-1}, θ = 45°, T = 36 min, and p_t = 1.5 hPa with tides.

Three simulations including tides were run, with high pass-filtered sea level results shown in Figure 4.11. With the best-estimate model forcing (U = 19 m s^{-1}; p_t = 1 hPa), the tidal model produced a 0.43-m maximum wave height at Boulogne, which was 0.07 m smaller than the nontidal model (14% decrease); at Dieppe the tidal model wave height was 0.15 m, which was 0.18 m smaller than the nontidal model (56% decrease). Reducing the atmospheric forcing speed to 18 m s^{-1} and increasing the pressure perturbation to 1.5 hPa produced a meteotsunami that was closer to observations and best estimate results. The 18 m s^{-1}, 1.5-hPa, tidal model produced a 0.30-m maximum wave height at Dieppe and 0.58-m maximum wave height at Boulogne. A model with U = 18 m s^{-1} and p_t = 1 hPa was also run (not shown), with maximum wave heights of 0.2 m at Dieppe and 0.39 m at Boulogne. All tidal simulations produced small wave heights at Le Havre and Newhaven.

With tides included, the wave height changed at Dieppe because the Proudman resonant region shifted away from the coastline. In the numerical model, this occurred because southwestward tidal currents slowed the northeastward-propagating meteotsunami by up to 1 m s^{-1} (about 5%–6% decrease), and the tidal elevation lowered water levels by up to 0.5 m, reducing the meteotsunami wave speed by 0.1 m s^{-1} (about 0.5%–0.6% decrease). Therefore, currents were mainly responsible for slowing the wave. Combined tidal effects reduced the shallow-water wave speed by

1.1 m s^{-1}, meaning that the Proudman resonant region shifted toward deeper water, farther from the coast. This partially explains how larger wave heights at Dieppe were reproduced when the forcing speed was decreased by 1 m s^{-1}—the Proudman resonant region moved nearer the coastline.

However, when forcing speed was decreased, increasing pressure amplitude by 1.5 times was required to simulate similar wave heights to the best-estimate model. This may be because of refraction of the wave due to currents offshore, leading to larger wave heights toward the center of the basin. The processes acting to decrease the coastal wave height were more important than steepening of the wave as it was moved against the current, leading to an overall decrease in wave height.

These simulations show that tides can change the location where Proudman resonance occurs, leading to a decrease of coastal wave height on the same order of magnitude as changing the atmospheric forcing parameters. Previous studies suggest that, even in macrotidal regimes, tides only change wave heights in open basins (i.e. no seiching) by 17% (Choi et al. 2014). This study shows that, even when tides are near still water level, tidal currents can considerably change the location of wave amplification and halve coastal wave heights.

Here, the best-estimate model underpredicted wave height even without tidal influence. Meteotsunamis are often difficult to simulate in both synthetic and NWP models (Anderson et al. 2015), particularly after the first peak (Choi et al. 2014) and across multiple locations (Hibiya and Kajiura 1982; Bechle and Wu 2014). Here, the tide reduced the meteotsunami wave height, decreasing the best-estimate wave height accuracy from 77% to 35% at Dieppe and from 71% to 61% at Boulogne. When the atmospheric forcing was altered within observational uncertainties, the wave height accuracy increased to 83% at Boulogne and to 70% at Dieppe, but the observed wave height was not fully resolved. These tidal results highlight the importance of accurately interpreting sparse observations, implementing accurate model forcings, and accounting for observational uncertainty when modeling meteotsunamis.

4.5 Conclusions

We have combined observations and numerical models to show that meteotsunamis are generated in the English Channel by convective weather systems. We demonstrate for the first time in an English Channel case study that atmospheric pressure forcing, Proudman resonance, and shoaling were key amplification mechanisms. Wind stress was a secondary forcing and increase the first wave peak by 16% on average because of combined low wind speeds and deep water. Including tide in our model decreased the coastal wave height by more than 50%, mostly because tidal currents shifted the Proudman resonant region away from the coastline (rather than depth changes affecting the shallow-water wave propagation speed directly).

The synthetic forcing simplicity may explain differences between best-estimate model results and observations. The best-estimate simulated arrival times and wave period within minutes and captured Proudman resonance, leading to estimates of wave heights accurate to within tens of centimeters (23%–29% underestimates). Here, ensembles accounted for this uncertainty, testing the sensitivity of the meteotsunami height to pressure perturbation amplitude, forcing velocity and forcing period. Nevertheless, considerable changes were found in wave height when testing sensitivity to each parameter. Wave height was linearly proportional to pressure amplitude, which is a well-known result. Forcing velocity and forcing period produced more complex changes in final wave height. Varying forcing speed between 17 and 19 m s^{-1} and forcing direction between 35º and 55º changed wave heights between 0.19 and 0.59 m at Dieppe and between 0.20 and 0.52 m at Boulogne, by changing where wave amplification occurred through Proudman resonance. Changes in forcing period resulted in complex wave behavior after the primary peak, due to superposition of different components of the meteotsunami. We recommend that future studies use an ensemble approach including tides, and varying forcing period and forcing velocity.

This study has also shown, through models covering observational uncertainty, that cross correlation of radar-derived precipitation is accurate enough to estimate atmospheric forcing velocity. Advantages of the cross-correlation method are that interpretations of gust fronts are not needed, estimates of velocity error are obtained, and the forcing velocity is calculated over water. It is also possible to calculate in near–real time in the United Kingdom—given radar measurements every 5 min. To obtain

accurate results from precipitation cross correlation in convective systems, the effects of individual cell motion should be minimized by using longer time steps and rain-rate thresholds. Once these sources of error are addressed, cross correlation of radar data is an accurate, simple method to calculate atmospheric system velocity.

Although atmospheric observations have both high temporal and spatial resolution, oceanographic observations could be improved with higher-frequency observations at tide gauges. Tide gauges in the United Kingdom and elsewhere use long averaging periods to improve the accuracy of data for long-term sea level studies. However, this hinders an improved understanding of potentially hazardous meteotsunamis where a shorter averaging period is recommended. It is also unclear how sea level rise will affect future meteotsunami hazard. Predicted increases in the average sea level could decrease the return period of 1 in 100 year storm surges by 25–40-fold (Wahl 2017). If meteotsunamis also become more frequent (for example from increased convective activity in a warmer atmosphere), the ability to observe them will be fundamental to coastal protection. High-frequency radar tide gauges could be a solution; they are capable of measuring water level at 1-min intervals and are relatively cheap and easy to maintain (Woodworth and Smith 2003).

We have demonstrated that convective system generated meteotsunamis can be simulated using simple synthetic models. This could lead to potentially useful hazard warning systems for northwestern European seas, as has been conducted in the Adriatic (Šepić et al. 2015a). We have also shown that meteotsunamis around the United Kingdom can be explained using dynamical arguments, and we have accurately simulated an observed meteotsunami by using sufficiently sampled pressure, wind, and radar data.

Acknowledgements. David Williams is funded by the National Environmental Research Council's Understanding the Earth, Atmosphere and Ocean Doctoral Training Programme, Grant NE/L002469/1. We thank Lotfi Aouf from MétéoFrance for providing 1-min atmospheric wind speed and pressure data, and two anonymous reviewers for their comments.

Chapter 5

Proudman resonance with tides, bathymetry and variable atmospheric forcings

5.0 Preamble

Study Motivation

Thus, in Chapter 4, the first numerical simulations based on observations of a meteotsunami in north-west Europe have been produced. Nevertheless, this work alone does not sufficiently reveal a general understanding of how Proudman resonance is affected by realistic conditions, including tidal elevation, tidal currents and variable bathymetry.

A question also arises from Chapter 4: how were the simulated meteotsunami wave heights relatively accurate, despite the numerous assumptions in the synthetic atmospheric forcing about the atmospheric convective system? The synthetic atmospheric forcing ignored that the observed atmospheric convective system changed speed, that the measured surface pressure perturbations changed amplitude, and ignored two-dimensional aspects of the atmospheric sea-level pressure. This chapter resolves these issues, by developing a more generalised understanding of Proudman resonance through analytical approximations and idealised numerical simulations.

Publication and Author Contribution

The work in this chapter will be submitted to a special edition in *Natural Hazards*, which followed from conversations at *The First World Conference on Meteotsunamis* in May 2019, Croatia. The work will be submitted with four authors: David A Williams, Kevin J Horsburgh, David M Schultz and Chris W Hughes.

David A Williams wrote the publication, developed the fundamental ideas, and completed simulations and analytical analyses. Kevin J Horsburgh was the primary supervisor for the project and secondary author, secured funding, provided editorial critique, and helped with discussion across all sections. David M Schultz is listed as the third author of the publication, provided editorial critique, and ensured clarity and

concision in the atmospheric sections. Chris W Hughes is listed as fourth author of the publication, provided editorial critique, and was involved in discussion for the proper physical interpretation of mathematical results.

Related Appendices

Supplementary figures to simulations are provided in Appendix B, showing more explicitly how the analytical and numerical solutions compare. The finite-difference model is outlined in Appendix C, with details on the governing equations and boundary conditions. A numerical simulation of an idealised linear atmospheric convective system was also produced in WRF, but the results from using this model as a forcing for Telemac were not expanded upon enough for an article-format chapter. These simulations, results and a discussion of the implications are presented in Appendix D.

Citation and Reference

This chapter is cited as Williams (2019a), and can be found in the bibliography:

Williams, D.A, 2019a: *Proudman resonance with tides, bathymetry and variable atmospheric forcings*. Meteotsunami generation, amplification and occurrence in north-west Europe, PhD dissertation, University of Liverpool, pp. 225.

5.1 Paper Abstract

Proudman resonance is a primary amplification mechanism for meteotsunamis, which are shallow-water waves generated by atmospheric forcings. The effect of tides, sloping bathymetry, and the speed, amplitude and aspect ratio of the atmospheric forcing on Proudman resonant wave growth are investigated using analytical approximations and numerical models. With tides included, maximum wave growth through Proudman resonance occurred when the atmospheric-forcing speed matched the tidal-wave speed. Growth greater than Proudman resonance occurred with a positive tidal elevation together with a tidal current in the opposite direction to wave propagation, due to linear growth combined with further amplification from wave-flux conservation. Near-Proudman resonant growth occurred when the forced-wave speed or free-wave speed varied by either a small amount, or varied rapidly, around a speed appropriate for Proudman resonance. For a forcing moving at Proudman resonant speed, resultant wave growth was proportional to the total, time-integrated forcing amplitude. Finally, Proudman-resonant wave growth was lower for forcings with lower aspect ratios (A_P), partly because forced-wave heights are proportional to $1 + A_P^2$, but also because free waves could spread in two dimensions. Whilst the assumptions of strict Proudman resonance are never met, near-Proudman resonant growth may occur over hundreds of kilometres if the effective Froude number is near 1 and the resultant wave propagates predominantly in one dimension.

5.2 Introduction

Meteotsunamis are atmospherically generated, potentially dangerous, shallow-water waves with periods between 2–120 minutes (Monserrat et al. 2006). The wave amplification in meteotsunamis has been commonly attributed to Proudman resonance (e.g. Hibiya and Kajiura 1982; Monserrat et al. 2006), which occurs when the speed of an atmospheric pressure forcing matches the shallow-water wave speed (Proudman 1929). Shallow-water waves that are confined to one dimension x propagate as

$$c(x) \approx \sqrt{gH(x)} + u_c(x), \tag{5.1}$$

where $c(x)$ is the wave speed, g is gravitational acceleration (here taken as 9.81 ms^{-2}), $H(x)$ is the water depth and $u_c(x)$ is a background current. The net shallow-water wave speed increases with increasing depth and along-propagation currents and decreases with decreasing depth and counter-currents.

The assumptions used to construct strict Proudman resonance mean that the mathematical model is highly simplified compared to reality. Strict Proudman resonance has *oceanographic assumptions* of a still (u_c = 0), flat-bottomed, one-dimensional basin, and *atmospheric assumptions* of a constant-speed, constant-amplitude, one-dimensional pressure forcing (Proudman 1929). There are also more fundamental physical assumptions: the ocean is frictionless, non-rotating and non-advecting, and the wave has negligible height. For such a modelled ocean, with an atmospheric pressure forcing P, moving at speed U in time t, the sea-level elevation, η, is

$$\eta(x, t) = -\frac{1}{\rho g}\left\{\frac{P(x - Ut)}{1 - (U/c)^2} - \frac{P(x - ct)}{2\,(1 - U/c)} - \frac{P(x + ct)}{2\,(1 + U/c)}\right\}, \tag{5.2}$$

where ρ is water density. Equation 5.2 describes the sea-level elevation as the sum of a rightward forced wave (speed U), a rightward free wave of opposite sign (speed c), which both grow as $U/c \rightarrow 1$, and a smaller leftward free wave (Levin and Nosov 2016). Typically, the Froude number Fr (Fr = U/c) is used to indicate when forced-wave and free-wave speeds match.

As Fr $\rightarrow$ 1, the physical separation between the rightward forced wave and rightward free wave decreases, until they are at an infinitesimally close superposition (Levin and Nosov 2016). Then, as x increases (whilst the superposition remains infinitesimally close), the sea-level elevation simplifies to

$$\eta(x, t) \approx -\frac{x}{2\rho g} P_x, \tag{5.3}$$

where $P = P(x - Ut)$ and the subscript x refers to partial differentiation in the along-propagation direction. The approximation in Equation 5.3 (found by integrating equation A14 from Churchill et al. (1995), assuming that the initial wave height is negligible) shows three important wave characteristics. First, the resultant Proudman-resonant wave grows linearly with distance moved. Second, the wave shape is that of the atmospheric pressure gradient. Third, the wave is scaled by $-1/\rho g$ (inverted barometer effect). As the wave grows, eventually the assumption of negligible wave height is broken, and linear wave growth stops (Levin and Nosov 2016).

Despite the rigid assumptions required for strict Proudman resonance, Proudman-like resonance can occur when these assumptions are not met. We consider two types of

assumptions: oceanographic and atmospheric. Oceanographic assumptions considered here are the stillness and flat-bottom assumptions. Proudman-like resonance has been previously simulated in two-dimensional oceanographic models with tides and variable bathymetry (e.g. Choi et al. 2014; Williams et al. 2019). Atmospheric assumptions considered here are the constant forcing speed, constant forcing amplitude and one-dimensionality assumptions. Proudman resonance has been inferred (Wertman et al. 2014) and simulated (Anderson et al. 2015) for linear convective systems moving at varying speeds, with varying amplitude with two-dimensional surface pressure fields. A few case studies have attempted to discuss the effect on wave amplification when these multiple assumptions are unmet. Nevertheless, these case studies do not give much insight to underlying wave dynamics.

The purpose of this study is to determine the sensitivity of wave growth when relaxing the assumptions of strict Proudman resonance. Specifically, this study will focus on *oceanographic factors* (tides and sloping bathymetry) and *atmospheric factors* (varying forcing speed, varying pressure forcing amplitude and two-dimensionality of atmospheric pressure forcings). This study presents more general dynamic explanations of wave growth by assuming that forced-wave and free-wave speeds are close, and that wave flux is conserved. These dynamic explanations are found by using idealised analytical and numerical models, with mathematically prescribed pressure disturbances that are termed synthetic atmospheric forcings for consistency with literature (e.g. Ličer et al. 2017).

This work is presented as follows. Section 5.3 describes the three different models that will be used in this study and the synthetic atmospheric pressure forcing that will be applied. Section 5.4 presents a baseline simulation of strict Proudman resonance. Section 5.5 tests the effect of oceanographic factors on this wave amplification and, similarly, section 5.6 tests the effect of atmospheric factors. Section 5.7 summarises these results.

5.3 Methods

To investigate the effect on wave growth from oceanographic and atmospheric factors, three oceanographic modelling methods (2D finite-element, 2D finite-difference and 1D finite-difference) were used to solve the shallow-water equations. We call these models 2D-FE, 2D-FD and 1D-FD respectively.

5.3.1 Hydrodynamic models

For the 2D hydrodynamic models studied here, the linear, frictionless, non-rotating, hydrostatic momentum equation and the nonlinear continuity equation were solved, given as

$$u_t = -\rho^{-1} P_x - g\eta_x, \tag{5.4}$$

$$v_t = -\rho^{-1} P_y - g\eta_y, \tag{5.5}$$

and

$$-\eta_t = [(H + \eta)u]_x + [(H + \eta)v]_y, \tag{5.6}$$

where u is the along-propagation current, v is the cross-propagation current, and y is the cross-propagation direction. Equations 5.4, 5.5 and 5.6 were solved in the domain $0 \leq x \leq L$, $0 \leq y \leq W$, with radiating boundary conditions at $x = 0$ and $x = L$, and reflecting boundary conditions at $y = 0$ and $y = W$.

The finite-element model Telemac (Hervouet 2000) was used and has been validated for tsunamis and tides (called 2D-FE). For reduced computation time, and to allow multiple rapid simulations, a finite-difference method was also developed in one and two dimensions (called 1D-FD and 2D-FD respectively). The finite-difference method is outlined in Appendix C. The differences between 2D-FE, 2D-FD and 1D-FD numerical solutions were small after convergence.

5.3.2 Synthetic atmospheric forcing

The hydrodynamic model was forced with a synthetic atmospheric pressure field prescribed as two orthogonal cosines (Figure 5.1, Equation 5.7). This synthetic atmospheric pressure forcing P can be summarised as

$$P = \begin{cases} P_0 \cos\psi \cos\gamma + P_\mathrm{b}\,, & \text{if} \quad -N\pi \le \psi \le N\pi,\ y_0 - \frac{\lambda_y}{4} \le \gamma \le y_0 + \frac{\lambda_y}{4} \\ P_\mathrm{b}, & \text{otherwise.} \end{cases} \quad (5.7)$$

The cosine arguments prescribed the two-dimensional pressure forcing position and extent (Equation 5.7). The first argument ψ prescribed the along-propagation speed and wavelength of the atmospheric forcing, $\psi = kx - \omega t$. The along-propagation wavenumber was $k = 2\pi/\lambda_x$, where λ_x was the along-propagation wavelength (40 km), and the angular frequency was $\omega = 2\pi/\tau$, where τ was the wave period (28–37 minutes). The speed of the atmospheric forcing U was ω/k. The bounds of the argument, $\pm N\pi$, ensured that N wavelengths were simulated (here, $N = 1.5$).

The second argument γ prescribed the cross-propagation forcing extent, explicitly $\gamma = m(y - y_0)$. The cross-propagation wavenumber was $m = 2\pi/\lambda_y$, where λ_y was the cross-propagation wavelength and $y_0 = W/2$. The argument bounds ensured half of the cross-propagation wavelength was prescribed as the forcing width, $W_\mathrm{F} = \lambda_y/2$ (Figure 5.1a). For planar pressure forcings, we set $m = 0$ (Figure 5.1b).

Finally, P_0 prescribed the maximum amplitude of the pressure forcing disturbance, and the pressure perturbation was added to a background pressure, $P_\mathrm{b} = 1013$ hPa. The parameters chosen here represented observed values for meteotsunami-generating convective systems (e.g. Anderson et al. 2015) and atmospheric gravity waves (e.g. Ličer et al. 2017).

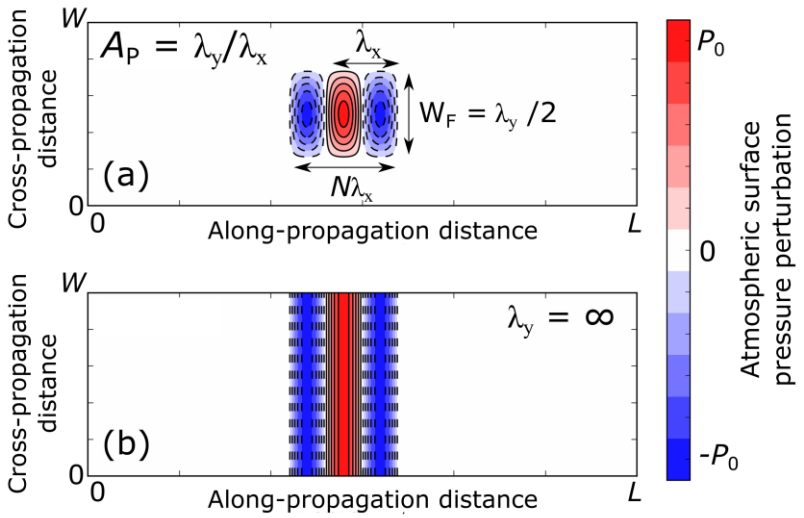

Figure 5.1 Synthetic atmospheric pressure in the domain $0 \leq x \leq L$, $0 \leq y \leq W$ at different values of λ_y. Here the pressure field is shown between $-P_0$ and $+P_0$, $N = 1.5$ and λ_y varied between a) $m > 0$ and b) $m = 0$. Panel a) shows the cross-propagation wavelength (λ_y) compared to the total forcing width ($W_F = \lambda_y /2$), and along-propagation wavelength (λ_x) compared to the total forcing length ($N\lambda_x$) of the pressure disturbances, with the definition of the aspect ratio $A_P = \lambda_y/\lambda_x$.

Next, the model simulation results and discussion are divided into three sections: strict Proudman resonance, oceanographic factors and atmospheric factors. First, strict Proudman resonance is simulated in section 5.4 to give baseline simulations. Second, the effect of oceanographic factors on wave amplification are tested in section 5.5. This section quantifies the effect of tides and sloping bathymetry on wave amplification through a hierarchy of simulations. This hierarchy progresses from simulating the effects on wave amplification of separate uniform elevations (5.5.1) and uniform currents (5.5.2). Then, a combination of uniform elevations and currents are modelled together (5.5.3). After these simulations, the effect of variable free-wave speed through bathymetric slopes are found (5.5.4). Finally, in the hierarchy, spatially and temporally co-varying elevations and currents are simulated together (5.5.5). After oceanographic factors are tested, the effect of atmospheric factors on wave amplification are tested in section 5.6. These simulations quantify the effect on wave amplitude by varying the average forcing speed (5.6.1), allowing the forcing speed (5.6.2) and then forcing amplitude (5.6.3) to vary in time, finally, including the two-dimensionality of forcings (5.6.4).

5.4 Strict Proudman resonance simulation results and discussion

First, the strict Proudman resonance simulation is presented, to provide baseline results for the following simulations and to demonstrate consistency with previous simulations from Vilibić (2008). Only the 1D-FD results are presented (Figure 5.2), although two-dimensional solutions were made equivalent to one-dimensional solutions by setting reflecting boundary conditions at $y = 0$ and $y = W$. All three models were run with λ_x = 40 km, P_0 = 100 Pa, in a H = 50 m, L = 400 km domain. The atmospheric forcing moved 10 wavelengths, corresponding to the distance scales (100s km) and the time scales (several hours) of mesoscale atmospheric systems that produce waves through Proudman resonance (Monserrat et al. 2006). The atmospheric forcing was also smoothed with a 5-km running average to ensure that the atmospheric forcing edges gradually returned to background pressure, rather than an unphysical, sharp cut off.

The 1D-FD pressure forcing and resulting sea-level elevation were made dimensionless. The sea-level elevation η was divided by $P_0/\rho g$, giving the dimensionless amplification, η^*, and the distance travelled was divided by wavelength λ_x, giving dimensionless wavelengths travelled, x^* (Figure 5.2).

There are three main features of the one-dimensional solution. First, the wave shape was that of the atmospheric pressure disturbance gradient multiplied by negative 1. The wave shape is explained by the wave shape from free-wave and forced-wave superposition as $\mathrm{Fr} \rightarrow 1$.

Second, the wave amplification increased linearly for every wavelength moved (Figure 5.2b). The maximum wave amplification of this simulation is shown in Table 5.1. Table 5.1 is the synthesis of all simulations, showing the simulation number (e.g. 0), model type (e.g. 1D-FD), feature changed within a factor (not applicable here, but an example is tidal elevation), test simulation (e.g. baseline or +4 m), maximum recorded amplification (e.g. 31.1) and location of maximum recorded amplification (e.g. 9.9). The strict Proudman resonance simulation has simulation number 0 to indicate that it is the baseline model. This simulation has a maximum recorded amplification of 31.1 and location of maximum recorded amplification of 9.9, and the wave grew 3.1454-fold ($3.1454 \approx \pi + 0.12\%$) for every wavelength moved.

The maximum modelled amplification and wave growth is understood through the analytic solution of the maxima and minima of amplification. By inputting an infinite and planar sinusoidal pressure forcing into Equation 5.3 and taking the solution maxima, the amplification envelope η^*_{env} is

$$\eta^*_{env} = \pm \pi x^*, \tag{5.8}$$

showing that a wave produced from a resonant sinusoidal pressure forcing will amplify π-fold for every wavelength moved. The numerical model overpredicted analytical growth by 0.12%, partly because of small numerical errors that could not be avoided. The forcing was not precisely specified as a sinusoid that smoothly moved with time, but as a discretised series of points on a line that approximated a sinusoid, and this forcing discretely (rather than smoothly) moved at specific time steps. Despite small discrepancies between numerical and analytical solutions, under strict Proudman resonance, an atmospheric forcing will produce an envelope according to

$$\eta^*_{env} = \pm \mu x^*, \tag{5.9}$$

where μ is the growth factor, which is the gradient of the envelope and is dependent on the pressure-forcing shape. A growth factor $\mu = 2$ is well-known for a piecewise linear forcing (Hibiya and Kajiura 1982; Vilibić 2008).

Third, simulations showed a smaller leading trough and smaller trailing peak (respectively LT and TP in Figure 5.2b). The smaller leading trough and trailing peak were because the pressure forcing was smoothed at its edges.

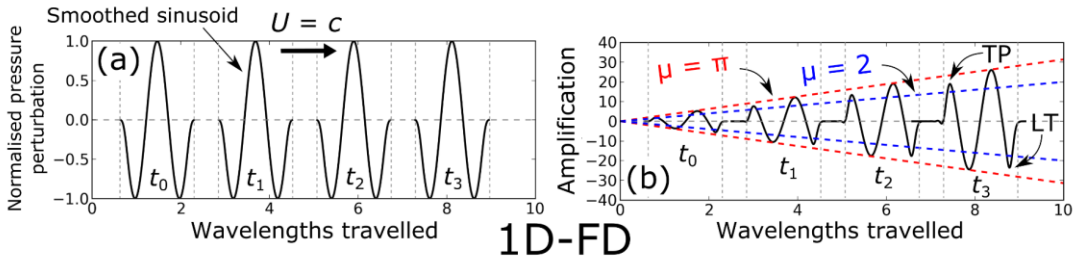

Figure 5.2 Flat-bottom strict Proudman resonance simulation results at four timesteps (t_0, t_1, t_2, t_3) for a rightward moving pressure forcing. The x-axis shows the number of wavelengths travelled. The vertical grey dashed lines indicate pressure forcing extent at each time step. a) normalised pressure disturbance, b) amplification (the normalised sea-level response). The red dashed lines show the wave envelope analytic solution for a sinusoidal pressure disturbance, and the blue dashed lines show the same for a piecewise-linear pressure disturbance with the same peak amplitude. Normalised pressure disturbances and amplifications magnitudes < 0.001 are not shown.

5.5 Oceanographic factors – results and discussion

Once the model had been validated through strict Proudman resonance stimulations, the effect of oceanographic factors on wave growth were quantified. A hierarchy of simulations was used to quantify the effect of tides and sloping bathymetry on Proudman resonant wave growth.

5.5.1 Uniform elevation change (1D-FD)

First, uniform elevation changes were modelled. To model the effect of tides, and because most tidal ranges are less than 8 m, water depths were changed between –4 m and +4 m. For a typically fast-moving atmospheric forcing that generates meteotsunamis, this tidal range was represented here by elevation changing from a baseline depth H_0 of 50 m by a uniform change ΔH.

When changing the water depth (simulations 1–4), the maximum wave amplification was smaller than from strict Proudman resonance. For example, when ΔH = –2 m (simulation 2) wave amplification was 6.4% smaller than strict Proudman resonance and when ΔH = +2 m (simulation 3), the maximum wave amplification was 3.8% smaller than strict Proudman resonance. Comparing ΔH = –2 m (simulation 2) with ΔH = +2 m (simulation 3), and ΔH = –4 m (simulation 1) with ΔH = +4 m (simulation

4), waves were slightly larger when elevation increased than for an equivalent elevation decrease.

These maximum wave amplifications are the maxima of the wave-amplification envelopes (see relationship in Figure 5.3a and Figure 5.3b). These wave-amplification envelopes are now explained through changes to shallow-water wave speed affecting Proudman resonance. For similarity with the literature, we define 'near-Proudman resonance' to occur when $0.9 \leq \mathrm{Fr} \leq 1.1$ or, equivalently, when the free-wave speed and forced-wave speed are within 10% of each other (e.g. Vilibić 2008; Šepić et al. 2015c). In these simulations, the approximate shallow-water wave speed is given by Equation 5.1 with water depth $H(x) = H_0 + \Delta H$ and $u_c = 0$. When the atmospheric forcing is near the shallow-water wave speed (i.e. near-Proudman resonance), and assuming an infinite, planar sinusoidal pressure forcing in Equation 5.2, the sea-level amplification η* can be approximated as

$$\eta^*(x,\, t;\, k,\, U,\, c) \approx 2\overline{A}(\mathrm{Fr}) \cdot \sin\left[k\frac{U-c}{U+c}x\right] \cdot \cos\left[k\left(x\ -\frac{U+c}{2}t\right)\right] = E(x)\,W(x-\overline{U}t), \quad (5.10)$$

which describes the sea-level elevation as a wave propagating at the mean speed, $\overline{U}$, of the forced and free wave (cosine term). This propagating wave is modulated by a sinusoid with an envelope wavenumber given as the atmospheric forcing wavenumber k multiplied by a Doppler shift $(U - c)/(U + c)$. The wave amplitude is then multiplied by the mean Proudman-resonant amplitude $\overline{A}(Fr)$, which is the mean of the coefficients of the rightward forced and free waves in Equation 5.2. The factor of 2 arises from using the trigonometric identity in the approximation. This approximation is summarised as the envelope $E(x)$ multiplied by a wave $W(x - \overline{U}t)$. Equation 5.10 has been adapted from Ličer et al. (2017) to include wave amplitude and to make the envelope wavenumber more explicit. Equation 5.10 was originally used to explain meteotsunami propagation speed, but we use it to explain the envelopes.

Envelopes matched the maximum wave amplification within 4.3% across simulations 1–4. Waves were larger when elevation was increased because the change in shallow-water wave speed was smaller when increasing elevation, leading to closer approximations of Proudman resonance. Therefore, these models suggest that it is slightly more important to account for elevation decreases (e.g. low tide) than elevation increases (e.g. high tide) because wave growth deviates more from strict Proudman resonance with elevation decreases than with elevation increases.

Summarising these results, when Proudman resonance was more closely approximated, larger waves were generated. Although simulations 1–4 only covered four combinations, a more general form for the amplification envelope has been developed (Equation 5.10) that can be used to describe any combination of atmospheric-forcing speed and water-depth change (Figure 5.3c). This more general amplification envelope is used later to help explain the effect of other oceanographic assumptions, and is appropriately adjusted to include other physical phenomena, for example wave-flux conservation with currents.

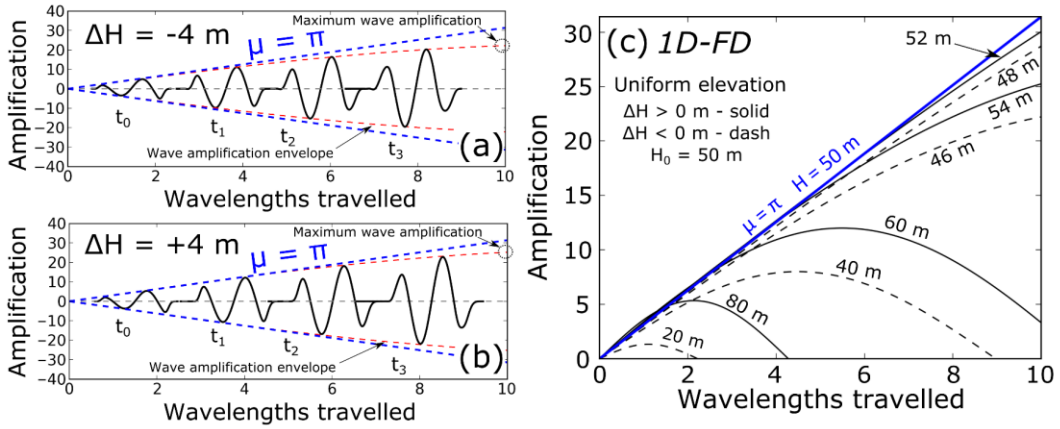

Figure 5.3 Flat-bottom 1D-FD model results at 4 timesteps (t_0, t_1, t_2, t_3) for a rightward moving pressure forcing at U = 22.15 ms^{-1} at different elevation changes (ΔH) where a) ΔH = –4 m (simulation 1), b) ΔH = +4 m (simulation 4). The x-axis is the dimensionless wavelengths travelled and the y-axis is dimensionless amplification. The dashed blue lines show the analytical solution to the wave envelope for a sinusoidal pressure disturbance at resonance, the dashed red lines show the wave envelope approximations. c) Analytical envelope approximations with uniform elevation changes that closely matched maximum amplification from 1D-FD simulations. Dashed black lines are elevation decreases and solid black lines are elevation increases.

5.5.2 Uniform current (2D-FE)

Once the wave amplification with uniform elevation changes were simulated and explained, uniform currents were modelled. Strict Proudman resonance requires a still ocean, so the suite of simulations in this section allows us to explore the sensitivity of the wave growth to a uniform ocean current. In our simulations 5–12 (Table 5.1), the model initial conditions and boundary conditions were the along-propagation tidal current speed u_c. The current effects were isolated by excluding friction, meaning that

background water depth remained constant. We simulated $-3.0\ \mathrm{ms}^{-1} \leq u_c \leq +3.0\ \mathrm{ms}^{-1}$, where positive currents were rightward.

The maximum wave amplitudes were consistently larger as the magnitude of u_c decreased. The maximum wave amplitude was on average 3.8-times larger with 0.5 ms^{-1} than 3 ms^{-1} magnitude currents (cf. simulations 8 and 9 with simulations 5 and 12). Wave growth was also different for currents of the same magnitude moving in different directions. When $|u_c| = 3\ \mathrm{ms}^{-1}$, the maximum amplification was 4% smaller and occurred 1.1 wavelengths leftwards with counter-currents (simulation 5) compared to along-propagation currents (simulation 12). Similarly, when $|u_c| = 2\ \mathrm{ms}^{-1}$, maximum amplification occurred 0.7 wavelengths leftwards with counter-currents (simulation 6) than along-propagation currents (simulation 11), but the maximum amplifications were of similar magnitude. Conversely, when currents were smaller ($|u_c| = 0.5$ and $|u_c| = 1\ \mathrm{ms}^{-1}$), maximum wave amplifications were on average 8% larger with counter-currents (simulations 7–8) compared to along-propagation currents (simulations 9–10). Therefore, smaller currents always produced larger waves, but maximum wave amplification was different for opposite currents of the same magnitude by a few percent.

The resultant wave amplification for all constant currents can be explained by a near-Proudman resonant envelope approximation (Equation 5.10) combined with wave-flux conservation. A small-amplitude wave (as studied here) entering a region with a current will change wave height to conserve wave energy flux according to

$$\eta_c / \eta_0 = 1 / (1 + f_c), \tag{5.11}$$

where the subscript ‘c’ refers to the variable with a current and subscript ‘0’ refers to the variable without a current. The dimensionless current factor f_c refers to the ratio of current speed to shallow-water wave speed ($u_c/\sqrt{gH}$). A current in the same direction as a wave (along-propagation current) will decrease the wave height and a counter-current will increase the wave height. Finally, wavelength also changes with currents according to

$$\lambda_c / \lambda_0 = 1 + f_c, \tag{5.12}$$

showing that along-propagation currents increase wavelengths and counter-currents decrease wavelengths (Li and Herbich 1982; Choi et al. 2014).

An additional simulation was performed with an atmospheric-forcing speed U = 15 ms^{-1} (Fr = 0.68) to confirm the effect of currents on forced waves and free waves (not in Table 5.1 because the purpose of this simulation is separate to the focus of main study results). Over 4.4 hours (16,000 seconds) of simulation time, forced waves and free waves separated, and the effect of currents were seen on both waves. When currents were included, both the forced-wave and free-wave heights changed according to Equation 5.11. The free-wave wavelength also changed according to Equation 5.12. However, the forced-wave wavelength did not change, because it was fixed by the forcing wavelength. Therefore, both waves were amplified by currents, but only the free wave changed wavelength.

This information was then used to approximate the envelope wavelength and magnitude with currents (Figure 5.4). The envelope wavelength was calculated with the average of forced-wave and free-wave wavelengths and the envelope magnitude was multiplied by the right-hand side of Equation 5.11. This envelope approximated maximum wave amplification within 5.2%. The envelopes were different for positive and negative currents for two reasons – wave amplification (Froude number and wave-flux conservation) and free-wave wavelength modification (wave-flux conservation).

Wave envelopes have so far been described for elevation-only changes (simulations 1–4) and current-only changes (simulations 5–12). In the real world, these simulations may represent how standing-wave tides at different tidal states (e.g. high tide, flooding tide) may affect wave growth. For standing-wave tides, when the tidal elevation is 0 m, the current is flooding (maximum positive current) or ebbing (maximum negative currents). Conversely, slack tide (u_c = 0 ms^{-1}) occurs at high tide and low tide. These envelopes may be used to predict how much tidal elevations and currents individually affect wave growth.

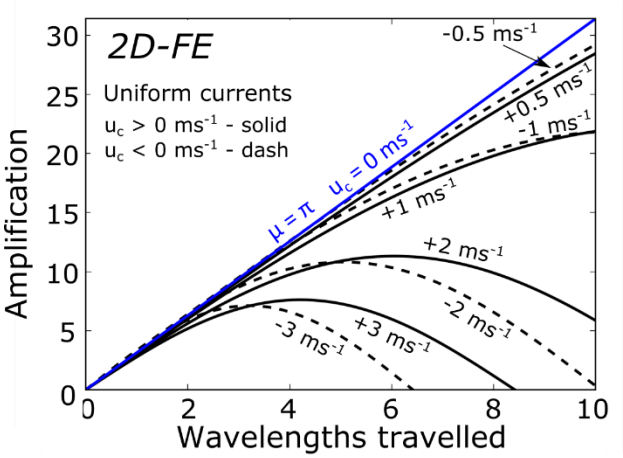

Figure 5.4 Analytical envelopes with uniform currents that closely matched maximum wave amplification from 2D-FE simulations. Dashed black lines are counter-current and solid black lines are along-propagation currents.

5.5.3 Uniform elevation and current (2D-FE)

In the real ocean, elevation changes and currents may not be separated. Therefore, uniform elevation and currents were modelled together in simulations 13–20 (Table 5.1). As before, the bottom elevation was changed from H_0 = 50 m by ΔH, where ΔH was –4 m, –2 m, +2 m and +4 m. This elevation was combined with a constant current of either –1 ms^{-1} or +1 ms^{-1}.

The resultant waves were dependent on combined elevation and currents. With counter-currents (simulations 13–16), as elevation increased from –4 m to +4 m, the maximum wave amplifications increased by 174% and moved 3.9 wavelengths rightward. With along-propagation currents (simulations 17–20), as the elevation decreased from +4 m to –4 m, the maximum wave amplifications increased by 128% and moved 3.4 wavelengths rightward. Each combination of elevation and current produced unique wave amplification envelopes.

The envelope approximations used the combination of both the elevation effect on Proudman resonance and current effect on Proudman resonance and wave-flux conservation (Figure 5.5). Accounting for both elevation and currents, envelopes approximated maximum wave amplifications to within 4.4%.

Most combined current and elevation simulations 13–20 produced sub-Proudman resonant wave amplification. However, the wave growth with u_c = –1 ms^{-1} and ΔH =

+4 m (simulation 16), produced growth that was 3% larger than Proudman resonance predictions, termed super-resonant wave growth.

This super-resonant growth occurred firstly because the wave-speed changes from elevation were compensated by counter-currents and secondly because of wave-flux conservation. This super-resonant growth is not confined to elevation and current changes together. It may also occur with an atmospheric forcing that is moving slower than the depth-dependent wave speed against a counter-current such that the Froude number is near 1.

In the real world, simulations 13–20 may represent Proudman resonance in a progressive tide, with floods at high tide and ebbs at low tide. In progressive tides, currents and tidal elevation are in phase, meaning that, across a tidal cycle, shallow-water wave speed may be more variable than in standing-wave tides. Therefore, meteotsunami generation within progressive-wave tides may be more controlled by tidal state (e.g. high tide, falling tide) than generation within standing-wave tides.

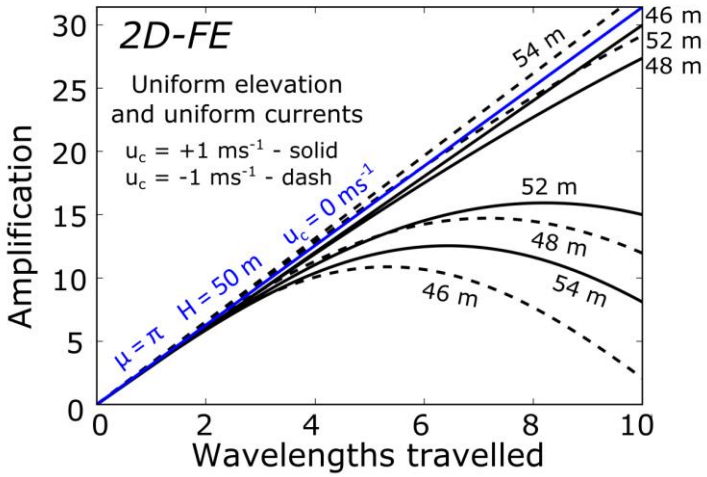

Figure 5.5 Analytical envelopes with uniform elevation and currents that closely matched maximum wave amplification from 2D-FE simulations. Dashed black lines are counter-currents, solid black lines are along-propagation currents, elevation changes are annotated.

5.5.4 Bathymetric slope (2D-FE)

Next, we varied the bathymetric slopes. Strict Proudman resonance requires a flat-bottomed ocean, so the suite of simulations 21–24 in this section allows us to explore the sensitivity of wave growth to the magnitude and sign of a bathymetric slope (upward or downward). Previous studies have numerically modelled Proudman

resonance with sloping bathymetry (e.g. Vilibić 2008; Ličer et al. 2017). However, we explicitly design our models to isolate the effect of a linear slope even with an average Froude number of 1, which others have not done.

To understand how a slope may affect wave growth, we refer to the interaction between forced waves and free waves generated by a forcing. Recall from the derivation of Equation 5.3, as Fr → 1, the physical separation between the forced wave and free wave decreases and Proudman resonance occurs. However, across variable bathymetry, individual free waves are continuously generated, which combine to form a free-wave superposition (Ličer et al. 2017). Therefore, the separation is dependent on the positions of the forced wave and the free-wave superposition. The position of the forced wave leading edge x_U is given by the forcing speed U multiplied by time t. However, the position of the free-wave superposition is more complex than the forced-wave position because multiple free waves are generated.

To parameterise the position of the free-wave superposition, the leading edge position of the farthest free wave from the forced wave was calculated. This free-wave position x_c was calculated for a basin of length L with depths $H(x = 0) = H_0$ and $H(x = L) = H_1$. By first integrating the inverse free-wave speed $c^{-1}(x)$ with respect to x, and then rearranging, we obtained

$$x_c(t) = \frac{g(H_1 - H_0)}{4L} t^2 + \sqrt{gH_0}\, t, \tag{5.13}$$

showing that x_c is quadratic in time. Then, the difference between $x_U(t)$ and $x_c(t)$ was calculated, giving the separation $\Delta x(t)$.

The slopes were then set such that $\Delta x = 0$ at the start and end of propagation. In other words, the average free-wave speed was made equal to the average forced-wave speed to isolate the slope effect. Four simulations were completed: simulation 21) H_0 = 30 m, H_1 = 75.1 m (steep downslope); simulation 22) H_0 = 40 m, H_1 = 61.1 m (shallow downslope); simulation 23) H_0 = 60 m, H_1 = 40.9 m (shallow upslope); and simulation 24) H_0 = 70 m, H_1 = 33.4 m (steep upslope). These slopes were similar magnitude to realistic bathymetry in shallow shelves, seas and lakes (0.05–0.1 m km^{-1}).

With all slopes, the maximum wave amplification was lower than from strict Proudman resonance (cf. simulation 0 with simulations 21–24, Figure 5.6). However, maximum wave amplifications were 32% larger with shallow slopes (simulations 22–

23) than steep slopes (simulations 21 and 24) and 17% larger with upwards slopes (simulations 23–24) than downwards slopes (simulations 21–22). These results are illustrated by the smallest wave being generated with the steep downslope (simulation 21) and the largest wave with the shallow upslope (simulation 23).

In each sloping bathymetry simulation, but most notably in the steep downslope, the wave envelope amplification was smaller and modulated along the wave propagation direction (Figure 5.6). For all other slopes, there was a qualitatively similar, though smaller, envelope modulation. These envelope modulations were related to the magnitude of Δx in time.

We suggest that the wave envelopes may be better approximated by accounting for $\Delta x(t)$, rather than simply using the average free-wave speed (c = 22.15 ms^{-1}). Nonetheless, directly accounting for $\Delta x(t)$ is complicated. A simpler way to include the separation effect is to account for the maximum separation,

$$\Delta x_{\max} = \frac{c_0 - U}{4} T. \tag{5.14}$$

Equation 5.14 shows that the maximum separation was directly proportional to both the difference in free-wave and forced-wave speeds and the time taken to cross the basin. The separation was positive for upward slopes and negative for downward slopes.

To account for $\Delta x_{\max}$, we introduced a constant, effective free-wave speed c_{eff}. This effective free-wave speed gave the same maximum separation over the propagation time T of the free wave and forced wave, and was calculated as

$$c_{\text{eff}} = \bar{c} + \frac{\Delta x_{\max}}{T}, \tag{5.15}$$

where $\bar{c}$ was the mean free-wave speed (22.15 ms^{-1}). The *effective* Froude number, here $\text{Fr}_{\text{eff}} = U/c_{\text{eff}}$ shows that effective Froude number was within ranges of near-Proudman resonance. For example, the *effective* Froude number was 0.96 for the steep upwards slope, compared to an *instantaneous* Froude number between 0.82–1.18. The envelope from an effective Proudman resonance was calculated with Fr_{eff} in Equation 5.10. Fr_{eff} was nearer 1 for shallower slopes and upward slopes, which may explain why waves were larger for shallow slopes than steep slopes, and larger for upward slopes than downward slopes.

The wave heights may also have been larger for upwards slopes than downward slopes because of wave-flux conservation. Thus, the wave-height increase from shoaling was also accounted for according to Green's Law,

$$\frac{\eta(x)}{\eta_0} = \left[\frac{H(x)}{H_0}\right]^{-1/4}. \tag{5.16}$$

This shoaling contributed wave height for upward slopes and reduced wave height for downward slopes. The free-wave wavelength also decreased with decreasing depth. Thus, average wavelength changes were included, but their effect seemed negligible.

The envelopes with effective wave speed and shoaling produced better approximations of wave growth than strict Proudman resonance by parameterising the effect of variable free-wave speeds (Figure 5.6). However, the envelopes derived from the effective wave speeds were not useful indicators of instantaneous wave height. Discussion of the effective Froude number continues in section 5.6.2.

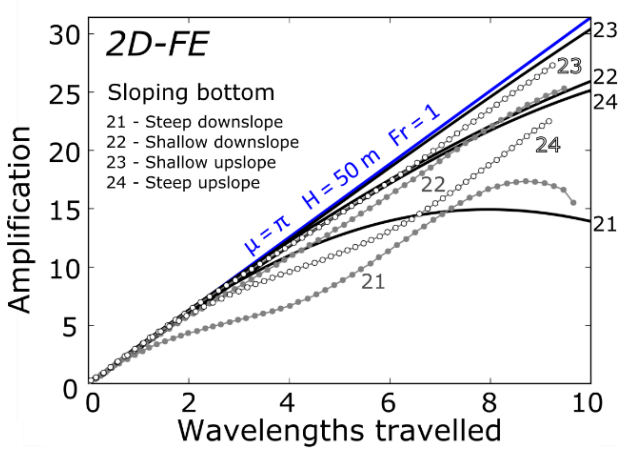

Figure 5.6 Sloping bottom maximum wave amplifications from 2D-FE simulations. Black solid lines are effective Froude number envelopes. Grey dots are simulation maxima for downward slopes and white dots are simulation maxima for upward slopes. Maxima are joined by grey lines (linear interpolation). Simulation envelopes and envelope approximations are annotated with simulations numbers 21–24.

5.5.5 M_2 progressive tides (2D-FE)

Finally, in the hierarchy, co-varying depths and currents were modelled with an M_2 tide approximation in simulations 25–28. The M_2 constituent was chosen because it is normally the largest tidal constituent in basins (e.g. Pugh and Woodworth 2014). The model was spun-up over 6 days with a boundary condition at $x = 0$, prescribing a 12.4-

h period sinusoid with 4-m amplitude. For model stability with a time-variable boundary condition, a constant horizontal diffusivity was included (150 m^2s^{-1}). An additional simulation without tides and with diffusivity showed that diffusivity reduced maximum wave amplification by < 1%.

Once the tidal simulation was spun-up and stable, the tidal-wave speeds were approximated. Here, the tidal-wave speed was the speed at which the relevant phase of the sinusoid moved across the domain. At four tidal states, the tidal-wave speeds were estimated within one standard deviation. These speed estimates were 20.1 ± 0.6 ms^{-1} at low tide, 20.5 ± 1.3 ms^{-1} at rising tide, 23.4 ± 0.9 ms^{-1} at high tide and 21.7 ± 0.6 ms^{-1} at falling tide. The tidal-wave speed varied between tidal states primarily because tidal amplitude was about 8% of the total water depth.

The water depths and currents were similar to those previously modelled in subsections 5.5.1–5.5.4. The maximum water level varied between 46 and 54 m, and the current co-varied between –1.8 and +1.7 ms^{-1}, within the ranges examined in sections 5.5.1–5.5.3. During falling and rising tide, the current was between about –0.5 ms^{-1} and +0.5 ms^{-1} and the water depth was between about 49 m and 51 m across the full atmospheric forcing length ($N\lambda_x$) (Figure 5.7a), meaning that free-wave speed varied across the forcing length similarly to examined in section 5.5.4. Therefore, the analyses developed in previous sections were applied to these M_2 tidal simulations.

For each simulation, an atmospheric pressure forcing was applied, moving rightward at speed U = 22.15 ms^{-1}. The centre of the atmospheric pressure perturbation ($P = P_b$+100 Pa) first coincided with each tidal state at $x = 0$, but the atmospheric forcing's tide-relative position slightly drifted along propagation. This drift was because the atmospheric-forcing speed differed from tidal-wave speed. The resulting sea-level elevation from the atmospheric forcing moving over falling tide is shown in Figure 5.7a.

To analyse the wave amplification separately from tidal elevation, a fourth-order 2–100 km bandpass Butterworth filter was applied to the sea-level elevation (implemented as the digitised 'butter' function from SciPy, which was adopted from Butterworth (1930)). The wave growth at falling tide was 10% larger than strict Proudman-resonant growth and thus super-resonant (Figure 5.7b). All other simulations produced near-resonant wave growth (Figure 5.7c). The maximum wave

amplification was also 23% larger at high tide than low tide, and 5.4% larger at falling tide than rising tide. These resultant amplifications are similar to the results from tidal elevation and tidal current simulations in section 5.5.3.

As the tide is a shallow-water wave, the free-wave speeds were approximated by the tidal-wave speed $c_{p,T}$ and currents were approximated by the tidal currents at the centre of the wave $u_{c,T}$. Single values of the $c_{p,T}$ and $u_{c,T}$ were applied in the same way as with sloping bottoms (section 5.5.4), but errors associated with this simplification were accounted for in the estimations.

The largest errors in the stationary and the wave's reference frames were accounted for when estimating the tidal-wave speed and current. The stationary reference frame error was from tidal wave-speed approximations (stated within one standard deviation). Two more errors from the wave's reference frame were also estimated. The first error was from the atmospheric forcing drifting relative to tidal state, and the second error was from changes in water depth and currents across the full atmospheric forcing length. The estimates of $c_{p,T}$ and $u_{c,T}$ that produced wave envelope approximations that were closest to numerical solutions are shown in Figure 5.7c. These simulations reiterated the results from previous simulations 1–24; wave growth may be closely approximated in dynamic tidal regimes by accounting for Proudman resonance and wave-flux conservation using single, representative values of free-wave speed and currents.

So far, we have explained wave growth with changes to uniform water depth (simulations 1–4), uniform currents (simulations 5–12), uniform elevation and currents (simulations 13–20), bathymetric slope (simulations 21–24) and progressive M_2 tides (simulations 25–28). At least for the water depths considered here, when examined individually, currents were more important than elevations within typical tidal ranges. However, elevation changes and currents should be considered together to properly understand the resultant non-linear changes to maximum wave amplification. Understanding the combination of elevations and currents allowed close approximations of maximum wave growths from progressive tidal simulations. Overall understanding was supplemented by bathymetric slope simulations, which showed that near-Proudman resonant wave growth could occur even when the

instantaneous Froude number varied between 0.82–1.18, because the effective Froude number was near 1.

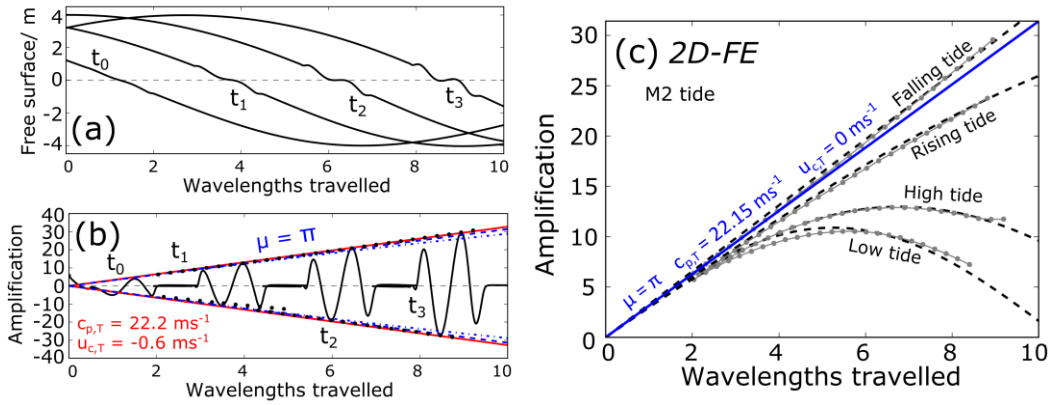

Figure 5.7 Sea-level elevation and amplification from a moving forcing with a dynamic progressive tide with 2D-FE simulations. a) Sea-level elevation directly from the falling tide simulation at 4 time steps (t_0, t_1, t_2, t_3) and b) band-passed filtered sea-level elevation converted to amplification. Blue dash-dots are initial estimates of $c_{p,T}$ (21.7 m s^{-1}) and $u_{c,T}$ (0 m s^{-1}), and the red solid line is the envelope with improved $c_{p,T}$ and $u_{c,T}$. Black dots are maxima and minima of sea-level amplification at 500-s intervals between 4,500–15,000 s. Amplification values more than $0.5\lambda_x$ ahead of and behind the forcing have been cropped for clarity. c) Black dashed lines are the envelope approximations with lowest error of the maxima recorded amplitude. The grey dots are simulation maxima, joined by grey lines (linear interpolation).

5.6 Atmospheric factors – results and discussion

Next, the atmospheric forcing assumptions of constant speed, constant amplitude and one-dimensionality were investigated for flat bathymetry without elevation changes or currents.

5.6.1 Average forcing speed (1D-FD)

Common methods to estimate atmospheric-forcing speed use land-based in-situ high-frequency measurements (Orlić 1980; Vilibić et al. 2008; Choi et al. 2014), radar reflectivity (Wertman et al. 2014; Williams et al. 2019) or numerical weather prediction models (Horvath and Vilibić 2014; Anderson et al. 2015). However, it is sometimes difficult to calculate atmospheric-forcing speed within 10% accuracy (Wertman et al. 2014), leading to uncertainty in the maximum wave growth due to Proudman resonance. This uncertainty can occur even with high fidelity bathymetry and accurate tidal modelling (Williams et al. 2019). To account for uncertainty in

average atmospheric-forcing velocity, multiple simulations with different velocities may be required (e.g. Ličer et al. 2017).

To test the wave growth from different atmospheric-forcing speeds, the baseline speed U_0 = 22.15 ms^{-1} was changed by –2 ms^{-1} ≤ ΔU ≤ +2 ms^{-1} (simulations 29–32). These simulations were modelled with H = 50 m, λ_x = 40 km and N = 1.5. The resultant wave amplification for constant atmospheric-forcing speeds produced near-Proudman resonance wave growth, giving results that were explained using the same envelope as for water depth changes (Equation 5.10), which were accurate within 0.9%.

Reasonable uncertainties in the average speed of a fast-moving atmospheric forcing (± 10%, simulations 29–31) produced larger changes in sea-level elevation than reasonable uncertainties due to large tidal elevation ($|\Delta H|$ = 4 m, simulations 1 and 4) and weak currents ($|u_c|$ < 1 ms^{-1}, simulations 7–10) alone. The wave growth from changing atmospheric-forcing speeds were similar to large tidal elevation with currents (ΔH = – 4 m, u_c = +1 ms^{-1}, simulation 17), strong currents alone ($|u_c|$ > 1 ms^{-1}, simulations 5, 6, 11 and 12), steep downward slopes (simulation 21), M_2 low tide (simulation 25) and M_2 high tide (simulation 28).

Therefore, obtaining accurate estimates of average forcing velocity is as important as quantifying the combined effect of tidal elevation and currents. We speculate that, for the purposes of meteotsunami generation, a calculated forcing velocity is more accurate when obtained from measurements over water (e.g. radar) than from measurements over land (e.g. *in situ* land stations). A lower velocity may be calculated over land, because land is more heterogeneous and has a higher coefficient of friction than the ocean. Therefore, for the purpose of inferring Proudman resonance or using velocity calculations in synthetic models, when it is possible, atmospheric forcing velocities should be obtained through measurements of the atmospheric system over water.

5.6.2 Variable forcing speed (1D-FD)

The motion of mesoscale atmospheric systems that generate meteotsunamis, such as convective systems, can be highly variable due to internal processes within the mesoscale systems and external environmental conditions. For example, there is discrete propagation from gust fronts, interactions between convective and stratiform components of storms, and how the storm evolves within the larger-scale

environmental conditions such as wind shear or rear inflows (Markowski and Richardson 2011 pp. 245–265) (for which we assume the pressure field is related to the precipitation field observed by radar). However, strict Proudman resonance assumes a constant motion of the forcing. Even for convective systems that form meteotsunamis, the system velocity can be highly variable over time (Wertman et al. 2014) and differ across scales within a convective system (Williams et al. 2019). Thus, we quantify the effect of variable atmospheric-forcing speeds on wave amplification in simulations 33–40.

First, the sensitivity of wave growth with linear forcing speed changes were investigated (simulations 33–36). When the forcing speed changed linearly (i.e. constant acceleration), resultant wave growth was qualitatively similar to sloping bottoms (section 5.5.4). Effective Froude numbers for variable forcing speeds were quantitatively the same as for linearly sloping bathymetry (Equation 5.15); the effective Froude number can be used for either free waves or forced waves with variable speed.

Next, a sinusoidal pressure forcing speed was applied such that the average speed was 22.15 ms^{-1}, the speed at the start and end of the movement was 22.15 ms^{-1} and the difference between the highest and lowest forcing speed was the speed change ΔU. A weak speed change of 4 ms^{-1} and a strong speed change of 8 ms^{-1} were modelled. Also, a slow speed modulation (number of cycles = N_u = 1) and a rapid speed modulation (N_u = 2) were modelled to investigate the effect the frequency of speed oscillations.

Again, smaller changes in atmospheric-forcing speed meant that wave growth was more closely approximated by linear growth (Figure 5.8). However, more rapidly changing atmospheric-forcing speeds also produced wave growth that was more closely approximated by linear growth. Interestingly, the maximum wave amplification from the weak, slow speed modulation was equivalent to the maximum wave amplification from strong, rapid speed modulation (cf. simulations 38 and 39 in Table 5.1 and Figure 5.8).

To explain these results, the relationship between maximum separation, speed change and number of cycles was found. Analysis between forced and free waves with sinusoidally varying atmospheric-forcing speed gave a maximum separation

$$\Delta x_{\max} = \frac{\Delta U}{2\pi N_u} T, \tag{5.17}$$

where $\Delta x_{\max}$ was positive for an atmospheric forcing that initially moved faster than the shallow-water wave speed. More rapidly varying atmospheric-forcing speeds (higher N_u) also had smaller maximum separations. Also, Equation 5.17 shows that maximum separation was the same for the weak, slow modulation simulation 38 and the strong, rapid modulation simulation 39 because $\Delta U/N_u = 4$ ms^{-1} for both simulations.

The effect of $\Delta x_{\max}$ was then applied through the effective Froude number (Fr_{eff}) calculated with the effective forcing speed and free-wave speed. Fr_{eff} better approximated the growth of the wave than the average Froude number (Figure 5.8). Across simulations 29–40 (except simulation 37), the average Froude number overpredicted maximum amplification by 17% on average, whereas Fr_{eff} overpredicted maximum amplification by 1.2% on average. Where Fr_{eff} overpredicted amplitude by 42% in simulation 37, the average Froude number performed even more poorly, overpredicting amplitude by 124%.

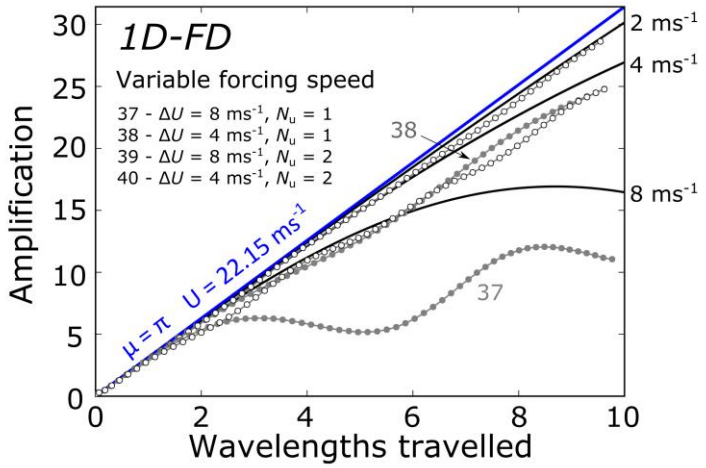

Figure 5.8 Maximum wave amplification with sinusoidally varying forcing speed, from 1D-FD simulations. Black solid lines are effective Froude number envelopes. Grey dots are simulation maxima for $N_u = 1$, and white dots are simulation maxima for $N_u = 2$. Maxima are joined by grey lines (linear interpolation). The values of $\Delta U/N_u$ are annotated in metres per second.

Even when the instantaneous Froude number strongly varied from 1 (e.g. simulation 36, 0.82–1.18), if the effective Froude number was near 1 (e.g. 0.96), then near-

Proudman resonant wave growth could occur. The effective Froude number was nearer 1 when the mean atmospheric forcing and free-wave speeds were equal, when the variations around the mean forced or free speed were small, and when those variations were rapid. Often studies have used instantaneous Froude numbers between 0.9–1.1 to indicate Proudman resonant regions (e.g. Šepić et al. 2015c). Based on the results of our simulations, we suggest that this range may be increased to between 0.8–1.2.

The effective Froude number was not a useful quantity to give predictions of instantaneous amplification along propagation. The effective speed poorly approximated the instantaneous sea-level elevation in all simulations, especially at the maximum separation between forced waves and free waves (Figure 5.6, Figure 5.8). However, the effective Froude number may successfully parameterise the bulk effect of variable forced-wave or free-wave speeds on wave growth.

The usefulness of the effective Froude number may depend on the maximum separation of the waves compared to their wavelength. The maximum separation of the waves is dependent on the total forcing time (T), the rate of the speed change (N_u), and the maximum speed difference (ΔU). When using the effective Froude number to predict envelopes, smaller separations gave smaller errors. For example, when $\Delta x_{max} = 0.58\lambda$ (simulation 37) there was a 42% over-prediction and when $\Delta x_{max} = -0.45\lambda$ (simulation 33) there was a 6.4% under-prediction. Further research may reveal under which conditions the effective Froude number is most useful. However, these results indicate that the effective Froude number is a more useful bulk parameter than the average Froude number to indicate Proudman resonant wave growth.

5.6.3 Time-varying amplitude of atmospheric forcing (1D-FD)

Mesoscale atmospheric processes will vary over the time that the wave is coupled to the forcing (a few hours), and these variations may increase or decrease atmospheric forcing amplitude. For example, during the life cycle of a convective system, the system will initiate, grow, mature and decay (e.g. Johnson 2001).

Rather than first simulating the sea-level elevation and finding analytical approximations to numerical simulations to help explain the results, in this section, analytical solutions were directly found for variable amplitude forcings. This approach was taken because the analytical solution required only a simple generalisation of the

forcing amplitude. Then, numerical simulations 41–43 were completed as supporting evidence.

Here, analytical solutions were found for sea-level elevation from a variable amplitude forcing moving at Proudman resonant speed, for a one-dimensional, linear, frictionless, non-rotating ocean. A pressure forcing Π was prescribed in a moving reference frame $\xi = x - ct$ as a non-varying component $P(\xi)$ multiplied by a time-varying component $\alpha(t)$ ($-1 \leq \alpha(t) \leq 1$).

The derivation of Proudman resonance under a constant amplitude forcing from Churchill et al. (1995) was used as guidance, producing

$$\eta(\xi, t) \approx -\frac{H}{2c\rho} P_{\xi} \int \alpha \, dt. \tag{5.18}$$

Under Proudman resonant speeds, the sea-level elevation in the moving reference frame is proportional to the time-integrated forcing amplitude. When $\alpha(t) = 1$ (i.e. $d\alpha/dt = 0$), Equation 5.18 recovers linear wave growth according to strict Proudman resonance (Equation 5.3). In the case that $d\alpha/dt \neq 0$, Equation 5.18 suggests non-linear wave growth under Proudman resonance. We show this relationship under the simple case of α(t) 1) linearly increasing (growth), 2) linearly decreasing (decay) and 3) as a half-wavelength sinusoid (growth from zero, maturation and decay back to zero).

The linearly changing amplitude forcings ($0 \leq \alpha(t) \leq 1$) gave quadratic growth (Figure 5.9a). For the linearly increasing forcing, the amplification quadratically increased at an increasing rate, and for the linearly decreasing forcing, the amplification quadratically increased at a decreasing rate. Simulations 41–42 reiterated these analytical solutions. Analytical solutions show that maximum amplification for both linear increase and linear decrease, $\eta^* = 5\pi$ at $x^* = 10$, which is half of the maximum amplification from a constant-amplitude forcing.

For a sinusoidally modulated atmospheric pressure forcing that grew, matured and decayed over time T, the resultant envelope is shown in Figure 5.9b. Analytical solutions show that when a pressure disturbance returns to 0 amplitude at $x = L$ ($x^* = 10$), the simulated wave amplification would be $\eta^* = 20$, giving a mean growth factor $\bar{\mu} = 2$. This was also reinforced by simulation 43. Interestingly, a sinusoidally modulating, sinusoidal disturbance produces the same amplitude wave at $x = L$ as a

constant amplitude, piecewise linear disturbance, the amplitude of which was first derived by Hibiya and Kajiura (1982).

These one-dimensional results suggest that a wave can occur when the amplitude of the atmospheric forcing is 0 at $x = L$. This idealised model is analogous to the real-world case that a wave could occur with no measurable atmospheric forcing at the coastline. Therefore, there may be no strong relation between meteotsunami wave heights and forcing magnitude at coastlines. Rather, several oceanographic measurements might be necessary to infer correlation between the time-integrated forcing magnitude and the final wave height. For similar reasons, we also speculate that only using in-situ land observations as atmospheric forcing indicators may lead to underpredicting meteotsunami occurrences in climatologies.

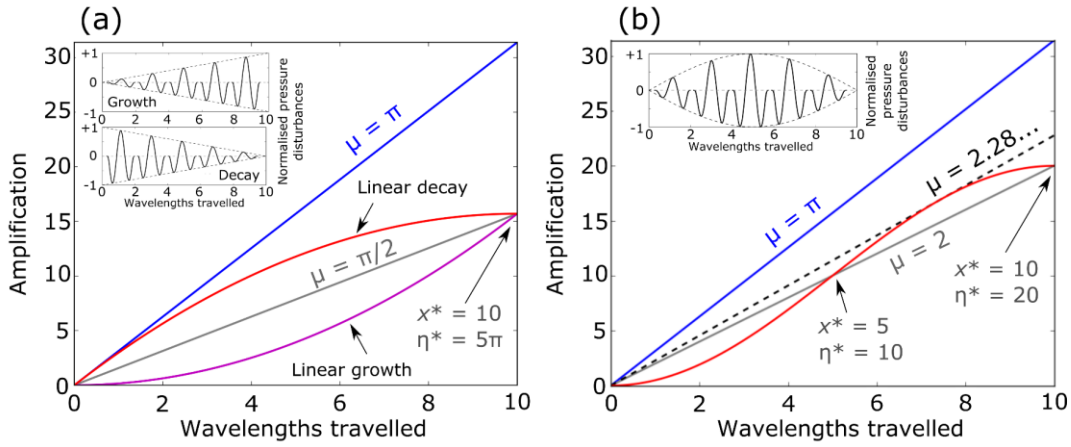

Figure 5.9 Analytical envelopes for a sinusoidal pressure disturbance with: a) constant amplitude (blue), linear growth (purple), linear decay (red) and the equivalent envelope with the average growth (grey); b) constant amplitude (blue), sinusoidal modulation (red), and the equivalent envelope for a constant-amplitude ramp-like pressure disturbance (grey). The black dashed line is the equivalent maximum growth factor of the sinusoidally modulated, sinusoidal pressure disturbance. Insets show the dimensionless pressure-forcing amplitude as the forcing moves across the basin in numerical simulations.

5.6.4 Forcing aspect ratio (2D-FD)

Although strict Proudman resonance assumes one-dimensional forcings (Proudman 1929), observed meteotsunami-generating atmospheric surface forcings are two-dimensional (e.g. Wertman et al. 2014). We investigate the direct effect of two-dimensionality on wave generation through Proudman resonance by varying the pressure forcing aspect ratio A_P in simulations 44–49. The aspect ratio is defined here

as the cross-propagation wavelength divided by along-propagation wavelength, such that $A_P = \lambda_y/\lambda_x$ (see Figure 5.1 for visual representation of A_P).

In this study, we investigate the effect of A_P by changing the cross-propagation wavelength, whilst maintaining along-propagation speeds appropriate for strict Proudman resonance ($U = \omega/k = c$) and a constant along-propagation wavelength. The forcing was applied over a domain L = 100 km, W = 100 km, H = 100 m, with a 200-m horizontal grid spacing and 1-s time step. The forcing had along-propagation wavelength λ_x = 10 km. The cross-propagation wavelength was changed between 10 km $\leq \lambda_y \leq$ 500 km, corresponding to $1 \leq A_P \leq 50$ (Table 5.1).

Wave amplifications were closely approximated by strict Proudman resonance at the centre of the forcing when $A_P \geq 10$ (simulations 48–49, λ_x = 10 km, $\lambda_y \geq$ 100 km). As the aspect ratio decreased, the amplitude at the centre of the forcing also decreased (simulations 44–47, Table 5.1, Figure 5.10). When A_P = 1 (simulation 44) the maximum sea-level amplification at the end of the simulation was about five times smaller (x^* = 9.6, $\eta^* \approx$ 6.1) than predicted from strict Proudman resonance (x^* = 9.6, $\eta^* = 9.6\pi \approx 30.2$).

One reason that more circular forcings produced smaller waves than more linear forcings is found by analysing the amplitude of the forced wave at resonance. Inputting a forcing specified by Equation 5.7 into the two-dimensional wave equation (found by rearranging Equations 5.4, 5.5 and 5.6 and assuming $\eta \ll H$), indicated that when $U = \omega/k = c$, the forced-wave height η_F was proportional to the aspect ratio as

$$\eta_F \propto 1 + A_P^2. \tag{5.19}$$

Therefore, the forced-wave height is limited for forcings moving at strict Proudman resonant speeds when there is a finite aspect ratio. A more physically intuitive explanation is that circular forcings are inefficient at maintaining the one-dimensional velocity convergence required for Proudman resonance. This inefficiency is seen partly as free waves spreading in the cross-propagation direction. Nonetheless, these numerical simulations suggest that more linear systems preferentially generate meteotsunamis.

The aspect ratio derived from radar reflectivity, A_R, defined as the ratio between the major and minor axes of an ellipse fitted to radar reflectivity, is often used to classify

observed mesoscale atmospheric systems (e.g. Fairman et al. 2016; Fairman et al. 2017). Typically, more circular systems may be represented with A_R less than about 3 and more linear systems with A_R more than about 3–5 (Liu and Zipser 2013; Fairman et al. 2016; Fairman et al. 2017). Note that $A_P \neq A_R$ but A_P and A_R should be somewhat proportional. For example, radar can be used to indicate locations of high pressure in linear convective systems, as high pressure can occur in convective precipitation due to evaporation (Markowski and Richardson 2011). Nonetheless, the extent of radar reflectivity is not perfectly related to the atmospheric pressure forcing (e.g. Wertman et al. 2014). However, we speculate that radar reflectivity may provide observational evidence as to whether more linear systems preferentially generate meteotsunamis.

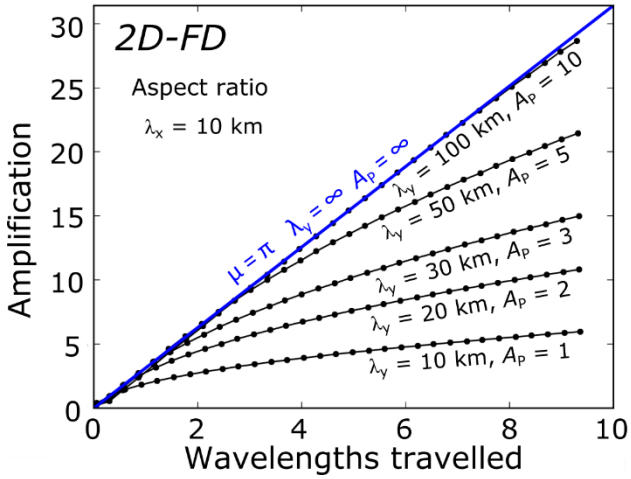

Figure 5.10 Aspect ratio simulations summary from 2D-FD simulations across $1 \leq A_P \leq 10$. Black dots are simulation maxima, joined by black lines (linear interpolation).

5.7 Conclusions

In this study, we extended the theory of strict Proudman resonance to include tidal elevation, tidal currents, bathymetric slopes, varying forcing speeds and varying forcing amplitudes, and showed the effect of forcing two-dimensionality on Proudman resonant wave growth. The numerical model baseline simulations of strict Proudman resonance agreed to within 0.12% of analytical solutions. We explained the strict Proudman resonance sea-level elevations as a wave resulting from a forcing moving at the shallow-water wave speed. This wave grew linearly according to a wave envelope with constant gradient $\mu \approx \pi$. For waves that grew near Proudman resonance, we generalised this explanation as a wave propagating with an average of the forced-wave and free-wave speed $W(x - \bar{U}t)$ multiplied by a wave envelope $E(x)$.

A hierarchy of simulations was used to examine tidal effects on wave growth. First, uniform depth changes were investigated. Wave amplifications decreased with non-zero tidal elevation because water depth changes made the free-wave speed deviate from the forcing speed. These results suggested that wave growth was slightly smaller at low tide than high tide.

Second, uniform currents caused wave amplifications to decrease compared to strict Proudman resonant growth. This amplification decrease was primarily because currents made the free-wave speed deviate from the forcing speed, but wave-flux conservation also slightly changed wave amplitude. Envelopes were different for the same magnitude current whether the wave was moving with or against the current. These differences were because wave-flux conservation changed 1) free and forced-wave amplitudes and 2) the free-wave wavelength.

Third, uniform currents and tidal elevation were modelled together. Counter-currents and increased water depth permitted wave growth greater than Proudman resonance, termed super-resonant growth. This super-resonant growth was because water depth increased free-wave speed and counter-currents almost equivalently decreased the free-wave speed. This wave-speed compensation meant that the Froude number was near 1, whilst wave-flux conservation further amplified waves.

Fourth, sloping bathymetry was modelled with simulations that isolated the slope effect. The wave growth was better approximated using an *effective* free-wave speed rather than the *average* free-wave speed. This effective free-wave speed was the average free-wave speed plus the speed difference that was calculated to give the correct maximum separation of the forced and free wave. The largest waves were created with gentle upwards sloping bathymetry, because the effective Froude was near 1 and waves shoaled to conserve wave flux (Green's Law).

Finally in the oceanographic section, a dynamic M_2 tide was simulated with forcings coinciding with low tide, rising tide, high tide and falling tide. The largest wave was modelled at falling tide, where super-resonant growth occurred that was 10% larger than strict Proudman resonance. This super-resonant growth was because the forcing speed approximated the tidal-wave speed and flux conservation further increased amplification.

Next, atmospheric forcing factors were investigated. Determining average forcing speed may be the largest uncertainty in determining Proudman resonance. However, variable atmospheric-forcing speeds (with average speeds appropriate for Proudman resonance) may still produce near-Proudman resonant wave growth if the effective Froude number is near 1. We found that for linear bathymetric slopes and linearly varying forcing speeds, the calculation of the effective Froude number was the same. For sinusoidal forcing speeds, the effective forcing speed showed that rapidly changing forcing speeds (high N_u) with small variations (small ΔU) more closely approximated Proudman resonance than slowly changing forcing speeds with large variations. This relationship may explain why atmospheric systems with variable speeds and sloping bottoms can still produce near-Proudman resonant wave growth even though Proudman resonance conditions ($0.9 \leq \mathrm{Fr} \leq 1.1$) are relatively rarely met.

Near-Proudman resonant growth occurred when the instantaneous Froude number varied between 0.82–1.18 because the effective Froude number was near 1. Commonly, instantaneous Froude numbers between 0.9–1.1 are used to indicate Proudman resonant regions in case studies. From these simulations, we speculate that instantaneous Froude numbers between 0.9–1.1 may be too conservative, and this range may be expanded to instantaneous Froude numbers of about 0.8–1.2.

By varying the amplitude of forcings that move at Proudman resonant speeds, waves grew according to the time-integrated forcing amplitude. These results suggest that there is no necessary relation between an instantaneous, point-measured forcing amplitude and wave height. Therefore, using only sparse, coastal measurements for atmospheric forcing verification in climatologies may systematically reduce the number of identified meteotsunamis.

Finally, the simulations presented here suggested that more circular forcings (i.e. aspect-ratio forcings near 1) are less effective at producing Proudman resonant wave growth than more linear forcings (i.e. higher aspect-ratio forcings). A question follows from these simulations: are meteotsunamis preferentially generated by higher aspect-ratio systems rather than lower aspect-ratio systems? If future observational analyses show that higher aspect-ratio systems preferentially produce meteotsunamis, it is unknown if this relation would occur because of direct alteration to resonance

mechanisms (as suggested here) or for other reasons, such as greater system stability increasing coupling time or higher average forcing amplitudes leading to larger waves.

Proudman resonant wave growth is mainly dependent on the forcing speed (i.e. the forced-wave speed) and the free-wave speed matching. For a wave to grow from Proudman resonance, factors that affect the average speed are more important than factors that affect variability around the average speed. The measurable factors investigated here that affect the average wave speeds are of about the same importance, and their total effect on wave speeds and wave-flux conservation should be considered together. However, from these simulations, tidal-elevation changes had the smallest effect on Proudman resonance, and from the literature, the most challenging to measure is the average forcing velocity. The aspect ratio is probably less important for wave growth than forcing and free-wave speeds matching, though the aspect ratio may determine whether a wave efficiently grows, or instead spreads. The average forcing amplitude is not important for efficient Proudman resonance. However, larger average forcing amplitudes will produce larger waves. Combined, these results suggest that the average forcing properties whilst over water and the average free-wave speed are most important to understand wave growth through Proudman resonance.

Table 5.1 Simulation number, model, feature changed, test simulation, maximum recorded amplification and location of maximum recorded amplification across 50 simulations.

Simulation number	Model	Feature changed	Test simulation	Maximum recorded amplification	Location of maximum recorded amplification
0	1D-FD	None	Baseline	31.1	9.9
1	1D-FD	Elevation	–4 m	22.7	9.9
2	1D-FD	Elevation	–2 m	29.1	9.9
3	1D-FD	Elevation	+2 m	29.9	9.9
4	1D-FD	Elevation	+4 m	25.4	9.9
5	2D-FE	Current	–3 ms^{-1}	7.1	3.1
6	2D-FE	Current	–2 ms^{-1}	10.9	5.1
7	2D-FE	Current	–1 ms^{-1}	22.3	9.3
8	2D-FE	Current	–0.5 ms^{-1}	28.5	9.4
9	2D-FE	Current	+0.5 ms^{-1}	27.1	9.6
10	2D-FE	Current	+1 ms^{-1}	20.4	9.4
11	2D-FE	Current	+2 ms^{-1}	10.8	5.8
12	2D-FE	Current	+3 ms^{-1}	7.4	4.2
13	2D-FE	Elevation / current	–4 m / –1 ms^{-1}	11.2	5.6
14	2D-FE	Elevation / current	–2 m / –1 ms^{-1}	15.2	7.3
15	2D-FE	Elevation / current	+2 m / –1 ms^{-1}	28.1	9.4
16	2D-FE	Elevation / current	+4 m / –1 ms^{-1}	30.7	9.5
17	2D-FE	Elevation / current	–4 m / +1 ms^{-1}	27.9	9.5
18	2D-FE	Elevation / current	–2 m / +1 ms^{-1}	25.5	9.6
19	2D-FE	Elevation / current	+2 m / +1 ms^{-1}	15.2	8.1
20	2D-FE	Elevation / current	+4 m / +1 ms^{-1}	12.2	6.1
21	2D-FE	Sloping bathymetry	Steep downwards	17.4	8.7
22	2D-FE	Sloping bathymetry	Shallow downwards	25.3	9.5
23	2D-FE	Sloping bathymetry	Shallow upwards	27.3	9.2
24	2D-FE	Sloping bathymetry	Steep upwards	22.5	9.2
25	2D-FE	M_2 tidal state	Low	10.5	5.5
26	2D-FE	M_2 tidal state	Rising	24.7	9.1
27	2D-FE	M_2 tidal state	High	12.9	6.6
28	2D-FE	M_2 tidal state	Falling	32.9	9.5
29	2D-FE	Average U, ΔU	–2 ms^{-1}	11.6	5.6
30	2D-FE	Average U, ΔU	–1 ms^{-1}	22.7	9.8
31	2D-FE	Average U, ΔU	+1 ms^{-1}	21.6	9.9
32	2D-FE	Average U, ΔU	+2 ms^{-1}	10.5	5.6
33	1D-FD	Linear U, ΔU	–8 ms^{-1}	22.2	9.3
34	1D-FD	Linear U, ΔU	–4 ms^{-1}	28.0	9.7
35	1D-FD	Linear U, ΔU	+4 ms^{-1}	25.7	9.3
36	1D-FD	Linear U, ΔU	+8 ms^{-1}	21.2	8.5

Table 5.1 contd.

37	1D-FD	Sinusoidal U, $\Delta U/N_u$	8 ms^{-1} / 1	11.9	8.5
38	1D-FD	Sinusoidal U, $\Delta U/N_u$	4 ms^{-1} / 1	24.6	9.7
39	1D-FD	Sinusoidal U, $\Delta U/N_u$	8 ms^{-1} / 2	24.6	9.7
40	1D-FD	Sinusoidal U, $\Delta U/N_u$	4 ms^{-1} / 2	28.6	9.6
41	1D-FD	Variable amplitude	Linear growth	15.7	9.9
42	1D-FD	Variable amplitude	Linear decay	15.6	9.5
43	1D-FD	Variable amplitude	Sinusoidal	19.9	9.5
44	2D-FD	Aspect ratio	1	6.1	9.6
45	2D-FD	Aspect ratio	2	11.0	9.6
46	2D-FD	Aspect ratio	3	15.2	9.6
47	2D-FD	Aspect ratio	5	21.8	9.6
48	2D-FD	Aspect ratio	10	29.4	9.5
49	2D-FD	Aspect ratio	50	29.9	9.5

Acknowledgements David Williams is funded by the National Environmental Research Council's Understanding the Earth, Atmosphere and Ocean Doctoral Training Programme, Grant NE/L002469/1. We thank Mirko Orlić for his personal communication regarding appropriate boundary conditions.

Chapter 6

An 8-yr meteotsunami climatology across north-west Europe: 2010–2017

6.0 Preamble

Study Motivation

Although more general explanations of Proudman resonance were developed in Chapter 5, a second problem remained from the case study in Chapter 4: there is little context for the meteotsunami of 23 June 2016. Although there have been a few observational case studies and localised climatologies across north-west Europe, it is still not known how frequently meteotsunamis of this size occur over the continental shelf, the usual time of year for meteotsunamis, nor which mesoscale atmospheric phenomena tend to generate them. The following work addresses these issues, providing context to north-west European meteotsunami case studies, including that of 23 June 2016.

Publication and Author Contribution

The work in this chapter has been prepared for submission to the *Journal of Physical Oceanography*. The work will be submitted with four authors: David A Williams, David M Schultz, Kevin J Horsburgh, and Chris W Hughes.

David A Williams wrote the publication, gathered the data, completed the manual analyses and identification, and wrote all processing scripts. David M Schultz is listed as the second author of the publication, provided editorial critique, and provided advice on mesoscale system classification and interpretation of synoptic atmospheric systems. Kevin J Horsburgh is listed as the third author, secured funding, provided editorial critique, and provided extensive discussion of tidal analysis. Chris W Hughes is listed as fourth author of the publication, provided editorial critique and was also involved in discussion of tidal analysis.

Related Appendices

During this research, considerable effort was made to reduce the tidal signal in tide-gauge records. After filtering and tidal harmonic analysis proved insufficient, a 'stacking correction' was developed. The details of the stacking algorithm, how well it worked on synthetic data, and how it was implemented with real tide gauge measurements are detailed in Appendix E. Finally, the effect on identified wave heights when sub-sampling tide gauge measurements from 5-min to 15-min intervals are also outlined in Appendix F.

Citation and Reference

This chapter is cited as Williams (2019b) and can be found in the bibliography:

Williams, D.A., 2019b: *An 8-yr meteotsunami climatology across north-west Europe: 2010–2017*. Meteotsunami generation, amplification and occurrence in north-west Europe, PhD dissertation, University of Liverpool, pp. 225.

6.1 Paper Abstract

Meteotsunamis are shallow-water waves that, despite often being small (~ 0.3 m), can cause damage, injuries and fatalities due to relatively strong currents (> 1 m s^{-1}). Previous case studies, modelling and localised climatologies have indicated that dangerous meteotsunamis can occur across north-west Europe. Using 71 tide gauges across north-west Europe between 2010–2017, a regional climatology was made to understand the typical sizes, times and atmospheric systems that generate meteotsunamis. 349 meteotsunamis (54.0 meteotsunamis per year) were identified with 0.27–0.40 m median wave heights. The largest waves (~ 1 m) were measured in France and the Republic of Ireland. Most meteotsunamis were identified in winter (43–59%), and all countries had the fewest identified meteotsunamis in either spring or summer (0–15%). There was a weak diurnal cycle, with most meteotsunami identifications between 1200–1859 UTC (30%) and fewest between 0000–0659 UTC (23%). To understand the kind of weather associated with meteotsunamis, radar-derived precipitation was used to identify and classify the morphologies of mesoscale precipitating weather systems occurring within 6 h of each meteotsunami. Most mesoscale atmospheric systems were quasi-linear systems (46%) or open-cellular convection (33%), with some non-linear clusters (17%) and a few isolated cells (4%). As an example of the synoptic weather patterns associated with commonly observed morphologies, ERA5 reanalyses were used to construct synoptic composites on 45 days with meteotsunamis on the French coast of the English Channel: 10 events with winter-time open cells, 26 events with winter-time quasi-linear systems and 9 events with summer-time quasi-linear systems. For all composites, there were low sea-level pressure anomalies to the north and west of the UK, for winter-time open cells and winter-time quasi-linear systems there was an unstable lower troposphere over the Celtic Sea and Atlantic Ocean and for 89% of summer-time quasi-linear systems convective available potential energy was over the ocean. Notably, 43 out of these 45 meteotsunamis were coincident with a region in the English Channel calculated to be favourable for Proudman resonance. Because many meteotsunamis occur on cold, precipitating winter days in regions with large tidal ranges may mean that many winter-time meteotsunamis are missed by eyewitness observations, weighting previously published case studies towards summer-time meteotsunamis.

6.2 Introduction

Meteotsunamis are shallow-water waves with periods between 2–120 minutes that are generated by moving atmospheric weather systems. The atmospheric pressure and wind fields associated with those weather systems can force resonant wave growth, known as external resonance (e.g. Proudman 1929; Greenspan 1956; Monserrat et al. 2006; Vilibić 2008), that amplifies waves from a few centimetres up to tens of centimetres (e.g. Orlić 1980; Hibiya and Kajiura 1982; Choi et al. 2014; Šepić et al. 2015a; Anderson et al. 2015; Ličer et al. 2017). External resonance occurs when atmospheric-system speeds match wave speeds, typically in regions of gently sloping bathymetry (< 0.1 m km^{-1}) shallower than 100 m. After growth through external resonance, meteotsunamis are further amplified by refraction and shoaling (e.g. Monserrat et al. 2006). Meteotsunamis that grow through external resonance, refraction and shoaling are commonly 0.1–1 m high. However, if the meteotsunami forms a standing wave, known as seiching or internal resonance, it can exceed 1 m high. Meteotsunamis that seiche can cause flooding and millions of US dollars in damages (e.g. Monserrat et al. 2006; Vučetić et al. 2009; Rabinovich 2009; Orlić et al. 2010). However, even meteotsunamis with modest wave heights may produce strong and hazardous currents. For example, a 0.3-m high meteotsunami produced rip currents in Lake Michigan on 4 July 2003 that caused seven people to drown (Linares et al. 2019).

Although meteotsunamis are dangerous in some situations, how common they are is unknown. A global climatology indicates that small non-seismic sea-level oscillations with tsunami timescales (NSLOTTs) are fairly common, contributing up to 50% of sea-level variance in basins with tidal ranges less than about 1 m (Vilibić and Šepić 2017). Table 6.1 includes other studies that have produced size-exceedance rates in regions that meteotsunamis tend to occur, including the Mediterranean (e.g. Šepić et al. 2012; Šepić et al. 2015b) and various US basins (e.g. Bechle et al. 2016; Olabarrieta et al. 2017; Dusek et al. 2019) where typically a moderately large meteotsunami (~1 m) is expected once every few years. The biggest similarity between these regions is that they contain a large area (~10^5 km^2) of gently sloping, shallow water, where external resonance tends to occur. However, a similarly large (6×10^5 km^2) region of gently sloping, shallow water that is known for meteotsunamis, has not been

represented by a regional climatology—the north-west European continental shelf (Figure 6.1).

Climatologies are useful because they quantify conditions during which meteotsunamis occur. These, in turn, allow testing of the scientific hypotheses about their occurrence, formation and amplification. For example, do meteotsunamis occur preferentially in certain seasons or at particular times of the day? If meteotsunamis were to occur mostly in the summer between 0700–1900 local time, beachgoers would be at greater risk than if meteotsunamis were to occur mostly in winter between 1900–0700 local time. In fact, historical case studies indicate that north-west European meteotsunamis may be a summer-time phenomenon with no clear diurnal preference (e.g. Douglas 1929; Haslett et al. 2009; Tappin et al. 2013; Frère et al. 2014; Sibley et al. 2016; Williams et al. 2019).

However, local analyses of tide gauges over several years sometimes suggest the opposite seasonality. Analysis of the Southampton tide gauge, on the south coast of the UK, has indicated that large waves (with slightly longer periods than meteotsunamis) typically occur in autumn and winter (Oszoy et al. 2016). Furthermore, a climatology of atmospherically-generated seiches in the port of Rotterdam, which we interpret as meteotsunamis, also showed that most Dutch meteotsunamis occur in autumn and winter (e.g. de Jong and Battjes 2004). Clearly, there is discrepancy between the seasonality of meteotsunamis in case studies, and the suggested seasonality from localised climatologies (loosely, we refer to a localised climatology as a statistical analysis of less than 10 tide gauges along a coastline).

Once the time and dates of events are known, we can also link the conditions of their identified occurrence time to oceanographic and atmospheric conditions across the meso-scales (10–500 km scales over a few hours) and synoptic scales (> 500 km scales over a few days) present at their formation. One question is whether meteotsunamis occur primarily from certain mesoscale atmospheric weather systems that occur in particular synoptic environments. For example, meteotsunamis in the Great Lakes tend to be generated by fronts, linear convective systems and non-linear convective complexes rather than discrete, individual cells (e.g. Bechle et al. 2015; Bechle et al. 2016). Such a result is consistent with idealised model simulations indicating that linear pressure forcings are more likely to generate meteotsunamis than circular

forcings with the same along-propagation wavelength (Williams 2019a). The question then arises as to whether there are particular synoptic atmospheric conditions that favour these mesoscale systems and allow meteotsunami amplification through external resonance (e.g. Vilibić and Šepić 2017).

Identifying a meteotsunami from observations can be difficult. To identify a meteotsunami, three steps are generally required. First, signals in the tsunami frequency band (2–120-min periods) are isolated from lower- and higher-frequency sea-level elevations. Second, a wave that is significantly larger than background noise in the residual signal is identified. Third, finally this wave must also be demonstrated to be atmospherically generated. There are multiple valid choices when implementing these three steps that have been made in other climatologies. For example, 10 different approaches are present in Table 6.1.

To illustrate the variety of choices available within each step, consider the choices one could make in the second step: the amplitude threshold to determine which waves are large enough be distinguished from background noise. Previous studies have used a significant wave height relative to the de-tided residual noise (e.g. Bechle et al. 2015; Kim et al. 2016; Olabarrieta et al. 2017; Carvajal et al. 2017), an absolute wave-height threshold (e.g. de Jong and Battjes 2004; Šepić et al. 2012; Linares et al. 2016; Bechle et al. 2016) and even a mix of the two methods (e.g. Šepić et al. 2009; Dusek et al. 2019). Each choice results in different detection rates of meteotsunamis, with lower-amplitude thresholds yielding more meteotsunamis. We discuss the amplitude threshold as the choice that, based on the results of previous studies, probably makes the biggest different to meteotsunami count. Nevertheless, how to remove lower-frequency energy (e.g. tides, storm surges), the time interval over which a certain number of tide gauges should identify a meteotsunami event, and how to identify an atmospheric forcing also influence meteotsunami climatological results.

Table 6.1 Choices made when producing meteotsunami climatological studies.

Study	Study type	Region	Study period	Tide gauge sampling interval	Tide gauges	Isolating wave periods	Amplitude thresholds	Tide gauges and event interval	Atmospheric system data	Number of waves and annual rate
de Jong and Battjes (2004)	Climatology and case studies	North Sea (Rotterdam)	1995–2001	1 min	7	Morlet wavelet analysis	Absolute (0.25 m)	Unknown	In situ	39 (5.6 per year)
Šepić et al. (2012)	Climatology and case studies	Mediterranean	1955–2010	Continuous, digitised to 2 min	1	Filter + Morlet wavelet analysis	Absolute (0.25 m)	Unknown	In situ	14 (and 2 with 140–150 min period)
Pattiaratchi and Wijeratne (2014)	Climatology and case studies	Australia	2000–2013	1–5 min	8	Tidal harmonic analysis + filter	Relative	Unknown	In situ	Unknown
Šepić et al. (2015b)	Climatology and case studies	Mediterranean	2010–2014	1 min	29	Tidal harmonic analysis + filter	Unknown	Recorded by at least 3 tide gauges.	Reanalysis	36 (7.2 per year)
Bechle et al. (2016)	Climatology	Laurentian Great Lakes	1994–2015	6 min	32	Filter	Absolute (0.3 m)	Grouped detections in 12-h intervals at the same station.	In situ + Radar	2332 across all lakes (106 per year)
Oszoy et al. (2016)	Case studies found from climatology	English Channel (Solent)	2000–2013	15 min	24	Tidal harmonic analysis + filter	Relative (Highest energy)	3 days between events.	In situ + reanalysis	Unknown (8 analysed, 3–5 h period waves)
Kim et al. (2016)	Climatology only	Korea	2002-2013	1 min	9	Filter	Relative (Highest amplitudes)	Recorded by at least 3 tide gauges.	Synoptic charts, radar, lightning, satellite.	92 (7.7 per year)
Vilibić and Šepić (2017)	Climatology only	Global	2004–2017	1 min	366	Filter	Relative (Highest amplitudes)	Unknown	Reanalysis	Unknown (15 further analysed)
Olabarrieta et al. (2017)	Climatology and case studies	Gulf of Mexico	1996–2016	6 min	3	Filter	Relative (6σ)	36 h imposed between waves.	In situ + Radar	18–25 per year per station
Dusek et al. (2019)	Climatology and case studies	US East Coast	1996–2017	1–6 min	125	Tidal harmonic analysis + filter	Relative (6σ) and absolute (0.20 m)	Recorded by at least 2 tide gauges.	In situ + Radar	548 (25 per year)

In this article, we consider meteotsunamis in north-west Europe. Although numerous case studies of meteotsunamis and localised climatologies in north-west Europe have been published (e.g. de Jong and Battjes 2004; Haslett et al. 2009; Tappin et al. 2013; Frère et al. 2014; Oszoy et al. 2016; Sibley et al. 2016; Williams et al. 2019), a regional climatology that quantifies the average (i.e. median) and extremes in their sizes, the times of identified occurrence time and the associated atmospheric systems has not been constructed. Without such an understanding of the size-exceedance rates, quantifying the hazard posed by meteotsunamis is not possible. The purpose of this article is to produce the first regional climatology of meteotsunamis for north-west Europe and identify the synoptic weather patterns and the mesoscale phenomena that are associated with meteotsunamis. This north-west European climatology will answer how frequently meteotsunamis of certain wave-heights occur (size-exceedance rates), when they occur (diurnal and seasonal variation), and which precipitating weather systems tend to co-occur with meteotsunamis in certain synoptic environments. This climatology will also provide evidence to test the hypothesis that linear systems tend to generate meteotsunamis.

The structure of the rest of this article is as follows. In section 6.3, we describe the data, how NSLOTTs and meteotsunamis were detected from this data, and the atmospheric system classification scheme. Then, in section 6.4, we present results and discussion of the size-exceedance rates, seasonal and diurnal variation and atmospheric conditions. Finally, we conclude in section 6.5.

6.3 Data and methods

To produce a meteotsunami climatology, we linked NSLOTT identifications, distinguished from tide-gauge measurements, to precipitating atmospheric systems that were measured by radar and identified from pre-processed images (Met Office 2003). This section outlines the data and choices used in this study to define a meteotsunami.

6.3.1 Tide-gauge data

We used 90 tide gauges between 1 January 2010 – 31 December 2017 (Figure 6.1). There was 5-minute data from Belgium and the Republic of Ireland (Ireland), 6-minute data also from Ireland, 10-minute data from France, the Netherlands and Germany,

and 15-minute data from the United Kingdom (the UK, with two letter country code UK). Typically, 1-minute data is deemed the highest-quality data to determine meteotsunami wave height and size-exceedance rates (e.g. Kim et al. 2016; Vilibić and Šepić 2017; Carvajal et al. 2017; Dusek et al. 2019). Tide gauges with 1-minute averaging intervals were available in all countries at some locations, but have not been used, partly because of the time it would take to process the 1-minute data manually (i.e. methods described in section 6.3.2 and section 6.3.3).

However, the data-averaging intervals should be short enough to identify meteotsunamis. In the US, 6-minute data has been used in climatologies to quantify size-exceedance rates and determine seasonal variability (Bechle et al. 2016; Olabarrieta et al. 2017; Dusek et al. 2019). Furthermore, a climatology of relatively high-frequency waves (3–5-h periods) was constructed in the UK using 15-minute averaging intervals (Oszoy et al. 2016). Therefore, we expected that 10-minute and 15-minute tide-gauge data could also be used to identify particularly large non-seismic sea-level oscillations at tsunami timescales (termed NSLOTTs for consistency with Vilibić and Šepić (2017)). However, wave heights from these 10-minute and 15-minute datasets will be aliased, and size-exceedance rates will likely be underestimated.

The tide gauges also covered different time periods. From the Copernicus download, data from Ireland, the UK and France were between Jan 2010 – Dec 2017, data from Belgium was between Jan 2010 – Dec 2016 and data from the Netherlands and Germany were between Oct 2014 – Dec 2017 (Table 6.2). Years of data that did not range from January to December were removed, eliminating bias towards any particular season in analysis of mesoscale weather systems. This policy meant that data between Oct 2014 – Dec 2014 was removed for the Netherlands and Germany. No corrections were made for missing data between January and December, but, overall, the tide gauges used here had a 92% median of complete data.

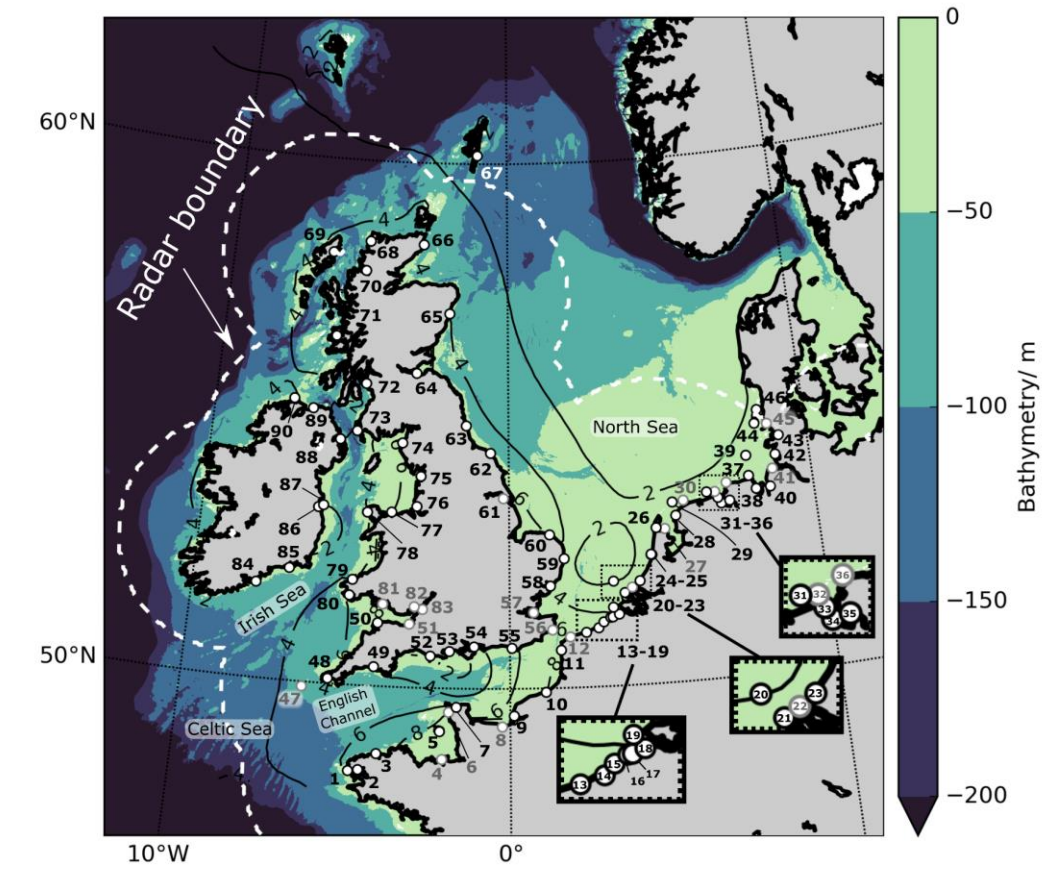

1. **Le Conquet (FR, 10)**
2. Brest (FR, 10)
3. Roscoff (FR, 10)
4. Saint Malo (FR, 10)
5. Jersey (UK, 15)
6. Dielette (FR, 10)
7. Cherbourg (FR, 10)
8. Ouistreham (FR, 10)
9. **Le Havre (FR, 10)**
10. **Dieppe (FR, 10)**
11. **Boulogne (FR,10)**
12. Calais (FR, 10)
13. **Dunkirk (FR, 10)**
14. Nieuwpoort (BE, 5)
15. **Ostend (BE, 5)**
16. **Blankenberge (BE, 5)**
17. Zeebrugge (BE, 5)
18. Cadzand (NL, 10)
19. Vlakte vd Raan (NL, 10)
20. Europlatform (NL, 10)
21. **Brouwershaven (NL, 10)**
22. Haringvliet (NL, 10)
23. Hoek van Holland (NL, 10)
24. IJmondstroompaal (NL, 10)
25. **IJmuiden (NL, 10)**
26. Den Helder (NL, 10)
27. Den Oever(buiten) (NL, 10)
28. Harlingen (NL, 10)
29. Terschelling (NL, 10)
30. Ballum (NL, 10)
31. Huibertgat (NL, 10)
32. Borkum (NL, 10)
33. Eemshaven (NL, 10)
34. Delfzijl (NL, 10)
35. Emden (DE, 10)
36. Norderney (DE, 10)
37. Wangerooge (DE, 10)
38. Willhelmshaven (DE, 10)
39. Helgoland (DE, 10)
40. Bremerhaven (DE, 10)
41. Cuxhaven (DE, 10)
42. Büsum (DE, 10)
43. **Husum (DE, 10)**
44. Hörnum (DE, 10)
45. Dagebüll (DE, 10)
46. List (DE, 10)
47. St. Mary's (UK, 15)
48. Newlyn (UK, 15)
49. Devonport (UK, 15)
50. Ilfracombe (UK, 15)
51. Hinkley Point (UK, 15)
52. Weymouth (UK, 15)
53. Bournemouth (UK, 15)
54. Portsmouth (UK, 15)
55. Newhaven (UK, 15)
56. Dover (UK, 15)
57. Sheerness (UK, 15)
58. Harwich (UK, 15)
59. Lowestoft (UK, 15)
60. Cromer (UK, 15)
61. Immingham (UK, 15)
62. Whitby Bay (UK, 15)
63. North Shields (UK, 15)
64. Leith (UK, 15)
65. Aberdeen (UK, 15)
66. Wick (UK, 15)
67. Lerwick (UK, 15)
68. **Kinlochbervie (UK, 15)**
69. Stornoway (UK, 15)
70. Ullapool (UK, 15)
71. Tobermory (UK, 15)
72. Millport (UK, 15)
73. Portpatrick (UK, 15)
74. Workington (UK, 15)
75. Heysham (UK, 15)
76. Liverpool (UK, 15)
77. Llandudno (UK, 15)
78. Holyhead (UK, 15)
79. Fishguard (UK, 15)
80. Milford Haven (UK, 15)
81. Mumbles (UK, 15)
82. Newport (UK, 15)
83. Avonmouth (UK, 15)
84. **Ballycotton (IE, 6)**
85. **Dunmore East (IE, 6)**
86. Dublin (IE, 5)
87. Howth Harbour (IE, 6)
88. Bangor (UK, 15)
89. Portrush (UK, 15)
90. **Malin Head (IE, 6)**

Figure 6.1 The study region GEBCO 2014 bathymetry in blue, filled contours from 0 m (light green) to 200 m (dark blue) below mean sea level. Shading saturates beyond 200 m below mean sea level. Tide gauges are shown as white dots, with corresponding numbers indicating locations in the tide gauge list. Only the tide gauges that were considered are shown. Black outlines and black lettering indicate that the tide gauge was used in further analysis, grey outlines and grey lettering indicate that the tide gauge was discounted. Bold names in the tide gauge list indicate tide gauges that measured a meteotsunami greater than 0.5 m. Two-letter country abbreviations and averaging interval (minutes) are included in brackets. Tide gauges 13–19, 20–23 and 31–36 are expanded for clarity in the bottom-right hand corner. Indicative tidal ranges were extracted from the POLCOMS North-East Atlantic model between 1–30 Sep 2008 and are shown as thin black lines, with ranges shown every 2 m with thin, black lettering.

The boundary of the European radar mosaic is shown as a white dashed line and is defined by the distance 200 km from the nearest radar in the radar networks owned by the meteorological services of the Republic of Ireland (Met Éireann), the UK (Met Office), France (MétéoFrance), Belgium (RMI), the Netherlands (KNMI) and Germany (DWD).

6.3.2 Isolating tsunami-like waves

First, any 120-minute high-pass filtered data that had a magnitude greater than four times the standard deviation of the residual was visually inspected. Upon visual inspection, data was removed if it included spikes, incorrect timings, missing-data replacement values, inappropriate absolute sea-level elevation or jumps in data.

After preliminary data cleaning, tidal components of the sea-level elevation and periods greater than 120 minutes were removed to isolate tsunami-period signals. The averaging intervals used here are 5–15 minutes and are unable to reliably show waves with periods less than 10–30 minutes nor properly represent wave heights with periods less than 50–150 minutes. As the sea-level elevation had already been low-pass filtered (due to long intervals), we applied a fourth-order, zero-phase, 120-minute high-pass Butterworth filter (Butterworth 1930) to retain signals with periods less than 120 minutes.

However, this filter did not remove all unwanted tidal noise. After high-pass filtering, there were repeating wavelets with wave heights on the order of tens of centimetres (peak to trough) with periods of about 90 minutes. These repeating wavelets were identified in the data from most tide gauges. Autocorrelation of the sea-level elevation time series showed that the wavelets repeated in 12 h 25 minute (i.e. semidiurnal) intervals, though this autocorrelation timescale varied by a few minutes over time and between stations. The wavelet amplitudes were also modulated over 28 days with the spring-neap cycle. The repeating wavelets could not be fully removed by first applying tidal harmonic analysis (U-tide in Python). Synthetic time series (M_2, M_4, M_6 and M_8 constituents) suggested that higher-frequency tidal components were damped, but not completely removed, by filtering and that these repeating wavelets were the superposition of these damped higher-frequency components.

Therefore, a stacking algorithm was designed to remove the mean repeating wavelet signal at 12-h 25-min intervals, leaving the non-repeating signal unaltered. Performing this algorithm on synthetic data with 4 tidal coefficients suggested that the stacking

algorithm could remove 94% of the tidal sea-level residual that was not removed by high-pass filtering. On the real data, the algorithm showed mixed success in suppressing wavelets, and in the worst cases did not suppress the wavelets at all during a spring-neap cycle. Therefore, peaks that were detected at the standard deviation of the signal, σ, multiplied by a factor of 6 (termed 6σ) were visually inspected. If the peak was part of the repeating wavelet cycle, it was removed. After this manual data processing, 71 out of the 90 tide gauges (79%) were accepted for further analysis (black outline and black text in Figure 6.1). Notably, all tide gauges in the Bristol Channel (station numbers 51, 81, 82 and 83) were removed, partly because of strong repeating wavelets that were not damped by the algorithm.

6.3.3 NSLOTT classification

A significant wave-event is distinguished from background noise by using an amplitude threshold. Here, an event passed the amplitude threshold if its wave height (peak to trough) was greater than 6σ. This 6σ-threshold meant that fewer than 1 in every 40 waves in a time series were further analysed in the UK, and fewer than 1 in 500 waves in Ireland. Across individual tide gauges, the largest detection within a 36-h interval was chosen to ensure that reflections from a single event were not repeatedly measured at the same location.

The 6σ-event dataset was then cross-referenced with seismic events. Two small seismic events, each 4.8 M_W, occurred in the North Sea during the study period but neither occurred on days with 6σ events. The methods and description of earthquake detection and analysis are outlined in Dziewoński et al. (1981) and Ekström et al. (2012). Therefore, the NSLOTT dataset only includes waves with a non-seismic origin.

After passing the amplitude threshold and confirmation of a non-seismic origin, individual events were then grouped into NSLOTT events if they were identified at two or more tide gauges within a 3-h interval (the event interval). This event interval was deemed appropriate because of the typical separation between tide gauges (about 10–100 km), shallow-water wave speeds in north-west Europe (about 25–100 km h^{-1}) and the time scales of mesoscale atmospheric systems (a few hours). There was no imposed maximum time limit for an NSLOTT event, meaning that the event interval controlled the number of NSLOTT events. A 3-h event interval meant that long chains

of events did not occur (by testing various event intervals, an unacceptable 4-day event occurred with 8-h event intervals), and also made determining an atmospheric source possible.

Thus, the conditions to determine an NSLOTT were 1) a wave height $\geq 6\sigma$ in the high-pass filtered sea-level elevation that 2) was non-seismic, and 3) was not a repeating wavelet from the tidal residual. Finally, an event was included in our dataset of NSLOTTs if it was detected at two or more tide gauges within 3 h. The largest measured wave height in an NSLOTT event was set as the NSLOTT wave height.

6.3.4 Meteotsunami classification

Amplitude threshold

An absolute wave-height threshold was then used to categorise possible meteotsunamis (e.g. Šepić et al. 2009; Šepić et al. 2012; Bechle et al. 2016). We used a 0.25-m threshold, which is between 0.2 m (Dusek et al. 2019) and 0.3 m (Bechle et al. 2016) used in the US on 6-minute data. Hereafter, an NSLOTT with an absolute wave-height threshold exceeding 0.25 m is called a high-amplitude NSLOTT.

From analysis on Belgian data, we suggest that because of aliasing effects on wave height, a 0.25-m threshold with 15-minute averaging intervals results in about the same number of events as a 0.3-m threshold with 5-minute averaging intervals. Exceeding this 0.25-m wave-height threshold was a necessary but not sufficient condition to classify an NSLOTT as a meteotsunami, which also required linking the event to an atmospheric weather system.

Identifying a coincident atmospheric system

To classify NSLOTTs as meteotsunamis, events needed to be linked to a corresponding precipitating atmospheric weather feature. Although meteotsunamis are created by moving atmospheric pressure gradients and wind stress on the water's surface, dense networks of pressure and wind sensors to identify possible meteotsunami-generating atmospheric features over the water are generally unavailable. As such, we resort to remotely-sensed data to identify possible meteotsunami-generating atmospheric features.

Specifically, weather radar can be used to remotely sense precipitation-sized particles in the atmosphere above the ocean surface. As these precipitating weather features are commonly associated with horizontal pressure gradients (e.g. Johnson 2001), such features can be associated with meteotsunamis (e.g. Wertman et al. 2014). Although not all atmospheric forcings that generate meteotsunamis are associated with precipitation (e.g. atmospheric gravity waves), we expected that a minority meteotsunamis would have been generated by non-precipitating forcings. This decision was justified by previous north-west European case studies and climatologies that all indicate precipitating weather features associated with high-frequency waves (e.g. de Jong and Battjes 2004; Haslett et al. 2009; Tappin et al. 2013; Frère et al. 2014; Oszoy et al. 2016; Sibley et al. 2016; Williams et al. 2019). We acknowledge that using weather radar means that we may miss meteotsunamis associated with non-precipitating weather features, but we assume this will result in a comparatively small number of missed meteotsunamis. Even by linking NSLOTTs to pressure and wind measurements, meteotsunamis may be missed if the atmospheric forcing decays before detection or is not measured by the station (Williams 2019a).

We used the radar mosaic across north-west Europe with 5-km grid spacing that is available from the Centre for Environmental Data Analysis at 15-minute intervals (pre-processed gifs), covering 69 out of 71 of the accepted tide gauges (Figure 6.1). Although outside of the radar boundary, Lerwick (station number 67) and List (station number 46) were close enough to the radar boundary to determine an atmospheric forcing in the North Sea. Radar data was processed through several steps at the Met Office before download (Met Office 2003; section 3a in Antonescu et al. 2013).

We decided to link a weather feature to an NSLOTT event if precipitation was over the basin at least 6 h before the first detection. This decision was based on the typical time scales of mesoscale convective systems (a few hours). If there was no precipitation over water, the NSLOTT was not classified as a meteotsunami, even if the wave height exceeded 0.25 m.

6.3.5 Classifying atmospheric weather systems

From radar-derived precipitation, meso-scale characteristics of atmospheric systems were catalogued. We classified the system motion into one of eight cardinal directions (e.g. north, north-east). This system motion was the overall motion of the entire

system, which is constituted of mean flow (cell motion) and propagation (e.g. new cells forming) (e.g. Markowski and Richardson 2011 p. 251). If possible, we classified the type of mesoscale atmospheric system. The classification of atmospheric systems was based on the system's morphology on radar (Figure 6.2).

We grouped mesoscale atmospheric systems into four classifications: isolated cells, quasi-linear systems, non-linear clusters and open-cellular convection (Figure 6.2). Isolated cells were discrete, small regions of precipitation, with precipitation rates exceeding 2 mm h^{-1}. Two types of isolated cells were seen. Most isolated cell morphologies were poorly organised cells (Figure 6.2a), but there was one example of more linearly-organised precipitation with cells that moved parallel to the line orientation (i.e. roll bands). This roll-band system was classified as isolated cells because of the cross-section of the system relative to its motion. Conversely, quasi-linear systems were more organised convective systems (Figure 6.2b). This category included broken lines, non-stratiform lines, stratiform lines, bow echoes, and frontal rain bands (e.g. Gallus et al. 2008; Cotton et al. 2011; Antonescu et al. 2013; Bechle et al. 2016). When cells were more poorly organised but were connected by regions of precipitation exceeding 2 mm h^{-1}, they were classified as non-linear clusters (Figure 6.2c). The final classification was open-cellular convection, or open cells (Figure 6.2d). Open-cellular convection was connected showery regions, with approximately hexagonal cells with clear centres (e.g. de Jong and Battjes 2004; Cotton et al. 2011). Though not a defining feature, open cells moved with a southwards or eastwards component and covered a large region (> 10,000 km^2), whereas isolated cells moved with a northwards component and covered a much smaller region (100–10,000 km^2) (cf. Figure 6.2a(ii) with Figure 6.2d(ii)).

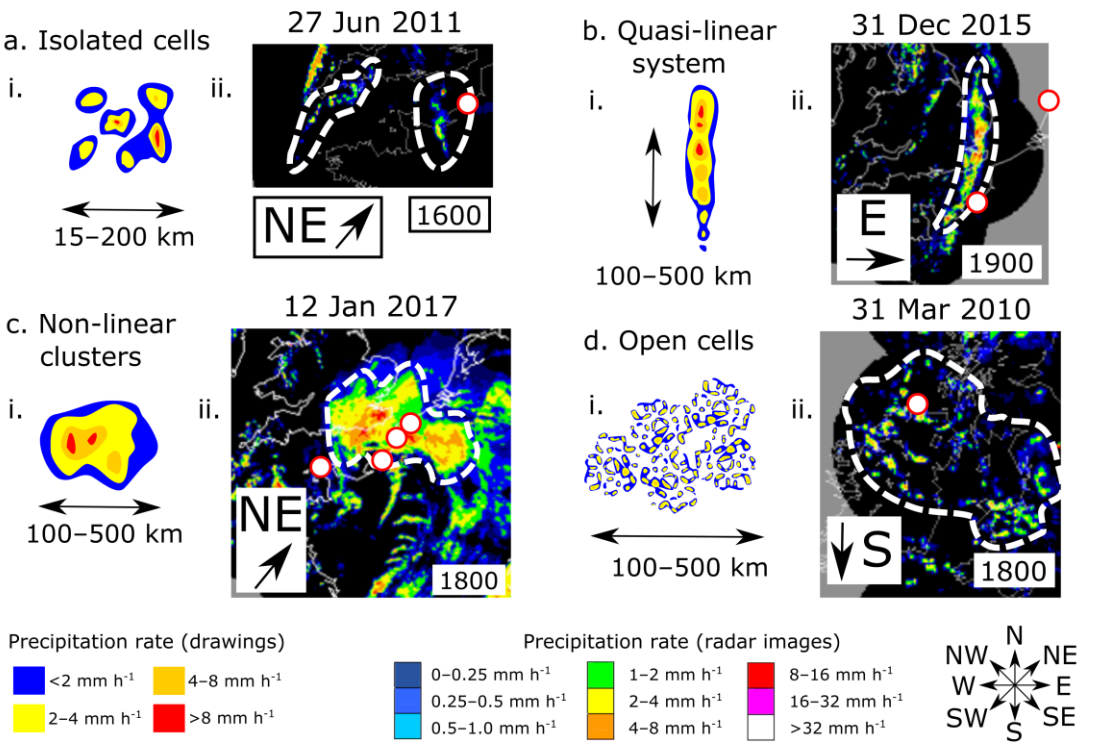

Figure 6.2 Classification scheme for atmospheric systems based on radar-derived precipitation and cardinal direction of overall system motion. a) isolated cells, b) quasi-linear systems, c) non-linear clusters, d) open cells. In each case, i) the general precipitation morphology used in classification with typical scale and simplified precipitation rate (drawings) and ii) an example of the morphology with the tide gauges that detected a meteotsunami (white dots with red outlines), date, time (UTC) and cardinal direction of motion with more detailed precipitation rates (radar images) copied from the National Meteorological Library and Archive, Fact sheet No. 15.

If there were multiple precipitating weather systems, those that occurred for longer times and were closer to the time and location of meteotsunami detection were favoured for classification. As there was uncertainty classifying the precipitating system morphologies, a confidence was assigned to each system classification. Classification confidence did not affect meteotsunami identification but if the wave occurred more than 6 h from the system and there were multiple systems in quick succession, or if the final system classification could have been in three or more categories, then the system type was ‘unclassified’. Confidently classified systems, which we further analyse, all occurred within 3 h of the meteotsunami and were firmly in one classification. Once the mesoscale systems were classified, the concurrent synoptic atmospheric environments for a subset of the most important mesoscale

systems were found from the ERA5 reanalysis dataset (Copernicus Climate Change Service 2017).

To summarise the methods, we classify an NSLOTT as a non-tidal wave with a 2–120-minute period and a wave height (peak to trough) that is at least 6 times greater than the standard deviation of the sea-level residual. The sea-level residual is the sea-level elevation with as much tidal signal suppressed as possible, through both 120-minute high-pass filtering and a stacking algorithm based on the autocorrelation timescale. An NSLOTT also had to have its signal identified at two or more tide gauges within 3 h. For the purposes of this climatology, a meteotsunami is an NSLOTT that had a minimum calculated 0.25-m wave height (i.e. a high-amplitude NSLOTT) and occurred within 6 h of a precipitating atmospheric system in the relevant basin. Atmospheric systems were then classified into one of four system morphologies, and only systems that were confidently classified are presented and used for synoptic composite analysis.

6.4 Results and discussion

After developing the meteotsunami and atmospheric system classification datasets, this section presents the typical meteotsunami size-exceedance rates (section 6.4.1), when meteotsunamis occurred (section 6.4.2), which mesoscale atmospheric systems were coincident with meteotsunamis (section 6.4.3) and their associated synoptic scale atmospheric systems (section 6.4.4). Towards the end of each section, the results are discussed relative to other regions and how they relate to previous north-west European studies.

6.4.1 Size-exceedance rates

Although case studies and localised climatologies suggest that meteotsunamis are typically smaller than 1 m in north-west Europe, if a large meteotsunami occurs (e.g. > 1 m), there is currently no information as to how common this occurrence is across each country or the overall region. In this section, the NSLOTT identification rate, meteotsunami identification rate and meteotsunami size-exceedance rates are presented to provide such information.

A total of 13,080 initial detections exceeded the 6σ-threshold (Table 6.2). From these initial detections, 2,339 NSLOTTs were identified at two or more tide gauges within 3 h (18% of initial detections). Of these NSLOTTs, 378 had wave heights greater than 0.25 m (16% of NSLOTTs). From these high-amplitude NSLOTTs, 349 (92%) occurred within 6 h of precipitation across the relevant basin and were classed as meteotsunamis.

Across the entire study region, an average of 355 NSLOTTs per year and 54.0 meteotsunamis per year were identified (Table 6.2). The country with the highest rate of identified meteotsunamis was France (15.4 per year), followed by Ireland (13.3 per year), the Netherlands (10.7 per year), Belgium (5.9 per year) and Germany (4.7 per year). The country with the lowest rate of identified meteotsunamis was the UK (4.0 per year), with only 32 meteotsunami identifications, despite over half of all NSLOTT identifications. A larger reduction between NSLOTT count and meteotsunami count occurred after the 0.25-m amplitude threshold was applied in the UK than any other country. In contrast, 31% of NSLOTTs were identified in Ireland and France but had 66% of identified meteotsunamis. Therefore, the combined processing of sea-level elevation meant that, overall, NSLOTTs occurred 6.6 times more frequently than meteotsunamis, and locations with the most identified NSLOTTs (the UK) did not necessarily have the most identified meteotsunamis (Ireland and France).

Table 6.2 Results of NSLOTT identifications grouped across countries, with the study period, number of tide gauges analysed and the interval of those tide gauges. Percentages refer to the number of NSLOTTs that have passed through the thresholds to the total number of events measured at individual stations.

Location	IE	UK	FR	BE	ND	DE	Sum
Study period	2010–2017	2010–2017	2010–2017	2010–2016	2015–2017	2015–2017	n/a
Tide gauges	5	32	8	4	13	9	71
Data interval/ min	5–6	15	10	5	10	10	5–15
Events ≥ 6σ (total)	1401	6602	2589	814	847	782	13,080
6σ-events at two or more tide gauges within 3 h (NSLOTTs)	196 (14%)	1219 (18%)	471 (18%)	170 (21%)	158 (19%)	125 (16%)	2339 (18%)
NSLOTTs per year	24.5	153	58.9	24.3	52.7	41.7	355
NSLOTTs exceeding 0.25 m (total)	116 (8.3%)	32 (0.5%)	140 (5.4%)	42 (5.2%)	33 (3.9%)	15 (1.9%)	378 (2.9%)
High-amplitude NSLOTTs with precipitation within 6 h (Meteotsunamis)	106 (7.6%)	32 (0.5%)	124 (4.8%)	41 (5.0%)	32 (3.8%)	14 (1.8%)	349 (2.7%)
Meteotsunamis per year	13.3	4.0	15.4	5.9	10.7	4.7	54.0

Although large (> 1 m) meteotsunamis occurred four times during the study period, most detected meteotsunamis were small. The median meteotsunami wave height was between 0.27–0.40 m between each country. Of 349 meteotsunamis, 213 were larger than 0.3 m (61%) and only 72 were larger than 0.5 m (21%) (Figure 6.3). Meteotsunamis larger than 0.5 m were mainly identified in France (51%) and Ireland (36%) and were only detected at 14 out of 71 tide gauges (bold location names in Figure 6.1). Of the four meteotsunamis that were larger than 1 m, one was identified at Dunmore East (station number 86) and three were identified at Le Havre (station number 9). Summarising, the largest meteotsunamis were identified in France and Ireland consistently and, specifically, the Le Havre (station number 9) tide gauge had the largest identified meteotsunamis.

Countries with smaller intervals (5–6 minutes) had lower annual size-exceedance rates for smaller thresholds than countries with larger intervals (Figure 6.3). In other words, smaller NSLOTTs were detected less often with smaller intervals. For example, Belgium and Ireland, with the smallest intervals (5–6 minutes), 24–25 NSLOTTs exceeding 0.1 m were identified each year (Figure 6.3). Next, in Germany, the Netherlands and France with larger intervals (10 minutes), 32–56 NSLOTTs

exceeding 0.1 m were identified each year. Finally, the UK with the largest interval (15 minutes), 61 NSLOTTs exceeding 0.1 m were identified each year. Interestingly, in the UK only 4 NSLOTTs exceeding 0.25 m were identified each year, the fewest of any country.

Wave-height aliasing likely meant that NSLOTTs exceeding 0.1 m were identified more frequently with longer intervals. This increase in small NSLOTT identifications occurred because aliasing had two effects. First, the 6σ thresholds were lower with longer intervals than with shorter intervals, implying that more, smaller NSLOTTs were identified at tide gauges with longer intervals. Second, because wave heights were aliased, fewer large waves were identified that met the 0.25-m minimum NSLOTT wave height. In locations with shorter intervals, larger waves were more frequently identified as the NSLOTT wave height, even though there were other smaller detections.

Although the UK had smaller meteotsunamis identified than elsewhere (0.27-m median wave height), these meteotsunamis may have been larger but were reduced the 15-min averaging period. The largest meteotsunamis in the UK were measured at Lowestoft (station number 59 in Figure 6.1), north Scotland (station numbers 67–70) and along the south coast (station numbers 48, 49, 52 and 55), of which Lerwick (station number 67) and the south coast have historically experienced meteotsunamis and seiching (e.g. Sibley et al. 2016; Pugh et al. 2019 in prep.).

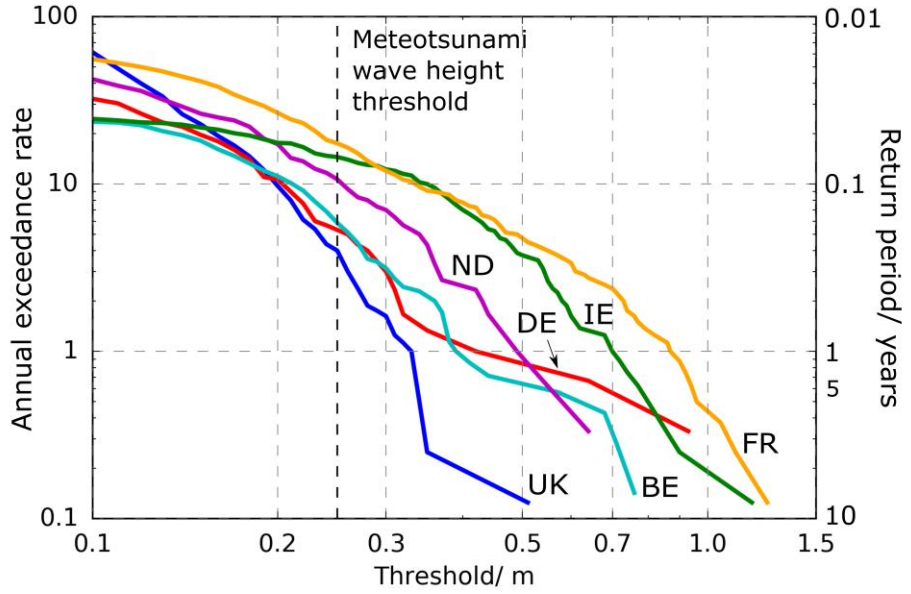

Figure 6.3 NSLOTT annual size-exceedance rate for thresholds between 0.1–1.5 m from tide gauges grouped across each country. IE – green, UK – blue, FR – orange, BE – cyan, ND – purple, DE – red. Dashed black vertical line is at 0.25 m, which is the meteotsunami wave-height threshold. Return period in years is shown on the right-hand vertical axis. A return period of *n* years indicates that on average, one NSLOTT exceeds the threshold every *n* years.

The effect of wave-height aliasing was less obvious in Ireland, the largest 6σ-thresholds and most NSLOTTs exceeding 0.25 m were identified with these tide gauges compared to the total number of NSLOTTs (116 out of 196). Interestingly, more detections were filtered out here than elsewhere when applying the event interval. Only 14% of 6σ events were identified at two or more tide gauges within 3 h (Table 6.2). This relatively low conversion rate occurred because there were only five tide gauges that were spread across three different coastlines. For example, although three waves greater than 1-m were detected at Malin Head (station number 90), none of these waves were detected at the other Irish tide gauges within this analysis. In contrast, 21% of 6σ-events in Belgium passed the event interval (Table 6.2). This higher conversion rate was probably because the four Belgian stations only spanned 40 km of coastline, all of which bordered the North Sea. Therefore, sparser measurements also reduced the number of detected meteotsunamis.

Of the identified meteotsunamis, the median and maximum wave heights were similar to those found in the Great Lakes (Bechle et al. 2015; Bechle et al. 2016), the US East Coastline (Dusek et al. 2019), the Gulf of Mexico (Olabarrieta et al. 2017) and most of the Mediterranean (Šepić et al. 2015b). These regions have median wave heights of about 0.4 m and waves that rarely exceed 1 m (e.g. Olabarrieta et al. 2017; Dusek et al. 2019). Interestingly, we identified about a tenth as many small meteotsunamis (0.25–0.3 m) as the Great Lakes, but a similar number of large meteotsunamis (0.5–1 m) (Bechle et al. 2016). We probably identified fewer small meteotsunamis because we applied stricter amplitude thresholds and event intervals than applied in the Great Lakes (Table 6.1). However, a similar number of large meteotsunamis indicates a similar (if not directly comparable) meteotsunami wave-height climate in north-west Europe and the US basins. No meteotsunamis larger than 3 m were identified, such as those that have occurred in Japan (Hibiya and Kajiura 1982; Asano et al. 2012) and the Mediterranean (Orlić et al. 2010; Bubalo et al. 2019) from further seiching.

Although meteotsunamis in north-west Europe are about the same height as elsewhere, there are only a few reported events of flooding in the media (e.g. 27 June 2011 in the UK, 29 May 2017 in the Netherlands). Meteotsunamis may not be as hazardous in this region as elsewhere, because the typical tidal ranges (peak to trough) are about 3–8 m (Figure 6.1), which is an order of magnitude larger than the median meteotsunami wave height (0.27–0.4 m). Similarly, small meteotsunamis in relatively large tidal ranges have been reported in British Columbia (Thomson et al. 2009) and across the globe (Vilibić and Šepić 2017). Although meteotsunami wave heights may be an order of magnitude smaller than tides, meteotsunami currents may still be dangerous. Overall, meteotsunami-related flooding rarely happens in north-west Europe because meteotsunamis are typically much smaller than the tidal range, although the currents associated with meteotsunamis may still pose a hazard.

Finally, although the reduction of size-exceedance rates may be progressively larger with longer intervals, relative comparisons between countries are possible. In this dataset, we can directly compare countries with the same interval. This means that more and larger meteotsunamis were detected in France than in Germany and the Netherlands. Furthermore, we can also deduce that because larger meteotsunamis were identified more frequently France with longer averaging intervals (10 mins) than Ireland with shorter averaging intervals (5 mins and 6 mins), then more meteotsunamis

probably occurred in France than Ireland. Also, in France (10 mins), Ireland (5 and 6 mins), the Netherlands (10 mins) and Germany (10 mins), large meteotsunamis were detected more frequently than in Belgium (5 mins), meaning that fewer meteotsunamis probably occurred in Belgium than these other countries. However, it is unknown how the rate of meteotsunami occurrence in the UK compares to the other countries. Because the 15-minute averaging interval appears to be too long to properly identify NSLOTT wave heights (only 0.5% of NSLOTTs passed the 0.25-m amplitude threshold), it is possible that more meteotsunamis could have been detected in the UK than other countries if there were shorter averaging intervals in the UK.

6.4.2 Seasonal and diurnal variation

The seasonal and diurnal variation analyses show when meteotsunamis occur. This information is useful because meteotsunami identifications can be cross-referenced with times that people go to the beach and when ports are in use. These analyses allow us to relate the hazard that meteotsunami risk poses to exposure.

Across every country, more meteotsunamis were identified in winter than any other season (Figure 6.4). In Ireland and the UK, about 59% of all meteotsunamis were identified in winter, and about 45% occurred in December and January. In France, Belgium, the Netherlands and Germany most meteotsunamis also occurred in winter (43–46% of all meteotsunamis).

Every country apart from the UK had an annual cycle with a single winter-time peak and the fewest meteotsunamis in either spring or summer (Figure 6.4). The season with fewest meteotsunamis was between 0–15% of each country's total meteotsunami count. In contrast, the UK showed an annual cycle with a secondary summer-time peak. Even though only 32 meteotsunamis were recorded in the UK, summer-time meteotsunamis were identified in 5 out of 8 years.

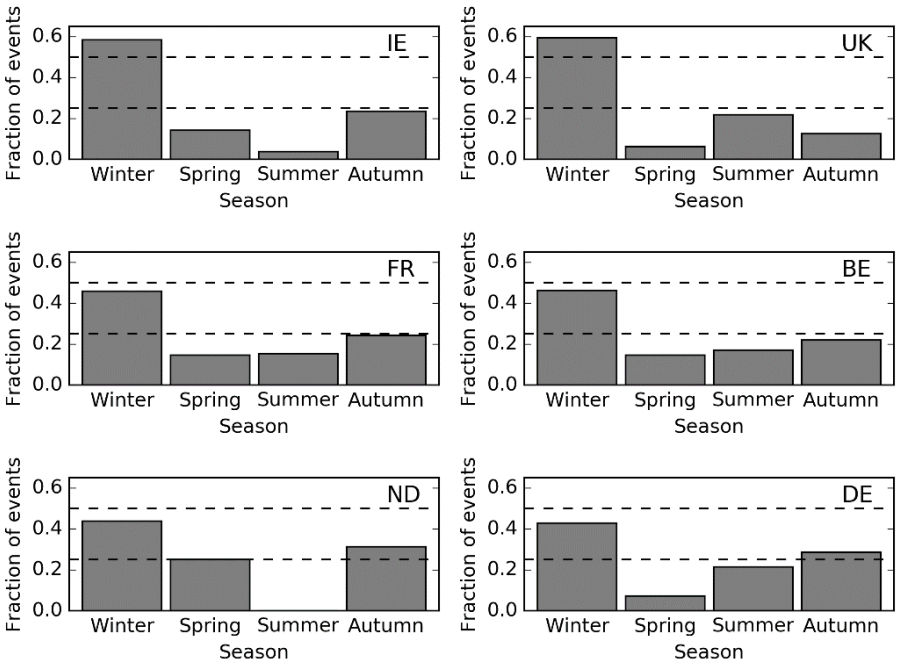

Figure 6.4 Seasonal variation of meteotsunamis across: a) Republic of Ireland (IE), b) the United Kingdom (UK), c) France (FR), d) Belgium (BE), e) the Netherlands (ND), f) Germany (DE). Thin dashed lines at 0.25 and 0.5 for reference. Winter is defined as DJF, Spring is MAM, Summer is JJA and Autumn is SON.

All detections related to high-amplitude NSLOTTs were then grouped by hour (e.g. 1400–1459 UTC) and month (e.g. Jan), allowing analysis of both seasonal and diurnal variation. In total, 1368 detections were analysed. Again, there was strong seasonal variation, with over 52% of detections occurring in winter and only 7% in summer (Figure 6.5). A higher winter-time maxima and lower summer-time minima were found by analysing all of the available detections than from analysing meteotsunamis as a single event with the largest wave height, because more tide gauges identified a 6σ-event per high-amplitude NSLOTT during winter than summer (e.g. in the UK, 4.3 stations per NSLOTT in winter and 3.2 stations per NSLOTT in summer). Thus, winter-time events were detected more frequently and by more tide gauges than summer-time events.

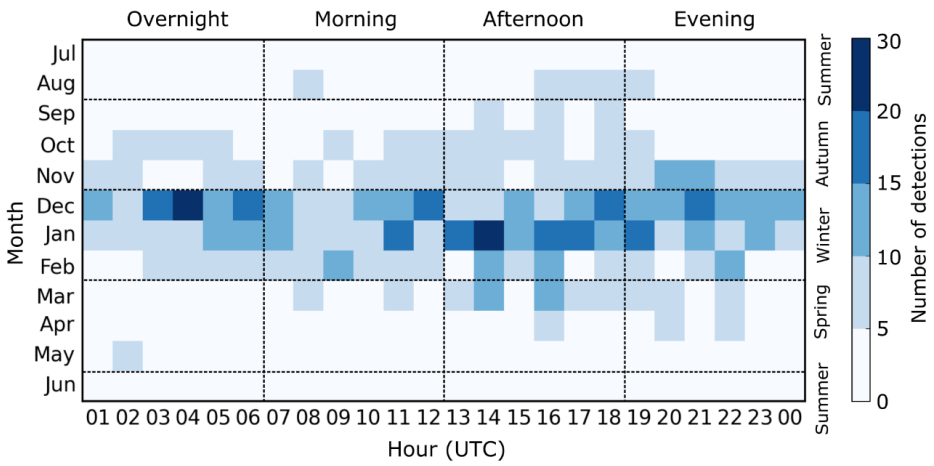

Figure 6.5 Seasonal and diurnal NSLOTT variation across all tide gauge stations. Number of detections are coloured according to the scale. Black dashed lines separate times of identification. Overnight was 0100–0659 UTC, morning is 0600–1159 UTC, afternoon is 1200–1859 UTC and evening is 1900–0059 UTC. Summer is JJA, Autumn is SON, Winter is DJF and Spring is MAM. Dashed lines and annotations were inserted in Inkscape.

Throughout the year, there was a weak diurnal cycle, with detections peaking in the afternoon (30%) and falling overnight (23%) (Figure 6.5). Most meteotsunamis occurred in winter, primarily in the afternoon (14% of all detections), although there was also a secondary winter-time peak overnight (12% of all detections). The diurnal cycle was about 5–6 times weaker than the seasonal cycle and was slightly variable throughout the year. For example, the overnight peak occurred in winter and autumn, but not spring or summer.

Although most meteotsunamis in north-west Europe occurred in autumn and winter, case studies over the 10 years have focussed on meteotsunamis from eye-witness reports in late spring (Sibley et al. 2016) and summer (Tappin et al. 2013; Frère et al. 2014). The first known occurrence of a fatal wave in the English Channel that was generated by a squall-line also occurred in summer (Douglas 1929). This study suggests that these case studies are not representative of the meteotsunami seasonality in north-west Europe. Other localised climatologies have suggested that winter-time waves are more frequent. In the Netherlands, over half of seiches in Rotterdam occurred in winter, and the fewest occurred in late spring and summer (de Jong and Battjes 2004). In the Solent (Southampton) and south coast of the UK, eight of the largest waves with 3–5-h periods were in autumn or winter (Oszoy et al. 2016). Our

results in Figure 6.4 and Figure 6.5 are consistent with the seasonality of these localised climatologies.

We suggest that this discrepancy in the seasonality between case studies and climatologies is not explained because meteotsunamis are larger in summer than winter. For example, in this study, in France the average meteotsunami was 0.47-m high in winter versus 0.38-m high in summer. Therefore, in combination with the increased frequency, meteotsunamis should be noticed more frequently in winter than summer. It may be that identifying a meteotsunami amongst other waves may be more difficult in the winter, when there are also larger wind waves (e.g. Woolf et al. 2002; Shi et al. 2019) and storm surges (e.g. Haigh et al. 2010). Furthermore, eyewitness reports may be biased towards the summer, because there are longer daylight hours and more people in coastal regions to make the observations.

One of the most noticeable results for a single country is that none of the 32 meteotsunamis in the Netherlands were detected in the summer (Figure 6.4). This result is unusual, given that in neighbouring countries, about 20% of meteotsunamis were identified summer. A lack of summer-time identifications in the Netherlands may have occurred because only three years of data were analysed. Nonetheless, these results are consistent with a 7-year climatology in Rotterdam (de Jong and Battjes 2004); summer-time meteotsunamis rarely occur in the Netherlands.

6.4.3 Analyses of coincident mesoscale weather systems

Finally, atmospheric conditions at the time of meteotsunami detections were examined to identify atmospheric phenomena that generated meteotsunamis. From 378 high-amplitude NSLOTTs, eight were not classifiable because of missing radar data (2%). Of the remaining 370 high-amplitude NSLOTTs, 349 (94%) occurred within 6 h of precipitation, compared to 21 (6%) that did not (Table 6.2). A lack of precipitation within this period meant that either these high-amplitude NSLOTTs were formed by atmospheric phenomena did not produce precipitation (e.g. ducted atmospheric gravity waves, non-precipitating fronts) or were formed by non-atmospheric phenomena (e.g. landslides).

Of the identified precipitating systems, only 254 out of 349 (73%, Table 6.2) were confidently classified into one of the four precipitation morphologies (outlined in Figure 6.2). Out of 138 high-amplitude NSLOTTs in Ireland and the UK, only 93 systems were confidently classified (67%), because most systems moved in from the west (109 out of 138, 79%), near the radar boundary edge (Figure 6.1). However, confidence was also low because in several cases, quasi-linear systems were often followed by open cells and it was difficult to determine which system generated the meteotsunami. Furthermore, confidence was low at Ballycotton (station number 84) and Dunmore East (station number 85) as some quasi-linear systems were slow-moving, with predominant motion of precipitation parallel to the line orientation. In these instances, it was unclear whether these generating systems were more similar to non-linear clusters (moving parallel to the line orientation) or quasi-linear systems (moving approximately perpendicular to the line orientation). The proportion of confidently classified systems generally increased southwards and eastwards (cf. Figure 6.1 and Figure 6.6c), as these coastlines were farther from the radar boundary.

Most of the confidently classified systems were quasi-linear systems (118, or 46%) or open cells (84, or 33%) (Figure 6.6a). Fewer classifications were non-linear clusters (44, or 17%) and isolated cells (10, or 4%). However, the variation within this average shows both seasonal and regional variation. The seasonal cycle of meteotsunamis was mostly a result of the seasonal pattern of quasi-linear systems and open cells (Figure 6.6b). Both quasi-linear systems and open cells followed an annual cycle, with most occurring in winter and fewest in summer, whereas the isolated cells and non-linear clusters varied around the annual average with no clear seasonal cycle (Figure 6.6b).

Though the number of quasi-linear systems followed an annual cycle, the proportion of quasi-linear systems was consistently between 41–56% (Figure 6.6b). In contrast, the proportion of open cells varied between 3–41%. This difference in proportionality was because the annual cycle of quasi-linear systems was slightly weaker than open-cells, but also because non-linear clusters counterbalanced that there were fewer open cells in spring and summer.

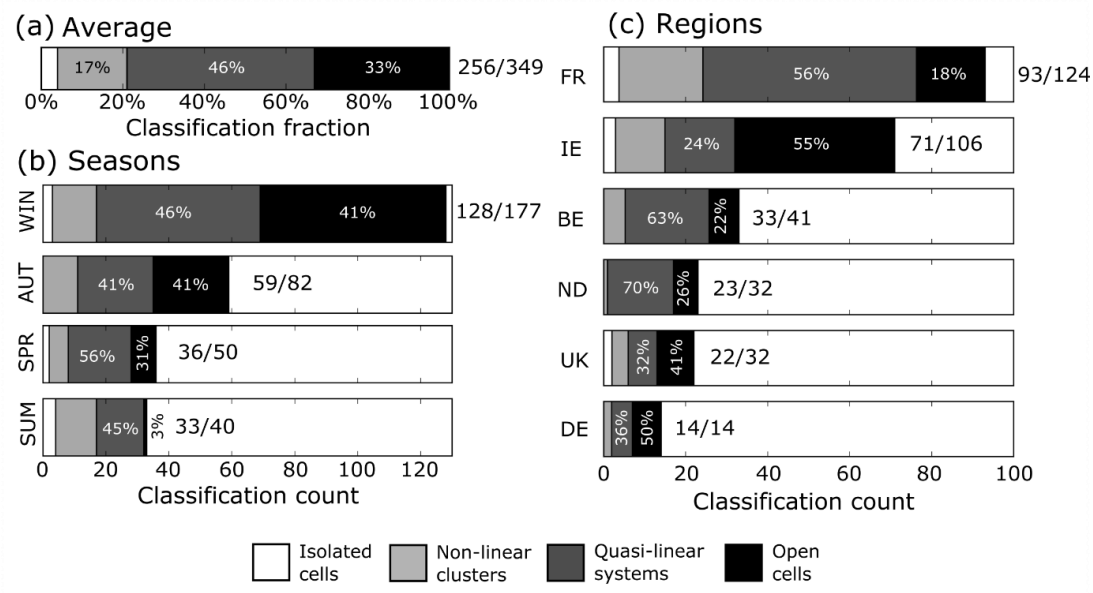

Figure 6.6 Fraction and count of classified events for isolated cells (white bars on left), non-linear clusters (light grey), quasi-linear systems (dark grey) and open cells (black). Results are shown for (a) the average, (b) each season (WIN = winter (DJF), AUT = autumn (SON), SPR = spring (MAM) and SUM = summer (JJA)) and (c) each country. To the right of each bar, the number of classified systems is shown compared to the total number of meteotsunamis. Countries and seasons are ordered from most classifications at the top to fewest classifications at the bottom.

Regionally, locations with more meteotsunamis tended to have higher counts of every classification, but those with proportionally more winter-time meteotsunamis (e.g. Ireland and the UK) tended to have even more open-cell classifications (Figure 6.6c). Non-linear cluster identifications tended to increase with total number of meteotsunamis, remaining between 14–22% for every country apart from the Netherlands (only 4%). Quasi-linear system classifications also increased with larger totals, with the exception of Ireland, which had fewer quasi-linear classifications than Belgium. However, despite similar seasonal patterns between countries, there was surprisingly strong regional variation between open-cell classifications. Open-cell classifications were much higher in Ireland, the UK and Germany than France, Belgium and the Netherlands. Across individual countries, if the proportion of open cells was relatively low compared to average (< 33%), the proportion of quasi-linear systems was relatively high (> 46%) and vice versa.

These results support and extend the mesoscale analysis of de Jong et al. (2003) across north-west Europe, who originally showed that cold fronts, split cold fronts (here both quasi-linear systems) and open cells can generate seiching in the Netherlands. From the data provided here, when no other system moved over the water prior to open cells and multiple tide gauges detected a wave, open cells generated about 25% of meteotsunamis (84 out of 349). However, the mechanisms through which open cells generate meteotsunamis remains uncertain. Therefore, because the meteotsunami generation mechanisms are unclear, the evidence presented here (15-minute radar reflectivity) is not enough to distinguish whether systems with more linear systems (e.g. quasi-linear systems) tend to generate meteotsunamis more often than more circular systems (e.g. non-linear clusters).

More generally, the 5-km radar with 15-minute intervals and tide gauges with 5–15-minute intervals were too coarse to properly identify the specific feature of an atmospheric system that generated a meteotsunami in systems with multiple components (particularly with non-linear clusters and open cells). Notably, the 23 June 2016 meteotsunami in France was categorised as a non-linear cluster because a defined, linear precipitation band was not apparent on this radar. However, more detailed observations (radar with 1-km grid spacing and 5-minute output intervals) and modelling (using 1-minute interval surface pressure and 10-m wind speeds) showed that a smaller-scale quasi-linear system generated the meteotsunami (Williams et al. 2019). This one example indicates that the method presented here may under-estimate the number of meteotsunamis generated through more linearly organised cells on smaller scales. Thus, smaller quasi-linear systems may have been classified as non-linear clusters on the scales apparent here, even though our confidence criteria removed those systems that we were unsure of how to classify.

However, this analysis broadly agrees with those conducted in the Laurentian Great Lakes, which showed that less than 5% of meteotsunamis were generated by isolated cells (Bechle et al. 2015; Bechle et al. 2016). This may be partially explained by inefficient transfer of energy to the ocean by small, circular surface forcings even when moving at Proudman-resonant speeds (Williams 2019a). However, fewer meteotsunami may be formed by isolated cells because they also cover a smaller area than other systems and because they may have lower surface pressure gradients and wind stresses.

We suggest that using radar to classify meteotsunamis is about as successful as using *in situ* surface pressure and wind speed measurements. We linked 92% of NSLOTTs exceeding 0.25 m to atmospheric weather systems using the radar method. Comparably, in the Great Lakes, slightly fewer NSLOTTs were classified as meteotsunamis by linking waves with pressure and wind fluctuations measured at coastlines (87%) (Bechle et al. 2016). This comparably high identification rate validates the radar-only method for north-west Europe. As suggested by Bechle et al. (2016), radar classification may also be useful information for future operational meteotsunami forecasting, and given the results provided here, may be useful for up to 92% of meteotsunami events in north-west Europe.

6.4.4 Analyses of coincident synoptic environments

Next, we present the synoptic composite atmospheric analyses associated with meteotsunamis in this climatology. Synoptic-scale composite analyses are average atmospheric fields for a group of events with similar morphologies, seasonalities and locations, which allow understanding of the average thermodynamic and kinematic weather patterns associate with mesoscale phenomena that generate meteotsunamis (e.g. Šepić et al. 2015b; Vilibić and Šepić 2017). To generate these composites, we use the ERA5 (fifth-generation European Centre for Medium-Range Weather Forecasts (ECMWF) Reanalysis) because such reanalyses adequately represent the atmospheric synoptic environments at the time of meteotsunamis (e.g. Belušić et al. 2007; Tanaka 2010; Denamiel et al. 2019; Shi et al. 2019). The reanalyses were calculated and output on a 0.25° × 0.25° (20–30 km) horizontal grid, produced by the ECMWF Integrated Forecast System with assimilated observational data (Copernicus Climate Change Service 2017). Such reanalyses typically do not resolve surface pressure perturbations and wind stresses associated with mesoscale phenomena.

However, external resonance may be inferred from reanalysis fields. By using the tropospheric wind speed at a specified level that represents the translation speeds of mesoscale phenomena (e.g. 500 hPa or 700 hPa), external resonance may be inferred where the tropospheric wind speed and shallow-water wave speed match within a pre-defined threshold (e.g. Šepić et al. 2016). Therefore, we also show how the tropospheric wind speed compared to the shallow-water wave speed in the composites as an indicator of external resonance.

Here, we focus on the synoptic composite analyses for meteorological conditions favourable for meteotsunamis that affected the French coastline that we studied here. Most of these tide gauges border the English Channel (station numbers 1, 2, 3, 7, 9, 10 and 11), except for Dunkirk, which borders the North Sea (station number 13). The English Channel coastline of France was chosen for two reasons. First, a localised region was required in order to prevent the large variability in weather patterns that would exist should a larger region be chosen. Second, the large number of events and the variety of meteorological conditions during which meteotsunamis in this area occurred meant that we could investigate synoptic composite analyses associated with the most frequent (quasi-linear systems and open cells in winter), and most noticeable (quasi-linear systems in summer) mesoscale atmospheric systems along a contiguous coastline. Accordingly, this synoptic composite analysis included 10 events with winter-time open cells, 26 events with winter-time quasi-linear systems and 9 events with summer-time quasi-linear systems. We examined sea-level pressure, 500-hPa geopotential height, a measure of low-level static stability (temperature difference between 850 hPa and the sea surface), and a measure of deep-level moist instability (convective available potential energy, CAPE, which is calculated in ERA5 as the largest CAPE below 350 hPa) (Figure 6.7).

The 500-hPa geopotential height, which is at a height of 5–6 km in midlatitudes, can be used to interpret mid-tropospheric flow. At the 500-hPa level, the wind is in approximate gradient-wind balance, meaning that environmental flow is nearly parallel to lines of constant geopotential height with the lower heights to the left of the flow in the northern hemisphere.

Next, we show the difference between the 850-hPa air temperature (which is about 1.5 km above surface level and is insensitive to surface heating in the diurnal cycle) and the sea-surface temperature (e.g. de Jong and Battjes 2004). The 850-hPa air-temperature minus the sea surface temperature, ΔT_{SS}, is a measure of the static stability of the near-surface layer. If the magnitude of ΔT_{SS} is sufficiently large, this temperature difference suggests that the atmosphere is conditionally unstable ($-13°C < \Delta T_{SS} < -8°C$) or absolutely unstable ($\Delta T_{SS} < -13°C$) (e.g. Holroyd 1971).

The distribution of the percentage of events with convective available potential energy (CAPE) above 100 J kg $^{-1}$ is shown as an indicator of potential convection and vertical

motion. Higher percentages at a location mean that the model more frequently modelled CAPE above 100 J kg^{-1} at that grid cell. CAPE is a measure of moist instability that is necessary (but not sufficient) for deep moist convection (e.g. Markowski and Richardson 2011 pp. 32–34). Physically, CAPE is the energy that an air parcel gains by rising through the atmosphere from the level of free convection to the equilibrium level, and positive CAPE indicates that free convection could occur if an air parcel were lifted to its level of free convection. Larger values of CAPE occur with warm and moist low-level conditions near the surface and steep lapse rates.

The deepest composite low was associated with winter-time open cells (> 33 hPa below mean sea-level pressure) and was north of the UK, bringing westerly flow at mid-levels (Figure 6.7a(i)). The temperature difference between the air at 850-hPa level and the sea-surface (ΔT_{SS}) indicates that, on average, the mesoscale precipitating systems were associated with conditional instability in the lower troposphere over the English Channel and Irish Sea (i.e. $-13°C < \Delta T_{SS} < -8°C$) and instability over Celtic Sea (i.e. $\Delta T_{SS} < -13°C$). Particularly for winter-time open cells, the deep low-pressure systems brought cold, polar air (< 535 dam, Figure 6.7a(i)) over the relatively warm winter-time ocean, resulting in unstable lower-tropospheric air over Atlantic water. Coupled with the average westerly flow, this meant that unstable, cold air was advected eastwards over the English Channel towards France. Only moderate CAPE occurred (~ 100 J kg^{-1}) and was more often over ocean than land. For winter-time open cells, the CAPE distribution over the deep Atlantic water and the English Channel resulted from 8 out of the 10 open cell events (80%).

A slightly shallower composite low co-occurred with winter-time quasi-linear systems than open cells (> 25 hPa below mean sea-level pressure). This low was located further north-east, being the farthest low from the English Channel out of all synoptic composites. At mid-levels, there was north-westerly flow (Figure 6.7a(ii)). Compared to winter-time open cells, for winter-time quasi-linear systems the more northward, weaker low did not bring cold air as far south but there was still, on average, a broad region of conditional instability over the English Channel and instability over the Irish Sea and Atlantic Ocean. As with winter-time open cells, only moderate, discrete patches of CAPE occurred. These CAPE areas were more often over the water than land, and for winter-time quasi-linear systems the CAPE distribution resulted from 14 out of 26 events (54%).

In contrast to winter-time systems, the summer-time quasi-linear systems were associated with a relatively shallow low (8 hPa below mean sea-level pressure) that was closer to the English Channel, and there was south-westerly flow at mid-levels (Figure 6.7a(iii)). The average temperature fields showed that there was conditional instability in the lower troposphere across the north-west European continental shelf and Atlantic. The distribution of CAPE exceeding 100 J kg^{-1} shows that events were associated with widespread CAPE over land and the ocean in summer (Figure 6.7c(iii)). In the summer and over land, CAPE exceeding 100 J kg^{-1} were most often modelled over France and the Netherlands (Figure 6.7c(iii)). Over the Netherlands, the 40–50% summer-time maxima resulted from 6 out of 9 summer-time events that overlapped (Figure 6.7c(iii)). However, particularly high values of CAPE (exceeding 1000 J kg^{-1}) were only modelled in 5 out of 9 summer-time events over France and, for two of these events, fewer than 10 grid cells had CAPE exceeding 1000 J kg^{-1}. Thus, severe CAPE over land was commonly, but not always, coincident with summer-time meteotsunamis.

Although most CAPE occurred over land in the summer, there was always positive CAPE (> 0 J kg^{-1}) over the ocean. Most of this ocean CAPE was less than 100 J kg^{-1} but indicated that free convection was possible. The summer-time ocean distribution of CAPE exceeding 100 J kg^{-1} (Figure 6.7c(iii)) resulted from 8 out of 9 events overlapping. Therefore, whilst the highest values of CAPE occurred in summer over land (excluding the Mediterranean), moderate CAPE occurred more often over the ocean than land (89% compared to 67%).

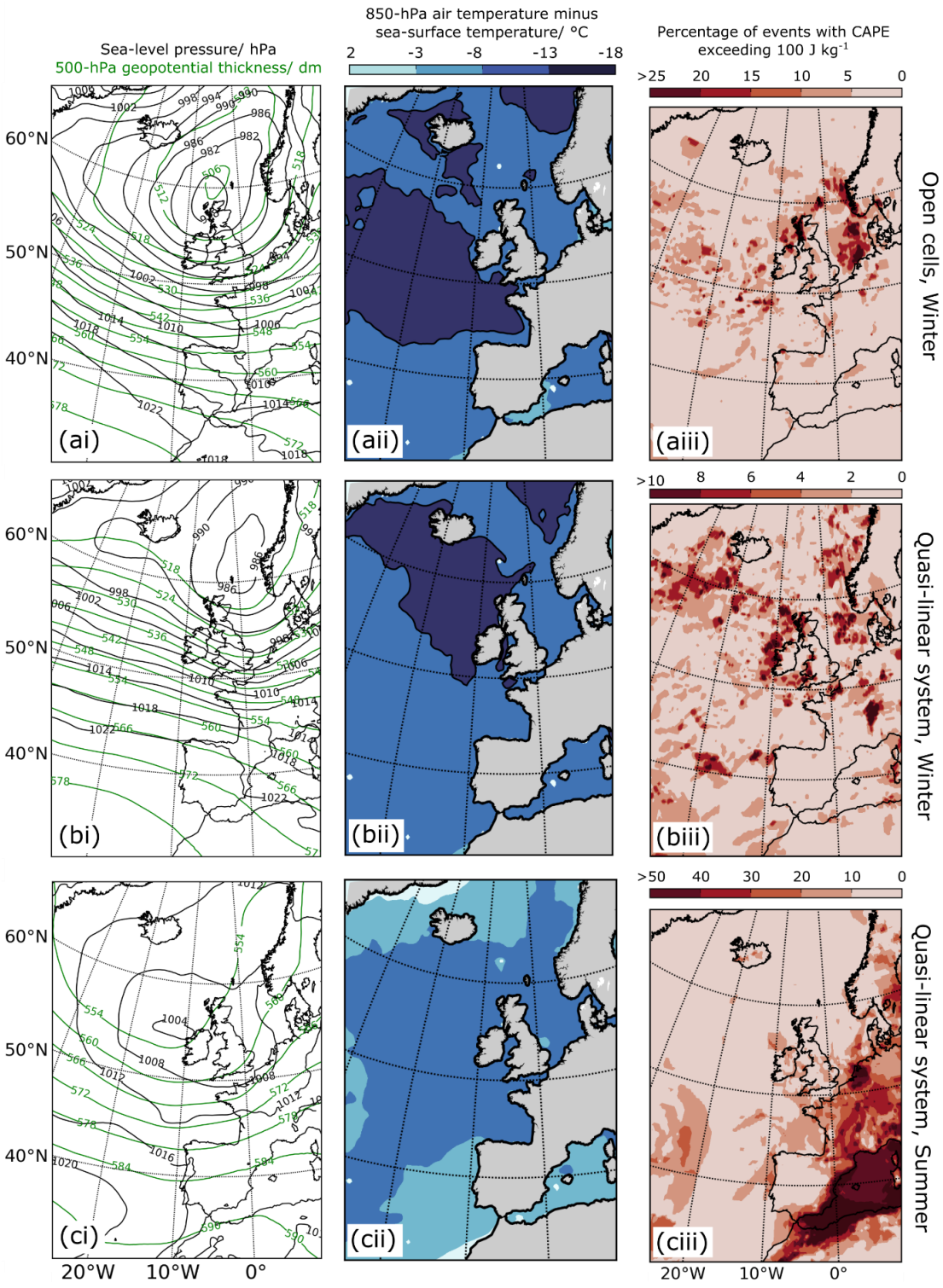

Figure 6.7 Synoptic composite analyses from 0.25° × 0.25° ERA5 reanalysis datasets, at the closest hour to meteotsunami detection for a) winter-time open cells (10 meteotsunamis), b) winter-time quasi-linear systems (26 meteotsunamis) and c) summer-time quasi linear systems (9 meteotsunamis). On the left, (i) shows the mean sea-level pressure (thin black lines) at 4-hPa spacing and 500-hPa height (thin green lines) at 6 dam spacing. In the middle, (ii) shows the mean of 850-hPa air temperature minus the sea-surface temperature (°C), with darker blues

indicating colder air compared to the sea-surface, and a black line contour at –13°C indicating instability. On the right, (iii) shows the percentage of events with convective available potential energy > 100 J kg^{-1}, note the scales for CAPE occurrence between a, b and c.

Finally, to indicate the occurrence of Proudman resonance, we estimated the Froude number (Fr), which is the speed of the mesoscale surface forcing divided by the meteotsunami wave speed, with an alternative, representative Froude number using environmental flow speed. Specifically, we calculated the ratio between the still-water, non-tidal shallow-water wave speed, c, ($\sqrt{gH}$, where g was 9.81 ms^{-2} and H was still water depth in Figure 6.1) and the environmental wind speed at 700 hPa, giving Fr_{700}. The 700-hPa level is about 3 km above ground level and may be better at characterising mesoscale system velocities than the 500-hPa level, for example, the environmental flow is closest to squall line speed at about 700 hPa (Markowski and Richardson 2011 p. 251). In locations where Fr_{700} was near 1, Proudman resonance could have been an external resonance mechanism. Because the surface system velocity and wave speed were approximated (environmental flow at 700-hPa is not equivalent to mesoscale system surface speed and we neglect tides), we equally weighted Fr_{700} between $0.8 \leq Fr_{700} \leq 1.2$. This equal weighting meant that up to 20% errors were not penalised. For locations that $0.8 \leq Fr_{700} \leq 1.2$, we assigned values of 1, and for locations that $Fr_{700} < 0.8$ or $Fr_{700} > 1.2$, we assigned a value of 0. These assigned values were then summed over all events, and divided by the total number of events, to produce a percentage distribution of events where $0.8 \leq Fr_{700} \leq 1.2$.

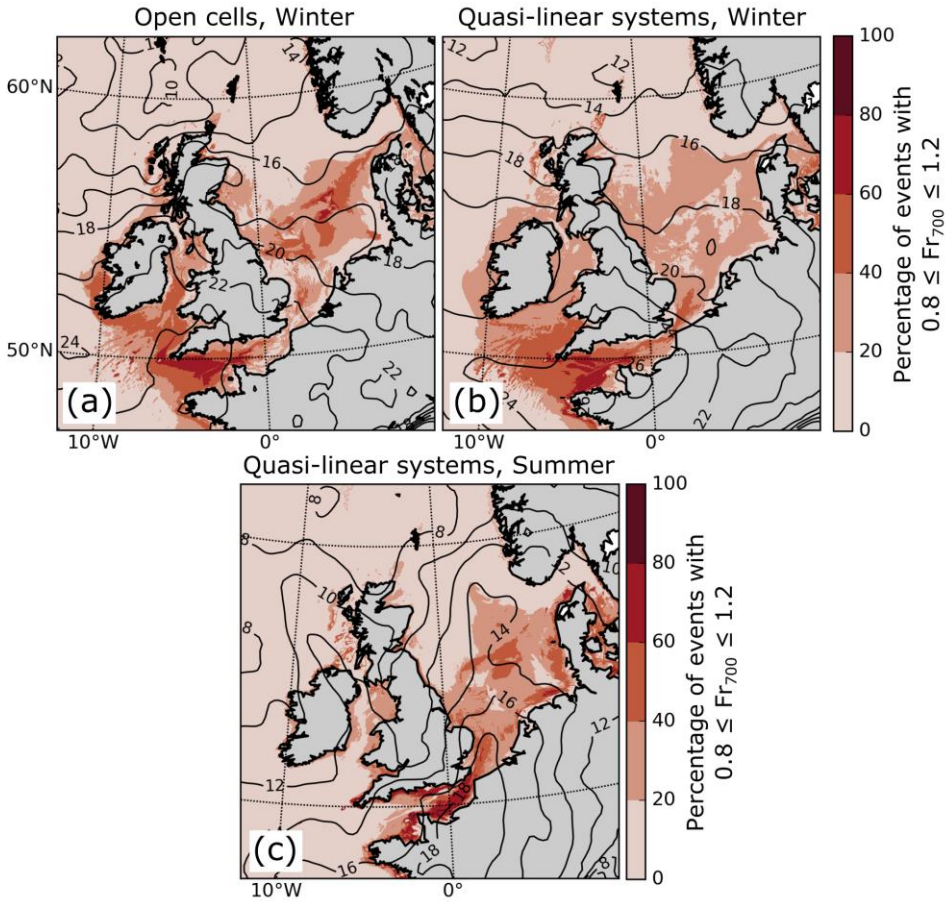

Figure 6.8 The distribution of percentage of events that $0.8 \leq Fr_{700} \leq 1.2$ for a) winter-time open cells, b) winter-time quasi-linear systems and c) summer-time quasi-linear systems that were measured in France. The average 700-hPa wind speed is shown with black contours (m s^{-1}).

Overall, Proudman-resonant conditions were fulfilled somewhere in the English Channel in 43 out of 45 events (96%). In the two other events, Proudman-resonant regions were in the Celtic Sea. Therefore, Fr_{700} fields indicated that Proudman resonance was a plausible external amplification mechanism in almost every meteotsunami in France. For each of the three synoptic composites (Figure 6.7), there was also at least one region in the English Channel that could have supported Proudman resonance in 60–80% of cases (Figure 6.8). For winter-time open cells and winter-time quasi-linear systems, this region was in the west of the English Channel ($22 \leq c \leq 31$ ms^{-1}) (Figure 6.8a and Figure 6.8b), whereas for summer-time quasi linear systems this was in the east of the English Channel ($c \leq 22$ ms^{-1}) (Figure 6.8c). This

eastward shift was primarily because the 700-hPa wind speeds were lower in summer-time events (Figure 6.8c) than winter-time events (Figure 6.8a and Figure 6.8b).

Across these events, the most frequent value of Fr_{700} in the English Channel (spanning 5°W–2°E, 48°N–51°N, and only accounting for Fr_{700} values less than 2) was 1.04 for winter-time quasi-linear systems, 0.99 for winter-time open cells and 0.71 for summer-time quasi-linear systems. When accounting for only the eastern side of the English Channel (2°W–2°E, 48°N–51°N), where most Proudman resonance occurred for summer-time quasi-linear systems (Figure 6.8c), the modal Fr_{700} increased to 0.87. Summer-time quasi-linear systems had a lower modal Fr_{700} than winter-time systems because a larger region of Fr_{700} was below 1 in the English Channel (cf. Figure 6.8a and Figure 6.8b with Figure 6.8c). Nonetheless, overall, the most frequent value of Fr_{700} was close to 1 over the English Channel.

Because the wind speed is not a perfect predictor of the speed of motion of the meteotsunami-generating mesoscale weather system, the sensitivity of the existence of Proudman-resonant regions in the English Channel to the wind speed at a chosen pressure level was examined. For comparison to other levels, the average 500-hPa wind speed was up to 5–10 ms^{-1} faster than the 700-hPa wind speed over the English Channel. This speed increase shifted the location of Proudman-resonant regions westward, towards deeper water in the Celtic Sea (not shown). Likewise, the average 850-hPa wind speed was up to 6 ms^{-1} slower over the English Channel, shifting Proudman-resonant regions eastward and towards coastlines. Although the resultant distribution of Fr_{700} changed depending on chosen pressure level (e.g. 500 hPa or 700 hPa), the result that a large region favourable for Proudman resonance frequently occurred was relatively insensitive to the chosen pressure level.

All synoptic environments indicate that the dominant synoptic weather feature at the time of meteotsunami detection were extra-tropical cyclones north or west of the UK. Although sea-level pressure lows were associated with all meteotsunamis, the associated extra-tropical cyclones were farther north and about 20 hPa deeper in winter than in summer. In each case, cyclones north of the English Channel favoured near-surface geostrophic flow from west to east (i.e. westerly flow). The 500-hPa height also shows this general flow pattern. The mean westerly lower- and middle-tropospheric winds were also supportive of eastward-moving mesoscale precipitation

systems. Of the 10 open cells, 8 (80%) moved eastward. Likewise, of the 26 winter-time quasi-linear systems, 11 (42%) moved eastward and 9 (35%) moved south-eastward. Finally, of the 9 summer-time quasi-linear systems, 4 (44%) moved north-eastward and 3 (33%) moved eastward. In 43 out of 45 instances, meteotsunamis were formed with Proudman-resonant regions across the English Channel. These Proudman-resonant regions were common between mesoscale systems, despite synoptic sea-level pressures lows with different magnitudes and locations.

Our results agree with previously documented synoptic environments and can be used to explain the seasonality of each mesoscale system. Open cells are typically generated from flows of cold polar air moving over relatively warmer water, which tends to occur in winter (e.g. Agee and Dowell 1974; Bakan and Schwarz 1992; de Jong et al. 2003; Vincent et al. 2012). Therefore, as open cells generated more meteotsunamis in winter (Figure 6.6b), this may simply happen because open-cellular convection also occurs most frequently in winter. Interestingly, the sea-level pressure fields, air temperatures and environmental flow patterns presented here are similar to those observed for other seiches (3–5 h periods) in the English Channel (Oszoy et al. 2016). The average 2-m air temperature was also less than 5°C during winter events and more than 15°C for summer events.

The weaker seasonal variation of meteotsunamis generated by quasi-linear systems was because the quasi-linear system classification included a wide range of precipitating systems that occurred throughout the year. An example of more winter-time quasi-linear systems were narrow cold frontal rain bands (e.g. Figure 6.2b), which occur more often when extra-tropical cyclones dominate to the north (e.g. Fairman et al. 2017). In the summer, quasi-linear systems can also be created from mesoscale convective systems (MCS) that become linearly organised (not shown here). These MCS also occur with extra-tropical cyclones, although more often in the warm sector, and are generated when moisture, instability and lift are present from warm, moist air moving northwards and undercutting drier air. This environment is sometimes known as a Spanish Plume (e.g. Carlson and Ludlam 1968; Morris 1986; Lewis and Gray 2010). The synoptic composites of summer-time quasi-linear systems have, high land CAPE over continental Europe, consistent with the Spanish Plume pattern. With a source of lift and moderately strong environmental vertical wind shear (~ 5 ms^{-1} km^{-1}), mesoscale convective systems can form and become more organised, leading to

summer-time quasi-linear systems (e.g. Markowski and Richardson 2011 pp. 201–213).

6.5 Conclusions

This study has produced a regional climatology of meteotsunamis across north-west Europe. Through a combination of manual filtering, automatic peak detection and a stacking algorithm designed to remove tidal signals, 13,080 events greater than a 6σ-threshold were identified across 71 tide gauges between 2010–2017. From these events, 2339 NSLOTTs were identified (occurring at two or more stations within 3 h) and 349 meteotsunamis were identified (high-amplitude NSLOTTs occurring within 6 h of a precipitating system), yielding 355 NSLOTTs per year or 54.0 meteotsunamis per year. From this meteotsunami dataset, the typical sizes and times of 349 meteotsunamis were extracted, the morphology of 256 mesoscale atmospheric systems that generated meteotsunamis were classified and 45 synoptic atmospheric composites were determined for a subset of meteotsunamis in France.

Although tide-gauge intervals were large (5–15 minutes) compared to the typical period of meteotsunamis (2–120 minutes), median wave heights were between 0.27–0.40 m for each country. The largest meteotsunamis in north-west Europe occurred most frequently in France and the Republic of Ireland. From all meteotsunamis, the three largest meteotsunamis (~ 1 m) were measured in Le Havre (10-minute intervals). Most meteotsunamis were small, with 79% smaller than 0.5-m high.

We recognise that relatively long intervals in tide gauges were used to study meteotsunamis compared to elsewhere. We suggest that, the 15-minute interval in the UK is too long to provide a representative meteotsunami wave-height climatology. However, this analysis does not answer what would be a sufficiently small interval. It is highly likely that smaller intervals would increase meteotsunami size-exceedance rates. It is also strongly recommended in future climatologies that smaller intervals from tide gauges are analysed, but considering the manual processing challenges faced here, 1-minute data may need automated methods with rigorously removed tidal signals.

Despite the large intervals used, we expect that the seasonal cycle extracted is valid, as there is no reason to expect seasonal bias in aliasing from tide gauge measurements.

Furthermore, all seasonal analyses from tide gauges tended to agree. In Ireland, France, Belgium, the Netherlands and Germany, there was a single annual cycle, with most meteotsunamis in winter (42–59%) and fewest in spring or summer (0–15%). There was also a diurnal cycle, with most between 1200–1859 UTC (30%) and fewest between 0000–0659 UTC (23%), although it was about 6 times weaker than the seasonal cycle.

To understand the which mesoscale weather phenomena were associated with the meteotsunamis, the north-west European radar mosaic with derived precipitation was used to identify and classify mesoscale atmospheric weather systems occurring within 6 h of each meteotsunami. A mesoscale precipitating feature was identified in 349 out of 378 (92%) large NSLOTT events. This fraction of events identified to occur with a coincident precipitating atmospheric phenomenon is slightly higher than using *in situ* surface pressure and 10-m wind speeds across the Great Lakes (87%). We suggest that this relatively high conversion rate validates the radar-only method of atmospheric generation for meteotsunamis in north-west Europe. From the 256 classified precipitating mesoscale phenomena, most were quasi-linear systems (46%) or open cells (33%), with some non-linear clusters (17%) and very few isolated cells (4%) (Figure 6.2, Figure 6.6). Most quasi-linear systems and open cells occurred in the winter and fewest occurred in summer, whereas non-linear clusters and isolated cells had no clear seasonal cycle. Open cell classifications were dominant in Ireland and the UK, whereas quasi-linear systems were dominant along the French, Belgian, Dutch and German coastlines.

To further analyse the conditions where mesoscale atmospheric phenomena formed, we analysed the synoptic atmospheric composites using output from the ERA5 reanalysis. These synoptic composites were focussed on the French coastline, with data between 2010–2017 from seven tide gauges bordering the English Channel and one tide gauge bordering the North Sea. The synoptic composites showed that the winter-time open cells and winter-time quasi-linear systems were formed with deep pressure lows (< 990 hPa) north and west of the UK, westerly mid-level flow and lower-tropospheric instability over the English Channel and Celtic Sea. On the other hand, summer-time quasi-linear systems were formed with shallow pressure lows (1004 hPa), south-westerly mid-level flow and CAPE regularly exceeding 100 J kg^{-1} over the Bay of Biscay and English Channel and 1000 J kg^{-1} over France and the

Netherlands. The synoptic composites that are presented here are well documented to produce winter-time open cells, winter-time quasi-linear systems and summer-time quasi-linear systems. Notably, 43 out of 45 analysed meteotsunamis from the French coast of the English Channel were coincident with a region that the ratio between the wind speed at 700 hPa and shallow-water wave speed without tides was between 0.8–1.2. From this result, we infer that Proudman resonance is a plausible explanation for most of the meteotsunamis along the French coastline, and possibly across north-west Europe.

To conclude, we detected 349 meteotsunamis, with an average rate of 54.0 per year, which is similar to the Great Lakes, Gulf of Mexico, US east coastline and parts of the Mediterranean. However, at least four factors identified in this study may combine to mean that meteotsunamis are not typically considered common in the region, at least from eye-witness accounts. In short, the detected meteotsunamis in north-west Europe were: frequently small (only 21% of meteotsunamis were larger than 0.5 m), occurred in basins with tides an order of magnitude larger than their wave height (0.27–0.4 m median wave height compared to 3–8 m tidal range), mostly occurred in winter (48–52%) and within a few hours of precipitating systems (92%).

Acknowledgements David Williams is funded by the National Environmental Research Council's Understanding the Earth, Atmosphere and Ocean Doctoral Training Programme, Grant NE/L002469/1. Atmospheric data was accessed from the Centre for Environmental Data Analysis (which collated data from Met Éireann, the Met Office, Météo France, the Royal Meteorological Institute of Belgium, the Royal Netherlands Meteorological Institute and Deutscher Wetterdienst). Oceanographic tide gauge data was accessed from the Marine Institute, the British Oceanographic Data Centre, and the Copernicus Marine Environment Monitoring Service (which collated data from the Naval Hydrographic and Oceanographic Service, the Belgian Marine Data Centre, the National Oceanographic Data Centre for the Netherlands and the German Oceanographic Data Centre).

Chapter 7

How open-cellular convection generates meteotsunamis

7.0 Preamble

Study Motivation

From the climatology in Chapter 6, a surprising result emerged—about a quarter of meteotsunamis in north-west Europe (84 out of 349) were associated with open-cellular convection. Although de Jong and Battjes (2004) proposed a generation mechanism for seiches in the Port of Rotterdam through open cells, this climatology showed that open-cellular convection frequently generates meteotsunamis across the north-west European continental shelf. This chapter provides a new explanation for how open-cellular convection may generate meteotsunamis.

Publication and Author Contribution

The work in this chapter has been produced for a Letters-style publication.

David A Williams wrote the publication, developed the modelling tools and completed the numerical simulations. Kevin J Horsburgh was the primary supervisor for the project, secured funding and provided editorial critique. David M Schultz provided editorial critique and was involved in discussion of ideas.

7.1 Paper Abstract

Meteotsunamis are potentially dangerous tsunami-like waves generated by mesoscale atmospheric systems. Open-cellular convection in the atmosphere (open cells) can generate meteotsunamis in north-west Europe. However, given that isolated cells do not tend to generate meteotsunamis, even though they appear to have similar cell diameters, sea-level pressure perturbations and 10-m wind speeds to open cells, the mechanism through which open cells generate meteotsunamis has been unclear. Numerical simulations show that a collection of sea-level pressure perturbations (individual cells) with rectangular symmetry (rectangular cells), amplified meteotsunamis by 2.0-times more than an otherwise identical, single individual cell with rectangular symmetry (isolated cell). Hexagonal cells, which had a more realistic arrangement of individual cells than rectangular cells, also amplified meteotsunamis by 1.4-times more than the isolated cell. Repetition of individual cells in the cross-propagation direction was twice as important as repetition in the along-propagation direction for wave amplification, although these repetitions were necessary for long wave crests and wave trains respectively. Alternating rectangular cells and gaps (double-spaced rectangular cells) produced meteotsunamis with the same amplification as isolated cells, showing that denser individual cells are necessary for wave amplification. A new explanation of how open-cellular convection generates meteotsunamis was developed: each individual cell produces an individual wave, and these individual waves constructively interfere, producing a meteotsunami that is a superposition of these individual waves.

7.2 Introduction

Meteotsunamis are potentially dangerous, shallow-water waves generated by atmospheric sea-level pressure gradients and surface wind stresses, with wave periods appropriate for a tsunami classification. Atmospheric phenomena that tend to generate meteotsunamis are in the mesoscale, being tens to hundreds of kilometres across and lasting a few hours (e.g. Hibiya and Kajiura 1982; Monserrat et al. 2006; Šepić et al. 2015a; Bechle et al. 2016; Olabarrieta et al. 2017), which are sometimes embedded within extra-tropical cyclones (e.g. Bechle et al. 2016) or tropical cyclones (e.g. Olabarrieta et al. 2017). Identified mesoscale atmospheric forcings that generate meteotsunamis include fronts (Hibiya and Kajiura 1982; Bechle et al. 2016), atmospheric gravity waves (Orlić 1980; Šepić et al. 2015a; Ličer et al. 2017), and various mesoscale convective systems. These mesoscale convective systems include non-linear clusters, squall lines and bow echoes (e.g. Bechle et al. 2016; Olabarrieta et al. 2017; Dusek et al. 2019).

Of the common mesoscale convective systems morphologies, such as non-linear clusters, squall lines, bow echoes and isolated cells (e.g. Gallus et al. 2008), isolated cells do not tend to generate meteotsunamis. In fact, isolated cells only generate about 5% of meteotsunamis in north-west Europe (Williams 2019b) and the Great Lakes (Bechle et al. 2016). A rare example of isolated cells that generated a 0.3-m high meteotsunami in the United Kingdom is shown in Figure 7.1a. Isolated cells are a collection of individually precipitating convective cells that have no (or weak) dynamic interactions (hence *isolated*), which have cell diameters on the order of 10 km (Figure 7.1a(ii)), sea-level pressure perturbations on the order of 1 hPa and 10-m wind speeds of about 10 m s^{-1} (where the surface wind stress is proportional to the square of 10-m wind speed). Isolated cells are formed when there is sufficient low-level moisture, a source of lift, and tropospheric instability, which together allow free convection to occur. Isolated cells sometimes originate from warm, moist air lower tropospheric air masses that may individually cover relatively small surface areas (10^2–10^3 km^2). When these lower tropospheric conditions are combined with low vertical shear in the environmental wind, isolated cells remain relatively poorly organised (at least compared to squall lines or bow echoes).

However, another collection of individual cells that have seemingly similar cell diameters, sea-level pressure perturbations, and 10-m wind speeds to isolated cells do generate meteotsunamis. This other collection of individual cells is called open-cellular convection (or open cells). Open cells were associated with about 25% (84 out of 349) of meteotsunamis across north-west Europe (Williams 2019b) and have repeatedly produced seiches in Rotterdam (de Jong et al. 2003). Open cells are a collection of hexagonally-arranged cells that have diameters on the order of 10 km (Figure 7.1b), 10-m wind speeds less than 10 m s^{-1}, and sea-level pressure perturbations of about 1 hPa. They are *open* cells because they form with clouds and precipitation in the cell walls (updrafts) and cloud-free cell centres (downdrafts) (Figure 7.1b). Open cells are also formed with low vertical shear in the environmental wind, but with strong surface heat fluxes covering much larger surface areas (10^4–10^5 km^2) than isolated cells (e.g. Agee and Dowell 1974; Bakan and Schwarz 1992; de Jong and Battjes 2004; Vincent et al. 2012) and is akin to Rayleigh–Bénard convection (Rayleigh 1916) with warming on the bottom boundary. For this reason, open cells are

typically formed in the winter, in the air behind cold fronts, and over relatively warm water (e.g. Figure 7.1b).

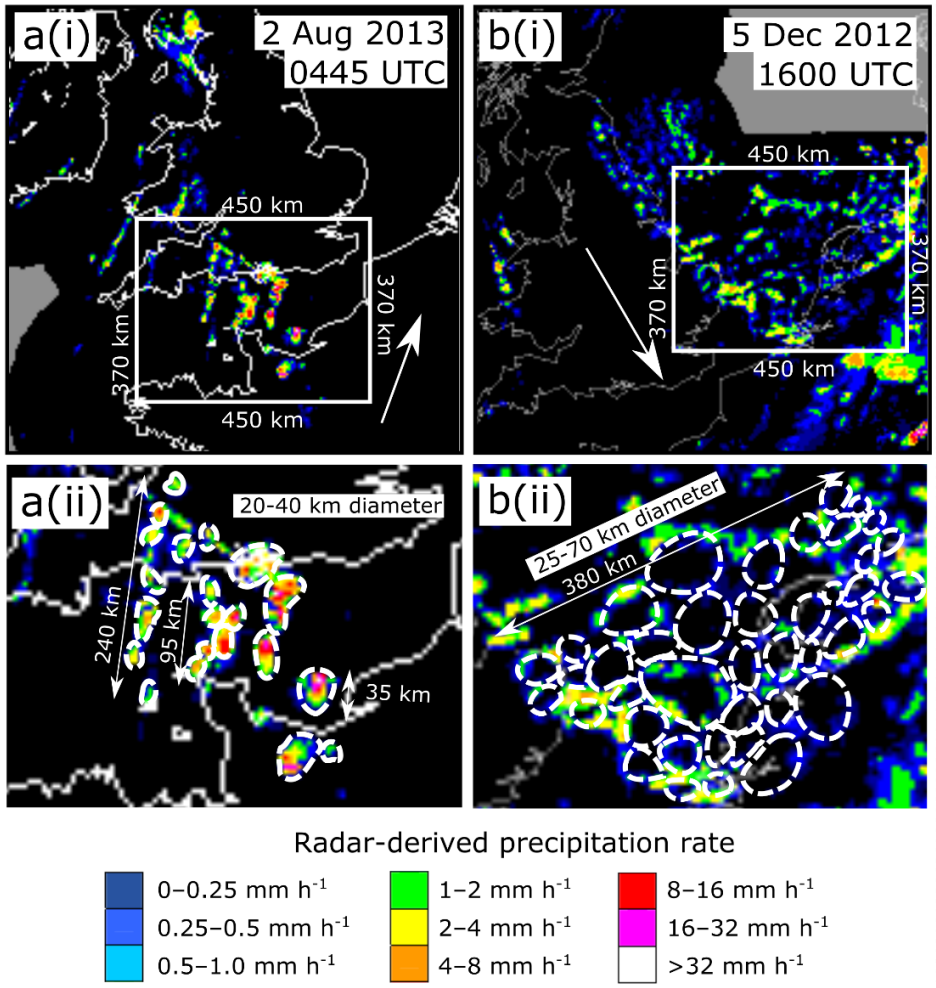

Figure 7.1 Radar-derived precipitation from the radar mosaic across north-west Europe of a) isolated cells on 2 August 2013 and b) open cells on 5 December 2012. Each system generated meteotsunamis greater than 0.3-m high in north-west Europe (taken from the dataset of Williams (2019b)). In a(i) and b(i), the white arrow is the approximate direction of precipitation motion. The white box in a(i) and b(i) is the area that is expanded in a(ii) and b(ii) respectively. The individual cells are highlighted with white dashed lines. Data downloaded from the Centre for Environmental Data Analysis between January 2019–August 2019. The precipitation scale bar is taken from the Met Office (2003). Sizes estimated using the ruler tool in Google Earth, and rounded to the nearest 5 km.

Thus, open cells and isolated cells have similar cell diameters, sea-level pressure perturbations and 10-m wind speeds, which raises a question. Why do open cells rather than isolated cells generate meteotsunamis, even though the individual cells in each system are so similar? Previous hypotheses have proposed that surface wind stresses

with open cells could generate seiches (de Jong and Battjes 2004), though this hypothesis does not recognise the sea-level pressure perturbations or repeating horizontal structure of open cells. To understand how the generation of meteotsunamis through isolated cells and open cells may differ, the generation mechanisms of meteotsunamis need to be considered.

First, meteotsunamis are generated by an atmospheric surface forcing, either from a sea-level pressure perturbation and/or a surface wind stress. Considering only the sea-level pressure perturbations (though similar arguments can be followed for wind stress by replacing sea-level pressure forcings with wind stress forcings), the gradient of the sea-level elevation is proportional to the gradient of the sea-level elevation, and is known as the inverted barometer effect:

$$\nabla\eta_0 = -\frac{\nabla P}{\rho g}, \tag{7.1}$$

where ∇ is the two-dimensional gradient vector, η_0 is the sea-level elevation due to the inverted barometer effect, P is the sea-level pressure perturbation from the background pressure, ρ is the water density (1025 kg m^{-3}), and g is gravitational acceleration (9.81 m s^{-2}) (e.g. Pugh and Woodworth 2014). The inverted barometer effect means that a 1-hPa increase in atmospheric sea-level pressure over a given distance is balanced by a corresponding 0.01-m decrease in sea-level elevation over the same distance.

After initial formation from sea-level pressure perturbations (and surface wind stresses), amplification mechanisms cause meteotsunamis to grow. External resonance between the atmospheric system and the wave is often inferred for meteotsunami formation (e.g. Orlić 1980; Hibiya and Kajiura 1982; Šepić et al. 2015a; Ličer et al. 2017). Two candidate external resonances for a meteotsunami are Proudman resonance, occurring when the forcing speed matches the shallow-water wave speed (Proudman 1929), and Greenspan resonance, occurring when the along-shore forcing speed matches an edge-wave speed (Greenspan 1956). We focus on Proudman resonance, because there is evidence suggesting that open cells can generate meteotsunamis through Proudman resonance (e.g. de Jong and Battjes 2004; Williams 2019b), but there is no evidence as of yet for Greenspan resonance.

Generally, "Proudman resonance" refers to the amplification of waves when the forcing speed moves close to the shallow-water wave speed (e.g. Ličer et al. 2017).

We use the term "strict Proudman resonance" to refer to the mathematical idealisation that only applies with several unrealistic assumptions, such as a constant atmospheric forcing speed moving over water with a constant shallow-water wave speed (Proudman 1929). Furthermore, strict Proudman resonance only applies for one-dimensional forcings in one-dimensional basins, and states that a one-dimensional wave will grow (1) linearly and (2) proportionally to the gradient of the sea-level pressure for a given sea-level pressure perturbation *P*, such that after travelling a long distance *x*, the sea-level elevation η is

$$\eta = -\frac{x}{2}\frac{P_x}{\rho g}, \tag{7.2}$$

where the subscript *x* denotes the partial derivative in the *x*-direction (equivalent to a one-dimensional gradient vector). For two-dimensional sinusoidal forcings, waves do not amplify by as much as suggested from strict Proudman resonance because both the forced waves (directly beneath the atmospheric forcings) are smaller, and other generated free waves can propagate away from the atmospheric forcing (Williams 2019a). Possibly then, because open cells repeat, and are closer together than isolated cells, more free waves are generated and interact (possibly through a constructive superposition), which together could combine to produce larger meteotsunamis.

After external resonance, meteotsunamis are usually of the order of 0.1-m high. Meteotsunamis then further grow through shoaling (moving into shallower water), refraction (as rays perpendicular to wave crests become closer together) and seiching (standing wave formation in a semi-enclosed basin). Together, external resonance, shoaling, refraction and seiching can result in meteotsunamis that are up to 6-m high (e.g. Bubalo et al. 2019).

The purpose of this work is to propose a new explanation for how open cells can generate meteotsunamis. By representing the sea-level pressure fields from open cells and isolated cells through synthetic models (e.g. Šepić et al. 2015a; Ličer et al. 2017), we show how open cells can amplify meteotsunamis through Proudman resonance. We also show how wave amplification differs between the repeating pressure fields of open cells, compared to non-repeating pressure fields of isolated cells.

7.3 Modelling sea-level pressure perturbations and resultant waves

We modelled analytically specified sea-level pressure perturbations assumed to be similar to open cells. To produce sea-level pressure perturbations with a similar horizontal structure to open cells, we prescribed component sinusoids multiplied by one another to give a total pressure perturbation field *P*. This sea-level pressure perturbation was

$$P = P_0 \prod_{n=1}^{n=N} \sin(\cos\theta_n \cdot k \cdot [x - Ut] + \sin\theta_n \cdot m \cdot y + \phi_n), \qquad (7.3)$$

where P_0 is the maximum amplitude of the pressure perturbation (1 hPa), *n* refers to a specific component sinusoid, *N* is the maximum number of component sinusoids, θ_n is the angle between the component sinusoid and the *x*-axis, *k* and *m* represent the wavenumbers in the *x* and *y* direction respectively ($k = m = 2\pi/40$ km^{-1}), *U* is translational speed of the pressure field, *t* is time, and ϕ_n is the phase shift of the component sinusoid.

For open cells with a more realistic hexagonal symmetry (hexagonal cells), we prescribed three sinusoidal components ($N = 3$), each offset by 60° ($\pi/3$ radians). The horizontal angle and phase shift of each component were $\theta_1 = 0$, $\phi_1 = 0$, $\theta_2 = \pi/3$, $\phi_2 = 0$, and $\theta_3 = 2\pi/3$, $\phi_3 = \pi/2$. This combination of angles and phases meant that the forcing had hexagonal symmetry, but with approximately circular sea-level pressure perturbations. Though this structure does not represent optimal hexagonal packing, it is a plausible representation for open-cellular convection (cf. Figure 7.1b and Figure 7.2a(i)). Then, the pressure field was clipped to zero amplitude ($P = 0$ Pa) where $P < 0$ Pa. Therefore, only positive pressure perturbations were modelled, with positive values in the centre of each cell.

Then, to more easily manipulate how the repetition of cells affected wave heights, open cells with rectangular symmetry (rectangular cells) were modelled with two component sinusoids ($N = 2$). The applied horizontal angles and phase shifts were $\theta_1 = 0$, $\phi_1 = 0$ and $\theta_2 = \pi/2$, $\phi_2 = 0$ (Figure 7.2b(i)). Because there were only two component sinusoids at right angles, rectangular cells could be more easily manipulated than hexagonal cells to produce isolated cells, lines of cells and different spacings between cells (Figure 7.2b(i)). To simulate one isolated cell with rectangular symmetry (isolated cell), the pressure fields with rectangular symmetry were set to

only allow one-half wavelength in the along-propagation and cross-propagation direction (cf. Figure 7.1b and Figure 7.2c(i)). To investigate the relative importance of extending the pressure field in the cross-propagation direction or along-propagation direction, two more simulations were produced. We used a single line to investigate the repeating pressure perturbations in the cross-propagation direction and a pressure train to investigate the repeating pressure perturbations in the along-propagation direction (cf. Figures 7.2b(i), 7.3a(i) and 7.3b(i)). To investigate how spacing between individual cells changes wave amplification, we produced rectangular cells with alternating 20-km cells and 20-km gaps (double-spaced rectangular cells) (Figure 7.3c).

The synthetic pressure fields moved rightwards at the shallow-water wave speed, $U = \sqrt{gH}$, where H was the still water depth (50 m). Thus, the total pressure perturbation field moved rightward at 22.15 m s^{-1}. We simulated the hydrodynamics by solving the two-dimensional forced-wave equation over a flat bottom:

$$\eta_{tt} - gH\nabla^2\eta = \frac{H}{\rho}\nabla^2 P, \tag{7.4}$$

where the subscript t denotes partial differentiation in time and ∇^2 is the Laplacian operator. We assumed inviscid and non-rotating flow, which is validated with a scaling analysis (not shown). We imposed radiation boundaries on all sides, allowing the simulated meteotsunamis to pass through the top-, bottom-, left- and right-hand sides of the domain. The numerical solution was found on a finite-difference grid, spanning 200 km in the x- and y-direction, with 500-m grid spacing and a 2-s time step (Figure 7.2). The simulations were run for 9000 s, allowing the pressure perturbation to move across the domain (22.15 m s^{-1} × 9000 s = 199.4 km).

7.4 Results and Discussion

At the final time step of the simulations, we took the highest sea-level elevation and the lowest sea-level elevation from transects in the along-propagation direction (x-direction) in the range 90 km ≤ y ≤ 110 km. The difference between these two values was taken as a representative maximum wave height η_{max} and a subsequent amplification A was calculated. The amplification is the maximum wave height divided by the wave height expected from the inverted barometer effect ($A = \eta_{max}/\eta_0$). Also, whether repeating trains of waves occurred was noted (wave train), and the crest

length was calculated as the maximum contiguous length of the positive sea-level elevation in the cross-propagation direction that was greater than 0.05 m.

The maximum magnitude of the gradient in sea-level pressure was large but plausible at the synthetic forcing edges (P_t = 22.15 m s^{-1} × 0.015 Pa m^{-1} ≈ 0.2 hPa/min). The arbitrary choice of how to manage the edges of individual cells affected the magnitude of the sea-level pressure gradient, and the sea-level elevations could change depending on threshold choice and sea-level pressure field smoothing. However, the sea-level pressure gradient at the edge of each individual cell was consistent between simulations, and the sea-level elevations seemed reasonable compared to other synthetic simulations that investigate external resonance mechanisms (i.e. the resultant meteotsunamis were about 0.1–0.2-m high). Nonetheless, our explanations for wave growth do not rely on the absolute sea-level elevation; we focus on the relative amplifications between simulations.

Open cells generated larger meteotsunamis than isolated cells (Figure 7.2). Hexagonal cells amplified meteotsunamis by 1.4-times more than isolated cells (A_{HC} = 15 compared to A_{IC} = 11, meaning that A_{HC} = 1.4A_{IC}), and rectangular cells amplified meteotsunamis by 2.0-times more than isolated cells (A_{RC} = 22 = 2A_{IC}) (Table 7.1). Also, both the hexagonal cells and rectangular cells produced wave-trains with approximate 180-km wave crests, whereas the isolated cell only produced one wave that had a shorter, 20-km wave crest (Table 7.1, Figure 7.2).

Table 7.1 Maximum sea-level elevation and minimum sea-level elevation along transects in the x-direction in the range 90 km $\leq y \leq$ 110 km, from which the maximum wave height and amplification for each simulation are calculated.

	Hexagonal cells (HC)	Rectangular cells (RC)	Isolated cell (IC)	Single line (SL)	Pressure train (PT)	Double-spaced rectangular cells (DSRC)
Maximum sea-level elevation/ m	0.08	0.14	0.06	0.11	0.10	0.07
Minimum sea-level elevation/ m	–0.07	–0.08	–0.05	–0.08	–0.05	–0.04
Maximum wave height/ m	0.15	0.22	0.11	0.19	0.15	0.11
Amplification (A)	15	22	11	19	15	11
Relative amplification (A/A_{IC})	1.4	2	1	1.7	1.4	1
Wave train	Yes	Yes	No	No	Yes	Yes
Crest length/ km	180	180	20	180	50	60

To understand whether the repetition of cells in the along-propagation or cross-propagation was more important to produce wave amplification, meteotsunamis from a single line and a pressure train were simulated. The amplifications from both the single line (A_{SL} = 19 = 1.7A_{IC}) and from the pressure train (A_{PT} = 15 = 1.4A_{IC}) were greater than from isolated cells, but smaller than from rectangular cells (A_{RC} = 2A_{IC}) (Table 7.1). Both the extent in the cross-propagation direction (single line) and the along-propagation direction (pressure train) were needed to produce the simulated amplification from rectangular cells. However, the extent in the cross-propagation direction was twice as important for amplification than extent in the along-propagation direction at generating the amplification seen for rectangular cells (calculated as (A_{SL} – A_{IC})/(A_{PT} – A_{IC})).

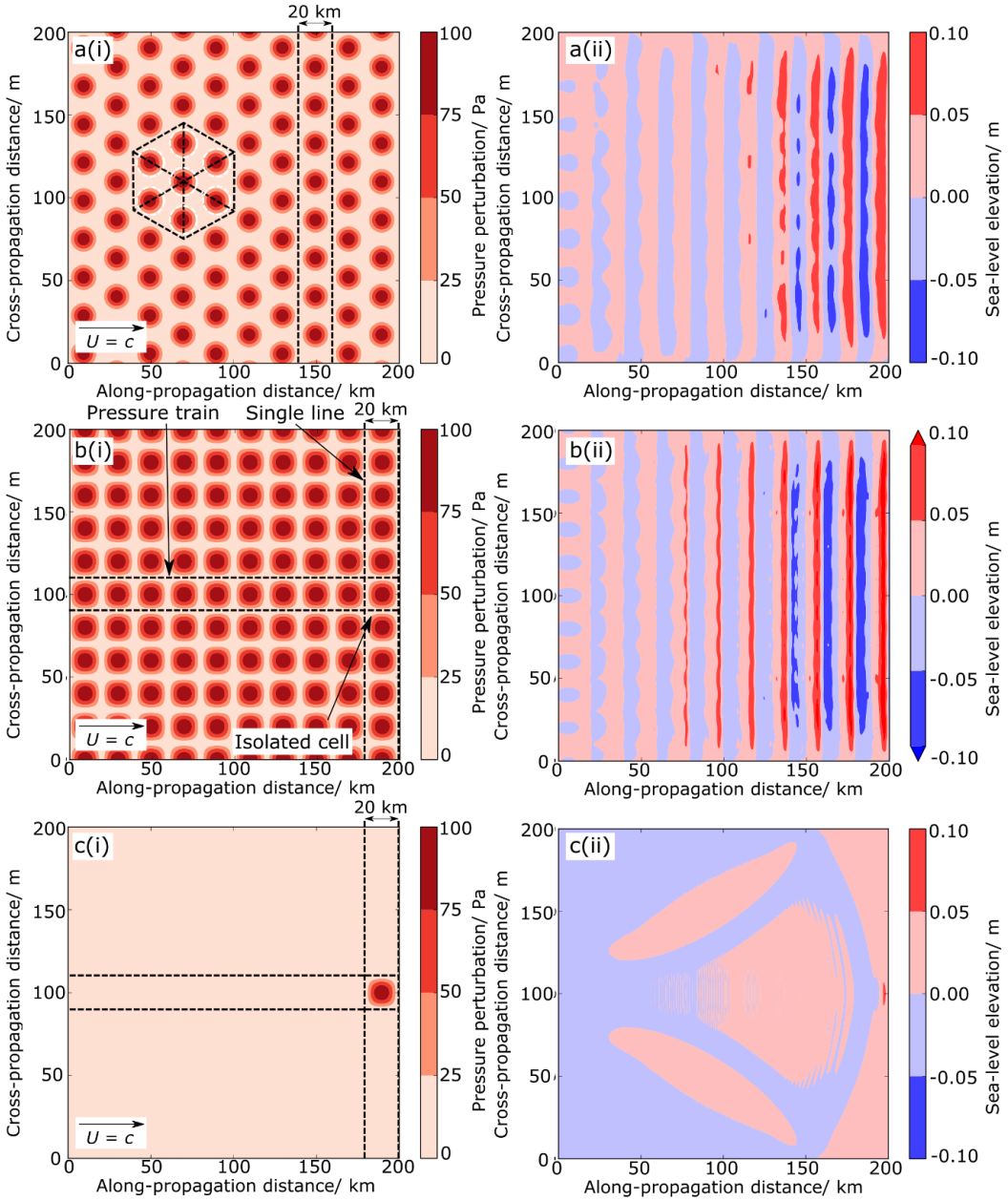

Figure 7.2 A synthetic representation of the sea-level pressure field associated moving rightwards at Proudman resonant speed for a(i) cells with hexagonal symmetry, b(i) cells with rectangular symmetry and c(i) an isolated cell with rectangular symmetry, with the resultant sea-level elevation after moving 200 km for each case in a(ii), b(ii) and c(ii).

The repetition of cells in the cross-propagation direction was important for more than wave amplification. The single line and open cells produced longer wave crests (180 km) than isolated cells (20 km) and the pressure train (60 km). These long wave crests from single lines and open cells mean that there was a higher wave flux available for focussing through refraction and shoaling than from isolated cells.

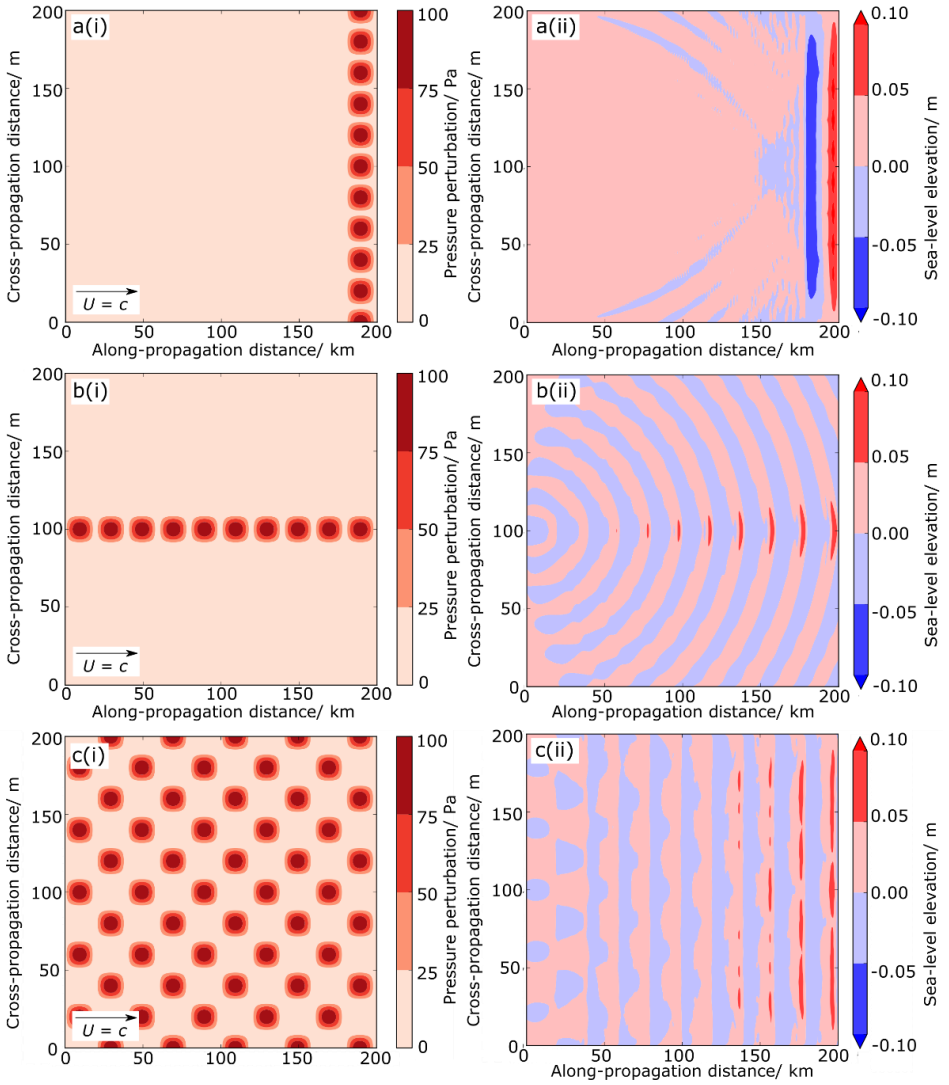

Figure 7.3 As for Figure 7.2, but with (a) a single line and (b) a pressure train and (c) double-spaced rectangular cells.

Likewise, the repetition of cells in the along-propagation was necessary to generate a wave train. Wave trains were only simulated with the open cells and pressure train, and not the single line or isolated cell (cf. Table 7.1, Figure 7.2 and Figure 7.3). These wave trains could be important for seiching. If meteotsunamis become trapped in semi-enclosed basins with narrow inlets, then repeated incoming meteotsunami waves will increase the overall trapped energy and seiches will become larger (Rabinovich 2009). These pressure trains are plausible, being similar to the train of isolated cells on 2 Aug 2013 (cf. Figure 7.1a and Figure 7.3a(i)).

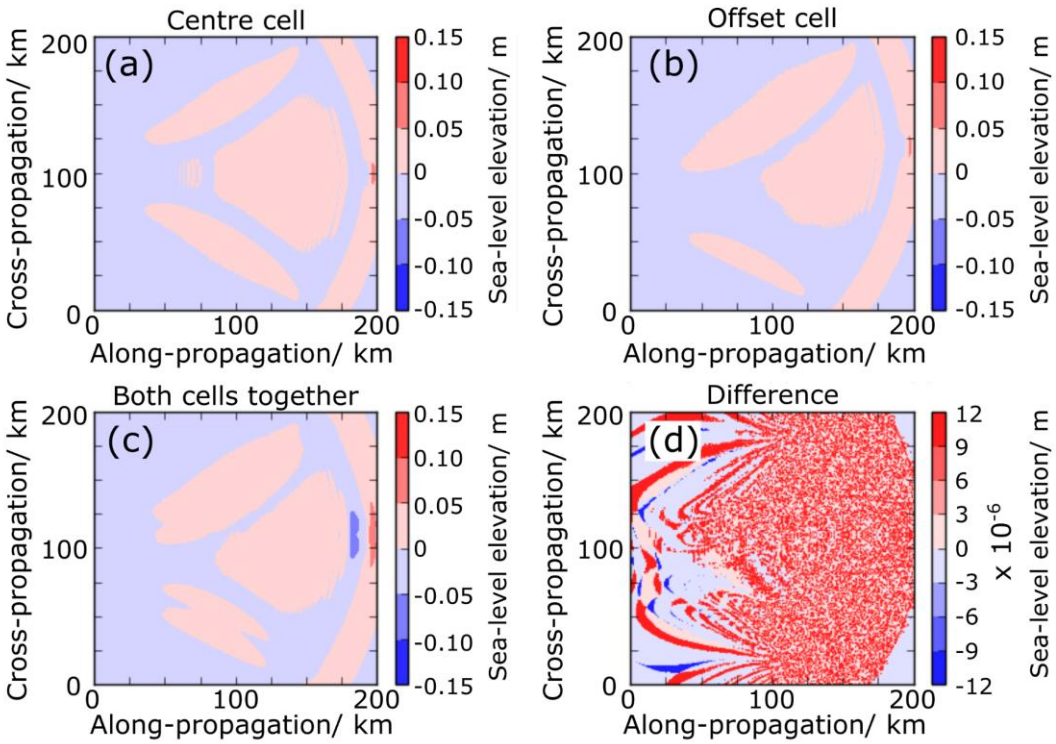

Figure 7.4 The simulated sea-level elevation for a) a single cell moving along the *x*-direction that is centred at y = 100 km, b) a single offset cell centred at y = 120 km, c) both the centred cell and offset cell at the same time, d) the difference between (c) and the summation of (a) and (b).

The amplification from the double-spaced rectangular cells had the same amplification as isolated cells ($A_{DSRC} = 11 = 1A_{IC}$), corresponding to half the amplification of the (single-spaced) rectangular cells ($A_{RC} = 2A_{IC}$). To help understand these results, we ran three more simulations. By separately simulating a single centred cell and a single offset cell (Figures 7.4a and 7.4b) and then simulating both cells at the same time (Figure 7.4c), the difference between the sum of separate isolated cell sea-level elevations (i.e. sum of Figures 7.4a and 7.4b) and both cells (Figure 7.4c) was on the order of 10^{-5} m (Figure 7.4d). The sea-level elevation from repeating cells was a linear superposition of the sea-level elevation from each individual cell. Small differences in sea-level elevations (Figure 7.4d) can be attributed to small numerical errors. Thus, with more densely packed individual cells, more individual waves are created. With linearly arranged cells, these waves are in phase and constructively interfere, leading to a large resultant superposition. This process is akin to Huygens' Principle for constructing wavefronts.

Generally, this linear superposition means that meteotsunamis generated by a collection of repeating individual cells (i.e. open cells) should be larger and have longer wave crests than meteotsunamis from single individual cells (i.e. isolated cells). However, if the repeating individual cells are too far away from each other (e.g. Figure 7.3c), then the individual waves do not necessarily constructively interfere to produce a larger wave, and the resultant meteotsunami would be the same height as produced by an isolated cell.

Therefore, through synthetic simulations we have provided a new explanation for how open cells generate meteotsunamis. This explanation is that repetition of individual cells produces many individual waves that constructively interfere to form a superposition, which does not happen with isolated cells that are spaced too far apart.

7.5 Conclusion

We have shown that open cells could produce about twice as much amplification through Proudman resonance than isolated cells because of the repeating horizontal structure of open-cellular convection and linear superposition of waves. Repeating pressure perturbations in the cross-propagation direction were necessary to produce long wave crests (providing a higher total wave flux when refracting) and were twice as important as repetition in the along-propagation direction for wave amplification. Nonetheless, repetition in the along-propagation direction was necessary for wave-trains (providing more incoming waves when seiching). Such a pressure train could plausibly happen, as exemplified by the train of isolated cells on 2 Aug 2013 (Figure 7.1a).

The model suggested here does not necessarily contradict the previously suggested wind-stress model of de Jong and Battjes (2004). However, we show that when the atmospheric forcing speed matches the shallow-water wave speed, that plausible sea-level pressure perturbations alone could produce 0.1–0.2-m high meteotsunamis through Proudman resonance. Also, as open cells are a field of repeating individual cells, we recognise that the structure of this repetition allows larger meteotsunamis to form through constructive superposition. Although our arguments could also apply to wind stress, the relative importance of sea-level pressure and wind stress from open cells remains an unanswered question.

This work ignored the thermodynamics of open-cellular convection, did not use realistic sea-level pressure fields, and ignored 10-m wind fields. These problems could be addressed by numerical weather prediction models, such as the Weather Research and Forecasting model (WRF), which solve the appropriate three-dimensional thermodynamic equations of motion. Idealised box-models of open-cellular convection (e.g. Vincent et al. 2012) that force a hydrodynamic model could complement these synthetic simulations with more realistic sea-level pressure and 10-m wind fields. A coupled atmosphere–ocean hindcast model could also provide more compelling evidence to link documented meteotsunamis to open-cellular convection.

Acknowledgements David Williams is funded by the National Environmental Research Council's Understanding the Earth, Atmosphere and Ocean Doctoral Training Programme, Grant NE/L002469/1.

Chapter 8

Conclusions

The aim of this dissertation was to provide new knowledge about the physical processes that generate meteotsunamis in north-west Europe, and to understand their frequency and variability over multiple time scales. This knowledge would allow a better preparedness for these potentially hazardous phenomena that, this thesis shows, occur more frequently in north-west Europe than previously thought.

To provide this new knowledge, a multidisciplinary approach was adopted that combined the fields of physical oceanography, atmospheric dynamics, and atmosphere–ocean interactions. Each of these three fields were incorporated across four distinct chapters. Each chapter answered a different question about meteotsunami generation in north-west Europe, producing a linked narrative through the dissertation.

8.1 The dissertation narrative

In Chapter 4, by producing synthetic simulations based on detailed observational analyses, it was demonstrated that a 0.70-m high meteotsunami was generated by an atmospheric convective system in the English Channel on 23 June 2016. The meteotsunami was primarily generated by sea-level pressure perturbations moving at the shallow-water wave speed. In case-study simulations, the meteotsunami grew in the region expected of Proudman resonance, and by an amount close to calculations that assumed strict Proudman resonance (Proudman 1929). The meteotsunami growth and propagation was also complemented by shoaling, refraction, and reflection from coastlines. Most interestingly, the simulated coastal wave heights reduced by more than 50% when tides were included in simulations. This wave-height reduction occurred because tidal currents reduced the shallow-water wave speed and the region that the meteotsunami grew from Proudman resonance moved away from the coastline. This study produced the first demonstration of meteotsunami height sensitivity to tides through the specific mechanism of tidal currents moving the Proudman resonant region away from the coastline, and consequently showed that tides are an important process to include when simulating meteotsunamis in the English Channel.

This case study provided the first numerical simulations that reproduced observations of a meteotsunami in north-west Europe. However, one credibly simulated case study was not sufficient to give a general understanding of how Proudman resonance could be affected by variable weather systems, bathymetry or tides. Further work was also needed to reconcile how the simulated meteotsunami wave heights and arrival times were relatively accurate, despite the numerous assumptions about the atmospheric convective system made by the synthetic atmospheric forcing. The synthetic atmospheric forcing ignored that the observed atmospheric convective system changed speed, that the measured surface pressure perturbations changed amplitude, and that the overall system was two-dimensional.

Therefore, in Chapter 5, by using both highly idealised simulations and analytical models, a more generalised understanding of Proudman resonance was developed. The most important factor for Proudman resonant wave growth was found to be the mean forcing speed and the mean free-wave speed matching, rather than factors that affected variability around the mean speeds. The factors investigated here that affected the average wave speeds were of about the same importance (e.g. currents, water depth, average forcing speed) and for any study, their total effect on wave speeds and wave-flux conservation should be considered together. Most interestingly, wave growth near the predictions of Proudman resonance was found to occur even with large deviations (±18%) from the mean forcing speed or the mean free-wave speed. Wave growth near the predictions of strict Proudman resonance could occur if these deviations varied rapidly enough for the forced wave and free wave to remain in superposition. This growth was termed ‘effective Proudman resonance’. Though the surface forcing two-dimensionality was less important for wave growth than mean forcing and free-wave speeds matching, the two-dimensionality alone could inhibit wave growth. Finally, it was demonstrated (perhaps not surprisingly) that larger average forcing amplitudes produced larger meteotsunamis, and that instantaneous forcing amplitudes were not useful to explain instantaneous meteotsunami wave heights. Combined, these results suggested that mean forcing properties and the mean free-wave speed were most important for wave growth.

The results from Chapter 5 provided some answers as to why the synthetic forcing in Chapter 4 was able to provide reasonable simulations of the observed meteotsunami wave height. In the case study of Chapter 4, the average atmospheric forcing properties

(speed, direction and amplitude), and the uncertainty around the average atmospheric forcing properties, were appropriately included in ensemble simulations. From the insight of Chapter 5, the variation in the speed of the convective system around the mean speed was small enough to be unimportant to accurately simulate meteotsunami wave heights, and the mean sea-level pressure perturbation amplitude was appropriately represented.

Yet a second problem remained from the case study in Chapter 4. There was little context for the 23 June 2016 meteotsunami. Although there have been a small number of meteotsunami case studies and localised climatologies across north-west Europe, it was still not known how frequently meteotsunamis of this size occur, the usual time of year for meteotsunamis, nor which mesoscale atmospheric phenomena tend to generate them.

This wider context of meteotsunami occurrences was given in Chapter 6 through a climatological study. This study answered how, where and when meteotsunamis are generated in north-west Europe. Between 2010–2017, 349 meteotsunamis were identified from tide gauge measurements and 256 coincident mesoscale atmospheric systems were classified from radar-derived precipitation rates. Of the identified meteotsunamis, 79% were smaller than 0.5 m and about half occurred in winter. Of the classified atmospheric systems, 46% were quasi-linear systems, 33% were open-cellular convection, 17% were non-linear clusters and 4% were isolated cells. For 45 meteotsunamis in France (constituted of 10 winter-time open cells, 26 winter-time quasi-linear systems and 9 summer-time quasi-linear systems), well-documented synoptic atmospheric conditions occurred. For 43 out of 45 of these synoptic composites, there was also evidence of favourable conditions for Proudman resonance within the Celtic Sea and English Channel.

From the climatology in Chapter 6, it can now be stated that early-morning, summer-time meteotsunamis, as examined in the case study Chapter 4, are actually rare in north-west Europe. Prior to this climatology, other north-west European case studies had focussed on meteotsunamis generated by similar summer-time convective systems. It is now known that winter-time meteotsunamis are far more common than summer-time meteotsunamis across the region. Speculatively, winter-time meteotsunamis may have been undocumented in case studies because there are also

larger wind waves, swell waves and storm surges in the winter than summer. To better understand how meteotsunamis are generated in north-west Europe, it may be sensible to also simulate winter-time meteotsunamis. These simulations should incorporate oceanographic processes that may affect atmosphere–ocean interactions, such as tides (e.g. Choi et al. 2014) and wind-wave surface roughness (e.g. Shi et al. 2019).

A weather system that predominantly generated meteotsunamis in winter was open-cellular convection (open cells). Although open cells had been previously suggested as triggers for seiches in the port of Rotterdam (e.g. de Jong et al. 2003; de Jong and Battjes 2004), the wider implication for meteotsunami generation in north-west Europe had not yet been recognised. How open cells generate meteotsunamis had also remained unclear. In Chapter 7, a new explanation for meteotsunami generation through open cells was developed. Open-cellular convection was synthetically modelled as a repeating field of individual cells moving at the shallow-water wave speed. It was demonstrated that each individual cell generated an individual wave, and these individual waves formed a linear superposition. When constructive interference occurred from waves produced by repeating cells (i.e. open cells), a larger meteotsunami occurred than would be expected from single cells (i.e. isolated cells).

Thus, new knowledge about the physical processes that generate meteotsunamis in north-west Europe has been produced. Specifically, how meteotsunamis are generated through Proudman resonance was developed with atmospheric and oceanographic context of north-west Europe through Chapters 4, 5 and 7. A lower bound of meteotsunami size-exceedance rates were found in north-west Europe, alongside the variability of meteotsunamis over diurnal and seasonal cycles in Chapter 6. These results were achieved by identifying meteotsunamis and mesoscale atmospheric systems from measurements, using analytical approximations and relationships to explain wave growth, and simulating meteotsunamis with numerical models.

8.2 Study limitations

8.2.1 Models

To develop new insights into meteotsunami generation for the physical processes that are relevant to north-west Europe, this dissertation consistently employed a synthetic modelling approach. The synthetic modelling approach relied on interpretation of atmospheric observations to apply the atmospheric sea-level pressure and 10-m wind velocities through analytic forcing functions. Understanding key physical processes (e.g. Proudman resonance) was developed by comparing expected wave heights from analytic solutions to numerical solutions, by simulating fully-controlled ensembles, and by selectively altering patterns of sea-level pressure fields. However, numerical weather prediction (NWP) models were not used to aid analysis for the main results within the chapters (see Appendix E for NWP modelling). Using NWP models in a hindcast approach could have provided more compelling evidence to link the convective system to the 23 June 2016 meteotsunami case study than possible from the synthetic models. Furthermore, NWP models could have illuminated important thermodynamic atmosphere–ocean interaction processes for meteotsunami generation through open-cellular convection in Chapter 7. Nonetheless, the synthetic models were sufficient to meet the aims of Chapters 4 and 7, even if more compelling evidence or physical insight could have been provided by more sophisticated NWP models.

Given that meteotsunamis can be simulated, and with the overall dissertation aim of preparing for another large meteotsunami, a natural question follows: “Is operational forecasting possible in north-west Europe?”. Currently, a sophisticated mix of heuristic approaches, coupled-models and statistical methods are being developed for meteotsunami forecasts and early warning systems across the Balearics (e.g. Renault et al. 2011; Tintoré et al. 2013; Romero et al. 2019), the Adriatic (e.g. Šepić and Vilibić 2011; Šepić et al. 2016; Denamiel et al. 2019), and the US (e.g. Linares et al. 2016). Currently in north-west Europe, the highest resolution numerical weather predictions models (e.g. UKV, ARPEGE) and hydrodynamic models (e.g. NEMO AMM15) operate at about 1-km grid spacing, which is suitable for storm surges but is probably the coarsest grid spacing sufficient for meteotsunami forecasts.

However, the results of simple synthetic models in this dissertation indicate that a heuristic approach might be possible in north-west Europe. This could be achieved by

taking advantage of atmospheric and oceanographic data with grid spacings of a few kilometres (e.g. radar), or *in situ* data with sampling intervals of a few minutes (e.g. tide gauges, 10-m wind speeds and surface pressures) and developing operational synthetic models. A heuristic approach could be a sensible first step before implementing a coupled-model forecast across north-west Europe.

8.2.2 Observations

Numerical models, forecasting and improved process understanding of meteotsunami dynamics depend critically on high quality observations. In this dissertation, meteotsunami observations were sometimes limited by tide-gauge intervals that were too long to properly resolve the meteotsunami signal. In the case study in Chapter 4, and the climatology in Chapter 6, meteotsunami wave heights, periods and arrival times were more poorly estimated when using tide gauges with longer intervals. As exemplified in both chapters, the British Oceanographic Data Centre releases tide gauge data around the UK coastline with 15-min averaging intervals, which is too long to sufficiently characterise meteotsunami properties. These longer averaging periods are designed for storm surge nowcasting and multi-annual mean sea-level analysis, and so deliberately filter out higher frequency waves. Nonetheless, these averaging intervals are not especially useful for meteotsunami studies. As exemplified around the world, and recommended by GLOSS, tsunamis and meteotsunamis are best studied with averaging intervals below 6-minutes (IOC 2006). Thus, a direct recommendation for future work in north-west Europe is to use tide-gauge data with shorter intervals.

Further analysis of meteotsunami occurrence in the region from higher frequency data, as it becomes available, would complement our north-west European climatology. Importantly, these climatologies may improve estimations of meteotsunami size-frequency distributions and extreme wave heights. Despite the drawbacks of longer averaging intervals, in Chapter 6, meteotsunamis were more easily distinguished from repeating tidal wavelets with longer intervals. Perhaps an automatic meteotsunami detection algorithm that accounts for the repeating tidal wavelets could alleviate the need for manual identifications. Subsequent climatologies could also address the suggested seasonality, mesoscale atmospheric phenomena and associated synoptic meteorology of this regional climatology, which were assumed to be independent of the effects of tide-gauge intervals.

8.3 Rising sea levels and a changing climate

One reason for the longer tide-gauge averaging intervals in the UK is because they remain suitable for characterising long-term sea-level rise. Globally (IPCC 2013) and across most of the north-west European continental shelf (Palmer et al. 2018), mean sea level is rising by 2–4 mm yr^{-1}. Across most of the north-west European continental shelf, the relative sea level is a combination of regional variations in sea level rise and vertical land movement (e.g. glacial isostatic adjustment) (Palmer et al. 2018). Sea-level rise projections vary primarily due to Representative Concentration Pathways (RCP2.6, RCP4.5, RCP6.0 and RCP8.5) and location. Compared to 1981–2000 average, by 2100 the sea level could rise in London and Cardiff by about 0.3–1.1 m and in Edinburgh and Belfast by about 0.1–0.9 m (Palmer et al. 2018). As of yet, the associated changes in tidal range and tidal currents have unknown consequences for meteotsunami generation processes. However, most importantly, the increase in the mean sea level will lead to an increase in the frequency and magnitude of extreme sea levels (e.g. Wahl 2017; Palmer et al. 2018), and any critical threshold such as a sea wall could be more easily overtopped.

A rising sea level is just one of the consequences of anthropogenic carbon emissions. There will also be changes to fundamental physical properties of the atmosphere that will affect weather systems. Global surface temperatures are likely to be more than 1.5ºC warmer by 2100 than the average surface temperatures between 1850–1900 for RCP4.5 to RCP8.5 emission scenarios (IPCC 2013). Alongside increasing air temperatures, the air will be able to hold more moisture, which is constrained by the Clausius-Clapeyron relation. Most simply, the maximum amount of water vapour that is able to be saturated in air increases by 7–8% when air temperature increases by 1ºC, meaning that in the future, the atmosphere will be able to hold more water vapour before precipitation occurs (O'Gorman and Muller 2010). One consequence of atmospheric warming is that there will very likely be more intense and frequent events with extreme precipitation rates over the mid-latitudes (IPCC 2013).

These changes to physical properties of the atmosphere may also affect the development of synoptic-scale atmospheric systems. Currently, there is agreement (albeit with low confidence) that tropical cyclones will become more intense (Knutson et al. 2010; IPCC 2013), and there is currently no consensus about how the intensity

or latitudinal distribution of extra-tropical cyclones will change (Palmer et al. 2018). Because there is so much uncertainty at these larger synoptic scales, we cannot answer how mesoscale atmospheric systems at mid-latitudes might be affected.

Nonetheless, from the work of this dissertation and others, the meteotsunami size-exceedance rates, spatial distribution, and seasonal variation will depend on changes to the average speed, intensity, frequency and distribution of mesoscale atmospheric systems. Possibly there will be no significant change to meteotsunami wave height due to atmospheric conditions, mirroring the current consensus that there will be no significant change to storm surge wave height (e.g. Palmer et al. 2018). Regardless of potential changes to meteotsunamis, in the context of sea-level rise, understanding meteotsunamis as a source of sea-level extremes may become more important in the coming decades.

Appendix A

Travel-time solutions for waves in the English Channel

A simple model was developed to determine the travel times from a tsunami made by a small, rectangular source (i.e. a landslide) in the English Channel. This simple travel-time model solved the Eikonal equation over the domain Ω,

$$|\nabla \tau_a(x, y)| = c^{-1}(x, y), \tag{A1}$$

where ∇ was the two-dimensional gradient vector in the x-direction and y-direction, τ_a was the arrival time of the wave, and c was the shallow-water wave speed, with the condition that for a small source region dΩ within Ω that

$$\tau_a(x, y) = 0. \tag{A2}$$

Physically, equations A1 and A2 meant that the wave originated within a pre-defined source region dΩ and spread out over the domain Ω at the shallow-water wave speed. The shallow-water wave speed was defined as

$$c(x, y) = \sqrt{gH(x, y)}, \tag{A3}$$

where g was gravitational acceleration (9.81 ms^{-2}) and H was the water depth defined by GEBCO 2014 bathymetry. Equation A1 was then numerically solved in Python using the fast-marching method (Sethian 1996), with the source defined over a small rectangle.

Numerical solutions were verified against analytical solutions for a flat bottom. Numerical solutions showed concentric circles of arrival times that were within minutes of the analytical solution, and the percentage error (time error relative to the total time) decreased with distance. The greatest discrepancy between analytical solutions and numerical solutions came from the representation of the point source in analytical models as a rectangular source in the numerical models.

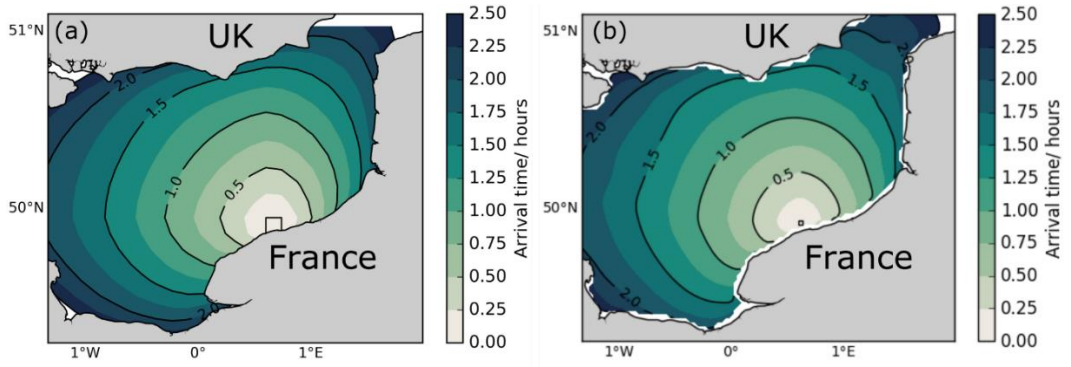

Figure A1 The numerical solution for arrival times of a small rectangular source in the English Channel for a) 40-km smoothing and b) 10-km smoothing.

The bathymetry was taken from GEBCO 2014 (IOC et al. 2003) and converted to a Cartesian grid using a constant scaling factor of 72,436 m for 1º longitude and 111,219 m for 1º latitude. The GEBCO bathymetry grid was then bilinearly interpolated to a grid with regular 100-m spacing in the zonal and meridional directions. All values greater than 0 m (land) were clipped to 0 m. The bathymetry was then filtered with a uniform filter to remove variability in the bathymetry at wavelengths shorter than the tsunami wavelength (there was little difference between 10-km, 20-km and 40-km uniform filtering). The bathymetry was then resampled with 10-km grid spacing for efficiency. The source area was defined as four grid cells, with the centre at the predefined landslide location. Several starting locations were used that were near the coastline. Specifically, these locations were (49.41 ºN, 0.93 ºW), (49.35 ºN, 0.51 ºW), (49.32 ºN, 0.19 ºW), (49.62 ºN, 0.10 ºE), (49.87 ºN, 0.62 ºE), (50.00 ºN, 1.23 ºE), (50.34 ºN, 1.53 ºE), (50.72 ºN, 0.83 ºW), (50.74 ºN, 0.18 ºE), and (50.88 ºN, 0.73 ºE). However, none of these initial locations could suitably explain the arrival times of the meteotsunami at Dieppe, Boulogne and Newhaven (e.g. Figure A1).

Appendix B

Supplementary figures to Chapter 5

The following figures are supplementary material to Chapter 5 and more explicitly show the simulation results and corresponding analytical envelopes.

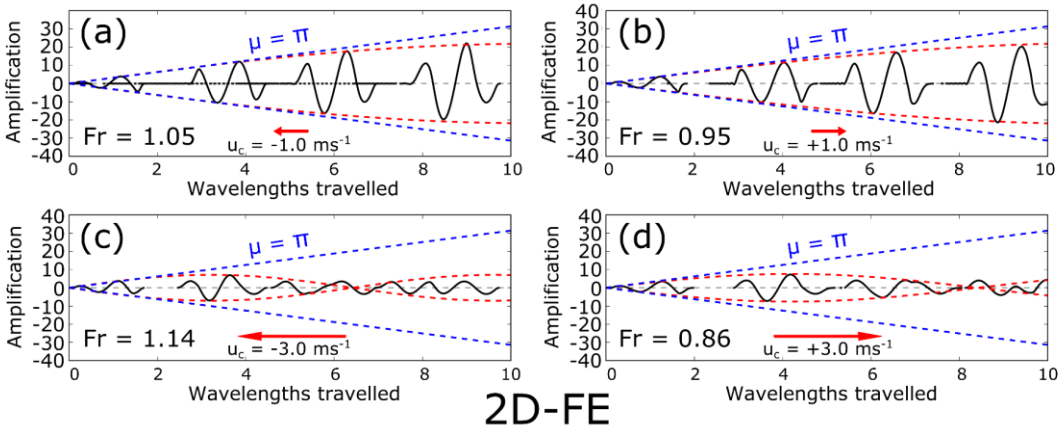

Figure B1 The sea-level response in the 2D-FE model (Telemac) with currents, due to a pressure forcing moving at $U = \sqrt{gH}$. Blue dashed lines indicate Proudman resonant response and red dashed lines indicate the wave envelope approximation. a) $u_c = -1$ ms^{-1}, b) $u_c = +1$ ms^{-1}, c) $u_c = -3$ ms^{-1}, d) $u_c = +3$ ms^{-1}.

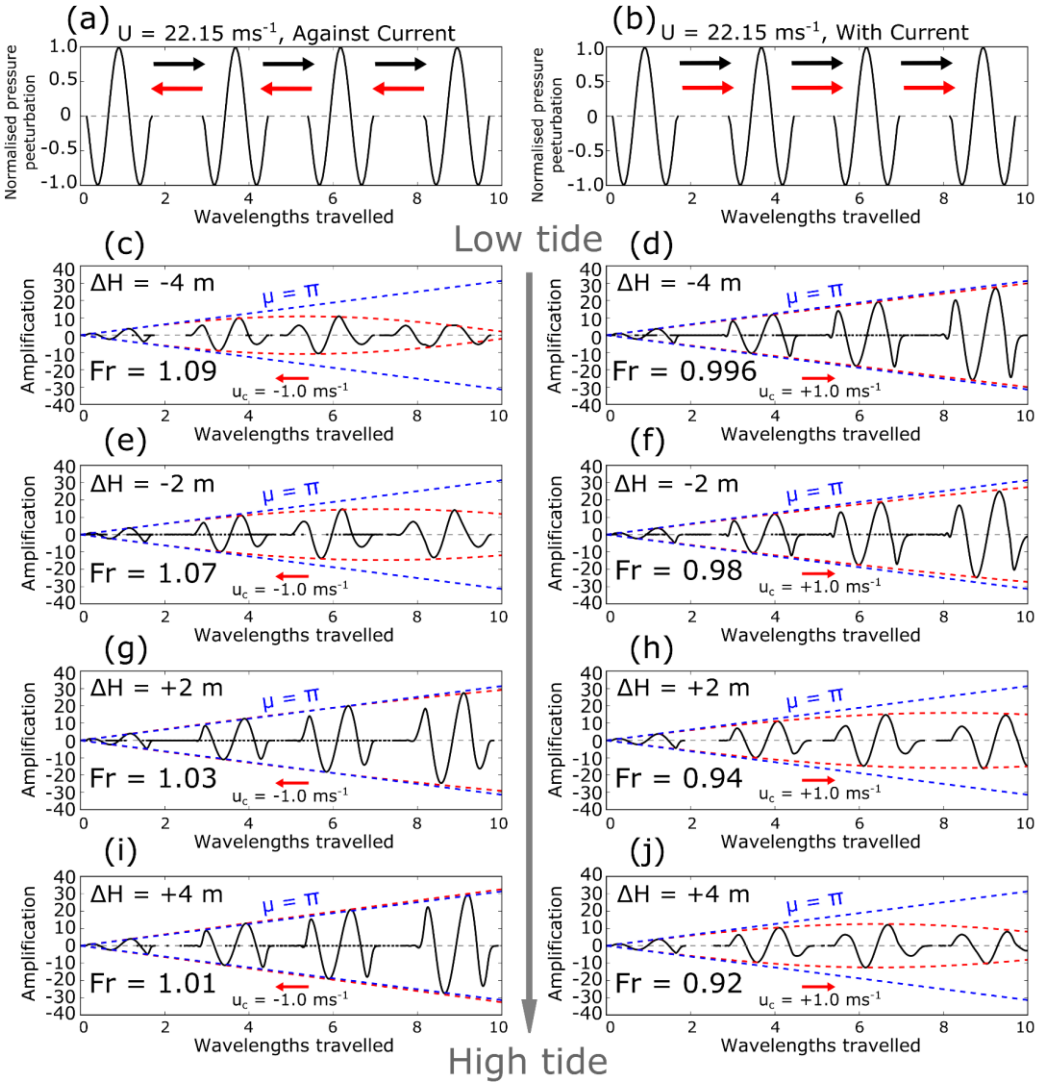

Figure B2 a) non-dimensional pressure forcing moving against currents (as with all left-hand side panels), b) non-dimensional pressure forcing moving against currents (as with all right-hand side panels). Tidal elevation is increasing from top to bottom. All other panels show sea-level amplification. (c, d) ΔH = –4 m, (e, f) ΔH = –2 m, (g, h) ΔH = +2 m, (i, j) ΔH = +4 m. Blue dashed lines is the expected envelope of sea-level elevation from Proudman resonance, the red dashed line is the envelope from a near-Proudman resonant approximation.

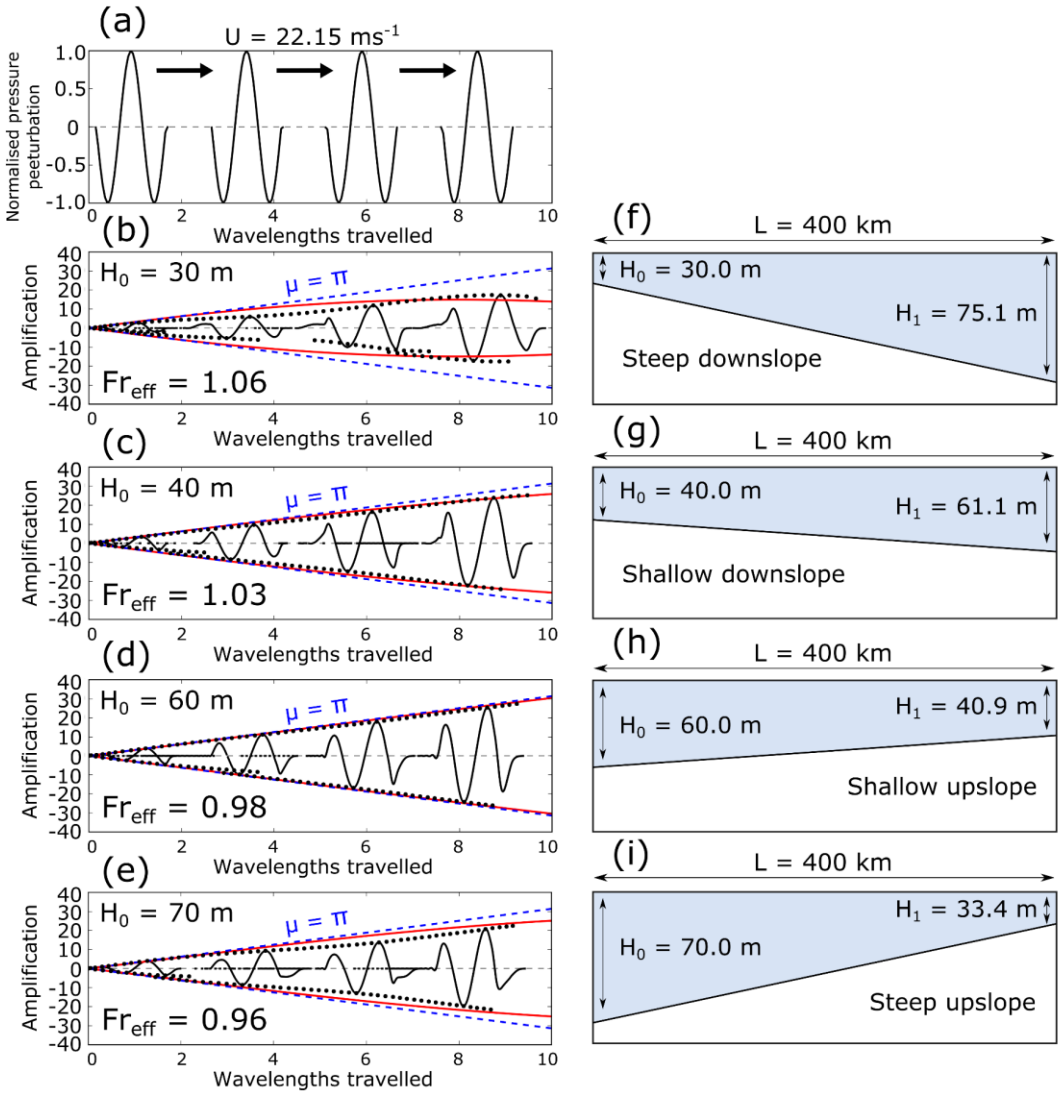

Figure B3 Sea-level response with sloping bottoms. a) non-dimensional pressure forcing moving at the mean shallow-water wave speed across the basin (U = 22.15 ms^{-1}). Sea-level amplification when b) H_0 = 30 m, c) H_0 = 40 m, d) H_0 = 60 m, e) H_0 = 70 m. Blue dashed lines are the expected envelope of sea-level elevation from Proudman resonance, the red solid line is the envelope from an effective Froude number approximation. Black dots are maxima and minima of sea-level amplification at 5-min intervals. Schematics of model set-up f) H_0 = 30 m, g) H_0 = 40 m, h) H_0 = 60 m, i) H_0 = 70 m.

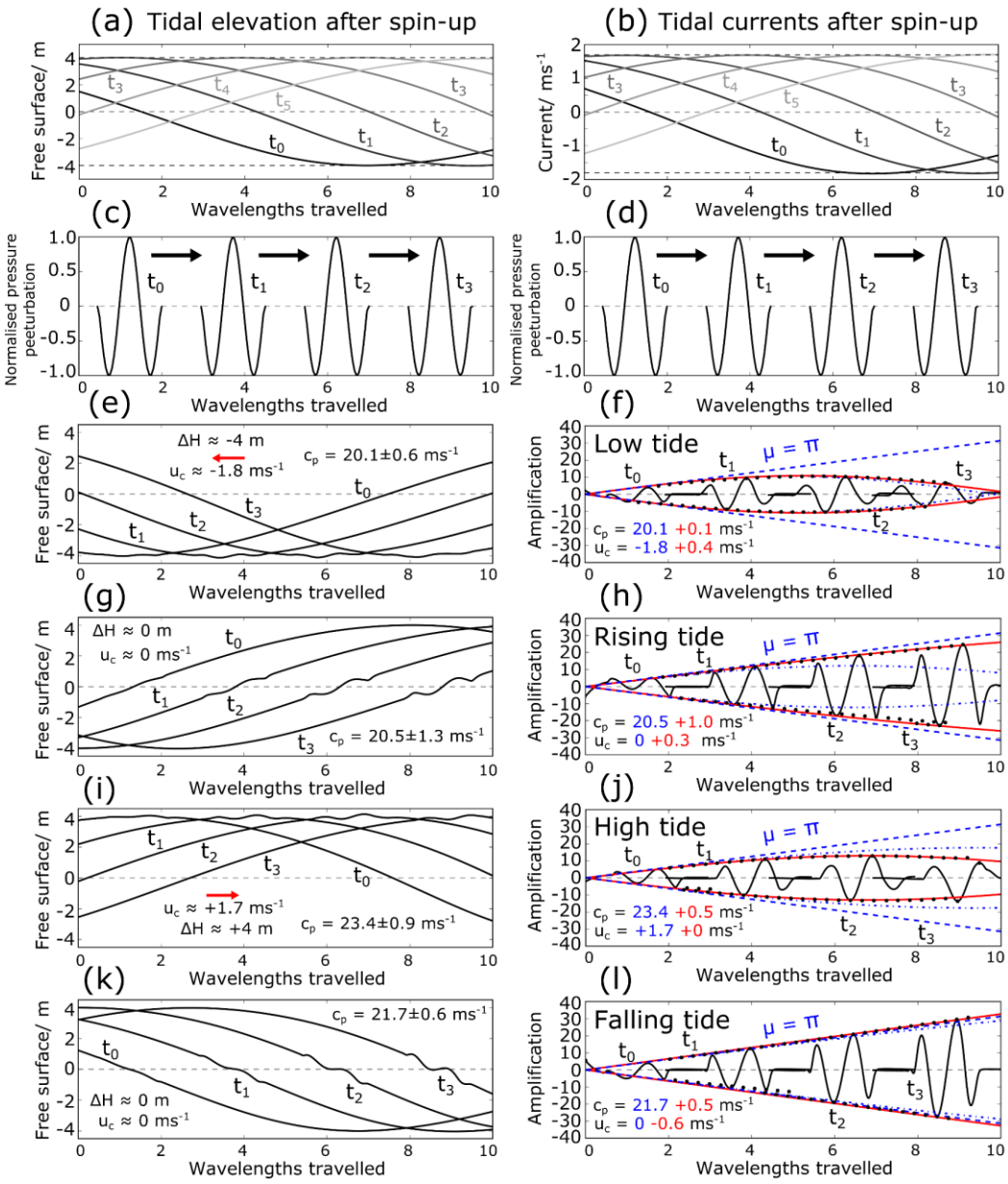

Figure B4 Sea-level elevation from a moving forcing with a dynamic progressive tide. a) free surface elevation across the domain at five time steps (solid lines from black to light grey). Dashed grey lines at η = –4 m, η = 0 m and η = +4 m. b) tidal current across the domain at five time steps (solid lines from black to light grey). Dashed grey lines at $u_{c,T}$ = –1.8 ms^{-1}, $u_{c,T}$ = 0 ms^{-1} and $u_{c,T}$ = +1.7 ms^{-1}. c, d) non-dimensional pressure forcing moving at the shallow-water wave speed from the ocean at rest (U = 22.15 ms^{-1}). Sea-level elevation and band-passed filtered amplification (sea-level elevation divided by inverted barometer) at (e, f) low tide, (g, h) rising tide, (i, j) high tide and (k, l) falling tide. Blue dashed lines are the envelope of sea-level elevation from Proudman resonance, blue dash-dots are initial estimates of $c_{p,T}$ and $u_{c,T}$, and the red solid line is the envelope from a near-Proudman resonant approximation with improved $c_{p,T}$ and $u_{c,T}$. Initial estimate and approximation improvement are shown as blue and

red speeds in bottom-left corner. Black dots are maxima and minima of sea-level amplification at 500-s intervals between 4,500–15,000 s. Amplification values more than $0.5\lambda_x$ ahead of and behind the forcing have been cropped for clarity.

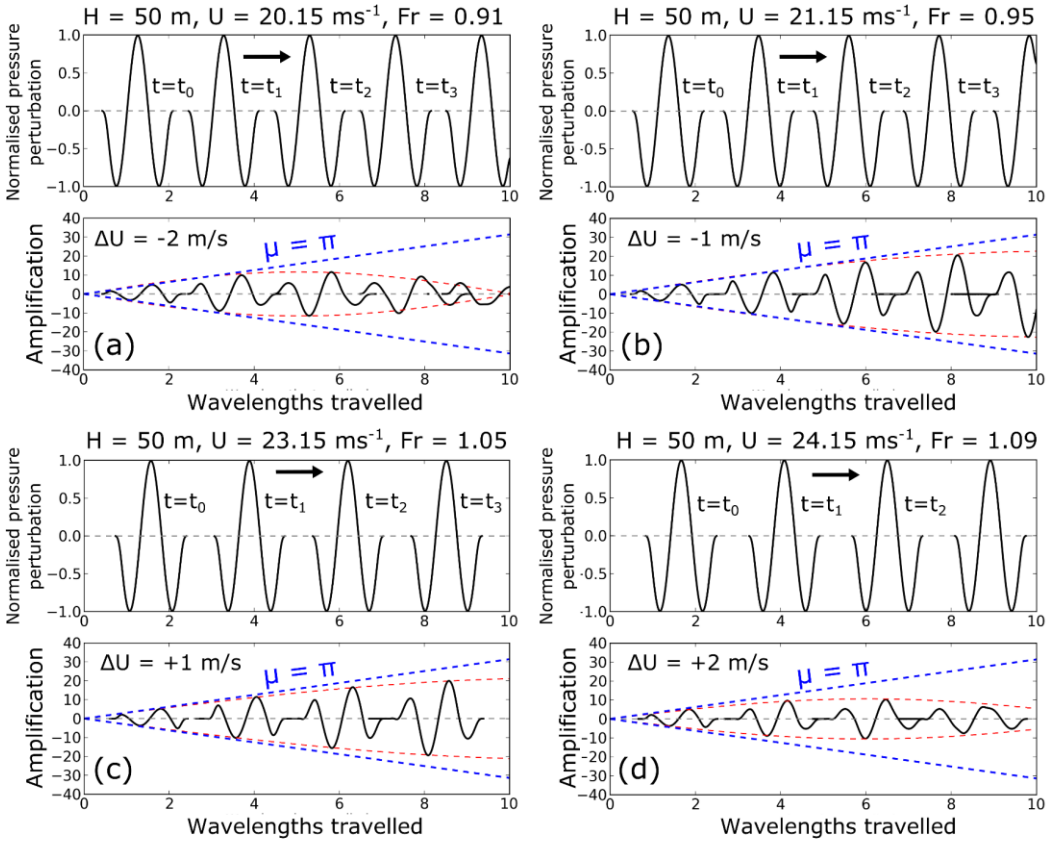

Figure B5 Sea-level responses to constant forcing speeds with a) $\Delta U = -2$ ms^{-1}, b) $\Delta U = -1$ ms^{-1}, c) $\Delta U = +1$ ms^{-1}, d) $\Delta U = +2$ ms^{-1} from the forcing speed required for Proudman resonance ($U_0 = 22.15$ ms^{-1}). Blue dashed lines are the Proudman resonant sea-level envelope responses, red dashed lines are the near Proudman resonance envelope approximations.

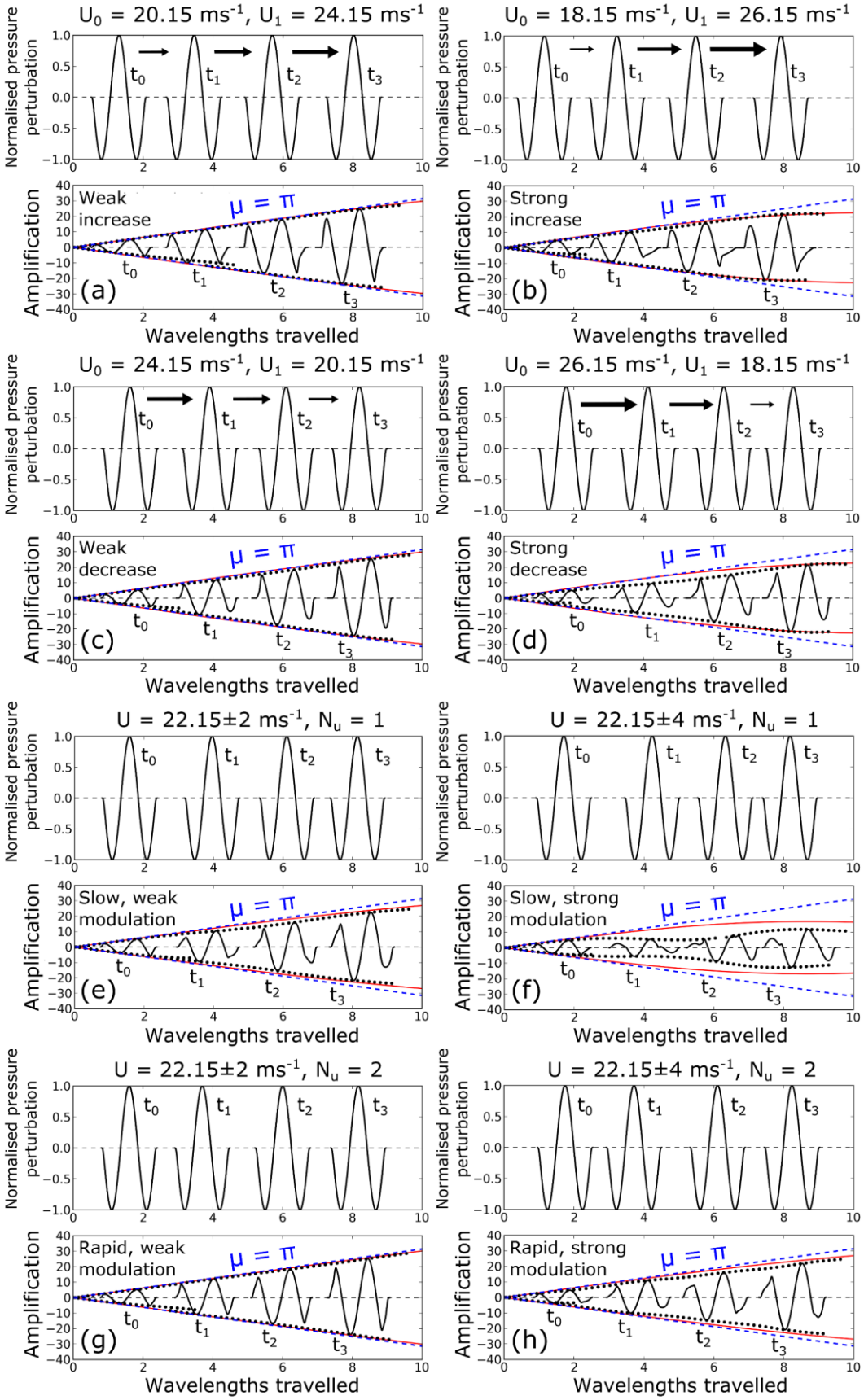
U0 = 20.15 ms-1, U1 = 24.15 ms-1
U0 = 18.15 ms-1, U1 = 26.15 ms-1
U0 = 24.15 ms-1, U1 = 20.15 ms-1
U0 = 26.15 ms-1, U1 = 18.15 ms-1
U = 22.15±2 ms-1, Nu = 1
U = 22.15±4 ms-1, Nu = 1
U = 22.15±2 ms-1, Nu = 2
U = 22.15±4 ms-1, Nu = 2
Normalised pressure perturbation
Amplification
Wavelengths travelled
t0
t1
t2
t3
μ = π
Weak increase
Strong increase
Weak decrease
Strong decrease
Slow, weak modulation
Slow, strong modulation
Rapid, weak modulation
Rapid, strong modulation
(a)
(b)
(c)
(d)
(e)
(f)
(g)
(h)

Figure B6 Sea-level elevation responses to forcings moving at variable forcing speeds with an average speed appropriate for Proudman resonance. Dashed blue lines is wave growth from the mean forcing speed (Proudman resonance). Solid red lines are the envelopes from approximations using an effective forcing speed. Black dots are maximum and minimum values of sea-level amplification at 5-minute intervals. a) linearly increasing speed from 20.15–24.15 ms^{-1}, b) linearly increasing speed from 18.15–26.15 ms^{-1}, c) linearly decreasing speed from 24.15–20.15 ms^{-1}, d) linearly decreasing speed from 26.15–18.15 ms^{-1}, e) sinusoidally varying speed between 20.15–24.15 ms^{-1}, $N_u = 1$, f) sinusoidally varying speed between 18.15–26.15 ms^{-1}, $N_u = 1$, g) sinusoidally varying speed between 20.15–24.15 ms^{-1}, $N_u = 2$, h) sinusoidally varying speed between 18.15–26.15 ms^{-1}, $N_u = 2$.

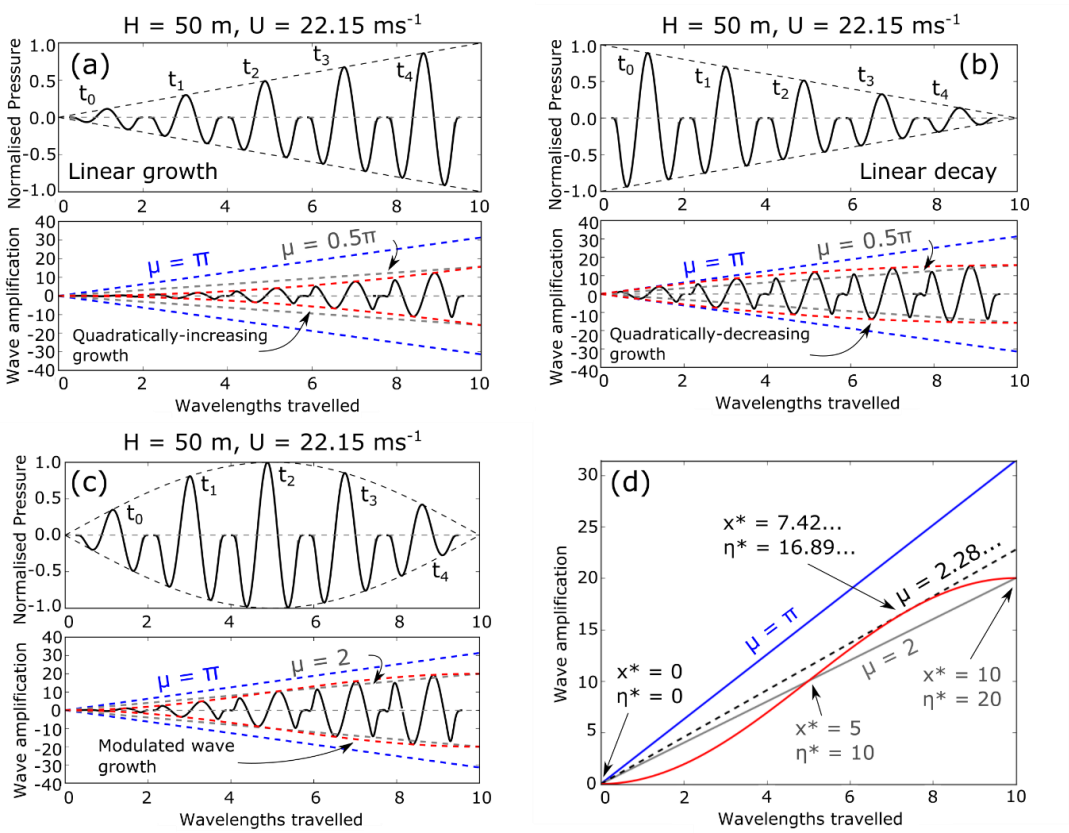

Figure B7 Sea-level elevation amplifications from normalised amplitude-varying atmospheric forcings moving at Proudman resonant speeds at 5 timesteps. a) linearly increasing pressure disturbance (top), resultant sea-level elevation (bottom). b) linearly decreasing pressure disturbance (top), resultant sea-level elevation (bottom). c) sinusoidally growing and decaying pressure disturbance (top), resultant sea-level elevation (bottom). d) sea-level envelopes resulting from a constant-amplitude sinusoidal pressure disturbance (blue), from a sinusoidally modulated sinusoidal pressure disturbance (red), constant-amplitude ramp-like pressure disturbance (grey), and the maximum growth factor of the sinusoidally modulated sinusoidal pressure disturbance (black dashed). Normalised pressure disturbances and amplifications with amplitudes lower than 0.01 and 0.001 respectively have not been shown for clarity.

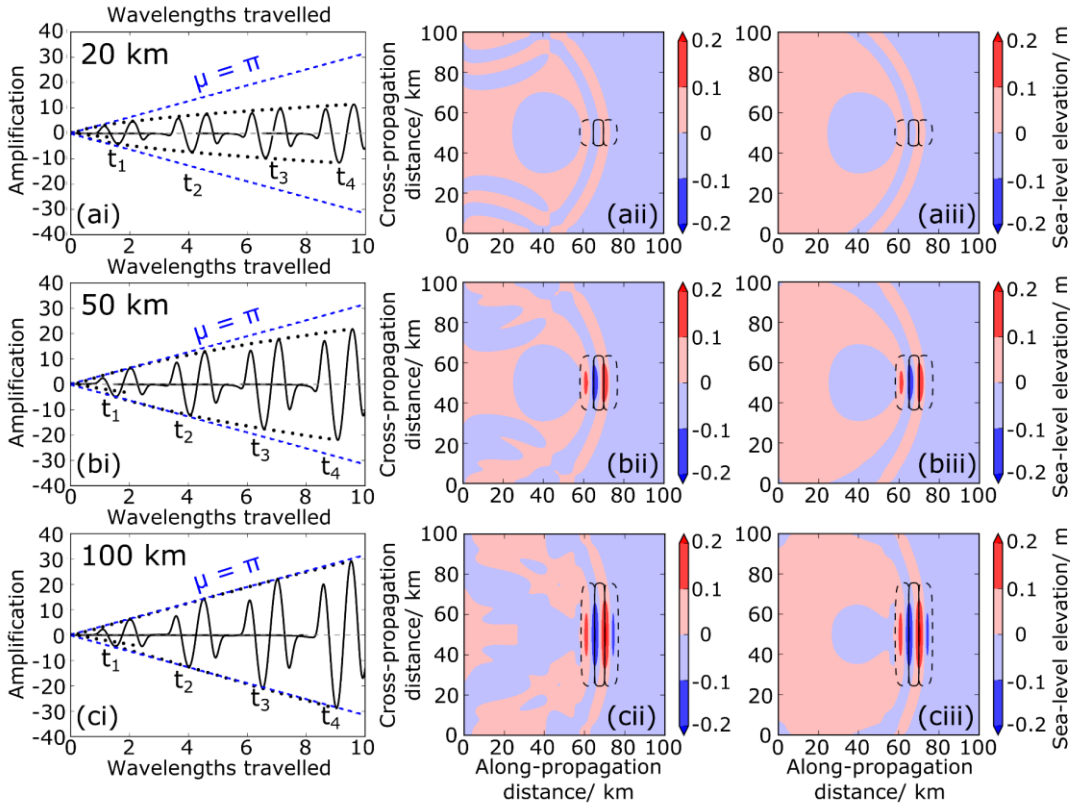

Figure B8 Amplification from synthetic forcings of cross-propagation wavelengths (λ_y) moving at the shallow-water wave speed ($U = \sqrt{gH}$) in the along-propagation direction. a) λ_y = 20 km, A_P = 2, b) λ_y = 50 km, A_P = 5, c) λ_y = 100 km A_P = 10. i) Amplification against wavelengths travelled at four time steps (t_1, t_2, t_3, t_4) along the transect $y = W/2$ = 50 km, with reflecting boundary conditions. Black dots are maximum and minimum amplifications at 100-second time steps. Blue dashed lines are the strict Proudman resonance envelopes ($\mu = \pi$). ii) Sea-level elevation with reflecting boundary conditions, shown as filled coloured contours at time step t_3. Applied synthetic air pressure contours (black) at +1 Pa (solid) and –1 Pa (dashed). iii) Sea-level elevation with radiation boundary conditions, shown as filled coloured contours at time step t_3. The colour bar saturates above 0.2 m and below –0.2 m. Applied synthetic air pressure disturbance contours (black) at ΔP = +1 Pa (solid) and ΔP = –1 Pa (dashed) visualising the extent of the applied pressure disturbance.

Appendix C

The finite-difference model

Both the two-dimensional and one-dimensional shallow-water equations were solved with the finite-difference method for a flat bottom with the assumption that sea-level elevation was much smaller than water depth ($\eta \ll H$). When the two-dimensional shallow-water equations were solved, Equations 5.4, 5.5 and 5.6 (in main text) were discretised on a regular grid. When the one-dimensional shallow-water equations were solved, Equations 5.4 and 5.6 were discretised on a line with $v_y = 0$. The two-dimensional case is outlined, but the method is similar in one dimension.

First, the continuous dimensions x, y and t were discretised. Along-propagation distance was discretised in the range $0 \leq x_i \leq L$ for $i = 0, 1, 2 \ldots I$, cross-propagation distance was discretised in the range $0 \leq y_j \leq W$ for $j = 0, 1, 2 \ldots J$, and time was discretised in the range $0 \leq t_n \leq T$ for $n = 0, 1, 2 \ldots N$. We introduce the notation that $\eta^n_{i,j}$ refers to $\eta = \eta(x_i, y_j, t_n)$. A grid spacing Δx in the x-direction, a grid spacing Δy in the y-direction ($\Delta x = \Delta y$), and a time step Δt were assigned.

Next, Equation 5.4 was differentiated with respect to x, Equation 5.5 was differentiated with respect to y and Equation 5.6 was differentiated with respect to t, and were rewritten as

$$u_{xt} = -\rho^{-1} P_{xx} - g\eta_{xx}, \tag{C1}$$

$$v_{yt} = -\rho^{-1} P_{yy} - g\eta_{yy} \tag{C2}$$

and

$$-\eta_{tt} = H\left(u_{xt} + v_{yt}\right) \tag{C3}$$

In the finite-difference scheme, the sea-level acceleration of the inner-domain free surface at the current time step $\eta^n_{i,j_{tt}}$ was then approximated using second-order central-spaced finite differences, such that

$$\eta^{n}_{i,j_{tt}} \approx H\left[\begin{array}{l}\frac{1}{\rho}\frac{\left(P^{n}_{i+1,j} - 2P^{n}_{i,j} + P^{n}_{i-1,j}\right)}{\Delta x^2} + g\frac{\left(\eta^{n}_{i+1,j} - 2\eta^{n}_{i,j} + \eta^{n}_{i-1,j}\right)}{\Delta x^2} \\ + \frac{1}{\rho}\frac{\left(P^{n}_{i,j+1} - 2P^{n}_{i,j} + P^{n}_{i,j-1}\right)}{\Delta y^2} + g\frac{\left(\eta^{n}_{i,j+1} - 2\eta^{n}_{i,j} + \eta^{n}_{i,j-1}\right)}{\Delta y^2}\end{array}\right]. \quad \text{(C4)}$$

Given this, $\eta^{n}_{i,j_{tt}}$ was integrated twice in time to find $\eta^{n}_{i,j}$. Given the initial condition that

$$\eta^{n=0}_{i,j_{t}} = 0, \quad \text{(C5)}$$

equation C4 was integrated with respect to time to find the current velocity of the free surface:

$$\eta^{n}_{i,j_{t}} \approx \eta^{n-1}_{i,j_{t}} + \eta^{n}_{i,j_{tt}}\Delta t\,, \quad \text{(C6)}$$

and given the second initial condition that:

$$\eta^{n=0}_{i,j} = 0, \quad \text{(C7)}$$

equation C6 was integrated in time to find the sea surface elevation at current time t_n:

$$\eta^{n}_{i,j} \approx \eta^{n-1}_{i,j} + \eta^{n}_{i,j_{t}}\Delta t\,. \quad \text{(C8)}$$

The boundaries reflected waves at $y = 0$ and $y = W$, specifying boundaries that were necessary for direct comparison to one-dimensional solutions with a planar forcing. The boundaries radiated waves (open boundary) at $x = 0$ and $x = L$. Each boundary condition was respectively calculated as

$$\eta_{i,j=0} = \eta_{i,j=1}, \quad \text{(C9)}$$

$$\eta_{i,j=J} = \eta_{i,j=J-1}, \quad \text{(C10)}$$

$$\eta^{n}_{i=I,j_{t}} = -c\frac{\left(\eta^{n}_{i=I,j} - \eta^{n}_{i=I-1,j}\right)}{\Delta x}\,, \quad \text{(C11)}$$

and

$$\eta^{n}_{i=0,j_{t}} = c\frac{\left(\eta^{n}_{i=1,j} - \eta^{n}_{i=0,j}\right)}{\Delta x}. \quad \text{(C12)}$$

Equations C9 and C10 correspond to reflecting boundaries that are accurate to first order, and equations C11 and C12 are radiation conditions that are accurate to first

order. The finite-difference boundary conditions were validated for reflecting boundaries on all sides (e.g. equations C9 and C10 repeated for all four boundaries), and radiation boundaries on all sides (e.g. equations C11 and C12 repeated for all four boundaries) by comparing the propagation of a Gaussian surface elevation initial condition with Telemac results. Our simulations suggest that the radiation conditions may slightly improve free wave height compared to analytical predictions by substituting the free wave speed c with the forcing speed U (error improved by < 1%, with the idea for using U instead of c originally from personal communication with Mirko Orlić), though this was not included in our modelling. We validated the finite-difference method capturing Proudman resonance through comparison to Telemac.

Appendix D

Effective Proudman resonance from an idealised NWP model

Introduction

The third version of the Weather Research and Forecasting model (WRF, or more specifically WRFv3.5) was used to simulate box-model idealisations of linear convective systems. The atmospheric surface pressure disturbance from these WRF simulations were then used as the atmospheric forcing for hydrodynamic simulations in Telemac. The aim of these simulations was to determine if meteotsunamis produced by atmospheric forcings from numerical weather prediction models (NWPs) could be understood using the concepts developed in Chapter 5 for variable atmospheric forcing speeds and amplitudes. Supplementary simulations with synthetic atmospheric forcings (Table D1) were then completed to understand sea-level elevation from NWP models.

WRF model setup

WRF was used to simulate an idealised linear convective system by solving the three-dimensional continuity equation, thermodynamic equation and non-hydrostatic momentum equation (Skamarock et al. 2008). The WRF simulations were achieved by combining the WRFv3 idealised super-cell module and the WRFv3 idealised two-dimensional squall line module.

Many idealisations were made in the WRF simulations. To initialise convection, we prescribed a warm, ellipsoid bubble (7 times longer in y-direction than x-direction) that was 3K warmer than the environmental temperature, in a three-dimensional box with dimensions 800 km × 60 km × 20 km (e.g. Figure D1). Idealised open boundaries (at x = 0 km and x = 800 km) were used to allow movement out of the domain and non-physical periodic boundaries (at y = 0 km and y = 60 km) were used to keep the convective system approximately one-dimensional. The environmental fields that influence how convection develops (e.g. potential temperature, mixing ratio, wind velocity) were prescribed homogeneously on horizontal layers and were constant over time (Table D2). The microphysical parameterisations were also idealised to simplify

development of convection. For further information about the model, the simulation input (Table D3) can be cross-referenced with the WRFv3 User Guide (NOAA 2019).

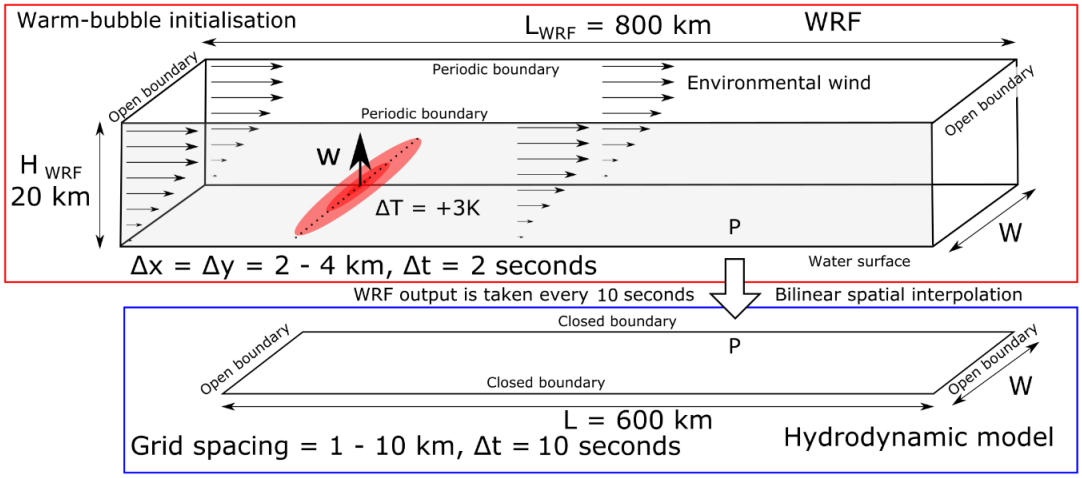

Figure D1 WRF model and Telemac model set-up.

To properly represent the dynamics of mesoscale convective systems, ~1-s time steps and ~1-km grid spacings are generally required (e.g. Horvath and Vilibić 2014; Anderson et al. 2015; Horvath et al. 2018). WRF simulations were run at 2-s time steps, which should be sufficient to model mesoscale convective processes. The model had 40 vertical layers, with finer vertical grid spacing at near the bottom (Table D2), which should also be sufficient to model mesoscale convective processes. Two WRF models were run with different horizontal grid spacings, one with 2-km grid spacing and the other with 4-km grid spacings. These horizontal grid spacings were slightly larger than what might be considered best practice to represent mesoscale processes (e.g. Bennett et al. 2006). However, the grid spacing was small enough for simulations to represent the variable speeds and variable atmospheric surface pressure disturbance amplitudes of observed linear convective systems (e.g. Johnson 2001). The atmospheric surface pressure fields were then taken from WRF and used as input for Telemac (Figure D1).

Telemac model setup

Telemac was used to simulate meteotsunamis produced by the linear convective system by solving the two-dimensional shallow-water equations. At each time step (10-s time step), we bilinearly interpolated the WRF atmospheric surface pressure fields to the Telemac triangular mesh (1-km node spacing). The Telemac domain was shorter (600 km) than the WRF domain (800 km), though the domains were aligned

at the right-hand boundary (Figure D1). This meant that the atmospheric surface pressure disturbance (the forcing) entered the Telemac domain from the left-hand boundary, after convection had initiated. For consistency, we state that the left-hand boundary of the WRF domain started at x = 0 km, and the left-hand boundary of the Telemac domains started at x = 200 km (Figure D1). In Telemac, we used open boundaries (x = 200 km and x = 800 km) to allow waves to move freely out of the domain and closed boundaries (y = 0 km and y = 60 km) to reflect waves from the sides, with the result of minimising two-dimensional wave effects (the Telemac domain acted as a wave guide that could support plane waves).

With the aim of using NWP models to understand external resonance in Telemac, we assigned a constant depth with a corresponding shallow-water wave speed that might be close to the forcing speed. We estimated that the linear convective system might move close to, or slightly slower than, the upper-level wind speed of 25 m s^{-1} (e.g. Markowski and Richardson 2011). Therefore, we assigned a constant depth of 50 m, corresponding to a shallow-water wave speed of 22.15 m s^{-1}.

Results

The high-pass filtered atmospheric surface pressure fields from both the 2-km and 4-km grid spacing WRF simulations showed a linear convective system moving rightwards across the domain (Figure D2a, Figure D2c). In both WRF simulations, the linear convective system also had a pre-squall low, mesohigh and, once the system was mature, a wake low (e.g. Markowski and Richardson 2011, Figure D2c). Although the atmospheric surface pressure disturbances (the forcings) were similar between simulations, the forcings were more heterogeneous with 2-km grid spacings than 4-km grid spacings. Here, the forcing from the 4-km simulation is presented, which has been averaged in the cross-propagation direction to help analysis (Figure D2c). The forcing amplitude increased between 350–550 km (up to about 3–4 hPa), and then the amplitude decreased between 550–800 km. The distance between the pre-squall low minima and wake low minima was about 40-km, corresponding to an approximate forcing wavelength of about 40 km.

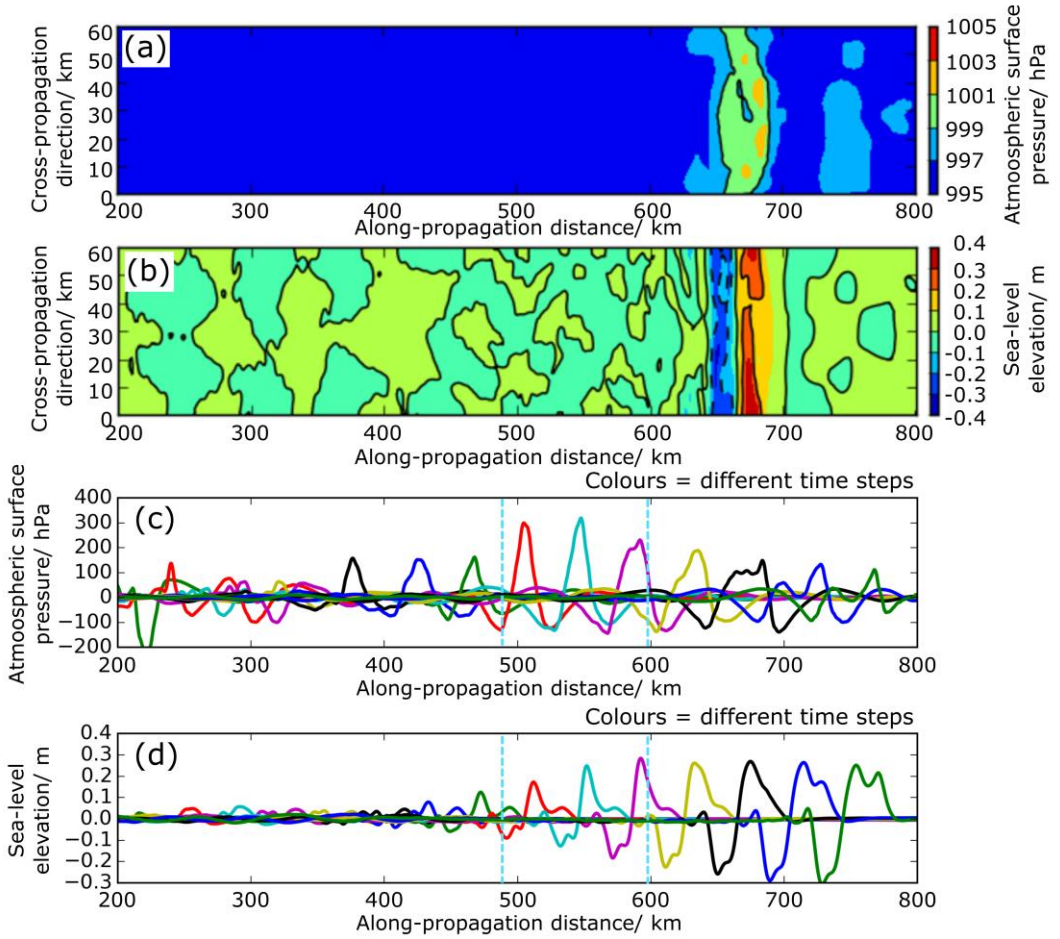

Figure D2 a) Atmospheric surface pressure disturbance from the WRF model with 4-km grid spacing and b) the sea-level disturbance from the Telemac model with 1-km grid spacing at 390-min simulation time, c) atmospheric surface pressure averaged in the cross-propagation direction and d) the sea-level elevation averaged in the cross-propagation direction. Different colours represent time steps that were output at 30-min intervals. Blue lines indicate the extract of Figure D3.

The sea-level elevation (Figure D2b) and high-pass filtered sea-level elevation that was averaged in the cross-propagation direction (Figure D2d) showed a meteotsunami that moved rightwards and grew underneath the forcing. The meteotsunami grew about 10 times (about 0.05 m to 0.50 m) at an increasing rate over about 200 km ($400 < x < 600$ km) and then the wave height remained approximately constant ($600 < x < 800$ km).

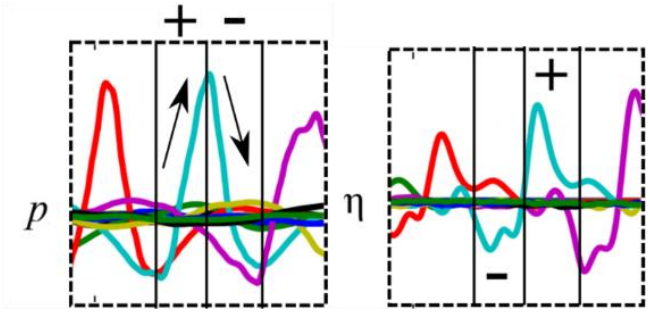

Figure D3 Extracted from Figure D2, showing that the sign of the gradient of the forcing (left) is opposite to the sign of the sea-level disturbance (right). Solid vertical lines are used as indications of where the gradient of the forcing was 0 Pa m^{-1}.

Discussion

To determine whether the meteotsunami grew through Proudman resonance, we quantified the meteotsunami amplification, we compared the sign of the forcing gradient with the sign of the sea-level disturbance, and we compared the forcing speed with the meteotsunami speed. First, we quantified the amount of amplification in comparison to expected amplification from analytical approximations to the forcing under strict Proudman resonance. The meteotsunami amplified by about 10-times over about 200 km (Figure D2d), which means that the meteotsunami amplified by a factor of about 2 for every wavelength moved ($\mu \sim 2$). This amplification is similar to analytical approximations for amplification through Proudman resonance for ramp-like forcings ($\mu = 2$, Hibiya and Kajiura 1982) and sinusoidal forcings ($\mu = \pi$). Thus, the amount of simulated amplification could have originated from a mechanism such as Proudman resonance.

Second, we analysed the sign of the sea-level disturbance relative to the forcing gradient. Directly beneath the forcing, the sign of the sea-level disturbance was opposite to the gradient of the forcing (Figure D3). This relationship would be expected if the forcing moved at the speed of the meteotsunami.

Third, we calculated the speed of the forcing and the meteotsunami. We calculated speeds using one-dimensional cross-correlation analysis on the horizontally averaged atmospheric surface pressure disturbance (Figure D2c) and horizontally averaged sea-level disturbance (Figure D2d) at 5-min intervals. Once the meteotsunami was larger than a few centimetres, the cross-correlation analysis resolved the speed of the meteotsunami, $c \approx 22.15$ m s^{-1}, which was expected from the shallow-water wave

speed (blue line, Figure D4). Over the same region, the calculated speed of the forcing U was on average about 23.2 m s^{-1} and varied between about 18–27 m s^{-1} (red line, Figure D4). Thus, the average Froude number ($\overline{U}/\overline{c}$) was about 1.04 and the instantaneous Froude number ($U(x)/c(x)$) varied between 0.8–1.2 (Figure D4).

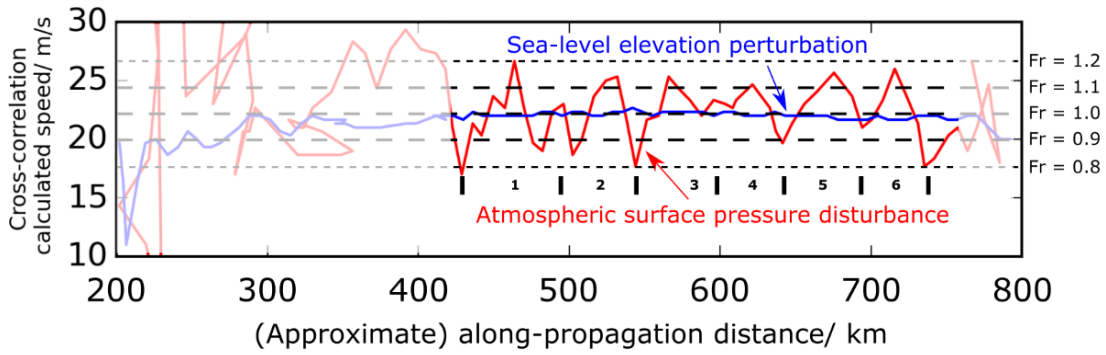

Figure D4 The forcing speed (red) compared to the meteotsunami speed (blue). The location in the along-propagation direction was approximated from the cross-correlation maxima. Dashed lines indicate the Froude number at 0.8, 0.9, 1.0, 1.1 and 1.2. Speeds that are inconsistent with the relevant disturbances are behind semi-transparent white blocks. Bold numbers and ticks refer to speed oscillations used for calculating maximum separation distance and effective forcing speed, N_u.

Then, we determined if the meteotsunami could have grown through effective Proudman resonance by using the relationship between instantaneous forcing speed and effective forcing speed that was developed in Chapter 5. First, we had to decide whether using the effective forcing speed would be appropriate. This decision was aided by calculating the maximum separation distance between the forcing and the meteotsunami. We assumed that the instantaneous forcing speed (Figure D4) could be approximated by a sinusoid and that the forcing speed would not change by calculating speed with intervals shorter than 5 min. Then, we estimated the maximum separation distance as

$$\Delta x_{\max} \approx \frac{\Delta U}{2\pi N_u} T, \tag{D1}$$

where ΔU was the maximum forcing speed variation (9 m s^{-1}), N_u was the number of cycles in the speed of the forcing (N_u = 6, Figure D4), and T was the time that the forcing was coupled to the meteotsunami (here about 9,000–15,000 seconds). Thus, the maximum separation distance was about 2–4 km, which was less than 10% of the forcing wavelength (40 km). This maximum separation distance is probably small

enough that effective Proudman resonance is appropriate. The effective forcing speed U_{eff} was then calculated as

$$U_{\text{eff}} = \overline{U} + \frac{\Delta U}{2\pi N_{\text{u}}}, \tag{D2}$$

giving an effective forcing speed U_{eff} of 23.4 m s^{-1} and an effective Froude number ($\text{Fr}_{\text{eff}} = U_{\text{eff}}/\overline{c}$) of 1.06. Therefore, by using analysis developed from Chapter 5, we propose that the meteotsunami growth can be explained with effective Proudman resonance. The meteotsunami grew, even though the forcing speed varied by 20% from the meteotsunami wave speed, because the forcing did not move too far away from the meteotsunami.

The average forcing speed, and the variability around the average forcing speed, did not change much between 400–750 km (Figure D4). However, the meteotsunami grew at an increasing rate between 400–600 km and grew at a decreasing rate between 600–750 km. To explain the meteotsunami growth, we completed multiple synthetic forcings, varying the average forcing speed (22.15 m s^{-1} or 23.20 m s^{-1}), including amplitude variability (sinusoidal growth, maturation and decay), and including speed variability (ΔU = 9 m s^{-1} and N_{u} = 6). The increasing growth rate (400 < x < 600 km) could only be explained by forcing amplitude variability (Simulations 2, 4, 6 and 8). However, the decreasing growth rate (600 < x < 800 km) would have occurred even without amplitude variability because the average forcing speed was faster than the shallow-water wave speed (e.g. Simulation 3). Including speed variability did not affect these results, which agrees with indications from the calculations of maximum separation distance and effective forcing speed.

Table D1 Synthetic simulations to investigate how average forcing speed, amplitude variability and speed variability affect meteotsunami growth rate.

Simulation number	Average speed/ m s^{-1}	Amplitude variability	Speed variability	Increasing growth rate ($400 < x < 600$ km)	Decreasing growth rate ($600 < x < 800$ km)
1	22.15	Off	Off	No	No
2	22.15	On	Off	Yes	Yes
3	23.20	Off	Off	No	Yes
4	23.20	On	Off	Yes	Yes
5	22.15	Off	On	No	No
6	22.15	On	On	Yes	Yes
7	23.20	Off	On	No	Yes
8	23.20	On	On	Yes	Yes

Conclusion

Therefore, we have explained how a meteotsunami can grow with an atmospheric forcing that has both a variable speed and variable amplitude. By quantifying meteotsunami amplification, relating the sign of the sea-level elevation disturbance to the sign of the forcing gradient, and quantifying the speed of the atmospheric forcing and the wave, we have demonstrated that effective Proudman resonance was the primary growth mechanism. We have also explained that the increasing growth rate were due to changes in the forcing amplitude, but the decreasing growth rate would have occurred even without amplitude variability, because the average forcing speed was faster than the shallow-water wave speed. Importantly, the dimensions, pressure fields and velocity of the simulated linear convective system were not directly controlled, which differentiated this NWP forcing from a synthetic forcing, and meant that wave growth mechanisms had to be diagnosed.

Table D2 WRF model set-up, applied homogeneously across the domain. See potential temperature and mixing ratio sounding profiles in Figure 1 of Weisman and Klemp (1982) and the speed profile (high shear) in Figure 2 of Weisman et al. (1997).

Level height/ m	Potential temperature/ K	Mixing ratio/ g kg^{-1}	u/ m s^{-1}	**Level height/ m**	Potential temperature/ K	Mixing ratio/ g kg^{-1}	u/ m s^{-1}
125	300.5	14	0.6	**6625**	320.5	1.19	25
375	300.6	14	1.9	**6875**	321.4	1.04	25
625	301.1	14	3.1	**7125**	322.4	0.90	25
875	301.6	14	4.4	**7375**	323.4	0.78	25
1125	302.2	14	5.6	**7625**	324.4	0.67	25
1375	302.9	13.1	6.9	**7875**	325.4	0.58	25
1625	303.5	11.9	8.1	**8125**	326.4	0.50	25
1875	304.2	10.7	9.4	**8375**	327.4	0.42	25
2125	304.9	9.7	10.6	**8625**	328.5	0.36	25
2375	305.7	8.8	11.9	**8875**	329.5	0.31	25
2625	306.4	7.9	13.1	**9125**	330.5	0.26	25
2875	307.2	7.1	14.4	**9375**	331.6	0.22	25
3125	308.0	6.4	15.6	**9625**	332.6	0.18	25
3375	308.8	5.7	16.9	**9875**	333.7	0.15	25
3625	309.6	5.2	18.1	**10125**	334.8	0.12	25
3875	310.5	4.6	19.4	**10375**	335.8	0.10	25
4125	311.3	4.1	20.6	**10625**	336.9	0.083	25
4375	312.2	3.7	21.9	**10875**	338.0	0.068	25
4625	313.1	3.3	23.1	**11125**	339.1	0.055	25
4875	313.9	2.9	24.4	**11375**	340.2	0.044	25
5125	314.8	2.6	25	**11625**	341.3	0.035	25
5375	315.8	2.3	25	**11875**	342.4	0.027	25
5625	316.7	2.0	25	**12125**	345.0	0.025	25
5875	317.6	1.8	25	**12375**	349.0	0.026	25
6125	318.6	1.6	25	**12625**	353.0	0.027	25
6375	319.5	1.4	25	**12875**	357.0	0.028	25

Table D2 cont.

Level height/ m	Potential temperature/ K	Mixing ratio/ g kg^{-1}	u/ m s^{-1}	**Level height/ m**	Potential temperature/ K	Mixing ratio/ g kg^{-1}	u/ m s^{-1}
13125	361.2	0.03	25	**19375**	481.1	0.09	25
13375	365.3	0.03	25	**19625**	486.6	0.09	25
13625	369.5	0.03	25	**19875**	492.2	0.09	25
13875	373.8	0.03	25				
14125	378.1	0.04	25				
14375	382.5	0.04	25				
14625	386.9	0.04	25				
14875	391.4	0.04	25				
15125	395.9	0.04	25				
15375	400.4	0.04	25				
15625	405.1	0.05	25				
15875	409.7	0.05	25				
16125	414.4	0.05	25				
16375	419.2	0.05	25				
16625	424.1	0.06	25				
16875	429.0	0.06	25				
17125	434.0	0.06	25				
17375	439.0	0.06	25				
17625	444.0	0.07	25				
17875	449.1	0.07	25				
18125	454.3	0.07	25				
18375	459.5	0.08	25				
18625	464.8	0.08	25				
18875	470.3	0.09	25				
19125	475.6	0.09	25				

Table D3 Relevant WRF input to replicate the simulation (NOAA 2019).

Input	Value	Meaning
mp_physics	10	"Morrison 2-moment" scheme for precipitation
ra_lw_physics	1	"Rapid Radiative Transfer Model" for long-wave radiation
ra_sw_physics	1	"Dudhia Scheme" for short-wave radiation
radt	2	Update radiation physics every 2 min
sf_sfclay_physics	1	"Monin-Obukhov Similar" scheme for the surface layer
sf_ocean_physics	1	Mixed layer ocean
oml_hml0	20	Mixed layer depth (m)
oml_gamma	0.14	Deep water lapse rate (K m^{-1})
bl_pbl_physics	1	YSU boundary layer
bldt	0	Update boundary layer every time step
cu_physics	1	Kain-Fritsch cumulus option
cudt	5	Update cumulus parametrisation every 5 min
sst_update	0	No sea-surface temperature update
rk_ord	3	3rd-order Runge Kutta time stepping
diff_opt	2	Mixing terms are calculated in "physical" space
km_opt	2	1.5 turbulent kinetic energy closure
damp_opt	2	Rayleigh damping
zdamp	5000	Damping depth (m) from model top
dampcoef	0.003	Damping coefficient (inverse time scale, s^{-1})
khdif	500	Horizontal diffusion (m^2 s^{-1})
kvdif	500	Vertical diffusion constant (m^2 s^{-1})
h_mom_adv_order	5	Horizontal momentum advection order
v_mom_adv_order	3	Vertical momentum advection order
non_hydrostatic	True	The model is non-hydrostatic
mix_full_fields	True	The vertical diffusion acts on full fields
pert_coriolis	True	Coriolis is calculated only on the perturbation wind fields.

Appendix E

The stacking correction

The stacking algorithm

A stacking correction was designed to remove unwanted tidal signals that high-pass filtering did not remove. First, the filtered time series were resampled at 1-minute intervals and separated into equal segments (e.g. 12-hr 25-min segments). Seven segments were consecutively taken, and the central (fourth segment) was taken to be the target segment. The correlation coefficient with the target segment and the six other segments (of which three were earlier in time, and three were later in time than the target segment) were calculated. The three segments with the largest correlation coefficients to the target segment were averaged, producing a mean segment. This mean segment was removed from the target segment, leaving a corrected residual. This was repeated for all segments, and the corrected residuals were chronologically recombined.

Synthetic data tests

First, we tested the algorithm on synthetic data, with known properties to test how well the algorithm removed unwanted repeating tidal signals. A synthetic time series with four constituents was created:

1. 12-hour period and 4.5-m amplitude,
2. 6-hour period and 0.10-m amplitude,
3. 4-hour period and 0.05-m amplitude, and
4. 3-hour period and 0.02-m amplitude.

This signal also included a proxy spring-neap (28 day) cycle. Random Gaussian noise was then added to the signal (blue line, Figure E1b) to create the full signal (Figure E1a). The full signal was then filtered with a 2-hour high-pass Butterworth filter (order 4). The result is the filtered-only residual (purple line, Figure E1b). In the filtered-only residual, there are repeating residual wavelets (spikes), that repeat every 12-hours and modulate with the 28-day cycle. These repeating wavelets are seen in the histogram

as long tails (Figure E1c) and large deviations from the perfect correlation between the added Gaussian noise and the recovered residual (Figure E2) and represent the repeating wavelets in the filtered-only residual from real data (Figure E3).

The stacking correction removed most of these repeating wavelets (red line, Figure E1b). The stacking correction also increased the correlation of the added noise with the recovered residual (Figure E2). The filtered-only residuals have a r^2-value of 0.08, whereas the filtered-stacked residuals have a r^2-value of 0.60. The amplitudes in the filtered-stacked residuals are, on average, slightly lower than the added noise but have no offset error (linear regression: gradient = 0.81, offset = 0).

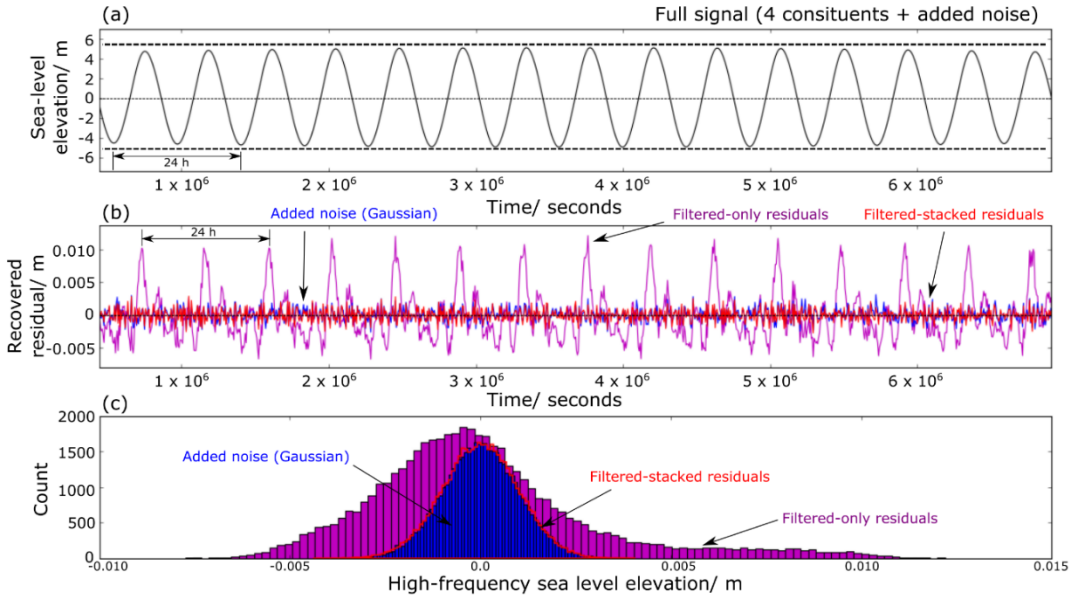

Figure E1 a) A time-series of the full synthetic signal, b) the recovered residual after filtering and stacking, c) a histogram compared the filtered-only residual and the filtered-stacked residuals with the added noise.

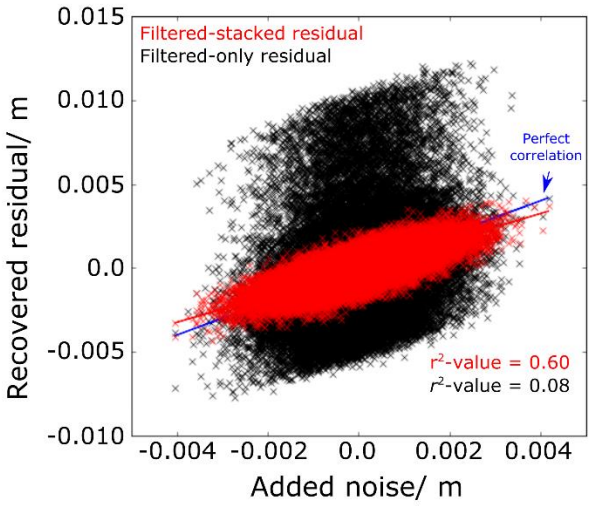

Figure E2 A scatterplot of amplitude of filtered-only residuals compared to added noise (black) and the filtered-stacked residuals to added noise (red). The red line is the linear regression of the filtered-stack residuals of form $y = mx + c$, where $m = 0.81$ and $c = 0$. The blue line is the perfect correlation.

Using the stacking correction on real data

Unfortunately, with real data the unwanted repeating residuals sometimes remained even when the stacking algorithm was applied (e.g. Figure E3). Therefore, after using the stacking correction on real data, the peaks were identified by overlaying the filtered-stacked residual on the filtered-only residual and the following rules were applied:

- If a "filtered-stacked" peak aligned with a "filtered-only" peak, and this peak was part of the repeating residual wavelet signal, then it was removed.
- If a "filtered-stacked" peak aligned with a "filtered-only" peak, and this peak was *not* part of the repeating residual wavelet signal, then it was *not* removed.
- If a "filtered-stacked" peak did not align with a "filtered-only" peak, then it was removed.
- If it was unclear whether a "filtered-stacked" peak should or should not be manually removed, then it was removed.

Manual filtering removed residual data that was considered tidal or erroneous. This included echoes from the stacking correction (e.g. over-corrections) and wavelets that were missed by the stacking correction. Any peak in the filtered-stacked residual to be non-tidal and have a tsunami period was then considered an NSLOTT.

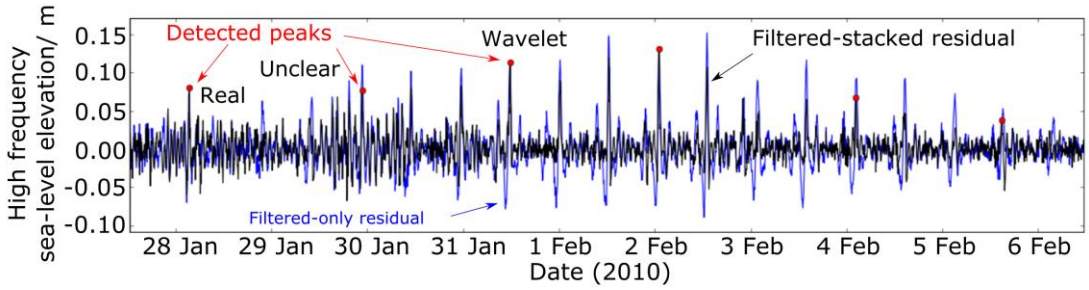

Figure E3 The filtered-only residual is in blue, the filtered-stacked tidal residual is in black. Peaks detected by the automatic peak detection are red dots. The 28 Jan 2010 peak is not part of the repeating wavelet signal. 29 Jan 2010 was unclear, and so was removed from further analysis. Peaks between 31 Jan – 5 Feb 2010 were part of the repeating wavelet signal, and so were removed from further analysis.

Appendix F

The effect of sub-sampling data

The tide gauges used in the climatology may under-represent wave heights in the tsunami-frequency band because of large sampling intervals. This study includes 15-min intervals (the United Kingdom), 10-min intervals (of validated data) in Europe (France, Germany, the Netherlands), 6-min intervals (Republic of Ireland) and 5-min intervals (Belgium and the Republic of Ireland). The aliasing effect was quantified by comparing 5-min data at Ostend and Nieuwpoort that was resampled to 10-min and 15-min intervals after high-pass filtering but before stack-correction (this data was filtered-only). Aliased data were used to compare the average NSLOTT wave height threshold, NSLOTT count (exceeding this threshold), NSLOTT count exceeding 0.3 m, and the largest measured wave height.

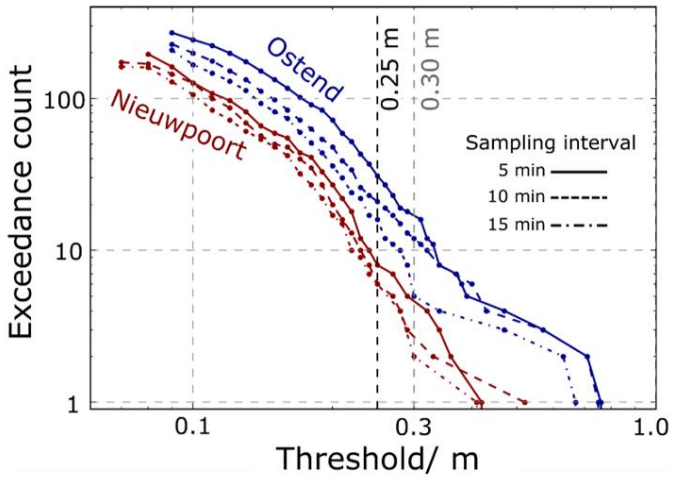

Figure F1 The effect of subsampling Belgian data from 5-min sampling intervals to 10-min and 15-min sampling intervals and Nieuwpoort (maroon) and Ostend (blue).

Table F1 The percentage change on each measurement averaged between Nieuwpoort and Ostend when sub-sampling 5-minute data to 10-min and 15-min intervals.

Sampling interval	10-min	15-min
Standard deviation (σ)	–3%	–4%
NSLOTTs above relative threshold (6σ)	–16%	–22%
NSLOTTs above absolute threshold (0.3 m)	–31%	–64%
Average maximum wave height/ m	+2%	–22%

Sub-sampling the data non-linearly reduced the number of NSLOTTs (Figure F1, Table F1). Sub-sampling Belgian data from 5-minute to 10-minute and 15-min intervals, the standard deviation (σ) only decreased by 3–4%, but the number of NSLOTTs above 6σ decreased by 16–22% and the number of NSLOTTs above 0.3 m decreased by 31–64%. Sub-sampling the data aliased the wave heights and disproportionately decreased the number of NSLOTTs above 0.3 m, reducing by more than half between 5-min to 15-min intervals. Sub-sampling from 5-min to 10-min intervals increased the average maximum wave height by 2%, because the wave period was aliased and one wave at Nieuwpoort appeared larger with 10-min intervals. However, with 15-min data, the average maximum wave height decreased by 22%. Each measure reduced by more with the 15-minute intervals than the 10-minute intervals, and the number of NSLOTTs above 0.3 m were most affected by longer sampling intervals.

Previous studies have used 0.3 m with 6-minute sampled data to determine meteotsunami occurrence (e.g. Bechle et al. 2016). From the Belgian data, 42 NSLOTTs exceeded 0.3-m high for 5-minute data (N = 42), however, only 15 NSLOTTs exceeded 0.3-m high for 15-minute data (N = 15). To achieve a similar count with aliased data to other climatologies, a lower threshold was used. A 0.25-m threshold produced an NSLOTT count for 15-minute data (N = 41) that was closest to the 5-minute data with 0.3-m threshold (N = 42) (Figure F1). Though this did not fully counteract the aliasing effect, we used a lower absolute amplitude threshold that acknowledged the lower sampling intervals.

Bibliography

Agee, E.M., and K.E. Dowell, 1974: Observational Studies of Mesoscale Cellular Convection. *J. Appl. Meteorol.*, **13**, 46–53, doi:10.1175/1520-0450(1974)013<0046:OSOMCC>2.0.CO;2.

Airy, G.B., 1841: art. Tides and waves. *Encyclopaedia Metropolitana* (1817–1845), Mixed Sciences, Vol. 3, ed. HJ Rose, et al. Also *Trigonometry, On the Figure of the Earth, Tides and Waves*. 396 pp. C Plates. n.d., n.p.

Anderson, E.J., A.J. Bechle, C.H. Wu, D.J. Schwab, G.E. Mann, and K.A. Lombardy, 2015: Reconstruction of a meteotsunami in Lake Erie on 27 May 2012: Roles of atmospheric conditions on hydrodynamic response in enclosed basins. *J. Geophys. Res. Oceans*, **120**, 8020–8038, doi:10.1002/2015JC010883.

Antonescu, B., G. Vaughan, and D.M. Schultz, 2013: A Five-Year Radar-Based Climatology of Tropopause Folds and Deep Convection over Wales, United Kingdom. *Mon. Weather Rev.*, **141**, 1693–1707, doi:10.1175/MWR-D-12-00246.1.

Asano, T., T. Yamashiro, and N. Nishimura, 2012: Field observations of meteotsunami locally called “abiki” in Urauchi Bay, Kami-Koshiki Island, Japan. *Nat. Hazards*, **64**, 1685–1706, doi:10.1007/s11069-012-0330-2.

Asano, T., T. Yamashiro, and T. Kakinuma, 2010: Field observations of seiche events in a T-shape bay of Kami-Koshiki island, Japan. *Proceedings of the 32nd International Conference on Coastal Engineering*, 30 June – 5 July 2010, Shanghai, China, 1–12.

Bakan, S., and E. Schwarz, 1992: Cellular convection over the North-Eastern Atlantic. *Int. J. Climatol.*, **12**, 353–367, doi:10.1002/joc.3370120404.

Baptista, M.A., S. Heitor, J.M. Miranda, P. Miranda, and L. Mendes-Victor, 1998: The 1755 Lisbon tsunami; evaluation of the tsunami parameters. *J. Geodyn.*, **25**, 143–157, doi:10.1016/S0264-3707(97)00019-7.

Bechle, A.J., and C.H. Wu, 2014: The Lake Michigan meteotsunamis of 1954 revisited. *Nat. Hazards*, **74**, 155–177, doi:10.1007/s11069-014-1193-5.

Bechle, A.J., C.H. Wu, D.A.R. Kristovich, E.J. Anderson, D.J. Schwab, and A.B. Rabinovich, 2016: Meteotsunamis in the Laurentian Great Lakes. *Sci. Rep.*, **6**, 37832, doi:10.1038/srep37832.

Bechle, A.J., D.A.R. Kristovich, and C.H. Wu, 2015: Meteotsunami occurrences and causes in Lake Michigan. *J. Geophys. Res. Oceans*, **120**, 8422–8438, doi:10.1002/2015JC011317.

Belušić, D., and N.S. Mahović, 2009: Detecting and following atmospheric disturbances with a potential to generate meteotsunamis in the Adriatic. *Phys. Chem. Earth.*, **34**, 918–927, doi:10.1016/j.pce.2009.08.009.

Belušić, D., B. Grisogono, and Z.B. Klaić, 2007: Atmospheric origin of the devastating coupled air-sea event in the east Adriatic. *J. Geophys. Res. Atmos.*, **112**, D17111, doi:10.1029/2006JD008204.

Bennett, L.J., K.A. Browning, A.M. Blyth, D.J. Parker, and P.A. Clark, 2006: A review of the initiation of precipitating convection in the United Kingdom. *Q. J. R. Meteorol. Soc.*, **132**, 1001–1020, doi:10.1256/qj.05.54.

Bourgeois, J., 2009: Geologic effects and records of tsunamis. *The Sea*, **15**, 53–91.

Bubalo, M., I. Janeković, and M. Orlić, 2018: Chrystal and Proudman resonances simulated with three numerical models. *Ocean Dynam.*, **68**, 497–507, doi:10.1007/s10236-018-1146-8.

Bubalo, M., I. Janeković, and M. Orlić, 2019: Simulation of flooding and drying as an essential element of meteotsunami modelling. *Cont. Shelf Res.*, **184**, 81–90, doi:10.1016/j.csr.2019.07.003.

Butterworth, S., 1930: On the Theory of Filter Amplifiers. *Exp. Wireless Wireless Eng.*, **7**, 536–541.

Canadian Hydraulics Centre, 2016: *Blue Kenue*. National Research Council Canada, 29 April 2016, https://www.nrc-cnrc.gc.ca/eng/solutions/advisory/blue_kenue_index.html.

Candela, J., S. Mazzola, C. Sammari, R. Limeburner, C.J. Lozano, B. Patti, and A. Bonanno, 1999: The "Mad Sea" Phenomenon in the Strait of Sicily. *J. Phys. Oceanogr.*, **29**, 2210–2231, doi:10.1175/1520-0485(1999)029<2210:TMSPIT>2.0.CO;2.

Candella, R.N., 2009: Meteorologically induced strong seiches observed at Arraial do Cabo, RJ, Brazil. *Phys. Chem. Earth.*, **34**, 989–997, doi:10.1016/j.pce.2009.06.007.

Carlson, T.N., and F.H. Ludlam, 1968: Conditions for the occurrence of severe local storms. *Tellus*, **20**, 203–226, doi:10.1111/j.2153-3490.1968.tb00364.x.

Carvajal, M., M. Contreras-López, P. Winckler, and I. Sepúlveda, 2017: Meteotsunamis occurring along the southwest coast of South America during an intense storm. *Pure Appl. Geophys.*, **174**, 3313–3323, doi:10.1007/s00024-017-1584-0.

Chen, Y., and X. Niu, 2018: Forced wave induced by an atmospheric pressure disturbance moving towards shore. *Cont. Shelf Res.*, **160**, 1–9, doi:10.1016/j.csr.2018.03.007.

Cho, K.H., J.Y. Choi, K.S. Park, S.K. Hyun, Y. Oh, and J.Y. Park, 2013: A synoptic study on tsunami-like sea level oscillations along the west coast of Korea using an unstructured grid ocean model. *J. Coast. Res.*, **65**, 678–683, doi:10.2112/SI65-115.1.

Choi, B.J., C. Hwang, and S.H. Lee, 2014: Meteotsunami-tide interactions and high-frequency sea level oscillations in the eastern Yellow Sea. *J. Geophys. Res. Oceans*, **119**, 6725–6742, doi:10.1002/2013JC009788.

Churchill, D.D., S.H. Houston, and N.A. Bond, 1995: The Daytona Beach Wave of 3–4 July 1992: A Shallow-Water Gravity Wave Forced by a Propagating Squall Line. *Bull. Amer. Meteor. Soc.*, **76**, 21–32, doi:10.1175/1520-0477(1995)076,0021: TDBWOJ.2.0.CO;2.

Copernicus Climate Change Service (C3S), 2017: *ERA5: Fifth generation of ECMWF atmospheric reanalyses of the global climate*. Copernicus Climate Change Service Climate Data Store (CDS), 26 July 2019, https://cds.climate.copernicus.eu/cdsapp#!/home.

Cotton, W.R., G.H. Bryan, and S.C. van den Heever, 2011: *Storm and Cloud Dynamics*. Second Edition, Academic Press, 809 pp.

Davies, A.M., 1986: A Three-Dimensional Model of the Northwest European Continental Shelf, with Application to the M_4 Tide. *J. Phys. Oceanogr.*, **16**, 797–813, doi:10.1175/1520-0485(1986)016<0797:ATDMOT>2.0.CO;2.

de Jong, M.P.C., and J.A. Battjes, 2004: Low-frequency sea waves generated by atmospheric convection cells. *J. Geophys. Res. Oceans*, **109**, C01011, doi:10.1029/2003JC001931.

de Jong, M.P.C., L.H. Holthuijsen, and J.A. Battjes, 2003: Generation of seiches by cold fronts over the southern North Sea. *J. Geophys. Res. Oceans*, **108**, 3117, doi:10.1029/2002JC001422.

Denamiel, C., J. Šepić, and I. Vilibić, 2018: Impact of Geomorphological Changes to Harbor Resonance During Meteotsunamis: The Vela Luka Bay Test Case. *Pure Appl. Geophys.*, **175**, 3839–3859, doi:10.1007/s00024-018-1862-5.

Denamiel, C., J. Šepić, D. Ivanković, and I. Vilibić, 2019: The Adriatic Sea and Coast modelling suite: Evaluation of the meteotsunami forecast component. *Ocean Modell.*, **135**, 71–93, doi:10.1016/j.ocemod.2019.02.003.

Douglas, C.K.M., 1929: The line-squall and channel wave of July 20th, 1929. *Meteorol. Mag.*, **64**, 187–189.

Dragani, W.C., E.E. D'Onofrio, F. Oreiro, G. Alonso, M. Fiore, and W. Grismeyer, 2014: Simultaneous meteorological tsunamis and storm surges at Buenos Aires coast, southeastern South America. *Nat. Hazards*, **74**, 269–280, doi:10.1007/s11069-013-0836-2.

Drago, A., 2009: Sea level variability and the 'Milghuba' seiche oscillations in the northern coast of Malta, Central Mediterranean. *Phys. Chem. Earth.*, **34**, 948–970, doi:10.1016/j.pce.2009.10.002.

Dusek, G., C. DiVeglio, L. Licate, L. Heilman, K. Kirk, C. Paternostro, and A. Miller, 2019: A Meteotsunami Climatology along the U.S. East Coast. *Bull. Amer. Meteor. Soc.*, **100**, 1329–1345, doi:10.1175/BAMS-D-18-0206.1.

Dziewoński, A.M., T.A. Chou, and J.H. Woodhouse, 1981: Determination of Earthquake Source Parameters From Waveform Data for Studies of Global and Regional Seismicity. *J. Geophys. Res. Solid Earth*, **86**, 2825–2852, doi:10.1029/JB086iB04p02825.

Egbert, G.D., and S.Y. Erofeeva, 2002: Efficient Inverse Modeling of Barotropic Ocean Tides. *J. Atmos. Ocean. Tech.*, **19**, 183–204, doi:10.1175/1520-0426(2002)019<0183:EIMOBO>2.0.CO;2.

Egbert, G.D., S.Y. Erofeeva, and R.D. Ray, 2010: Assimilation of altimetry data for nonlinear shallow-water tides: Quarter-diurnal tides of the Northwest European Shelf. *Cont. Shelf Res.*, **30**, 668–679, doi:10.1016/j.csr.2009.10.011.

Ekström, G., M. Nettles, and A.M. Dziewoński, 2012: The global CMT project 2004–2010: Centroid-moment tensors for 13,017 earthquakes. *Phys. Earth Planet. Inter.*, **200–201**, 1–9, doi:10.1016/j.pepi.2012.04.002.

Euler, L., 1761: Principia motus fluidorum. *Novi Commentarii Acad. Sci. Petropolitanae*, **6**, 271–311.

Ewing, M., F. Press, and W.L. Donn, 1954: An explanation of the Lake Michigan Wave of 26 June 1954. *Science*, **120**, 684–686, doi:10.1126/science.120.3122.684.

Fairman, J.G. Jr., D.M. Schultz, D.J. Kirshbaum, S.L. Gray, and A.I. Barrett, 2017: Climatology of Size, Shape, and Intensity of Precipitation Features over Great Britain and Ireland. *J. Hydrometeorol.*, **18**, 1595–1615, doi:10.1175/JHM-D-16-0222.1.

Fairman, J.G. Jr., D.M. Schultz, D.J. Kirshbaum, S.L. Gray, and A.I. Barrett, 2016: Climatology of Banded Precipitation over the Contiguous United States. *Mon. Weather Rev.*, **144**, 4553–4568, doi:10.1175/MWR-D-16-0015.1.

Frère, A., C. Daubord, A. Gailler, and H. Hébert, 2014: Sea level surges of June 2011 in the NE Atlantic Ocean: observations and possible interpretation. *Nat. Hazards*, **74**, 179–196, doi:10.1007/s11069-014-1103-x.

Funabashi, Y., and K. Kitazawa, 2012: Fukushima in review: A complex disaster, a disastrous response. *Bull. At. Sci.*, **68**, 9–21, doi:10.1177/0096340212440359.

Gallus, W.A. Jr., N.A. Snook, and E.V. Johnson, 2008: Spring and Summer Severe Weather Reports over the Midwest as a Function of Convective Mode: A Preliminary Study. *Weather Forecast.*, **23**, 101–113, doi:10.1175/2007WAF2006120.1.

Geist, E.L., V.V. Titov, D. Arcas, F.F. Pollitz, and S.L. Bilek, 2007: Implications of the 26 December 2004 Sumatra-Andaman Earthquake on Tsunami Forecast and Assessment Models for Great Subduction-Zone Earthquakes. *Bull. Seismol. Soc. Am.*, **97**, S249–S270, doi:10.1785/0120050619.

Giachetti, T., R. Paris, K. Kelfoun, and B. Ontowirjo, 2012: Tsunami hazard related to a flank collapse of Anak Krakatau Volcano, Sunda Strait, Indonesia. *Geological Society, London, Special Publications*, **361**, 79–90, doi:10.1144/SP361.7.

Goring, D.G., 2005: Rissaga (long-wave events) on New Zealand's Eastern Seaboard: A Hazard for Navigation. *Proceedings of the 17th Australasian Coastal Ocean Engineering Conference*, 20–23 September 2005, Adelaide, Australia, 137–141.

Green, G., 1838: On the motion of waves in a variable canal of small depth and width. *Trans. Cambridge Philos. Soc.*, **6**, 457–462.

Greenspan, H.P., 1956: The generation of edge waves by moving pressure distributions. *J. Fluid Mech.*, **1**, 574–592, doi:10.1017/S002211205600038X.

Grilli, S.T., D.R. Tappin, S. Carey, S.F.L. Watt, S.N. Ward, A.R. Grilli, S.L. Engwell, C. Zhang, J.T. Kirby, L. Schambach, and M. Muin, 2019: Modelling of the tsunami from the December 22, 2018 lateral collapse of Anak Krakatau volcano in the Sunda Straits, Indonesia. *Sci. Rep.*, **9**, 11946, doi:10.1038/s41598-019-48327-6.

Grilli, S.T., J.C. Harris, T.S.T. Bakhsh, T.L. Masterlark, C. Kyriakopoulos, J.T. Kirby, and F. Shi, 2013: Numerical Simulation of the 2011 Tohoku Tsunami based on a New Transient FEM co-seimic source: Comparison to Far- and Near-field Observations. *Pure Appl. Geophys.*, **170**, 1333–1359, doi:10.1007/s00024-012-0528-y.

Haflidason, H., H.P. Sejrup, A. Nygård, J. Mienert, P. Bryn, R. Lien, C.F. Forsberg, K. Berg, and D. Masson, 2004: The Storegga Slide: architecture, geometry and slide development. *Mar. Geol.*, **213**, 201–234, doi:10.1016/j.margeo.2004.10.007.

Haigh, I.D., M.P. Wadey, T. Wahl, O. Ozsoy, R.J. Nicholls, J.M. Brown, K.J. Horsburgh, and B. Gouldby, 2016: Spatial and temporal analysis of extreme sea level and storm surge events around the coastline of the UK. *Sci. Data*, **3**, 160107, doi:10.1038/sdata.2016.107.

Haigh, I., R. Nicholls, and N. Wells, 2010: Assessing changes in extreme sea levels: Application to the English Channel, 1900–2006. *Cont. Shelf Res.*, **30**, 1042–1055, doi:10.1016/j.csr.2010.02.002.

Haslett, S.K., and E.A. Bryant, 2009: Meteorological Tsunamis in Southern Britain: An Historical Review. *Geogr. Rev.*, **99**, 146–163, doi:10.1111/j.1931-0846.2009.tb00424.x.

Haslett, S.K., H.E. Mellor, and E.A. Bryant, 2009: Meteo-tsunami hazard associated with summer thunderstorms in the United Kingdom. *Phys. Chem. Earth.*, **34**, 1016–1022, doi:10.1016/j.pce.2009.10.005.

Hayashi, Y., H. Tsushima, K. Hirata, K. Kimura, and K. Maeda, 2011: Tsunami source area of the 2011 off the Pacific coast of Tohoku Earthquake determined from tsunami arrival times at offshore observation stations. *Earth Planets Space*, **63**, 809–813, doi:10.5047/eps.2011.06.042.

Heidarzadeh, M., J. Šepić, A. Rabinovich, M. Allahyar, A. Soltanpour, and F. Tavakoli, 2019: Meteorological Tsunami of 19 March 2017 in the Persian Gulf: Observations and Analyses. *Pure Appl. Geophys.*, **176**, 1–29, doi:10.1007/s00024-019-02263-8.

Hervouet, J.M., 2000: TELEMAC modelling system: An overview. *Hydrol. Process.*, **14**, 2209–2210, doi:10.1002/1099-1085(200009)14:13<2209::AID-HYP23>3.0.CO;2-6.

Hibiya, T., and K. Kajiura, 1982: Origin of the Abiki Phenomenon (a Kind of Seiche) in Nagasaki Bay. *J. Oceanogr. Soc. Japan*, **38**, 172–182, doi:10.1007/BF02110288.

Hill, J., G.S. Collins, A. Avdis, S.C. Kramer, and M.D. Piggott, 2014: How does multiscale modelling and inclusion of realistic palaeobathymetry affect numerical simulation of the Storegga Slide tsunami? *Ocean Modell.*, **83**, 11–25, doi:10.1016/j.ocemod.2014.08.007.

Holroyd, E.W. III, 1971: Lake-effect cloud bands as seen from weather satellites. *J. Atmos. Sci.*, **28**, 1165–1170, doi:10.1175/1520-0469(1971)028<1165:LECBAS>2.0.CO;2.

Horsburgh, K.J., C. Wilson, B.J. Baptie, A. Cooper, D. Cresswell, R.M.W. Musson, L. Ottemöller, S. Richardson, and S.L. Sargeant, 2008: Impact of a Lisbon-type tsunami on the U.K. coastline and the implications for tsunami propagation over broad continental shelves. *J. Geophys. Res. Oceans*, **113**, C04007, doi:10.1029/2007JC004425.

Horvath, K., and I. Vilibić, 2014: Atmospheric mesoscale conditions during the Boothbay meteotsunami: a numerical sensitivity study using a high-resolution mesoscale model. *Nat. Hazards*, **74**, 55–74, doi:10.1007/s11069–014-1055-1.

Horvath, K., J. Šepić, and M.T. Prtenjak, 2018: Atmospheric Forcing Conducive for the Adriatic 25 June 2014 Meteotsunami Event. *Pure Appl. Geophys.*, **175**, 3817–3837, doi:10.1007/s00024-018-1902-1.

Houze, R.A. Jr., 2014: *Cloud dynamics*. Academic press, 496 pp.

Hunt, J.E., R.B. Wynn, P.J. Talling, and D.G. Masson, 2013: Multistage collapse of eight western Canary Island landslides in the last 1.5 Ma: Sedimentological and geochemical

evidence from subunits in submarine flow deposits. *Geochem. Geophys. Geosyst.*, **14**, 2159–2181, doi:10.1002/ggge.20138.

IOC, 2006: *Manual on sea level measurement and interpretation.* Volume IV-An update to 2006. Intergovernmental Oceanographic Commission, Manuals and Guides, 14, Paris.

IOC, IHO, and BODC, 2003: *GEBCO Digital Atlas*. Centenary ed. British Oceanographic Data Centre, CD-ROM.

IPCC, 2013: *Summary for Policymakers. In: Climate Change 2013: The Physical Science Basis*. Contribution of Working Group I to the Fifth Assessment Report of the Intergovernmental Panel on Climate Change [Stocker, T.F., D. Qin, G.-K. Plattner, M. Tignor, S.K. Allen, J. Boschung, A. Nauels, Y. Xia, V. Bex and P.M. Midgley (eds.)]. Cambridge University Press, Cambridge, United Kingdom and New York, NY, USA.

Jan Konig, 2017: *Mini tsunami on European coast*. YouTube, 11 Sep 2019, https://www.youtube.com/watch?v=CjQk_xt_WU0.

Johnson, R.H., 2001: Surface Mesohighs and Mesolows. *Bull. Amer. Meteor. Soc.*, **82**, 13–32, doi:10.1175/1520-0477(2001)082<0013:SMAM>2.3.CO;2.

Kalnay, E., et al., 1996: The NCEP/NCAR 40-Year Reanalysis Project. *Bull. Amer. Meteor. Soc.*, **77**, 437–471, doi:10.1175/1520-0477(1996)077,0437:TNYRP.2.0.CO;2.

Kim, H., M.S. Kim, H.J. Lee, S.B. Woo, and Y.K. Kim, 2016: Seasonal Characteristics and Mechanisms of Meteo-tsunamis on the West Coast of Korean Peninsula. *J. Coast. Res.*, **75**, 1147–1151, doi:10.2112/SI75-230.1.

Kinsman, B., 1965: *Wind Waves: Their Generation and Propagation on the Ocean Surface.* Englewood Cliffs, New Jersey, Prentice Hall, 676 pp.

Knutson, T.R., J.L. McBride, J. Chan, K. Emanuel, G. Holland, C. Landsea, I. Held, J.P. Kossin, A.K. Srivastava, and M. Sugi, 2010: Tropical cyclones and climate change. *Nat. Geosci.*, **3**, 157–163, doi:10.1038/ngeo779.

Lagrange, J.L., 1781: Mémoire sur la théorie du mouvement des fluides. *Nouv. Mém. Acad.*, Berlin, p. 196. Also in 1867–1892. Oeuvres de Lagrange, **4**, 695–748. Paris: Gauthier-Villars.

Lagrange, J.L., 1786: Sur la manière de rectifier deux entroits des Principes de Newton relatifs à la propagation du son et au mouvement des ondes. *Nouv. Mém. Acad.*, Berlin. 1889. Also 1867–1892. Oeuvres de Lagrange, **5**, 591–609. Paris: Gauthier-Villars.

Lamb, H., 1932: *Hydrodynamics*. Cambridge University Press, Cambridge.

Laplace, P.S. Marquis de., 1776: Suite des récherches sur plusieurs points du système du monde (XXV–XXVII). *Mém. Présentés Divers Savans Acad. R. Sci. Inst*., France, pp. 525–552.

Large, W.G., and S. Pond, 1981: Open Ocean Momentum Flux Measurements in Moderate to Strong Winds. *J. Phys. Oceanogr.*, **11**, 324–336, doi:10.1175/1520-0485(1981)011,0324:OOMFMI.2.0.CO;2.

Latter, J.H., 1981: Tsunamis of volcanic origin: Summary of causes, with particular reference to Krakatoa, 1883. *Bulletin Volcanologique*, **44**, 467–490, doi:10.1007/BF02600578.

Levin, B.W., and M.A. Nosov, 2016: *Physics of Tsunamis*. Second Edition. Springer, 388 pp.

Lewis, M.W., and S.L. Gray, 2010: Categorisation of synoptic environments associated with mesoscale convective systems over the UK. *Atmos. Res.*, **97**, 194–213, doi:10.1016/j.atmosres.2010.04.001.

Li, Y.C., and J.B. Herbich, 1982: Effect of wave-current interaction on the wave parameter. *Proceedings of the 18th International Conference on Coastal Engineering*, 14–19 November 1982, American Society of Civil Engineers, Cape Town, South Africa.

Ličer, M., B. Mourre, C. Troupin, A. Krietemeyer, A. Jansá, and J. Tintoré, 2017: Numerical study of the Balearic meteotsunami generation and propagation under synthetic gravity wave forcing. *Ocean Modell.*, **111**, 38–45, doi:10.1016/j.ocemod.2017.02.001.

Lin, L.C., and M.C. Liang, 2017: Meteotsunamis produced by high frequency atmospheric pressure forcing. *Terr. Atmos. Ocean. Sci.*, **28**, 1033–1040, doi:10.3319/TAO.2017.03.20.01.

Linares, Á., and A.J. Bechle, 2018: Meteotsunami-induced rip currents on 4 July 2003 in Warren Dunes, Lake Michigan. *2018 Ocean Sciences Meeting*, 11–16 February 2018, Portland, Oregon, American Geophysical Union, PO31A-03.

Linares, Á., C.H. Wu, A.J. Bechle, E.J. Anderson, and D.A.R. Kristovich, 2019: Unexpected rip currents induced by a meteotsunami. *Sci. Rep.*, **9**, 2105, doi:10.1038/s41598-019-38716-2.

Linares, Á., A.J. Bechle, and C.H. Wu, 2016: Characterization and assessment of the meteotsunami hazard in northern Lake Michigan. *J. Geophys. Res. Oceans*, **121**, 7141–7158, doi:10.1002/2016JC011979.

Liu, C., and E. Zipser, 2013: Regional variation of morphology of organized convection in the tropics and subtropics. *J. Geophys. Res. Atmos.*, **118**, 453–466, doi:10.1029/2012JD018409.

Løvholt, F., G. Pedersen, and G. Gisler, 2008: Oceanic propagation of a potential tsunami from the La Palma Island. *J. Geophys. Res. Oceans*, **113**, C09026, doi:10.1029/2007JC004603.

Markowski, P., and Y. Richardson, 2011: *Mesoscale Meteorology in Midlatitudes*. Vol. 2. John Wiley & Sons, 430 pp.

Maskell, J.H., 2011: *Modelling Storm Surges in the Irish and Celtic Seas using a Finite Element Model (TELEMAC)*. PhD dissertation, University of Liverpool, 280 pp.

Masson, D.G., C.B. Harbitz, R.B. Wynn, G. Pederson, and F. Løvholt, 2006: Submarine landslides: processes, triggers and hazard prediction. *Phil. Trans. R. Soc. A*, **364**, 2009–2039, doi:10.1098/rsta.2006.1810.

Mecking, J.V., C.T. Fogarty, R.J. Greatbatch, J. Sheng, and D. Mercer, 2009: Using atmospheric model output to simulate the meteorological tsunami response to Tropical Storm Helene (2000). *J. Geophys. Res. Oceans*, **114**, C10005, doi:10.1029/2009JC005290.

Mehra, P., R.G. Prabhudesai, A. Joseph, V. Kumar, Y. Agarvadekar, R. Luis, and B. Viegas, 2012: A study of meteorologically and seismically induced water level and water temperature oscillations in an estuary located on the west coast of India (Arabian Sea). *Nat. Hazards Earth Syst. Sci.*, **12**, 1607–1620, doi:10.5194/nhess-12-1607-2012.

Mercer, D., J. Sheng, R.J. Greatbatch, and J. Bobanović, 2002: Barotropic waves generated by storms moving rapidly over shallow water. *J. Geophys. Res. Oceans*, **107**, 3152, doi:10.1029/2001JC001140.

Met Office, 2003: *Met Office rain radar data from the NIMROD system*. NCAS British Atmospheric Data Centre, http://catalogue.ceda.ac.uk/uuid/82adec1f896af6169112d09cc1174499.

Monserrat, S., A. Ibbetson, and A.J. Thorpe, 1991: Atmospheric gravity waves and the 'Rissaga' phenomenon. *Q. J. R. Meteorol. Soc.*, **117**, 553–570, doi:10.1002/qj.49711749907.

Monserrat, S., I. Vilibić, and A.B. Rabinovich, 2006: Meteotsunamis: Atmospherically induced destructive ocean waves in the tsunami frequency band. *Nat. Hazards Earth Syst. Sci.*, **6**, 1035– 1051, doi:10.5194/nhess-6-1035-2006.

Morris, R.M., 1986: The Spanish Plume – Testing the Forecasters Nerve. *Meteorol. Mag.*, **115**, 349–357.

Munk, W.H., 1949: Surf beats. *EOS, Transactions of the American Geophysical Union*, **30**, 849–854, doi:10.1029/TR030i006p00849.

Munk, W.H., F. Snodgrass, and G. Carrier, 1956: Edge Waves on the Continental Shelf. *Science*, **123**, 127–132.

Mutaqin, B.W., F. Lavigne, D.S. Hadmoko, and M.N. Ngalawani, 2019: Volcanic Eruption-Induced Tsunami in Indonesia: A Review. *IOP Conf. Ser.: Earth Environ. Sci.*, **256**, 012023, doi:10.1088/1755-1315/256/1/012023.

NOAA, 2019: *WRF NAMELIST.INPUT FILE DESCRIPTION*. 9 October 2019, https://esrl.noaa.gov/gsd/wrfportal/namelist_input_options.html.

O'Brien, L., J.M. Dudley, and F. Dias, 2013: Extreme wave events in Ireland: 14 680 BP–2012. *Nat. Hazards Earth Syst. Sci.*, **13**, 625–648, doi:10.5194/nhess-13-625-2013.

O'Gorman, P.A., and C.J. Muller, 2010: How closely do changes in surface and column water vapor follow Clausius–Clapeyron scaling in climate change simulations? *Environ. Res. Lett.*, **5**, 025207, doi:10.1088/1748-9326/5/2/025207.

Okal, E.A., J.N.J. Visser, and C.H. de Beer, 2014: The Dwarskersbos, South Africa local tsunami of August 27, 1969: field survey and simulation as a meteorological event. *Nat. Hazards*, **74**, 251–268, doi:10.1007/s11069-014-1205-5.

Olabarrieta, M., A. Valle-Levinson, C.J. Martinez, C. Pattiaratchi, and L. Shi, 2017: Meteotsunamis in the northeastern Gulf of Mexico and their possible link to El Niño Southern Oscillation. *Nat. Hazards*, **88**, 1325–1346, doi:10.1007/s11069-017-2922-3.

Orlić, M., 1980: About a possible occurrence of the Proudman resonance in the Adriatic. *Thalassia Jugoslavica*, **16**, 79–88.

Orlić, M., D. Belušić, I. Janeković, and M. Pasarić, 2010: Fresh evidence relating the great Adriatic surge of 21 June 1978 to mesoscale atmospheric forcing. *J. Geophys. Res. Oceans*, **115**, C06011, doi:10.1029/2009JC005777.

Oszoy, O., I.D. Haigh, M.P. Wadey, R.J. Nicholls, and N.C. Wells, 2016: High-frequency sea level variations and implications for coastal flooding: A case study of the Solent, United Kingdom. *Cont. Shelf Res.*, **122**, 1–13, doi:10.1016/j.csr.2016.03.021.

Palmer, M., et al., 2018: *UKCP18 Marine Report*. Met Office Hadley Centre, Exeter, pp. 133.

Papadopoulos, G.A., 1993: On some exceptional seismic (?) sea-waves in the Greek Archipelago. *Sci. Tsunami Hazards*, **11**, 25–34.

Papadopoulos, G.A., et al., 2014: Historical and pre-historical tsunamis in the Mediterranean and its connected seas: Geological signatures, generation mechanisms and coastal impacts. *Mar. Geol.*, **354**, 81–109, doi:10.1016/j.margeo.2014.04.014.

Papadopoulos, G.A., R. Caputo, B. McAdoo, S. Pavlides, V. Karastathis, A. Fokaefs, K. Orfanogiannaki, and S. Valkaniotis, 2006: The large tsunami of 26 December 2004: Field observations and eyewitnesses accounts from Sri Lanka, Maldives Is. and Thailand. *Earth Planets Space*, **58**, 233–241, doi:10.1186/BF03353383.

Pasquet, S., and I. Vilibić, 2013: Shelf edge reflection of atmospherically generated long ocean waves along the central U.S. East Coast. *Cont. Shelf Res.*, **66**, 1–8, doi:10.1016/j.csr.2013.06.007.

Pattiaratchi, C., and E.M.S. Wijeratne, 2014: Observations of meteorological tsunamis along the south-west Australian coast. *Nat. Hazards*, **74**, 281–303, doi:10.1007/s11069-014-1263-8.

Pattiaratchi, C.B., and E.M.S. Wijeratne, 2015: Are meteotsunamis an underrated hazard? *Phil. Trans. R. Soc. A*, **373**, 20140377, doi:10.1098/rsta.2014.0377.

Pellikka, H., J. Rauhala, K.K. Kahma, T. Stipa, H. Boman, and A. Kangas, 2014: Recent observations of meteotsunamis on the Finnish coast. *Nat. Hazards*, **74**, 197–215, doi:10.1007/978-3-319-12712-5_11.

Pingree, R.D., and L. Maddock, 1977: Tidal residuals in the English Channel. *J. Mar. Biol. Assoc. UK*, **57**, 339–354, doi:10.1017/S0025315400021792.

Poisson, B., C. Oliveros, and R. Pedreros, 2011: Is there a best source model of the Sumatra 2004 earthquake for simulating the consecutive tsunami? *Geophys. J. Int.*, **185**, 1365–1378, doi:10.1111/j.1365-246X.2011.05009.x.

Proudman, J., 1929: The Effects on the Sea of Changes in Atmospheric Pressure. *Geophys. J. Int.*, **2**, 197–209, doi:10.1111/j.1365-246X.1929.tb05408.x.

Pugh, D., and P. Woodworth, 2014: *Sea-level science: Understanding tides, surges, tsunamis and mean sea-level changes*. Cambridge University Press, Cambridge, 203 pp.

Rabinovich, A.B., 2009: Seiches and Harbor Oscillations. *Handbook of Coastal and Ocean Engineering*, World Sci., Singapore, pp. 193–236, doi:10.1142/9789812819307_0009.

Rabinovich, A.B., and S. Monserrat, 1998: Generation of Meteorological Tsunamis (Large Amplitude Seiches) Near the Balearic and Kuril Islands. *Nat. Hazards*, **18**, 27–55, doi:10.1023/A:1008096627047.

Rayleigh, O.M., 1916: On convection currents in a horizontal layer of fluid, when the higher temperature is on the under side. *Lond. Edinb. Dubl. Phil. Mag.*, **32**, 529–546, doi:10.1080/14786441608635602.

Renault, L., G. Vizoso, A. Jansá, J. Wilkin, and J. Tintoré, 2011: Toward the predictability of meteotsunamis in the Balearic Sea using regional nested atmosphere and ocean models. *Geophys. Res. Lett.*, **38**, L10601, doi:10.1029/2011GL047361.

Rhie, J., D. Dreger, R. Bürgmann, and B. Romanowicz, 2007: Slip of the 2004 Sumatra–Andaman Earthquake from Joint Inversion of Long-Period Global Seismic Waveforms and GPS Static Offsets. *Bull. Seismol. Soc. Am.*, **97**, S115–S127, doi:10.1785/0120050620.

Roger, J., and Y. Gunnell, 2012: Vulnerability of the Dover Strait to coseismic tsunami hazards: insights from numerical modelling. *Geophys. J. Int.*, **188**, 680–686, doi:10.1111/j.1365-246X.2011.05294.x.

Romero, R., M. Vich, and C. Ramis, 2019: A pragmatic approach for the numerical prediction of meteotsunamis in Ciutadella harbour (Balearic Islands). *Ocean Modell.*, **142**, 101441, doi:10.1016/j.ocemod.2019.101441.

Sandanbata, O., S. Watada, K. Satake, Y. Fukao, H. Sugioka, A. Ito, and H. Shiobara, 2018: Ray Tracing for Dispersive Tsunamis and Source Amplitude Estimation Based on Green's Law: Application to the 2015 Volcanic Tsunami Earthquake Near Torishima, South of Japan. *Pure Appl. Geophys.*, **175**, 1371–1385, doi:10.1007/s00024-017-1746-0.

Satake, K., 1988: Effects of bathymetry on tsunami propagation: Application of ray tracing to tsunamis. *Pure Appl. Geophys*., **126**, 27–36, doi:10.1007/BF00876912.

Seno, T., and K. Hirata, 2007: Did the 2004 Sumatra–Andaman Earthquake Involve a Component of Tsunami Earthquakes? *Bull. Seismol. Soc. Am.*, **97**, S296–S306, doi:10.1785/0120050615.

Šepić, J., and A.B. Rabinovich, 2014: Meteotsunami in the Great Lakes and on the Atlantic coast of the United States generated by the ''derecho'' of June 29–30, 2012. *Nat. Hazards*, **74**, 75–107, doi:10.1007/s11069-014-1310-5.

Šepić, J., and I. Vilibić, 2011: The development and implementation of a real-time meteotsunami warning network for the Adriatic Sea. *Nat. Hazards Earth Syst. Sci.*, **11**, 83–91, doi:10.5194/nhess-11-83-2011.

Šepić, J., I. Vilibić, A. Lafon, L. Macheboeuf, and Z. Ivanović, 2015b: High-frequency sea level oscillations in the Mediterranean and their connection to synoptic patterns. *Prog. Oceanogr.*, **137**, 284–298, doi:10.1016/j.pocean.2015.07.005.

Šepić, J., I. Vilibić, A. Rabinovich, and S. Tinti, 2018: Meteotsunami ("Marrobbio") of 25–26 June 2014 on the Southwestern Coast of Sicily, Italy. *Pure Appl. Geophys.*, **175**, 1573–1593, doi:10.1007/s00024-018-1827-8.

Šepić, J., I. Vilibić, A.B. Rabinovich, and S. Monserrat, 2015c: Widespread tsunami-like waves of 23-27 June in the Mediterranean and Black Seas generated by high-altitude atmospheric forcing. *Sci. Rep.*, **5**, 11682, doi:10.1038/srep11682.

Šepić, J., I. Vilibić, and I. Fine, 2015a: Northern Adriatic meteorological tsunamis: Assessment of their potential through ocean modelling experiments. *J. Geophys. Res. Oceans*, **120**, 2993–3010, doi:10.1002/2015JC010795.

Šepić, J., I. Vilibić, and S. Monserrat, 2009: Teleconnections between the Adriatic and the Balearic meteotsunamis. *Phys. Chem. Earth.*, **34**, 928–937, doi:10.1016/j.pce.2009.08.007.

Šepić, J., I. Vilibić, N.S. Mahović, 2012: Northern Adriatic meteorological tsunamis: Observations, link to the atmosphere, and predictability. *J. Geophys. Res. Oceans*, **117**, C02002, doi:10.1029/2011JC007608.

Šepić, J., I. Vilibić, and S. Monserrat, 2016: Quantifying the probability of meteotsunami occurrence from synoptic atmospheric patterns. *Geophys. Res. Lett.*, **43**, 10377–10384, doi:10.1002/2016GL070754.

Sethian, J.A., 1996: A fast marching level set method for monotonically advancing fronts. *Proc. Natl. Acad. Sci. USA*, **93**, 1591–1595, doi:10.1073/pnas.93.4.1591.

Sheremet, A., U. Gravois, and V. Shrira, 2016: Observations of meteotsunami on the Louisana shelf: a lone soliton with a soliton pack. *Nat. Hazards*, **84**, 471–492, doi:10.1007/s11069-016-2446-2.

Shi, L., M. Olabarrieta, A. Valle-Levinson, and J.C. Warner, 2019: Relevance of wind stress and wave-dependent ocean surface roughness on the generation of winter meteotsunamis in the Northern Gulf of Mexico. *Ocean Modell.*, **140**, 101408, doi:10.1016/j.ocemod.2019.101408.

Shiki, T., Y. Tsuji, T. Yamazaki, and K. Minoura, 2008: *Tsunamiites – Features and Implications*. Elsevier, Amsterdam, 411 pp.

Sibley, A., D. Cox, D. Long, D. Tappin, and K. Horsburgh, 2016: Meteorologically generated tsunami-like waves in the North Sea on 1/2 July 2015 and 28 May 2008. *Weather*, **71**, 68–74, doi:10.1002/wea.2696.

Skamarock, W.C., J.B. Klemp, J. Dudhia, D.O. Gill, D.M. Barker, M.G. Duda, X.Y. Huang, W. Wang, and J.G. Powers, 2008: *A Description of the Advanced Research WRF Version 3. NCAR Tech. Note NCAR/TN-475+STR.* pp. 113, doi:10.5065/D68S4MVH.

Sorensen, R.M., 2006: *Basic Coastal Engineering*. Third Edition, Springer Science & Business Media, New York, pp. 324.

Stokes, G.G., 1847: On the theory of oscillatory waves. *Trans. Cambridge Philos. Soc.*, **8**, 441–455. See Stokes 1880, Vol. 1. Appendices and Suppl.

Tanaka, K., 2010: Atmospheric pressure-wave bands around a cold front resulted in a meteotsunami in the East China Sea in February 2009. *Nat. Hazards Earth Syst. Sci.*, **10**, 2599–2610, doi:10.5194/nhess-10-2599-2010.

Tappin, D.R., A. Sibley, K. Horsburgh, C. Daubord, D. Cox, and D. Long, 2013: The English Channel 'tsunami' of 27 June 2011 – a probable meteorological source. *Weather*, **68**, 144–152, doi:10.1002/wea.2061.

Thiebaut, S., and R. Vennell, 2011: Resonance of long waves generated by storms obliquely crossing shelf topography in a rotating ocean. *J. Fluid Mech.*, **682**, 261–288, doi:10.1017/jfm.2011.221.

Thomson, R.E., A.B. Rabinovich, I.V. Fine, D.C. Sinnott, A. McCarthy, N.A.S. Sutherland, and L.K. Neil, 2009: Meteorological tsunamis on the coasts of British Columbia and Washington. *Phys. Chem. Earth.*, **34**, 971–988, doi:10.1016/j.pce.2009.10.003.

Tintoré, J., et al., 2013: SOCIB: The Balearic Islands Coastal Ocean Observing and Forecasting System Responding to Science, Technology and Society Needs. *Mar. Technol. Soc. J.*, **47**, 101–117, doi:10.4031/MTSJ.47.1.10.

Titov, V., A.B. Rabinovich, H.O. Mofjeld, R.E. Thomson, and F.I. González, 2005: The Global Reach of the 26 December 2004 Sumatra Tsunami. *Science*, **309**, 2045–2048, doi:10.1126/science.1114576.

Ulutas, E., 2013: Comparison of the seafloor displacement from uniform and non-uniform slip models on tsunami simulation of the 2011 Tohoku-Oki earthquake. *J. Asian Earth Sci.*, **62**, 568–585, doi:10.1016/j.jseaes.2012.11.007.

Ursell, F., 1952: Edge waves on a sloping beach. *P. Roy. Soc. A-Math. Phy.*, **214**, 79–97, doi:10.1098/rspa.1952.0152.

Vatvani, D., A. van Dongeren, J. Kroos, and M. van Ormondt, 2018: Simulation of 2017 meteo-tsunami event along the Dutch Coast. *2018 Ocean Sciences Meeting*, 11–16 February 2018, Portland, Oregon, American Geophysical Union, A107-A109.

Vennell, R., 2007: Long Barotropic Waves Generated by a Storm Crossing Topography. *J. Phys. Oceanogr.*, **37**, 2809–2823, doi:10.1175/2007JPO3687.1.

Vennell, R., 2010: Resonance and trapping of topographic transient ocean waves generated by a moving atmospheric disturbance. *J. Fluid. Mech.*, **650**, 427–442, doi:10.1017/S0022112009993739.

Vilibić, I., 2008: Numerical simulations of the Proudman resonance. *Cont. Shelf Res.*, **28**, 574–581, doi:10.1016/j.csr.2007.11.005.

Vilibić, I., and J. Šepić, 2017: Global mapping of nonseismic sea level oscillations at tsunami timescales. *Sci. Rep.*, **7**, 40818, doi:10.1038/srep40818.

Vilibić, I., J. Šepić, A.B. Rabinovich, and S. Monserrat, 2016: Modern approaches in meteotsunami research and early warning. *Front. Mar. Sci.*, **3**, 57, doi:10.3389/fmars.2016.00057.

Vilibić, I., J. Šepić, B. Ranguelov, N.S. Mahović, and S. Tinti, 2010: Possible atmospheric origin of the 7 May 2007 western Black Sea shelf tsunami event. *J. Geophys. Res. Oceans*, **115**, C07006, doi:10.1029/2009JC005904.

Vilibić, I., S. Monserrat, A. Rabinovich, and H. Mihanović, 2008: Numerical Modelling of the Destructive Meteotsunami of 15 June, 2006 on the Coast of the Balearic Islands. *Pure Appl. Geophys.*, **165**, 2169–2195, doi:10.1007/s00024-008-0426-5.

Vilibić, I., S. Monserrat, and A.B. Rabinovich, 2014: Meteorological tsunamis on the US East Coast and in other regions of the World Ocean. *Nat. Hazards*, **74**, 1–9, doi:10.1007/s11069-014-1350-x.

Vincent, C.L., A.N. Hahmann, and M.C. Kelly, 2012: Idealized Mesoscale Model Simulations of Open Cellular Convection Over the Sea. *Bound.-Lay. Meteorol.*, **142**, 103–121, doi:10.1007/s10546-011-9664-7.

Vučetić, T., I. Vilibić, S. Tinti, and A. Maramai, 2009: The Great Adriatic flood of 21 June 1978 revisited: An overview of the reports. *Phys. Chem. Earth.*, **34**, 894–903, doi:10.1016/j.pce.2009.08.005.

Wahl, T., 2017: Sea-level rise and storm surges, relationship status: Complicated! *Environ. Res. Lett.*, **12**, 111001, doi:10.1088/1748-9326/aa8eba.

Weisman, M.L., and J.B. Klemp, 1982: The Dependence of Numerically Simulated Convective Storms on Vertical Wind Shear and Buoyancy. *Mon. Weather Rev.*, **110**, 504–520, doi:10.1175/1520-0493(1982)110<0504:TDONSC>2.0.CO;2.

Weisman, M.L., W.C. Skamarock, and J.B. Klemp, 1997: The Resolution Dependence of Explicitly Modeled Convective Systems. *Mon. Weather Rev.*, **125**, 527–548, doi:10.1175/1520-0493(1997)125<0527:TRDOEM>2.0.CO;2.

Wertman, C.A., R.M. Yablonsky, Y. Shen, J. Merrill, C.R. Kincaid, and R.A. Pockalny, 2014: Mesoscale convective system surface pressure anomalies responsible for meteotsunamis along the U.S. East Coast on June 13th, 2013. *Sci. Rep.*, **4**, 7143, doi:10.1038/srep07143.

Whitmore, P., and B. Knight, 2014: Meteotsunami forecasting: sensitivities demonstrated by the 2008 Boothbay, Maine, event. *Nat. Hazards*, **74**, 11–23, doi:10.1007/978-3-319-12712-5_2.

Wijeratne, E.M.S., P.L. Woodworth, and D.T. Pugh, 2010: Meteorological and internal wave forcing of seiches along the Sri Lanka coast. *J. Geophys. Res. Oceans*, **115**, C03014, doi:10.1029/2009JC005673.

Williams, D.A., 2019a: *Proudman resonance with tides, bathymetry and variable atmospheric forcings*. Meteotsunami generation, amplification and occurrence in north-west Europe, PhD dissertation, University of Liverpool, pp. 225.

Williams, D.A., 2019b: *An 8-yr meteotsunami climatology across north-west Europe: 2010–2017*. Meteotsunami generation, amplification and occurrence in north-west Europe, PhD dissertation, University of Liverpool, pp. 225.

Williams, D.A., K.J. Horsburgh, D.M. Schultz, and C.W. Hughes, 2019: Examination of Generation Mechanisms for an English Channel Meteotsunami: Combining Observations and Modeling. *J. Phys. Oceanogr.*, **49**, 103–120, doi:10.1175/JPO-D-18-0161.1.

Woodworth, P.L., and D.E. Smith, 2003: A One Year Comparison of Radar and Bubbler Tide Gauges at Liverpool. *Int. Hydrogr. Rev.*, **4**, 42–49.

Woolf, D.K., P.G. Challenor, and P.D. Cotton, 2002: Variability and predictability of the North Atlantic wave climate. *J. Geophys. Res. Oceans*, **107**, 3145, doi:10.1029/2001JC001124.

Wünnemann, K., G.S. Collins, and R. Weiss, 2010: Impact of a cosmic body into Earth's ocean and the generation of large tsunami waves: insight from numerical modelling. *Rev. Geophys.*, **48**, RG4006, doi:8755-1209/10/2009RG000308.

Yoshida, Y., H. Ueno, D. Muto, and S. Aoki, 2011: Source process of the 2011 off the Pacific coast of Tohoku Earthquake with the combination of teleseismic and strong motion data. *Earth Planets Space*, **63**, 565–569, doi:10.5047/eps.2011.05.011.